Elucidating the Role of Lipid Metabolism and Peroxidation in Ferroptosis

Noelle Yvonne Reimers

A dissertation

submitted in partial fulfillment of the

requirements for the degree of

Doctor of Philosophy

University of Washington

2026

Reading Committee:

Libin Xu, Chair

Rheem Totah

Miklos Guttman

Program Authorized to Offer Degree:

Medicinal Chemistry

University of Washington

Abstract

Elucidating the Role of Lipid Metabolism and Peroxidation in Ferroptosis

Noelle Yvonne Reimers

Chair of the Supervisory Committee:

Libin Xu

Medicinal Chemistry

Ferroptosis is a form of cell death that is dependent on the iron-mediated peroxidation of lipids within a cell. Since its discovery in 2012, ferroptosis has been implicated in many disease states, including neurodegeneration, ischemia reperfusion injury, atherosclerosis, and cancer, making it an attractive therapeutic target. However, much is still unknown about the regulation of ferroptosis, hindering our ability to modulate this process. Since the peroxidation of lipids within a cell is a hallmark of ferroptosis, this thesis aims to explore the role that lipid metabolism and peroxidation play in mediating ferroptotic death by examining the metabolism, oxidation, location, and genetic regulation of lipids in cells undergoing ferroptosis. In this work, we first developed a strategy to trace the metabolism of a peroxidation-prone polyunsaturated fatty acid (PUFA), arachidonic acid, in-vitro using stable isotope labeling and mass spectrometry-based lipidomics. The strategy was then applied to other common PUFAs, including conjugated and nonconjugated linoleic acid. To facilitate the identification of potential lipid peroxidation products in complex lipidomics datasets, we created an experimental oxidized lipid

library by performing in-vitro peroxidation of various oxidizable lipids and characterizing the resulting products using mass spectrometry. Next, we sought to examine the subcellular location and morphological changes associated with lipid peroxidation in cells using stimulated Raman scattering (SRS) and confocal microscopy. Finally, we sought to further characterize the effect of genetic ablation of the enzyme acyl-CoA synthetase long chain family member 4, or *ACSL4*, which has been shown to confer robust ferroptosis protection in multiple cell types. We employed various -omics methodologies, including lipidomics, transcriptomics, sterolomics, and proteomics, to improve our understanding of the mechanism behind the ferroptosis resistance afforded by *ACSL4* knockout. The collective findings and implications of this work as well as potential future directions will be discussed in the final chapter.

Acknowledgements

A PhD is typically considered individual research, but for me, no part of this journey has been completed alone. First and foremost, I would like to thank my advisor, Libin Xu, who has been along this journey with me every step of the way. This project would not have been remotely possible without his scientific expertise, patience, kindness, and support throughout the years. I truly could not have asked for a better person to work with and learn from during my PhD. Libin's lab is a perfect reflection of who he is as an advisor; collaborative, supportive, and a wonderful place to perform research. I have learned so much from all of my labmates and acknowledge all of them for their contributions to this project and to my graduate school experience.

Specifically, I would like to thank Quynh Do, who graduated from the lab in 2022, for starting this lipid peroxidation project, training me on everything for my first year in the lab, and setting a wonderful example of a graduate student who I wanted to be. Rutan Zhang, who taught me so much about mass spectrometry and helped me immensely with proteomics experiments, especially during the last few months of my project. Vanessa Lopez, for being endlessly supportive every step of the way and for teaching me transcriptomics. Amy Li, for teaching me sterolomics and taking care of so many lab management responsibilities. Marie Brzoska, for always being open to chat and share her advice throughout all parts of grad school. Ryan Nguyen and Linxi Zhu, who are also my cohort members, for going through this journey together and supporting each other every step of the way. Ryan Seguin, for making the lab a safe and productive place to work. I would also like to thank our newest lab members, Griffin Rangel, Corrina Cooper, and Anvitaa Anandkumar, for bringing a new energy to the lab and making it a brighter place to be. Last but certainly not least, I would like to thank Angela Guo, who joined our lab as an undergraduate and ended up working on this project with me for three years. Angela contributed immensely to this project, managing cell culture, flow cytometry, transcriptomics, preparing dozens of samples for SRS and learning confocal microscopy. Angela became a friend to me as well and the hours at the bench passed so much faster when she was by my side.

I would also like to thank my research mentors from outside the Xu lab. I had the opportunity to perform undergraduate research under Gregory Ducker at the University of Utah, who opened my eyes to the world of lipid metabolism and greatly encouraged me to pursue graduate education. I would like to thank those who contributed to my internships at Recursion Pharmaceuticals and Merck, specifically Chad Bradford, Kevin Jessing, Imoh Etim, and Tanvi Desai. These experiences shaped who I am as a researcher and a scientist, and I am grateful to everyone who took time out of their busy lives to teach me along the way.

I would like to thank my thesis committee, Rheem Totah, Miklos Guttman, Abhi Nath, and David Beck, for their insights, advice, and support in this project. I would like to thank the rest of the Medicinal Chemistry faculty as well for providing an excellent educational experience and cultivating a departmental culture of camaraderie, collaboration, and support. I also thank the administrative staff of Medicinal Chemistry and the School of Pharmacy, specifically Sarah Lenti and Julia Kohut, for supporting all aspects of the department, enabling all of us to be successful, and for generally being wonderful people. I also thank the funding sources that made this work possible, including the Pharmaceutical Sciences Training Program and National Institutes of Health.

Finally, I would like to thank my support system outside the lab. Firstly, I thank my dad, Troy, who has always been my biggest supporter in life and continues to push me to be the best version of myself. None of this would have been possible without him. My sister, Natalie, who has been my best friend since the day she was born. My mom, Yvette, for always doing her best to brighten my day. My grandparents, Bruce, Carol, Bonnie and Larry, for inspiring me to pursue higher education and supporting me throughout. My late grandma Gerda, who taught me that education is the most valuable thing a person can have. My partner Justin, for supporting me wholly, always being willing to listen, and always making me the best coffee. My Seattle friends, for providing me with a break from my studies and always being ready for an adventure. Lastly, my dearest cat, Kitty, who I adopted when I was a first-year, for always being willing to provide cuddles and distractions whenever I need them (and when I don't!).

Contents

Chapter 1: Introduction 12
Ferroptosis 12
Lipid Peroxidation 13
Glycerolipids and glycerophospholipids 17
Sterols 22
Mass Spectrometry-Based Lipidomics 30
Summary and Dissertation Overview 32
Figures 34
Figure 1.1: Schematic of Ferroptosis 34
Figure 1.2: Lipid peroxidation mechanisms. 35
Figure 1.3: Structures of glycerophospholipids and notable fatty acids 36
Figure 1.4: Schematic of phospholipid biosynthesis and remodeling via Kennedy, CDP-DAG, and Lands cycles 37
Figure 1.5: Scheme of sterol synthesis and its role in mediating ferroptosis. 38
Figure 1.6: Structures and rate constant of notable isoprenoid-derived lipids and polyunsaturated fatty acids 39
Chapter 2: Isotope-labeling Lipidomics 40
Introduction 40
Methods 43
Materials: 43
Lipid internal standards: 43
Cell Culture: 43
Lipid Extraction: 44
HILIC-IM-MS Method 44
Data Analysis 45
Results and Discussion 46
Development of D-Tracer 46
Incorporation of Deuterated Arachidonic Acid 47
Incorporation of Deuterated Conjugated and Nonconjugated Linoleic Acid 50
Conclusion 51
Figures 52
Figure 2.1: A) Schematic of the Python-based software D-Tracer 52
Figure 2.2: A) Examples of signature doublet and triplet peaks 53
Figure 2.3: Flow cytometry with C11-BODIPY stained HT-1080 cells confirming increased levels of lipid peroxidation 54
Figure 2.4: Pie charts representing the percent of each lipid class 55

Figure 2.5: Scheme of the biosynthetic pathway of phospholipids via the cytidine diphosphate diacylglycerol (CDP-DAG) intermediate 56
Figure 2.6: Bar charts representing the approximate moles 57
Figure 2.7: Ratio of oxidized (m+14 Da) to parent PE(38:4) 58
Chapter 3: Development and application of an oxylipid LC-MS database 59
Introduction 59
Methods 60
In-vitro phospholipid oxidation: 60
MS analysis of oxylipid products: 61
Generation of theoretical spectral libraries: 62
Creation of experimental oxylipid database using Skyline: 62
Lipidomic analysis of HT-1080 cells: 63
Results: 63
Detection and identification of oxylipids from in-vitro oxidation of PLPC: 63
Oxidized lipids elute later than their parents proportionally to their degree of oxidation 64
Lipid oxidation products are not significantly compacted compared to the parents 64
LPPTiger software can be used to generate theoretical in-silico spectral libraries 65
Oxygen addition and truncated lipid oxidation products are formed from in-vitro oxidation of phospholipids 66
Application of the oxidized lipid library to HT-1080 cells treated with conjugated (CLA) and nonconjugated linoleic acid (NLA). 67
Linoleic acid-containing PC and PE parent lipids are detected and identified using the oxidized lipid library. 68
Lipid oxidation products derived from PE linoleic acid containing parents are detected and identified in CLA, but not NLA, treated cells using the oxidized lipid library. 68
Discussion 69
Figures: 72
Figure 3.1: Schematic of in-vitro oxidation 72
Figure 3.2: Results of in-vitro oxidation of palmitate-linoleate phosphatidylcholine (PLPC) 73
Figure 3.3: Mechanism of Hock rearrangement 74
Figure 3.4: Observed retention time shift with oxidation of phosphatidylcholine (PC) lipid species. 75
Figure 3.5: Depiction of collision cross section (CCS) and resulting compaction factor (C). 76
Figure 3.6: Conformational analysis of lipid oxidation products and parents using collision cross section (CCS). 77
Figure 3.7: Schematic of LPPTiger software. 78
Figure 3.9: Overview of identified oxylipids and parents contained in the oxidized lipid library 80
Figure 3.10: Mechanisms of lipid oxidation 81

Figure 3.11: Identification of parent lipid PE(16:0/18:2) (A) and oxidation product PE(16:0/18:2+OH) (B) using the oxidized lipid library in Skyline from CLA-treated cells. 82
Table 3.1: Lipids used in this study 83
Table 3.2: Oxidized lipids and parent precursors contained in the oxylipid database 84
Table 3.3: Parents and oxidation products detected in NLA and CLA treated HT-1080 cells 88
Chapter 4: Detection of Lipid Peroxidation in Cells Undergoing Ferroptosis Using Stimulated Raman Scattering Microscopy and Confocal Microscopy 90
Introduction: 90
Methods: 92
Cell Culture: 92
Stimulated Raman Scattering Microscopy Sample Preparation: 92
Flow Cytometry: 93
Hyperspectral SRS microscopy 93
Laser Scanning Confocal Microscopy 94
Results: 94
SRS imaging reveals morphological changes associated with ferroptosis 94
Confocal microscopy shows appearance of lipid droplets with exogenous fatty acid treatment 95
Isotopically labeling fatty acids does not affect their ferroptosis-inducing potential 96
SRS imaging shows loss of C-D signal in terminally labeled fatty acids 97
SRS spectral shift indicates differential oxidation mechanisms between conjugated and nonconjugated linoleic acid 98
Discussion 100
Figures: 102
Figure 4.1: SRS imaging of HT-1080 cells during RSL3-induced ferroptosis 102
Figure 4.2 A: Confocal imaging of HT-1080 104
Figure 4.2 B: Confocal imaging of HT-1080 cells 105
Figure 4.2 C: Confocal imaging of HT-1080 cells 106
Figure 4.2 D: Confocal imaging of HT-1080 cells 107
Figure 4.3: Structures of fatty acids used in this study and their isotopically labeled analogs. 108
Figure 4.4: Assessment of lipid peroxidation in HT-1080 cells 109
Figure 4.5: SRS spectral and signal intensity changes in cells incorporated with deuterated arachidonic acid (AA) 110
Figure 4.6: SRS imaging of lipid peroxidation of conjugated linoleic acid (CLA 18:2). 111
Figure 4.7: SRS imaging of lipid peroxidation of nonconjugated linoleic acid (NLA 18:2). 112
Chapter 5: Multi-omic Characterization of *ACSL4* Knockout in the Context of Ferroptosis 113
Introduction 113
Methods: 115
Cell culture: 115

C11-BODIPY flow cytometry: 115
Cell viability dose response assay: 115
Dual-isotope labeling lipidomics: 116
Targeted diPUFA lipid analysis: 116
Transcriptomics 117
Global Proteomics 117
Sterolomics: 118
Pulldown proteomics 119
Click-chemistry Western Blot: 120
Results: 120
ACSL4 knockout reduces ferroptosis sensitivity in HT-1080 cells. 120
ACSL4 knockout reduces but does not completely ablate arachidonic acid incorporation into phospholipids. 121
The lipidomes of KO and WT cells differ significantly in their response to RSL3. 121
DiPUFAs are significantly lower in abundance in KO than in WT cells. 122
Oxidation products of diPUFAs are identified and are more abundant in WT than in KO cells when treated with AA and RSL3 123
ACSL1 is upregulated in ACSL4 KO cells relative to WT but is not further induced by AA treatment. 125
Transcriptomics reveals altered expression of lipid metabolism regulator genes 125
Global proteomics reveals differential responses to ferroptosis by WT and ACSL4-KO cells. 127
Lipid transport protein FABP5 is upregulated in ACSL4 KO cells relative to WT. 128
KO cells have increased sterol abundance relative to WT, suggesting an alternative protective mechanism of ASCL4 KO. 128
Pulldown proteomics reveals enrichment of lipid-carbonyl-modified ER and mitochondrial membrane proteins in WT compared to ACSL4-KO HT-1080 cells. 129
Discussion: 131
Figures: 136
Figure 5.1: ACSL4 knockout confers ferroptosis resistance in HT-1080 cells 136
Figure 5.2: Incorporation of dAA into phospholipids in WT and ACSL4-KO cells. 137
Figure 5.3: Characterization of diPUFA lipid species. 138
Figure 5.4: Targeted analysis of diPUFA parent species in WT and ACSL4-KO cells. 139
Figure 5.5: Identification of DAPC oxidation products. 140
Figure 5.6A: Targeted analysis of +1O diPUFA oxidation products. 141
Figure 5.6B: Targeted analysis of +3O diPUFA oxidation products. 142
Figure 5.6C: Targeted analysis of truncated diPUFA oxidation products. 143
Figure 5.7: Differential expression of lipid metabolic regulator genes between WT and ACSL4-KO cells. 144

Figure 5.8: Differential expression of protein regulators in WT and ACSL4-KO cells 145
Figure 5.9: Sterolomics analysis of WT and ACSL4-KO cells. 146
Figure 5.10: Western blot assessment of lipid-adducted proteins in WT and ACSL4-KO cells by protein pulldown. 147
Figure 5.11: Venn diagrams of the identified carbonylated proteins in WT and ACSL4-KO cells.. 148
Figure 5.12: KEGG endoplasmic reticulum proteins enriched in WT compared to KO RSL3+AA treated cells 149
Figure 5.13: KEGG cholesterol metabolism proteins enriched in WT compared to KO RSL3+AA treated cells 150
Tables 151
Table 5.0: DiPUFA MRM MS parameters 151
Table 5.1: Differential expression of selected genes of interest from RNA sequencing. 153
Table 5.2: Global proteomics differential expression analysis. 155
Table 5.3: Top ten cellular compartment (CC) GO terms corresponding to carbonylated proteins enriched in WT versus KO RSL3+AA treated cells 156
Table 5.4: KEGG enriched pathways in carbonylated proteins from WT versus KO RSL3+AA treated cells 159
Chapter 6: Summary and Future Directions 163
References 170

Chapter 1: Introduction

Ferroptosis

Ferroptosis is a sub-type of regulated cell death that is distinct from other forms of cell death such as apoptosis and necroptosis. It was formally named by the Stockwell lab in 2012, though it had been observed as early as 2008 in the Conrad lab (Dixon et al., 2012; Seiler et al., 2008). It is iron dependent and mediated by lipid peroxidation (Stockwell et al., 2017). However, the exact biochemical steps leading to ferroptosis remain unclear.

In 2003, during a drug screening for cancer therapeutics in the Stockwell lab, a small molecule called erastin was found to induce a nonapoptotic form of cell death in cells with the RAS oncogenic mutation (Dolma et al., 2003). During another small molecule screening in 2008, another small molecule called RAS-selective-lethal 3 (RSL3) was found to induce a similar form of cell death in RAS mutated cancer cells (Yang & Stockwell, 2008). Further work was completed by the Stockwell lab to determine the nature of this form of cell death. It was found that this type of death was distinct from other established forms of cell death including necroptosis and apoptosis. While necroptosis and apoptosis inhibitors were ineffective at rescuing cells treated with erastin or RSL3, the iron chelator deferoxamine and antioxidant Trolox were able to rescue the cells from death. In addition, it was shown that the cells exhibited a high degree of lipid peroxide buildup preceding death. These unique characteristics led the researchers to coin the term ferroptosis for this new form of regulated cell death that is dependent on the presence of free iron and mediated by lipid peroxide buildup.

Both RSL3 and erastin induce ferroptosis through the inhibition of glutathione peroxidase 4 (GPX4) (Figure 1.1). There are 8 known glutathione peroxidase enzymes that function by using glutathione to reduce peroxides into non-toxic alcohols. GPX4 is a glutathione peroxidase that specifically detoxifies hydroperoxides from phospholipids and cholesterol in cellular membranes (Weaver & Skouta, 2022). Since the main role of GPX4 is to prevent the buildup of lipid peroxides in cell

membranes, and inhibiting its function induces ferroptosis, it was determined that lipid peroxidation is a hallmark of ferroptosis. RSL3 and ML162, another commonly used ferroptosis inducer, inhibit GPX4 through allosteric inactivation of its active site (H. Liu et al., 2022). Erastin induces ferroptosis by inhibiting the solute carrier protein known as System x_C^-, which depletes intracellular glutathione. System x_C^- is a cystine/glutamate antiporter that imports cystine by exporting glutamate. Once in the cell, the cystine is converted to cysteine and used in the synthesis of glutathione, a necessary cofactor for GPX4 (Dixon et al., 2014).

While targeting the GPX4/glutathione axis remains the most common method used for inducing ferroptosis, recent studies have demonstrated the involvement of other enzymatic networks in the regulation of ferroptosis. Lipid metabolism, iron metabolism, and coenzyme Q10 have all been shown to modulate ferroptosis in cells (Du & Guo, 2022). This thesis will examine the roles of lipid and sterol metabolism, oxidation, and distribution in the regulation of ferroptotic death.

Lipid Peroxidation

In biological environments, lipid peroxidation can be initiated by the abstraction of a reactive hydrogen atom from a lipid molecule by seeding radicals, such as alkoxyl or hydroxyl radicals, which can be formed from Fenton reactions between iron and hydrogen peroxide or lipid peroxides. The seeding lipid hydroperoxides can be formed from reactions catalyzed by lipoxygenases (Yang et al., 2016). The lipid-derived carbon radicals then react with molecular oxygen to generate a peroxyl radical, which propagates the chain reaction. The propagation step can proceed via two mechanisms: hydrogen atom transfer (HAT) and peroxyl radical addition (PRA). HAT proceeds with the abstraction of a hydrogen atom from an oxidizable lipid molecule. The resulting carbon radical reacts with molecular oxygen at a diffusion-controlled rate and generates a peroxyl radical, which then continues propagating the chain reaction. PRA proceeds with the addition of a peroxyl radical directly to a C=C double bond, often in a conjugated system containing two or more C=C double bonds. The resulting carbon radical can undergo

either intramolecular homolytic substitution (S_Hi) to give an epoxide or add another molecular oxygen to generate a new peroxyl radical (see Figure 1.2 for a scheme of HAT and PRA). Both the epoxide and the peroxyl radical can continue propagating the chain reaction. The rate constants of HAT (k_H) and PRA (k_{add}) can be measured using two generations of linoleate radical clock (Do et al., 2021; Roschek et al., 2006), which take advantage of the isomerization between trans,cis- and trans,trans-dienyl peroxyl radicals resulting from linoleate peroxidation. The overall rate constant of peroxidation is denoted as k_p, which is the sum of k_H and k_{add}. On the other hand, endogenous phenolic compounds, such as vitamin E and reduced form of coenzyme Q_{10}, can act as radical-trapping antioxidants because they are excellent H-atom donors and the resulting aroxyl radicals do not readily propagate the chain reactions due to their inherit stability.

Fatty acids, typically attached to phospholipid headgroups, can be prone to peroxidation. Fatty acids are alkyl chains terminating in a carboxylic acid. The chains vary in length, but most are between 14 and 22 carbons in eukaryotes (Cockcroft, 2021). They can be fully saturated, monounsaturated, or polyunsaturated. The accepted nomenclature for fatty acids is XX:Y where XX is the length of the alkyl chain and Y is the number of desaturations (Liebisch et al., 2020). Fully saturated fatty acids (SFAs) only have single bonds between all the carbons in the chain. Monounsaturated fatty acids (MUFAs) have one double bond in the carbon chain, typically at the omega-3, -6, or -9 position. Polyunsaturated fatty acids (PUFAs) can have as many as 6 double bonds in their carbon chain. These unsaturations can be conjugated, meaning they occur on neighboring carbons, or nonconjugated, meaning there is one or more carbon between each double bond. Nonconjugated fatty acids are more common in eukaryotes than their conjugated counterparts. The differences in length and degree of unsaturation have significant impacts on the properties of the fatty acids and their function.

MUFAs and especially PUFAs are more fluid than SFAs due to the ‘kinks’ in their carbon chain created by the presence of double bonds. Rigidity and fluidity are both important properties of cellular membranes, and therefore a careful balance of SFAs, MUFAs, and PUFAs must be maintained to uphold

the structural integrity of cell membranes (de Carvalho & Caramujo, 2018). For phospholipids, the most common configuration is to have an SFA in the sn-1 position of the glycerol backbone and a PUFA or a MUFA in the sn-2 position (Lordan et al., 2017). This arrangement allows cells to maintain proper membrane structure under a wide variety of conditions. While membrane integrity is an important characteristic of fatty acid structure, more relevant to this discussion is the role that fatty acid structure plays in mediating lipid peroxidation and ferroptosis.

As mentioned previously, lipid peroxidation can proceed via HAT or PRA. In HAT, the first and rate-limiting step of lipid peroxidation is the initial hydrogen atom abstraction. SFAs are not typically susceptible to lipid peroxidation due to the stronger C-H bonds and the resulting radicals not being stabilized by resonance structures. Therefore, it would be very energetically unfavorable for an SFA to undergo lipid peroxidation. MUFAs are not particularly oxidizable, as the lack of multiple double bonds lowers the resonance stabilization of radicals resulting from HAT. That said, peroxidation of MUFAs, such as oleic acid (18:1) has been observed (Howard & Ingold, 1967). The k_p for oleic acid was observed to be 0.9 $M^{-1}s^{-1}$ at 30˚ C. Due to their low propensity for oxidation, treatment with MUFAs has been shown to confer ferroptosis resistance in cells (Magtanong et al., 2019)

PUFAs are most susceptible to lipid peroxidation due to the much weaker bisallylic C-H bonds as the resulting radicals are stabilized by resonance with the neighboring double bonds. Nonconjugated linoleic acid (NLA 18:2) is a common omega-6 fatty acid whose peroxidation constant was measured to be 62 $M^{-1}s^{-1}$ at 30˚ C (Howard & Ingold, 1967). Its conjugated counterpart, conjugated linoleic acid (CLA 18:2), was shown to have a k_p of 118 0.9 $M^{-1}s^{-1}$, undergoing primarily PRA rather than HAT as observed for NLA 18:2 (Do et al., 2021). Therefore, the peroxidation potential of these two isomeric lipids varies greatly depending on the location of their double bonds. The number of double bonds also has a significant impact because more double bonds provide more potential sites for peroxidation. Nonconjugated linolenic acid (NLA 18:3) has a rate constant of 144 $M^{-1}s^{-1}$, while conjugated linolenic acid (CLA 18:3) has a rate constant nearly ten times higher at 1235 $M^{-1}s^{-1}$. Like CLA 18:2, CLA 18:3

peroxidation proceeds mainly via PRA while NLA 18:3 proceeds mainly via HAT (Do et al., 2021). Nonconjugated fatty acids are more common in mammalian systems, but CLAs have been found in certain plants (Yasui et al., 2005). In fact, CLA 18:3 is so prone to oxidation that it is able to induce ferroptotic death in HT-1080 cells without the addition of any other ferroptosis inducers (Do et al., 2023).

Arachidonic acid (AA, 20:4) is another common nonconjugated PUFA that is susceptible to both enzymatic and nonenzymatic lipid peroxidation. It is an essential omega-6 fatty acid that has many important physiological roles, notably acting as a precursor for prostaglandins and leukotrienes that regulate immune response, inflammation, angiogenesis, and more (Wang et al., 2021a). It can be synthesized in eukaryotes from the elongation and desaturation of linoleic acid (18:2), but dietary intake is a primary source. The peroxidation rate constant of AA is 197 $M^{-1}s^{-1}$ and it proceeds mainly via HAT (L. Xu et al., 2009). This rate constant does not take into account the enzymatic peroxidation of arachidonic acid, which proceeds via enzymes such as cyclooxygenases, lipoxygenase, and cytochrome P450 enzymes (Wang et al., 2021b). However, the membrane lipid peroxidation reactions that drive ferroptosis occur primarily via non-enzymatic lipid peroxidation, so this rate constant is relevant to the role that AA contributes to ferroptosis (Yan et al., 2021). Eicosapentaenoic acid (EPA, 20:5) is an omega-3 nonconjugated fatty acid similar in structure to AA, but with one additional unsaturation degree. Its peroxidation also proceeds mainly via HAT, and its k_p is 249 $M^{-1}s^{-1}$. Docohexaenoic acid (DHA, 22:6) is also a nonconjugated omega-3 fatty acid and its rate constant was measured to be 334 $M^{-1}s^{-1}$ (L. Xu et al., 2009)

There are many different classes of lipids, and not all of them are subject to peroxidation. This thesis will mainly focus on phospholipids and sterols. These classes differ greatly in their structure, function, synthesis, and propensity for oxidation.

Glycerolipids and glycerophospholipids

Glycerolipids typically consist of a glycerol backbone attached to 1, 2, or 3 fatty acid tails. They can also have a phosphodiester bridge attached to various functional headgroups. Those with the phosphodiester bridge are known as glycerophospholipids or simply phospholipids (Fahy et al., 2009). Their structure gives them a bipolar nature, as the head group is typically hydrophilic and the fatty acid tails are lipophilic. Phospholipids make up most of the total composition of cellular membranes, as their amphipathic structure easily creates a barrier between aqueous substances (van Meer et al., 2008). The plasma membrane and most inner membranes of eukaryotic cells are lipid bilayers, meaning they have two layers of phospholipids. The lipophilic tail end of both layers face in towards each other, while the hydrophilic head groups face out, towards the external environment and the cytosolic space. While the core structural backbone of these lipids is similar, there are a wide variety of different headgroups and fatty acids that make this class of biomolecules very diverse, with over 1000 different lipid species present in the average eukaryotic cell at a given time (Sud et al., 2007a). The oxidation of glycerolipids and glycerophospholipids has been observed extensively in the context of ferroptosis (Kagan et al., 2017; Lange et al., 2025a; Qiu et al., 2024a) and will be discussed in detail in the following section. See Figure 1.3 for structures of notable glycerophospholipids and fatty acids.

Glycerolipids consist of a glycerol backbone attached to two or three fatty acid tails, called diglycerides (DG) or triglycerides (TG), respectively. They are also known as neutral lipids because the glycerol backbone does not have a charge at physiological pH, in contrast with most phospholipids that carry a charge on the phosphodiester headgroups. The most prominent role that these lipids play in cells is as lipid storage molecules, storing fatty acids for later use. Within the cell, they are typically stored within lipid droplets, which have a monolayer membrane of phospholipids where the fatty acid tails face in towards the neutral lipids and the phosphate headgroups face out towards the cytosolic area. Lipid droplets are formed in the endoplasmic reticulum (ER), where the synthesis of TG and DG (and most other lipids) takes place (Bell et al., 1981).

Glycerophospholipids, also called phospholipids, have the same core glycerol backbone as DG and TG, but they also have a phosphodiester group attached to the glycerol backbone (Liebisch et al., 2020). There are 6 main headgroups seen in phospholipids, differing by the functional group attached to the phosphodiester. Phosphatidylcholine (PC) has a choline group attached to the phosphodiester. This choline group typically holds a positive charge, making PC bipolar. PC is an important membrane constituent, making up more than 50% of most eukaryotic lipid bilayers (van der Veen et al., 2017). PC is cylindrical in shape and will spontaneously form into fluid, flat bilayers in aqueous solution, rendering it integral to maintaining the structure of lipid membranes (van Meer et al., 2008).

Phosphatidylethanolamine (PE) has an ethanolamine group, consisting of 2 carbons and an amine group, attached to the phosphodiester. Like PC, the amine group typically holds a positive charge at physiological pH, making it bipolar. Because of these similar properties, it is also an important membrane constituent, the second-most abundant at about 30% of most eukaryotic membranes (van der Veen et al., 2017). PE has a conical chape where the headgroup is smaller than the fatty acid portion. Due to this geometry, PE is typically found on the inner leaflet of the plasma membrane and helps the membrane to curve around the inner contents of the cell, as well as assisting in membrane budding and fusion processes (Marsh, 2007).

Phosphatidylinositol (PI) has an inositol sugar group attached to the phosphate. Like PC and PE, it is bipolar with a negative charge typically on the inositol, and it is incorporated into most eukaryotic cellular membranes. However, it is only a minor constituent, making up less than 20% of the plasma membrane, and its primary role is as a signaling molecule (Vance, 2015). There are many downstream products of PI, including variants such as PIP3 and PI(4,5)P2, that are involved in the phosphoinositide signaling cascade (Di Paolo & De Camilli, 2006). This pathway regulates cellular processes such as growth, membrane transport, ion channels, and other membrane processes. It is typically found on the inner leaflet of the plasma membrane.

The other 3 main classes of glycerophospholipids are more minor membrane constituents, but they each have other roles within the cell that are important. Phosphatidic acid (PA) is the simplest of the phospholipids, as it has a hydroxy group on the phosphate where the other lipids have more complex functional groups. PA's main role is acting as a precursor for the synthesis of the other phospholipids. Functional groups like choline, ethanolamine, and inositol are added onto PA to make PC, PE, and PI lipids, respectively, via the CDP-DAG (cytidine diphosphate-diacylglycerol) pathway of phospholipid synthesis or via the Kennedy pathway of phospholipid synthesis (Gibellini & Smith, 2010; Kennedy & Weiss, 1956; Kent, 1995). The levels of PA in cells can change drastically to meet needs for phospholipid synthesis and to mediate cellular processes. Phosphatidylserine (PS) has a negatively charged serine functional group attached to the phosphate. Like PA, it is not a major membrane constituent in most membranes; however, its levels can be highly enriched in certain tissues such as the brain. PS plays an important immunomodulatory role, migrating from its usual place in the inner leaflet of the plasma membrane to the outer leaflet to signal to macrophages when a cell is stressed or dying (Birge et al., 2016). It is essential to proper neuronal function and initiates the blood clotting cascade by providing a place for clotting factors to bind (Glade & Smith, 2015). Phosphatidylglycerol (PG) has a neutral glycerol functional group attached to the phosphate. PG is a minor constituent of most animal cell membranes, but a major constituent of bacterial membranes (Vásquez et al., 2025). It is also the precursor to cardiolipin, a phospholipid essential in the inner layer of mitochondrial membranes (Tretiakova et al., 2024).

Since lipid peroxidation ultimately drives ferroptosis, the enzymes that produce, alter, and metabolize these lipids play an important role in mediating ferroptotic death. One particular family of enzymes that is integral to the ferroptosis process are the acyl-CoA synthetase long chain (ACSL) enzymes. These enzymes are responsible for ligating free fatty acids to acyl-CoA, which activates them for integration into neutral lipids and phospholipids. There are five isoforms in this family, and each has a distinct substrate preference, although some promiscuity has been observed for all of them (Klett et al., 2017). The isoforms are known as ACSL1, 3, 4, 5, and 6. What was first thought to be ACSL2 was later

determined to actually be ACSL1, hence why 2 is skipped in the nomenclature (Mashek et al., 2004). There are also short chain (ACSS), medium chain (ACSM), and very long chain families of acyl-CoA synthetase enzymes, though the very long group enzymes are denoted as fatty acid transport proteins (FATPs) and represented by the gene symbols SLC1-27 (Stahl, 2004; Steinberg et al., 2000). The long chain family is most relevant to ferroptosis and therefore will be the focus of the following section.

As mentioned in earlier sections, conjugated fatty acids such as CLA 18:3 are able to induce ferroptosis in cells independently (Beatty et al., 2021; Do et al., 2023). This effect is not specific to CLA 18:3, however. It was shown by Beatty et al. that a variety of fatty acid chain lengths could induce ferroptosis, as long as they had three or more conjugated double bonds (Beatty et al., 2021). The study went on to identify acyl-CoA synthetase long chain family member 1 (ACSL1) as the enzyme responsible for incorporation of these conjugated fatty acids into neutral lipids such as DG and TG, among other lipid classes. Knockout of ACSL1 was sufficient to rescue Pfa1 cells treated with CLA 18:3 from ferroptosis. Notably, knockout of ACSL1 is not protective against ferroptosis induced by RSL3 or erastin, it is only protective against ferroptosis induced by conjugated fatty acids. It is known that ACSL1 has a substrate preference for saturated fatty acids 16-18 carbons in length (Klett et al., 2017). The study by Beatty et al. shows that ACSL1 also preferentially activates conjugated PUFAs including CLA 18:3.

Like ACSL1, ACSL3 is known to have a substrate preference for saturated fatty acids (Klett et al., 2017). However, it was shown by Magtanong et al. that exogenous MUFAs inhibit ferroptosis in an ACSL3-dependent manner. They showed that treating HT-1080 cells with oleic acid (18:1) or palmitoleic acid (16:1) resulted in in cell death suppression when cells were co-treated with the ferroptosis inducer erastin-2, and went on to show that genetic ablation of ACSL3 abolished this effect (Magtanong et al., 2019). This demonstrates that ACSL3 is necessary for the incorporation of ferroptosis-protective MUFAs into cellular phospholipids. Interestingly, enrichment of MUFAs and upregulation of the enzyme that converts SFAs to MUFAs, SCD-1 (stearoyl-CoA desaturase 1), is a common phenotype in a variety of cancer tissues (Tracz-Gaszewska & Dobrzyn, 2019). It has been proposed that this enrichment of MUFAs

evolved as a mechanism to avoid ferroptotic death in the highly oxidation-prone tumor microenvironment (Jun-Mei Yi et al., 2020). The role of ACSL3 and MUFA incorporation to prevent ferroptosis represents a potential therapeutic avenue for the treatment of cancer.

In contrast to the protective effect of MUFAs, PUFA-containing phospholipids (PUFA-PLs) have relatively high peroxidation rate constants and their oxidation has been shown to be integral to the ferroptotic process. Their importance was elucidated in 2016 when a CRISPR gene knockout screening identified acyl-CoA long chain synthetase family member 4 (ACSL4) as an essential pro-ferroptotic gene in mouse Pfa1 cells (Doll et al., 2017; Yuan et al., 2016). In other words, genetic ablation of ACSL4 promotes a ferroptosis-resistant cell state. This finding has been recapitulated in many different cell types, highlighting the importance of ACSL4 in ferroptosis (Magtanong et al., 2022). Like the other ACSL enzyme family members, ACSL4 activates fatty acids into fatty acyl-CoAs that can be incorporated into phospholipids. ACSL4 has a strong substrate preference for PUFAs, particularly arachidonic acid. It has been shown that loss of ACSL4 results in altered lipid metabolism and reduces the amount of arachidonic acid and its elongation products that are incorporated into phospholipids in cells (Doll et al., 2017). Reducing the PUFA content of cellular membranes makes them less prone to ferroptotic death due to a lack of oxidizable substrates to propagate the peroxidation reaction through the membrane.

ACSL5 and 6 are less highly expressed than the other isoforms and perform specific biological functions. Due to their specificity and relatively low expression level, they are not as relevant to ferroptosis as the other ACSL isoforms. ACSL5 prefers saturated fatty acids as substrates and has been implicated in mediating immune response in cancer tissues (Deng et al., 2025; Lai et al., 2024). ACSL6 has a strong substrate preference for docosahexaenoic acid (DHA, 22:6) and plays a specific role in maintaining visual function as well as in spermatogenesis in males (Deng et al., 2025; Kurotaki et al., 2021). ACSL5 is expressed mainly in the mitochondria, while the subcellular location of ACSL6 is not known.

Though ACSL enzymes are integral to the incorporation of long-chain fatty acids into phospholipids, there are other enzymes involved in this process as well. Once fatty acids are activated to fatty acyl-CoAs, they must be ligated to phospholipid headgroups. Fatty acids can be incorporated into de novo phospholipids via the Kennedy pathway or CDP-DAG pathway. Alternatively, they can be incorporated into remodeled phospholipids via the Lands cycle (Shindou et al., 2009). See Figure 1.4 for a schematic of phospholipid synthesis and remodeling. All these pathways rely on a family of enzymes called the lysophospholipid acyltransferases (LPLATs). These enzymes catalyze the ligation of a fatty acyl-CoA to an existing phospholipid head group via ester bonds. Lysophosphatidylcholine acyltransferase 3 (LPCAT3) is one of these enzymes that is responsible for incorporating arachidonic acyl-CoAs into PC lipids. It is highly expressed in mammals and has been implicated in mediating ferroptosis because it is involved in the same pathway as ACSL4. Indeed, it was shown that genetic ablation of LPCAT3 promoted partial resistance to ferroptosis, but the effect was not as strong as ablation of ACSL4 (Doll et al., 2017). This could be due to multiple pathways by which arachidonic acyl-CoA can be incorporated into phospholipids, but all of them require activation by ACSL4.

Sterols

A detailed review of the role of sterols in ferroptosis and their peroxidation rate constants has been published (Reimers & Xu, 2025). Much of the following section has been adapted from that publication.

Cholesterol is a ubiquitous lipid that plays many biological roles across many different species. It assists in the synthesis of essential biomolecules including steroids, bile acids, and vitamin D, and facilitates the transport of triglycerides throughout the body in the form of lipoprotein particles. On a smaller scale, cholesterol is essential to maintaining the structural integrity of cellular lipid membranes (Craig et al., 2025; Luo et al., 2020). Cholesterol can be synthesized in all cells, but the primary site of

cholesterol synthesis in humans is the liver. Synthesis of cholesterol begins with the formation of 3-hydroxy-3-methyl glutaryl coenzyme A (HMG-CoA) from 3 molecules of acetyl-CoA. Next, in the rate limiting step of cholesterol synthesis, HMG-CoA reductase reduces HMG-CoA to mevalonate. Once mevalonate is produced, it is converted into the 5-carbon isoprene unit isopentenyl pyrophosphate (IPP), which condenses further into geranyl pyrophosphate (GPP, 10 carbons) and finally to farnesyl pyrophosphate (FPP, 15 carbons). FPP is then cyclized to form lanosterol. Lanosterol is then converted to either cholesterol via the Kandutsch-Russell pathway or desmosterol via the Bloch pathway in a series of steps (*KEGG PATHWAY: Steroid Biosynthesis - Reference Pathway*, n.d.). A diagram of this process can be seen in Figure 1.5.

Recently, it has been shown that metabolites along the cholesterol synthesis pathway, including cholesterol, desmosterol, 7-dehydrocholesterol (7-DHC), and squalene, can have a protective effect against ferroptosis in vitro (Freitas et al., 2024, p. 7; Garcia-Bermudez et al., 2019; Y. Li et al., 2024; C. Liu et al., 2023; Q. Sun et al., 2023a; Zhao et al., 2023). Furthermore, other isoprenoids, such as vitamin D_3 and A, have also been found to inhibit ferroptosis (Do et al., 2023). Therefore, isoprenoid-derived lipids are emerging as key players in mediating ferroptotic death. The peroxidation rate constants of these lipids vary widely, but they generally display anti-ferroptotic properties.

The rate constants of various isoprenoid-derived lipids have been measured using the linoleate radical clock. See Figure 1.6 for structures of notable isoprenoid-derived lipids and their peroxidation rate constants. Cholesterol is not a highly oxidizable molecule with a k_p of 11 $M^{-1}s^{-1}$ (L. Xu et al., 2009), but cholesteryl ester has a larger rate constant at 31-36 $M^{-1}s^{-1}$ (Do et al., 2021; Zielinski & Pratt, 2019). That said, both are much less reactive than the least reactive polyunsaturated fatty acid (PUFA), linoleic acid (LA 18:2), which has a k_p of 62 $M^{-1}s^{-1}$ (Howard & Ingold, 1967). On the other hand, the immediate precursor to cholesterol, 7-dehydrocholesterol (7-DHC), is extremely reactive toward peroxyl radicals, with a k_p of 2260 $M^{-1}s^{-1}$ and 2737 $M^{-1}s^{-1}$, measured in 2009 and 2021 using the two generations of the linoleate radical clock (Do et al., 2021; L. Xu et al., 2009). We suggest that the latter rate constant, 2737

$M^{-1}s^{-1}$, should be used for future studies because the new generation of radical clock accounts for both HAT and PRA rate constants, even though 7-DHC still undergoes lipid peroxidation primarily via HAT. Oxidation of 7-DHC proceeds predominantly via the HAT mechanism as the hydrogen atoms on carbons 9 and 14 are well-positioned for abstraction by a peroxyl radical with an easily accessible transition state (L. Xu et al., 2009).

Other cholesterol precursors are mostly more reactive than cholesterol, except for lanosterol and dihydrolanosterol. Specifically, lathosterol and zymostenol have a k_p of 57 and 77 $M^{-1}s^{-1}$, respectively (Lamberson et al., 2017). The Bloch pathway cholesterol precursors all have an additional double bond in the isoprene unit on the side chain. Although the rate constants of the Bloch pathway precursors have not been directly measured, the rate constant for the isoprene unit was determined to be 5.6 $M^{-1}s^{-1}$ (in the form of 2-methyl-2-heptene) (Lamberson et al., 2017). The single isoprene unit presumably predominantly undergoes HAT reaction at the secondary allylic methylene position due to smaller bond-dissociation energy and the more stabilized allylic radical with four substitutions, which can stabilize the radical through hyperconjugation (L. Xu & Porter, 2015). However, we cannot rule out that the isoprene unit can also undergo PRA reaction at the double bond, generating a relatively stable tertiary radical, but less stable than the allylic radical. Therefore, the k_p for these precursors, lanosterol, desmosterol, 24-dehydrolathosterol, zymosterol, and 7-dehydrodesmosterol, were estimated to be 6, 17, 63, 83, and 2743 $M^{-1}s^{-1}$, respectively (Lamberson et al., 2017). Squalene is the immediate precursor to lanosterol, the first sterol, and is composed of six isoprene units. Thus, the k_p of squalene can be estimated to be 56 $M^{-1}s^{-1}$ because it has ten allylic methylene groups (compared to one in 2-methyl-2-heptene), which is more reactive than cholesterol and comparable to that of LA 18:2. More detailed discussion on the effect of various factors on the reactivity of cholesterol and its precursors and the mechanisms of their peroxidation can be found in a previous review (L. Xu & Porter, 2015).

Vitamin D_3, or cholecalciferol, is also a highly oxidizable isoprenoid lipid, which is derived from 7-DHC upon UV irradiation, with a measured k_p of 1031 $M^{-1}s^{-1}$. However, unlike 7-DHC, it undergoes

oxidation via both PRA and HAT due to the presence of a conjugated double bond system in its structure, with a k_{add} of 601 $M^{-1}s^{-1}$ and a k_H of 430 $M^{-1}s^{-1}$. Vitamin A contains 6 conjugated double bonds, making it highly prone to oxidation. Indeed, its k_p was measured to be 5656 $M^{-1}s^{-1}$ with the oxidation proceeding entirely via the PRA mechanism (Do et al., 2021). This is the largest rate constant for lipid peroxidation that has been measured via the linoleate radical clock to date. The oxidized form of coenzyme Q_{10} (CoQ_{10}), or ubiquinone, is an endogenous isoprenoid that was also found to be highly oxidizable, with a rate constant of 695 $M^{-1}s^{-1}$, proceeding entirely via PRA (Do et al., 2021).

Endogenous phenolic isoprenoids are potent free radical-trapping antioxidants against lipid peroxidation. α-Tocopherol, the major form of vitamin E, has a k_H (k_{inh} to be more accurate) of 3.2 ´ 10^6 $M^{-1}s^{-1}$ at 30 °C and an extrapolated k_{inh} of 3.8 ´ 10^6 $M^{-1}s^{-1}$ at 37 °C based on measured rate constants at different temperatures (Burton et al., 1985; Pratt et al., 2001; Roschek et al., 2006). The reduced form of CoQ_{10}, ubiquinol ($CoQ_{10}H_2$), is also a radical-trapping antioxidant, with a k_{inh} of about 10-39% that of α-tocopherol in homogeneous solutions, depending on the solvent, but almost the same k_{inh} in liposomes (Landi et al., 1992; Yamamoto et al., 1990). The reduced form of vitamin K (also a quinone), VKH_2, is another radical-trapping antioxidant with a similar k_{inh} to α-tocopherol in homogeneous solutions, but four times larger k_{inh} in liposomes (Fiorentini et al., 1997). Although these isoprenoid lipids display a wide range of reactivity toward free radical oxidation, they all exert anti-ferroptotic properties based on the existing literature. Vitamin E, $CoQ_{10}H_2$, and VKH_2 have been found to act as potent ferroptosis inhibitors (Bersuker et al., 2019; Doll et al., 2019; Mishima et al., 2022). This is understandable because they terminate the free radical lipid peroxidation chain reactions. In fact, other endogenous and exogenous radical-trapping phenols or arylamines have been found to be effective ferroptosis inhibitors, such as ferrostatin-1 and liproxstatin-1.

The compound CoQ_{10}, or ubiquinone, is an electron carrier in the electron transfer chain. It is composed of a benzoquinone core linked to an isoprene chain and is synthesized in the mitochondria. CoQ_{10} is present in a wide variety of tissues and subcellular compartments, demonstrating its

multifunctionality (Arroyo et al., 1998; Takahashi et al., 1993). The isoprene chain of CoQ_{10} is synthesized via the mevalonate pathway, starting with acetyl-CoA and ending with farnesyl pyrophosphate, or FPP. The chain is made of ten isoprene units, and is responsible for the lipophilicity of CoQ_{10}, which allows it to accumulate in cell membranes and other lipid-rich spaces (Acosta et al., 2016). The reduced form of ubiquinone, $CoQ_{10}H_2$, not only acts as a radical-trapping antioxidant, but also detoxifies peroxides to nontoxic alcohols by transferring electrons from NADPH (Bentinger et al., 2007). $CoQ_{10}H_2$ has also been found to effectively regenerate vitamin E with a rate constant of $3.74 \times 10^5\ M^{-1}s^{-1}$ at 25 °C(Mukai et al., 1990).

Through genetic screening, it was found that the enzyme responsible for the regeneration of the reduced $CoQ_{10}H_2$ from its oxidized form, CoQ_{10}, acts as a ferroptosis suppressor (Bersuker et al., 2019; Doll et al., 2019). The enzyme was originally called flavoprotein apoptosis-inducing factor mitochondria-associated 2 (AIFM2) and was previously shown to be a pro-apoptotic gene (M. Wu et al., 2002). However, later studies by Doll et al. showed that the enzyme does not localize to the mitochondria, nor does it promote apoptosis. Therefore, it was renamed to ferroptosis suppressor protein 1, or FSP1, to reflect its newfound role in preventing lipid peroxidation. It was also shown by Doll et al. that cells overexpressing FSP1 showed marked resistance to ferroptosis-inducing compounds, such as RSL3, and continued to proliferate in the presence of these compounds. Bersuker et al. showed that FSP1 knockout cells displayed increased sensitivity to ferroptosis inducers, and that this effect could be ameliorated with the addition of iron chelators or radical-trapping antioxidants. It was determined by both groups that these effects are not dependent on the presence of glutathione or the activity of GPX4, but rather due to the antioxidant activity of the electron-carrying compound $CoQ_{10}H_2$. Therefore, FSP1 is a key regulator of ferroptosis that depends on CoQ_{10}, an antioxidant compound that is derived from the same mevalonate pathway as cholesterol biosynthesis. More recently, FSP1 was found to also reduce oxidized vitamin K, a naphthoquinone, to its reduced form (VKH_2), which protects cells from ferroptosis (Mishima et al., 2022).

The oxidized form of CoQ_{10} is also highly oxidizable and its oxidation proceeds predominantly via the PRA mechanism, with a measured k_p of 695 $M^{-1}s^{-1}$. It has been shown that the treatment of cells with exogenous CoQ_{10} decreases toxicity and lipid peroxidation associated with RSL3 and erastin treatment (Do et al., 2023). However, we cannot rule out the possibility that CoQ_{10} might exert its activity after being reduced in the cells by FSP1. Taken together, these studies suggest that $CoQ_{10}H_2$ is likely to protect the cells from ferroptosis through its radical-trapping property, but its oxidized form may also be able to protect the cells in a sacrificial manner by diverting free radicals away from PUFA-containing phospholipids.

7-DHC is the immediate precursor to cholesterol in the Kandutsch-Russell pathway of cholesterol biosynthesis. It is reduced to cholesterol via the enzyme 7-dehydrocholesterol reductase, or DHCR7. 7-DHC is an extremely oxidizable lipid with a k_p of 2737 $M^{-1}s^{-1}$ (Do et al., 2021). This is more than ten times higher than the peroxidation of arachidonic acid, which is a highly oxidizable PUFA (L. Xu et al., 2009). Recently, in a genome-wide CRISPR screen, it was shown that DHCR7 is an essential pro-ferroptotic gene (Freitas et al., 2024; Y. Li et al., 2024). Later studies confirmed that the knockout of *DHCR7* conferred resistance to ferroptosis in multiple cell lines. The resistance was lost, however, when SCD5, the enzyme that produces 7-DHC, was also knocked out. It was also shown that adding exogenous 7-DHC was able to protect cells from ferroptotic death, demonstrating that the resistance was due to the accumulation of 7-DHC, not due to any up or downstream effects of DCHR7 knockout.

Previous work has demonstrated that phosphatidylethanolamine, or PE, phospholipids are significantly oxidized during ferroptosis (Kagan et al., 2017). It was shown by Freitas et al. that while 7-DHC is highly oxidizable itself, its presence reduces the formation of oxidized PE phospholipids in cells. Phospholipid truncation products, which are closely associated with membrane permeabilization (Bacellar et al., 2018), were found to be significantly lower in DHCR7 knockout cells as compared to wild type (Freitas et al., 2024). Conversely, it was shown by Frietas et al. and Li et al. that DHCEO, a biomarker of 7-DHC peroxidation in biological systems (L. Xu et al., 2011), was significantly higher in cells treated

with RSL3. This suggests that 7-DHC could be oxidized more rapidly than phospholipids, sparing the phospholipids from oxidation and thereby preventing ferroptotic death in a sacrificial manner.

Recently, it was also shown that the addition of vitamin D or vitamin A can attenuate cancer cell death induced by the ferroptosis inducers RSL3 and erastin (Do et al., 2023). As discussed above, these two lipids are also highly reactive toward peroxyl radicals but favor the PRA oxidation mechanism. It is likely that the protective effect of vitamin D, vitamin A, and 7-DHD are due to their high propensity for oxidation with propagation rate constants significantly larger than those of PUFAs. Since they are more prone to oxidation than even highly unsaturated phospholipids, they could act as free radical diverters, redirecting free radical chain reactions away from PUFA-containing phospholipids. In other words, they could protect against ferroptosis through a sacrificial mechanism. When these lipids are co-oxidized with the PUFA LA 18:2, this PUFA is mostly spared from being oxidized (Do et al., 2021). In summary, they may protect cells from undergoing ferroptosis primarily by acting as sacrificial lipids due to their highly oxidizable structures and less membrane-damaging oxidation products.

Cholesterol itself is not particularly prone to oxidation, with a peroxidation rate constant of 11 $M^{-1}s^{-1}$ in the free form and 36 $M^{-1}s^{-1}$ in the ester form and its oxidation proceeding primarily via HAT (Do et al., 2023; L. Xu et al., 2009). However, in a 2023 paper by Sun, et al., it was shown that treatment of HT-1080 cells with 7-DHC, cholesterol, and desmosterol all attenuated cell death and lipid peroxidation induced by RSL3 treatment (Q. Sun et al., 2023a). Unlike 7-DHC, cholesterol and desmosterol did not directly reduce lipid peroxidation in liposomes as measured by C11-BODIPY. Because cholesterol and CoQ_{10} are both synthesized via the mevalonate pathway (Figure 4), which is sensitive to negative feedback from downstream products, the group reasoned that excess cholesterol could lead to increased production of CoQ_{10}. Indeed, treatment with exogenous cholesterol and desmosterol was shown to increase intracellular CoQ_{10} content, providing a potential mechanism of the ferroptosis resistance offered by cholesterol and desmosterol (Q. Sun et al., 2023a). In another recent study by Liu et al., cholesterol was found to regulate ferroptosis through the mTOR pathway (C. Liu et al., 2023). They found that

cholesterol, through SLC38A9, activates mTOR, which upregulates SLC7A11 (the cystine importer) and GPX4 and inhibits ferritinophagy, both conferring resistance to ferroptosis.

In addition to its regulatory roles, the amount of cholesterol in a cell membrane can have profound effects on its structure and function. It plays a regulatory role in many processes, including membrane fusion, permeation, transport, and protein-protein interactions. While the effects of cholesterol on cellular membrane function are diverse, it is generally accepted that the presence of cholesterol within a membrane increases its rigidity, particularly in regions of high PUFA content (Corvera et al., 1992). While older studies postulated that cholesterol could act as a sacrificial antioxidant via a mechanism similar to the highly oxidizable lipids discussed in this review, the relatively low peroxidation rate constant of cholesterol does not support this hypothesis (L. Xu et al., 2009). Indeed, it has been shown in more recent studies that the presence of cholesterol in membranes at a physiologically relevant concentration (30 mol %) can prevent the oxidation of polyunsaturated fatty acids by increasing membrane rigidity and slowing the rate at which peroxidation spreads through a lipid membrane (Zhang et al., 2018). This introduces an alternative non-sacrificial mechanism by which less oxidizable isoprenoid-derived lipids may protect cells from ferroptosis: through alteration of membrane physicochemical properties. Indeed, a recent study found that cholesterol decreased membrane fluidity and promoted lipid raft formation, which slowed the rate of lipid peroxidation (Zhao et al., 2023).

Another mechanism proposed by Sun. et al. to explain the anti-ferroptotic effect of cholesterol was the cholesterol-dependent inhibition of squalene epoxidase, or SQLE (Q. Sun et al., 2023a). SQLE, which catalyzes the second rate-limiting step in cholesterol biosynthesis, is negatively regulated by the presence of excess cholesterol (Gill et al., 2011; Howe et al., 2015). It was shown that ablation of SQLE conferred resistance to cell death induced by RSL3, to a similar extent as cholesterol and desmosterol supplementation. This agrees with previous work completed by Garcia-Bermudez in 2019, which showed that some cancer cells that rely on exogenous cholesterol for growth display significantly reduced expression of SQLE and increased resistance to ferroptotic death. Further study of these cells showed that

the knockout of FDFT1, the upstream enzyme that produces squalene, abolished the protective effect of diminished SQLE expression. This suggests that the protective effect comes from the presence of squalene. Interestingly, exogenous squalene supplementation did not recapitulate the protection, suggesting that squalene must be present in specific subcellular compartments to be protective (Garcia-Bermudez et al., 2019).

Squalene is synthesized in the endoplasmic reticulum (ER), which has been identified as an important site of lipid peroxidation in ferroptosis (von Krusenstiern et al., 2023a). Its accumulation in the ER membrane may slow the progression of lipid peroxidation by increasing membrane rigidity (Spanova et al., 2012). On the other hand, the estimated propagation rate constant of squalene, 56 $M^{-1}s^{-1}$, is comparable to that of linoleic acid (62 $M^{-1}s^{-1}$), so it is likely that they could compete with the oxidation of PUFAs to some extent, thus acting as another sacrificial lipid in the ER membrane specifically.

Mass Spectrometry-Based Lipidomics

The terms ‘lipidome’ and ‘lipidomics’ were first described in the early 2000’s and have since grown to be a field of significant interest in the scientific community (Han & Gross, 2003; Kishimoto et al., 2001). While various analytical methods have been used to study the lipidome over the years, including thin layer chromatography and nuclear magnetic resonance (NMR), mass spectrometry (MS) has emerged as the leading methodology to study lipids due to its high resolution, sensitivity, and versatility (Fedorova et al., 2026; Gerhardtova et al., 2024). At its most basic, a mass spectrometer is an analytical instrument that measures the mass-to-charge (m/z) ratio of ions. However, it is highly customizable due to the many different configurations of mass spectrometers, different analytical methodologies, and the ability to combine additional separational techniques including liquid chromatography (LC) and ion mobility (IM). Using MS in tandem with other analytical techniques, over

50,000 unique lipids have been characterized in the LipidMaps structure database (LMSD, https://www.lipidmaps.org/) as of 2026.

Despite the many advances to the lipidomics field since the early 2000's, various challenges remain in the measurement and identification of lipids using MS. Many lipids are structurally similar, with many isobaric and isomeric species that are impossible to resolve without the use of targeted fragmentation. In addition, reference data, particularly fragmentation spectra, as well as chromatographic retention times and ion mobility values, are lacking for many lipids, or may vary widely depending on the type of instrumentation and analytical methods used. As such, many lipids remain uncharacterized, sometimes referred to as 'the dark lipidome' (da Silva et al., 2015). Furthermore, the lipidomics field has grown even broader with a new branch of lipidomics called epilipidomics (*Epilipidome as a New Level of Cellular Regulation*, n.d.). The epilipidome is composed of lipid derivatives, including lipid metabolites and oxidation products. The identification of lipids within the epilipidome is difficult due to low abundance, structural diversity, and a lack of high quality reference data (Damiani et al., 2023a).

Nonetheless, interest in the lipidome and epilipidome continues to grow. Alterations in the lipidome have been extensively characterized in various disease states, including Alzheimer's, fatty liver disease, metabolic syndrome, and cancer (Huynh et al., 2020; Vvedenskaya et al., 2021; Wolrab et al., 2022). Given the role of deregulated lipid metabolism in many disease states, lipidomics has the potential to serve as a diagnostic tool for these ailments and others. As such, new solutions are emerging to address the inherent challenges of lipidomics to increase its utility in the clinical and research spaces (Vvedenskaya et al., 2022). In order to standardize the reporting of lipidomics data, new guidelines have been developed, known as the Lipidomics Minimal Reporting Checklist, to increase the robustness, confidence, and reproducibility of lipid analysis and identification (Kopczynski et al., 2024; McDonald et al., 2022). There are many software tools available to aid in the difficult task of identifying lipids, including LipoStar, LipidBlast, and even our lab's in-house software, LiPydomics (Goracci et al., 2017; Kind et al., 2013; Ross, Cho, Zhang, et al., 2020). The next challenge for the lipidomics field will be to

further illuminate the epilipidome. New software and databases are emerging for this purpose, however they are still in early stages of development and often limited by a lack of high-quality reference data (Damiani et al., 2023b; Ni et al., 2017). Therefore, more work is needed to improve our ability to detect, resolve, and identify lipids and their derivatives using MS and associated technologies.

Summary and Dissertation Overview

Ferroptosis is a unique and relatively new regulated form of cell death driven by iron-dependent lipid peroxidation. Glycerophospholipids and sterols are two major classes of lipids whose oxidation has been implicated in ferroptotic cell death. The propensity of these lipids to be oxidized depends on their structure and their peroxidation rate constants as determined by the linoleate radical clock method. Lipids containing highly unsaturated fatty acids are particularly prone to oxidation due to their high peroxidation rate constants, and these lipids have been shown to be of importance to ferroptosis. ACSL4, an enzyme that activates highly unsaturated fatty acids for incorporation into phospholipids, has been shown to be an essential pro-ferroptotic enzyme in many cell types. Sterol and other isoprenoid-derived lipids can be pro- or anti- ferroptotic in cells depending on their peroxidation rate constants. Many anti-ferroptotic isoprenoid-derived lipids have a high peroxidation rate constant and may protect other lipids from oxidation in a sacrificial manner. See **Table 1.1** for peroxidation rate constants of notable lipids.

Lipids are an integral part of the ferroptosis process, and this thesis aims to examine how the metabolism and peroxidation of lipids ultimately lead to ferroptotic death. Ferroptosis has been implicated in a wide range of diseases, and further elucidation of its underlying mechanisms, particularly involving lipid peroxidation, may reveal new therapeutic opportunities. In Chapter 2, we will present a study using deuterium-labeled lipids to trace their metabolic fate in cells undergoing ferroptosis using mass spectrometry. In Chapter 3, we will describe the creation of an oxidized lipid database to facilitate the identification of lipid oxidation products in mass spectrometric lipidomic datasets. In Chapter 4, we will

present a study that used stimulated Raman spectroscopy and confocal microscopy to observe the spatial distribution of intact lipids and the lipid oxidation process in cells. In Chapter 5, we will present a detailed multi-omic characterization of *ACSL4*-knockout cells and will propose a novel mechanism by which *ACSL4* ablation protects cells from ferroptosis. Finally, in Chapter 6, we will present conclusions from these studies and our recommendations for future work.

Figures

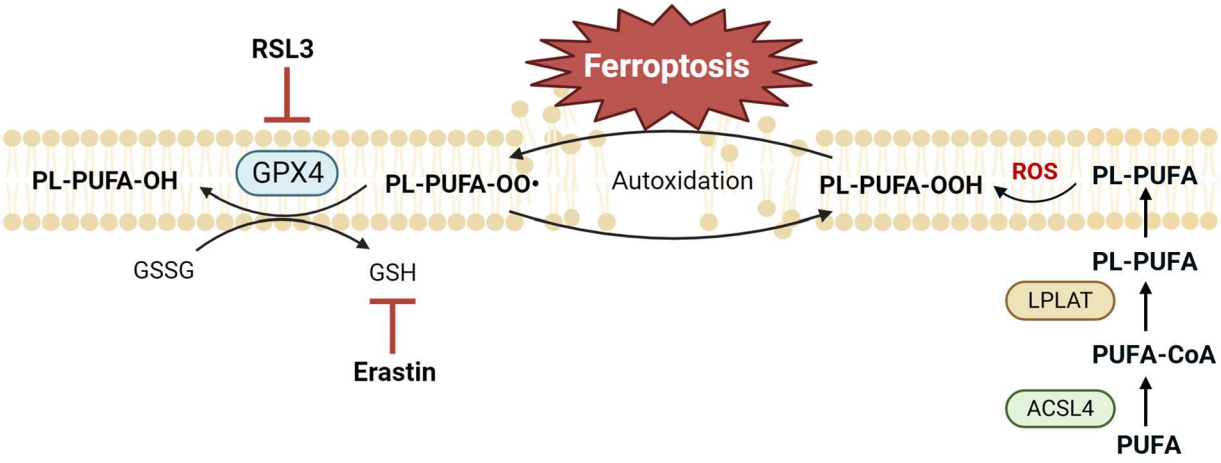

Figure 1.1: Schematic of Ferroptosis. PUFA: Polyunsaturated Fatty Acid, ACSL4: Acyl-CoA Long Chain Synthetase 4, LPLAT: Lysophospholipid Acyl Transferase, ROS: Reactive Oxygen Species, GSH/GSSG: Reduced/oxidized glutathione, GPX4: Glutathione Peroxidase 4

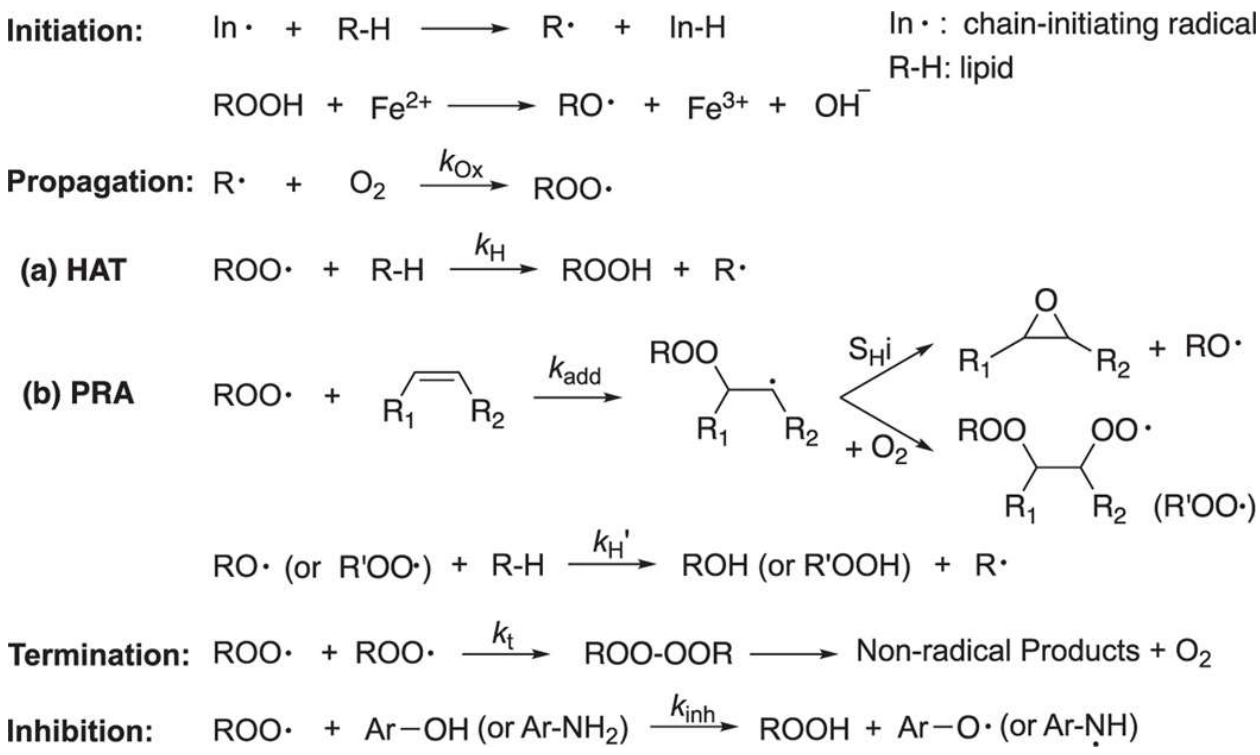

Figure 1.2: Lipid peroxidation mechanisms. **Adapted with permission from:**

Do Q, Xu L. How do different lipid peroxidation mechanisms contribute to ferroptosis? Cell Rep Phys Sci. 2023 Dec 20;4(12):101683. doi: 10.1016/j.xcrp.2023.101683. Epub 2023 Nov 17.

HAT: hydrogen atom transfer, PRA: peroxyl radical addition, S_Hi: intramolecular homolytic substitution, k_{ox}: oxygen addition rate constant, k_H: HAT rate constant, k_{add}: PRA rate constant, k_t: termination rate constant, k_{inh}: inhibition rate constant.

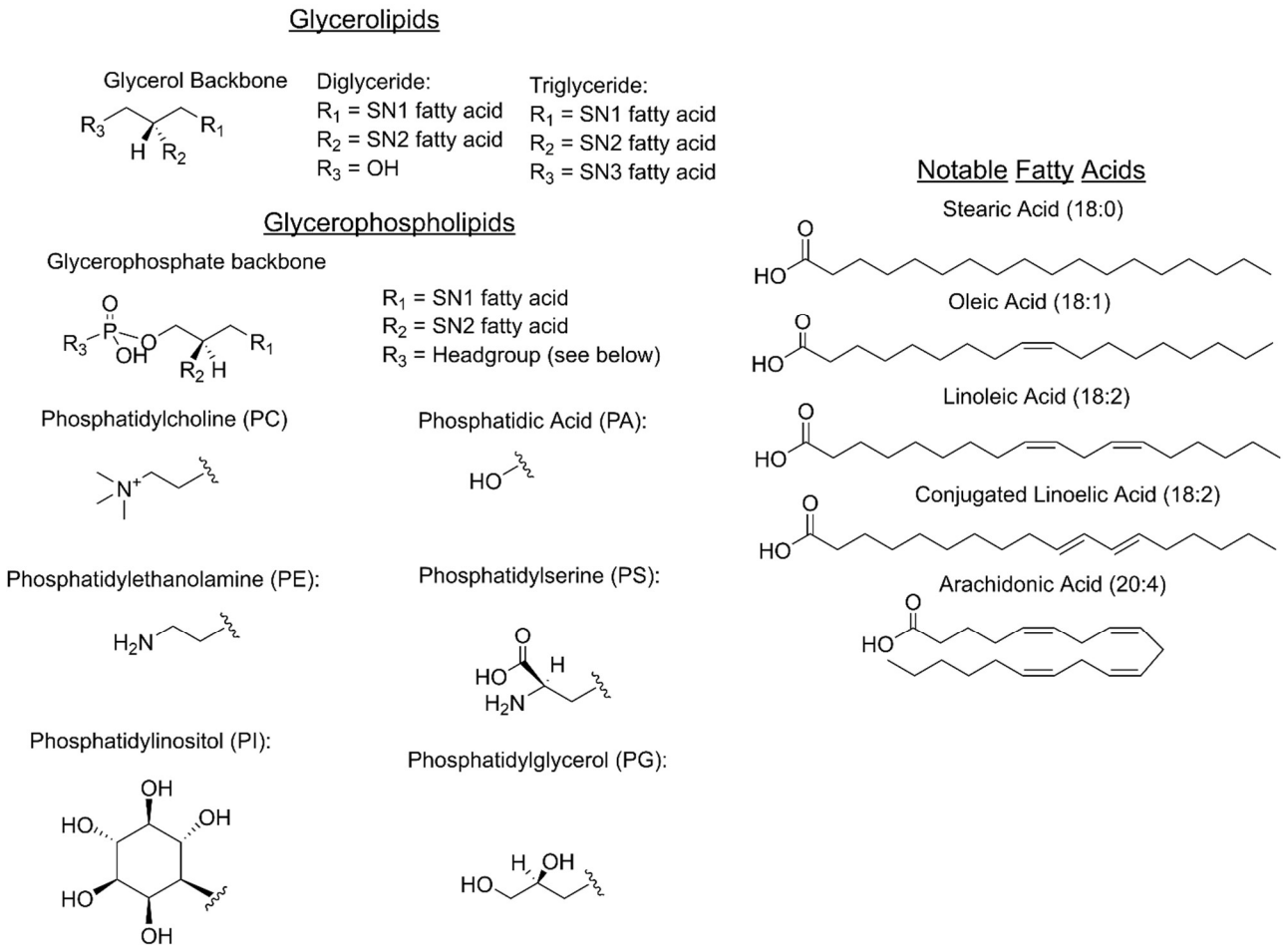

Figure 1.3: Structures of glycerophospholipids and notable fatty acids

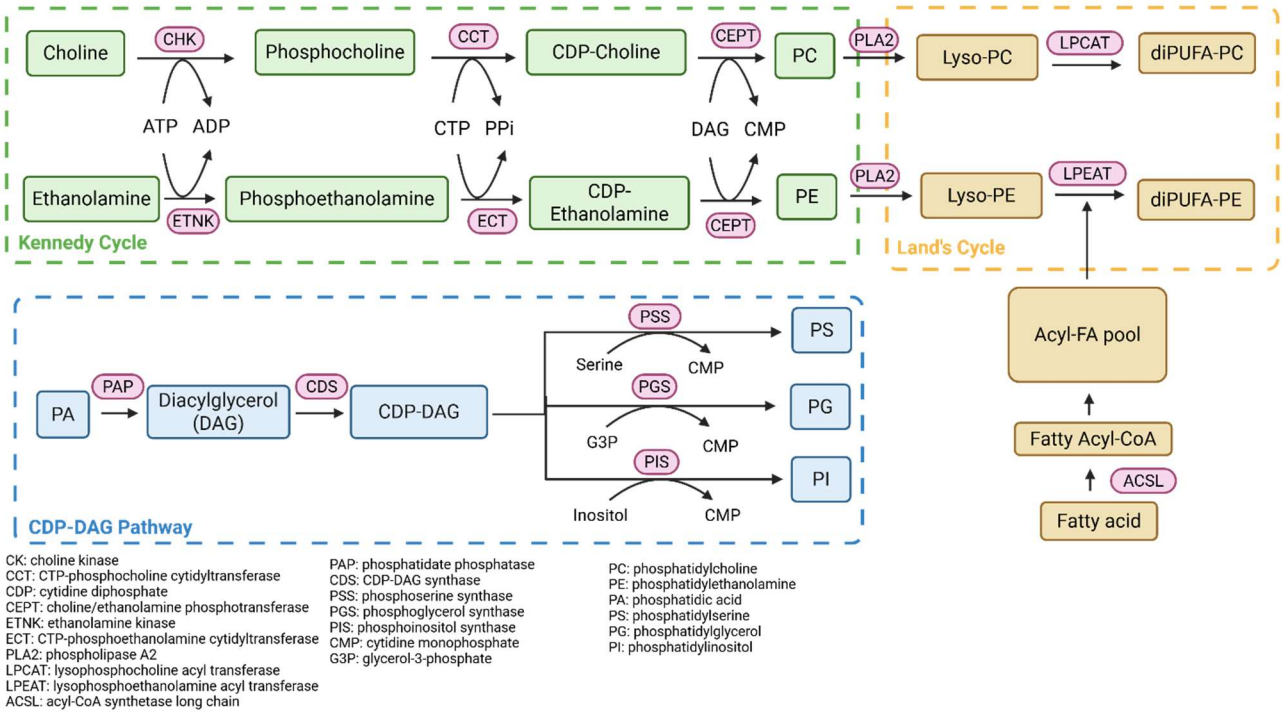

Figure 1.4: Schematic of phospholipid biosynthesis and remodeling via Kennedy, CDP-DAG, and Lands cycles. Generated using Biorender.com

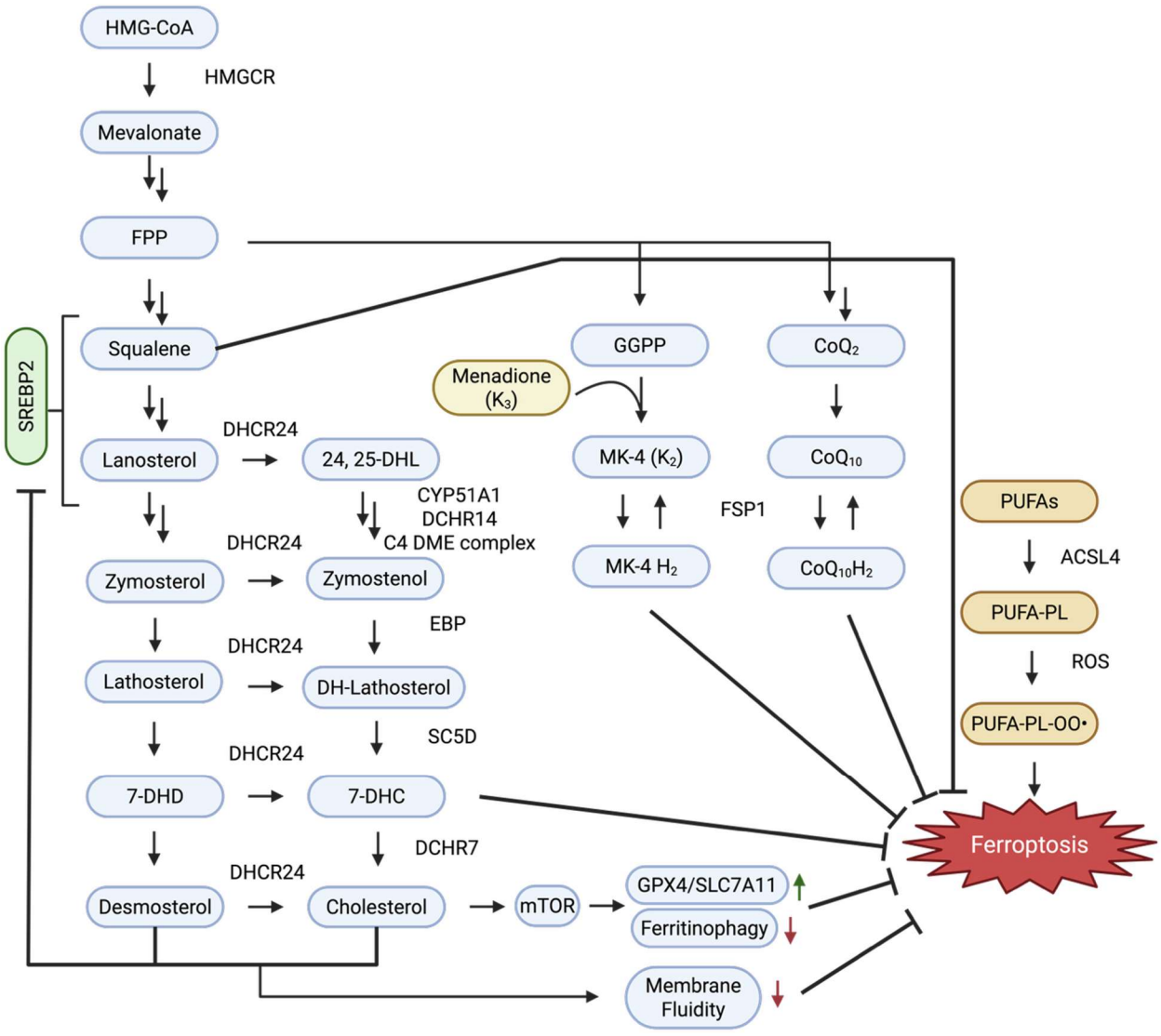

Figure 1.5: Scheme of sterol synthesis and its role in mediating ferroptosis. Adapted with permission from:

Reimers N, and Xu L (2025) Peroxidation rate constants and mechanisms of isoprenoid-derived lipids and their roles in ferroptosis. *Redox Biochemistry and Chemistry* **13**:100058

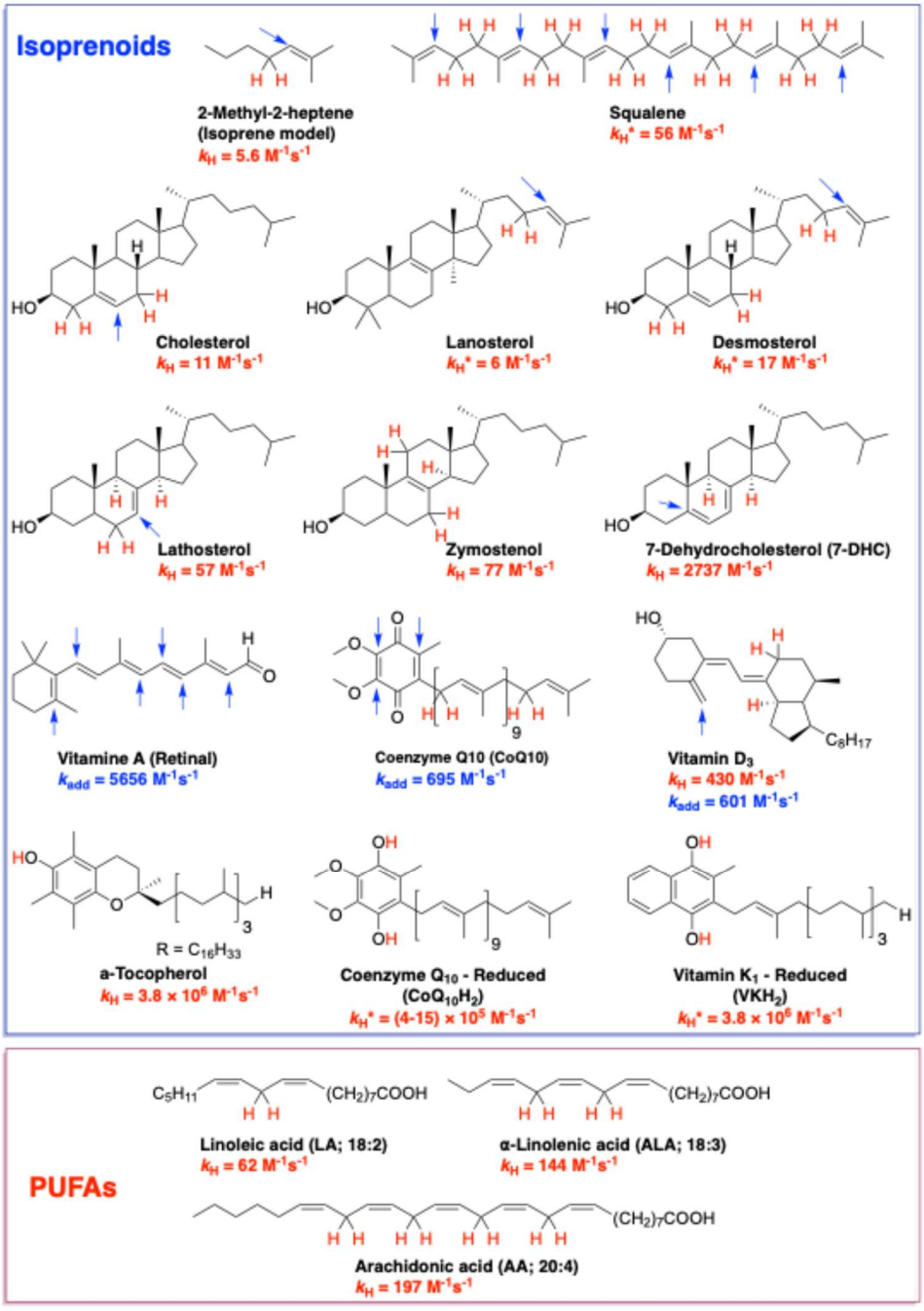

Figure 1.6: Structures and rate constant of notable isoprenoid-derived lipids and polyunsaturated fatty acids. Adapted with permission from:

Reimers N, and Xu L (2025) Peroxidation rate constants and mechanisms of isoprenoid-derived lipids and their roles in ferroptosis. *Redox Biochemistry and Chemistry* **13**:10005

Chapter 2: Isotope-labeling Lipidomics

Some of this work has been published. Much of the following chapter has been adapted with permission from the following publication:

Reimers N, Do Q, Zhang R, Guo A, Ostrander R, Shoji A, Vuong C, and Xu L (2023) Tracking the Metabolic Fate of Exogenous Arachidonic Acid in Ferroptosis Using Dual-Isotope Labeling Lipidomics. *J Am Soc Mass Spectrom*, doi: 10.1021/jasms.3c00181, American Society for Mass Spectrometry. Published by the American Chemical Society.

Introduction

The rise of genomics, proteomics, and metabolomics over the last 20 years has introduced a wealth of information to the field of biochemistry and greatly advanced our understanding of human health and diseases. Lipidomics is a branch of metabolomics that studies lipids and their metabolites within a biological system (Han & Gross, 2003). Lipidomics has revealed many roles of lipids beyond simple energy storage molecules, including acting as signaling molecules in inflammation and the immune response, metabolic regulation, and influencing cell death (Han, 2016). Altered lipid metabolism is a hallmark of many types of cancer, as cancer cells often alter their lipid metabolism to keep up with their need for energy, modulate signaling pathways, and evade cell death (Koundouros & Poulogiannis, 2020; Vriens et al., 2019; Yi et al., 2020). Altered lipid metabolism has also been implicated in cardiac dysfunction, liver disease, and neurodegeneration (Adibhatla & Hatcher, 2008; Goldberg et al., 2012; Reddy & Sambasiva Rao, 2006). Therefore, the advancement of the lipidomics field could yield important insights into these diseases and others.

In recent years, altered lipid metabolism and increased lipid peroxidation were found to play a critical role in the iron-dependent cell death form, ferroptosis (Dixon et al., 2012; Doll et al., 2017; Kagan et al., 2017; Yang et al., 2016). Polyunsaturated fatty acids (PUFAs) are crucial to the process of lipid

peroxidation because the hydrogen atoms at the bis-allylic position between two double bonds are especially labile and subject to hydrogen atom abstraction by a radical (Yin et al., 2011). Arachidonic acid (AA) is a biologically relevant omega-6 PUFA with 20 carbon atoms and 4 non-conjugated double bonds at the 5, 8, 11, and 14 positions. It is found at a concentration of approximately 400 μM in human plasma (Abdelmagid et al., 2015). Previous work has shown that AA treatment can sensitize cells to ferroptotic death, enhancing the lethality of canonical ferroptosis inducer RSL3 in cancer cells (Do et al., 2023). RSL3 inhibits the lipid peroxide-reducing enzyme glutathione peroxidase 4 (GPX4) However, the exact species and biochemical events that lead to peroxide buildup and eventual cell death are unclear.

Despite its biological importance, lipidomics has several inherent difficulties that hinder its advancement. There are upwards of 47,000 observed and computational lipids in the Lipid MAPs database, which continues to expand (Sud et al., 2007b). Most of these cellular lipids occur in a relatively narrow mass range, from 500 -1200 Daltons. Within this range, there are many isomeric and isobaric lipids that are impossible to identify by mass alone. These traits make the separation, resolution, and identification of lipids quite challenging. Mass spectrometry is the primary tool used in lipidomics due to its resolving power, throughput, and customizability (Han & Gross, 2003). The use of chromatography and ion mobility, along with soft ionization techniques such as electrospray ionization (ESI), has greatly improved our ability to resolve many of these compounds (Blanksby & Mitchell, 2010).

Most lipids within a cell share the same structural pattern of two or three fatty acid tails attached to a polar or semi-polar headgroup. The headgroup structures have enough variation in their polarity that they can be separated using hydrophilic interaction liquid chromatography (HILIC) (Schwalbe-Herrmann et al., 2010). In addition, lipid ions can adopt different conformations while in the gas phase. Depending on the headgroup and degree and location of double bonds within the fatty acid tails, a lipid may be more or less compact in space (Kyle et al., 2016; Leaptrot et al., 2019; Zhou et al., 2017). Ion mobility (IM) spectrometry can measure the apparent surface area, *i.e.*, collision cross section (CCS), of an ion as it traverses an inert background gas (Mason & Schamp, 1958). CCS values are shown to be highly

reproducible across different IM platforms (Hinnenkamp et al., 2018; Hinz et al., 2018; Ross, Cho, & Xu, 2020) and have been used to enhance the confidence of lipid identification (Hines et al., 2017a). While these advances have significantly improved the utility of lipidomics, some challenges remain.

One of these challenges is the ability to trace lipid metabolites, as is commonly done in other areas of metabolomics (Jang et al., 2018). ^{13}C and deuterium labeling can be used to trace the metabolism of many compounds, including lipids, (Donnelly et al., 2005; Kamphorst et al., 2013; Louie et al., 2013) amino acids, (Ducker et al., 2016) and xenobiotics (Hu et al., 2019; Suthers et al., 2007). When a compound is labeled with ^{13}C or deuterium, it results in an increase in mass that differentiates it from the endogenous, unlabeled, analog. This mass shift can be detected with analytical methods including mass spectrometry and nuclear magnetic resonance and can be used to identify the compounds into which the molecule is metabolized (Jang et al., 2018). Applying this tool to lipidomics has been challenging because the mass shift associated with the isotopic label is often not enough to differentiate it from other lipids in the lipidome since most lipids occur in a narrow mass range (Triebl & Wenk, 2018). It is likely that labeled peaks could be missed or incorrectly identified because they may be indistinguishable from other lipids in the same sample.

To overcome this challenge, we developed a dual-isotope labeling technique that uses an equimolar mix of two different deuterated fatty acids (referred to as dFA). These fatty acids are incorporated into the lipidome equally by the cells, resulting in mass spectra with a signature doublet or triplet peak. These signature spectra, along with the same retention time and CCS values, can be used to recognize the features associated with the metabolites of the labeled fatty acid with confidence. We then developed a Python software, D-Tracer, to automatically pick out labeled metabolite pairs and correct the isotope shift to generate the *m/z* values of the corresponding non-labeled lipids. We integrated this program with our previously developed Python package, *Lipydomics*, to identify the mass-corrected lipids using three-dimensional data that includes *m/z*, chromatographic retention time (RT), and CCS values

(Ross, Cho, Zhang, et al., 2020). Subsequently, we applied this method to characterize the metabolic fate of labeled AA, NLA, and CLA in HT-1080 endothelial cancer cells in the context of ferroptosis

Methods

Materials: Mass spectrometry-related materials were previously described. (Hines et al., 2017a; A. Li et al., 2020) Briefly, HPLC grade solvents (water, acetonitrile, methylene chloride, chloroform, and methanol) were purchased from Thermo Fisher Scientific. Optima LC/MS grade ammonium acetate and sodium chloride were also obtained from Thermo Fisher. d_5- and d_{11}- AA were purchased from Cayman Chemical (9000477 and 10006758, respectively). MS analysis of these dAA standards found that they do not contain d0-AA but contain a small amount of d_4-AA (<5%) and d_{10}-AA (~15%) in d_5-AA and d_{11}-AA standards, respectively. d_7- and d_0- CLA and d_{11}- and d_0- NLA were purchased from Cayman Chemical (item numbers 26482, 90145, 9002193, and 90150 respectively).

Lipid internal standards: PE (15:0/15:0), Cer (d18:1/17:0), PG (15:0/15:0), PC (15:0/15:0), PA (12:0/12:0), PS (12:0/12:0), SM (d18:1/17:0), LysoPC(15:0/0:0), LysoPE ((13:0/0:0), GluCer(d18:1/17:0) and d7-PI(15:0/18:1) were purchased from Avanti Polar Lipids. DG (13:0/13:0) and TG (15:0/15:0/15:0) were purchased from NuChek. All standards were dissolved in LC-MS grade methanol at a concentration of 10 mg/mL. To make the internal standard mix, the dissolved internal standards were diluted in DMSO such that each standard was at a final concentration of 240 μM.

Cell Culture: HT-1080 cells (ATCC) were cultured in DMEM high glucose media containing 10% fetal bovine serum, 1% penicillin-streptomycin (Gibco), and 1% non-essential amino acids (Gibco). 5.0×10^5 cells were plated in 10 cm dishes and incubated at 37 °C. 24 hours later, the media was exchanged to media containing 80 μM of each deuterated AA, each CLA, or each NLA in the presence and absence of 0.03 μM RSL3. The cells were harvested after another 24 hours of incubation. To harvest the cells, cell culture dishes were first placed on ice. To retain any dead cells that have undergone ferroptosis, the media was collected into labeled glass centrifuge tubes and centrifuged at 1000 RPM for 5 minutes. The media

was then aspirated, leaving behind a pellet of cell debris. The remaining cells were then rinsed with PBS, scraped off the plates, and added to the corresponding centrifuge tube. Another round of centrifugation afforded the final cell pellets.

Lipid Extraction: Lipid extraction from treated cells took place as previously described.(A. Li et al., 2020) Briefly, cells were collected as described above. The cell pellet was resuspended in 300 μL of ice-cold PBS and sonicated for 30 minutes to lyse the cells. Protein levels were quantified using the Bio-Rad BSA Protein Quantification assay and a BioTek Synergy Microplate Reader. Next, 1 mL of ice-cold 0.9% (w/v) NaCl aqueous solution, 4 mL of ice-cold Folch reagent (2:1 v/v chloroform/methanol), and 12 μL of the 240 μM internal standard mix were added to each tube. The tubes were vortexed and centrifuged at 1000 RPM for 5 minutes. Using a glass Pasteur pipet with a mechanical pipet pump, the resulting lower organic layer was recovered from each tube and placed into a fresh tube. The solution was dried using a speed vacuum concentrator (Thermo Fisher Savant SpeedVac). The dried extract was reconstituted in 300 μL of methylene chloride, transferred to HPLC screw-top vials, and stored at -80ºC until for up to two weeks until analysis. Immediately prior to MS analysis, 25 μL of each sample was transferred to an HPLC vial with an insert and dried under nitrogen, then reconstituted in 100 μL of acetonitrile:methanol (2:1) for injection.

HILIC-IM-MS Method: The samples were analyzed on a Waters Synapt XS ion mobility-QTOF mass spectrometer with ESI as previously described (A. Li et al., 2020). The instrument was calibrated for CCS using PC and PE standards before use (Hines et al., 2016). Sodium formate was used for mass calibration in both positive and negative modes. HILIC A mobile phase is 95% acetonitrile, 5% water, and 5 mM ammonium acetate while HILIC B mobile phase is 50% acetonitrile, 50% water, and 5 mM ammonium acetate. The stationary phase used was a HILIC Phenomenex Kinetex 2.1 x 100 mm, 1.7 μm, column. Leucine enkephalin was used as a lock mass and CCS calibrant in both modes. The injection volume was 5 μL and solvent flow rate was 0.5 mL/min. The TriWave settings were as described (A. Li et al., 2020).

The samples were injected in order with a blank and pooled sample between each treatment group. Each run lasted 12 minutes starting with 100% HILIC A and dropping to 70% HILIC A by 8 minutes.

CCS calibration: CCS calibration was carried out as previously described.(Hines et al., 2016) Briefly, a mixture of phosphatidylcholine and phosphatidylethanolamine standards was directly infused into the ESI source of the mass spectrometer at 15 μL/ min while m/z and CCS values were acquired. PE lipids were used as a negative mode calibrant while PC lipids were used for positive mode.

Data Analysis: Data analysis was carried out using Waters Progenesis QI, EZ Info, and two in-house Python programs. First, Progenesis is used to align spectra, perform lock-mass calibration, and pick peaks. Treatment groups are compared to each other using ANOVA. Compounds that are significantly (corrected *P*-value < 0.05) different between dFA-treated and untreated groups are exported to EZinfo for OPLS-DA analysis. Significantly increased features in the treatment group relative to controls are selected from the resulting S-plot and exported as a .csv file.

To find labeled lipid species, we developed a Python software, D-Tracer, with a web interface. The software searches for species that have an RT within 0.01 minutes, a CCS within 3%, and an *m/z* separated by (D2 – D1) x the mass of deuterium. D1 and D2 are user inputs that can be customized. For arachidonic acid, D2 is 11, and D1 is 5. For the NLA and CLA, D2 is 11 and 7, respectively, and D1 is set to 0 for the unlabeled analogs. The mass of the deuterium is then subtracted from each identified species, and the output .csv contains the original *m/z*, adjusted *m/z*, RT, CCS, and normalized intensities for each lipid. The number of samples is also a user input that can be customized. The software has been tested on peaklists containing up to 6,000 compounds and can complete analysis of these large datasets in less than 5 minutes. The source code is available on GitHub under the name D-Tracer (https://github.com/nreimers99/d-tracer).

To identify lipid species, we used LiPydomics, which is a Python software developed by our group (Ross, Cho, Zhang, et al., 2020). LiPydomics identifies lipids by comparing their RT, m/z, and CCS to known values in a database. Identifications are further confirmed using the LipidMaps database.

To quantify each lipid species, the intensities of individual lipid species were compared with an internal standard from the same class.

Results and Discussion

Development of D-Tracer: There are existing programs commonly used to analyze lipidomics data and identify lipids based on their *m/z*, RT, and CCS values, including LipidIMMS (Zhou et al., 2019), MS-Dial 4 (Tsugawa et al., 2015, 2020), and Lipydomics (Ross, Cho, Zhang, et al., 2020). However, these programs could not be used to identify isotope-labeled lipids due to the isotopic mass shift from deuterium incorporation. To identify the lipids using established databases, the mass of deuterium-containing lipids must first be adjusted to the mass of the corresponding non-labeled lipid. Some programs can analyze single-isotope labeling experiments, (Huang et al., 2014; *Isotope Distribution Calculator, Mass Spec Plotter, Isotope Abundance Graphs*, n.d.; Millard et al., 2012) but, to our knowledge, no program is currently available for dual-isotope labeling lipidomics. To address this, we developed a web-based Python program called D-Tracer to find and adjust the mass of deuterated lipids. The program was designed to be intuitive and accessible to those without prior coding experience. The simple web version can be accessed by a url: (https://nreimers99-d-tracer-original-d-tracerapplication-xji04u.streamlit.app/; see Supplementary Information for detailed instructions), whereas the full version can be used in the terminal. The program can analyze dual isotope deuterium labeling experiments with any degree of deuteration from 0 to 80 deuterium atoms and any .csv peaklist if it contains RT, CCS, and *m/z* columns. A schematic of D-Tracer is shown in Figure 2.1A.

To use the program, the user first uploads a peaklist and specifies the types of deuterium labels used in their experiments. The labels can be separated in mass by any number of deuterium atoms. D1 refers to the smaller number of atoms (0 is the smallest possible) and D2 refers to the larger number of atoms. The program will then scan through the peaklist and search for all species with a mass difference of the two masses as calculated below.

(D2 × deuterium – D1 × deuterium) = difference

In the AA case, this value is 6 × 1.0063 or 6.0378 Da. Once a match is identified, the program checks that the retention time is within 0.01 minutes and that the CCS values are within 3% of each other. These tolerance values are hard-coded into the web version but can be manipulated in the source code available on Github. If all three criteria are fulfilled, the feature pair is added to a new dataset. The program will then subtract the mass of the deuterium from the pairs so they can be identified using existing software for non-labeled lipids. To do this, the program subtracts the specified D1 and D2 masses from the smaller and larger mass, respectively, for each pair. The adjusted masses are added as a separate column to the pairs .csv file, which can then be exported for further analysis.

Incorporation of Deuterated Arachidonic Acid

Deuterated lipids were first identified from peak lists containing features that were significantly different between dAA-treated and untreated groups using D-Tracer. The lipids were then validated by manual inspection of the mass spectra. Correctly identified deuterated lipids appear as a doublet or triplet peak on the mass spectra. The doublet peak is formed when d_5 and d_{11}-AA (Figure 2.1B) are incorporated into the species at a higher concentration than unlabeled AA from the media (Figure 2.2A). The triplet peak is observed when two AAs are incorporated, giving lipid species with two d_5-AA, d_5-AA + d_{11}-AA, and two d_{11}-AA, separated by 6 Da each (Figure 2.2A bottom panel). The *m/z* values of the non-labeled version of such lipid species are then calculated manually accordingly.

Once dAA-containing lipids were extracted from the peaklists with D-Tracer, the resulting mass-adjusted lipid species were processed further using *Lipydomics*, which identifies lipids based on RT, CCS, and *m/z* values (Ross, Cho, Zhang, et al., 2020). The identifications were cross-validated using Lipid MAPS MS bulk data search, which searches for *m/z* matches in its lipid database.

Using the workflow described above, we carried out comprehensive dAA-tracing in the cancer cell line, HT-1080, in the presence of vehicle (Control or C), the ferroptosis inducer RSL3 (R), dAA only

(D), or co-treatment with dAA + RSL3 (DR). HT-1080 is a well-established cell line that is susceptible to ferroptosis when treated with various ferroptosis inducers, including RSL3 (Dixon et al., 2012). We first confirmed increased lipid peroxidation using flow cytometry after treatment with C11-BODIPY, (Drummen et al., 2002; Martinez et al., 2020) which specifically reacts with peroxyl radicals, suggesting the occurrence of ferroptosis when the cells were co-treated with dAA, dNLA or dCLA and RSL3 (see Figure 2.3). Using D-Tracer and *Lipydomics*, we found that dAAs were incorporated into triglycerides (TG), phosphatidylinositol (PI), phosphatidylethanolamine (PE), phosphatidylserine (PS), and phosphatidylcholine (PC) species. Representative doublet (one AA chain) and triplet (two AA chains) mass spectra are shown in Figure 2.2A. Untargeted fragmentation of various lipid classes using MS^E (Figure 2.2B) allowed the confirmation of the incorporation of d_5- or d_{11}-AA. Interestingly, elongation of dAA to 22:4 followed by incorporation to phospholipids was also observed as confirmed by targeted fragmentation, supporting the utility of dual-isotope tracking of AA metabolism (Figure 2.2B).

Quantification of the lipid classes was carried out by comparison with an internal standard from each class with a known concentration (Figure 2.4). The highest level of dAA incorporation was into TG (69% of total lipid quantity), followed by PI (14% of total lipid). Incorporation into PS, PC, and PE lipids comprised 10% or less of the total quantity in the dAA-only treatment group (Figure 2.4A). In the dAA+RSL3 treatment group, the level of incorporation into TG decreased from 69% to 64%, while incorporation into PI increased from 14% to 20% (Figure 2.4B). Incorporation into other classes did not change significantly in the co-treatment group from the dAA-only group. The high degree of incorporation into TG species is likely due to the increased formation of lipid droplets in response to high levels of exogenous fatty acids (Magtanong et al., 2019; von Krusenstiern et al., 2023a). The alterations in dAA-containing lipid composition in the presence of RSL3 may be a result of ongoing ferroptosis. For example, TGs may be preferentially oxidized in lipid droplets while PIs may not readily undergo lipid peroxidation. However, the elucidation of the detailed roles of these lipids in ferroptosis may involve quantitation of these lipids in specific organelles.

Not all lipid classes incorporated dAA in detectable quantities. Phosphatidic acid (PA) and diacylglycerol (DG) are precursors for PI, PE, PC, and PS phospholipids (Figure 2.5), but were not found to incorporate dAA. In addition, dAAs were not found in sphingolipids, suggesting sphingolipids do not readily incorporate AAs or promote ferroptosis. PUFA-containing ether lipids have been previously found to promote ferroptosis susceptibility (Zou et al., 2020). Indeed, we found that dAA was incorporated into plasmanyl ether lipids, including PE, PS, and PC ether lipids. As expected, the normalized intensities of all dAA-containing lipids are the highest in dAA-treated groups, D and RD.

In addition, the abundances of lipids in each class, as determined by comparison with the internal standards, were found to be higher in the dAA-only group than in the dAA + RSL3 group although not every class of lipids displayed statistical significance (Figure 2.6A). This could be due to the reduced viability of cells in the co-treatment group, which could lead to overall decreased lipid levels, and/or the oxidation of the parent lipids. Indeed, by manually inspecting the data, we were able to identify an oxidized PE species, PE(38:4) +14Da, which correspond to +O-2H of PE(38:4) (Figure 2.7).

Interestingly, the ratio of oxidized lipid to parent lipid was higher in the dAA + RSL3 group than in the dAA-only group, despite the overall lower lipid abundance in the cotreatment group (Figure 2.7). The identification of the oxidized PE demonstrates the utility of dual-isotope labeling in the confident detection of low-abundance metabolites. The observation of higher level of oxidized PE supports the important roles of PE peroxidation in the execution of ferroptosis, which is consistent with a previous report by Kagan et al. (Kagan et al., 2017). We note that there are a number of other dAA-containing lipids that were not identified through *Lipydomics* and LIPID MAPS. We speculate that these unidentified lipids are also likely oxidized lipids. However, due to the low abundance of these species, targeted fragmentation is not possible to obtain the fatty acid composition. Thus, a limitation of *Lipydomics* is the lack of coverage of the oxidized lipids in its RT and CCS database and a future direction of this work is to expand the three-dimensional database to include such lipids.

Incorporation of Deuterated Conjugated and Nonconjugated Linoleic Acid

To determine whether lipid incorporation depends on the conjugation of double bonds in PUFAs, we repeated the dual-isotope labeling experiment using deuterium-labeled conjugated linoleic acid (CLA) and nonconjugated linoleic acid (NLA). Both lipids are 18:2 fatty acids, however the double bonds in CLA are conjugated, which makes it more prone to peroxidation by reactive oxygen species (see structures in Figure 2.1C and D). Because CLA is highly oxidizable, it is more potent at inducing ferroptosis in cells and can even do so without the addition of any small molecule ferroptosis inducers at certain concentrations (Do et al., 2023). Like NLA, AA is a nonconjugated fatty acid, but it is more susceptible to peroxidation than NLA because it has 3 potential bisallylic sites for oxidation, whereas NLA only has 1 bisallylic site. We hypothesized that CLA and NLA would be incorporated into different phospholipids and have different responses to RSL3 treatment due to their different propensities for oxidation. To evaluate this hypothesis, we followed the same procedure that was used to evaluate the metabolism of AA, except we were unable to source two differently labeled analogs of these lipids. Instead, we used one labeled analog and one unlabeled analog as our dual-isotope pairs (Figure 2.1 C and D). Because NLA and CLA occur naturally in cell media, we used only the signal from the labeled lipids in the quantitation step to ensure we were accounting only for lipids incorporating exogenous fatty acids.

As with AA, we observed widespread incorporation of NLA and CLA into most major lipid classes (Figure 2.4). NLA was most incorporated into TG, PC, PI, and PG lipid classes while CLA was most incorporated into TG, PE, PC, and LysoPE lipid classes. Interestingly, unlike AA, neither dNLA or dCLA-containing TG lipid abundance decreased with RSL3 treatment. In fact, there were no significant differences in the abundance of incorporated lipids between cells treated with NLA alone and cells treated with NLA+RSL3 (Figure 2.6B). This is in contrast to AA-treated cells which showed a significant decrease in TG, PS, and PC dAA-containing lipids with RSL3 treatment. In CLA treated cells, there was a significant decrease in all lipid classes containing dCLA except for TG, in which there was a significant increase (Figure 2.6C).

The decrease in deuterated PUFA containing lipids observed in AA and CLA treated cells with RSL3 is consistent with the hypothesis that these lipids are being oxidized during ferroptosis because CLA and AA have a higher peroxidation rate constant than NLA, meaning that they are more susceptible to peroxidation (Do et al., 2021). Indeed, these lipids are also more potent at increasing the lethality of RSL3 than NLA, which demonstrates the role that their increased susceptibility to peroxidation may play in the ferroptosis process (Do et al., 2023). This hypothesis is confirmed by the greater degree of lipid peroxidation in AA and CLA treated cells than in NLA treated cells as assed by C11-BODIPY staining in Figure 2.3.

Conclusion

Here we report the development and application of dual-isotope labeling lipidomics to the study of *in vitro* AA, NLA, and CLA metabolism during ferroptosis. We developed a Python software, D-Tracer, to automatically analyze deuterium isotope labeling mass spectra with a user-friendly web interface. Combining this software and *Lipydomics* for lipid identification, we found that deuterated AA, NLA, and CLA are incorporated into several lipid classes in HT-1080 cells, with TG being the predominant one. The amount of deuterium-incorporated lipids decreased in AA and CLA treatment groups with RSL3 treatment, but not in the NLA treatment groups. Combined with the identification of oxidized AA-containing lipid products in the dAA+RSL3 treated group, this finding supports the idea that highly oxidizable PUFAs including AA and CLA are oxidized in cells during ferroptosis, resulting in the observed decrease in deuterium-containing lipids with RSL3 treatment. Thus, the dual isotope labeling combined with three-dimensional HILIC-IM-MS can effectively elucidate lipid metabolic changes associated with biological processes and disease states. The D-Tracer program can also be easily modified to characterize the metabolism of other biological molecules, such as sugar and peptides, potentially expanding its utility.

Figures

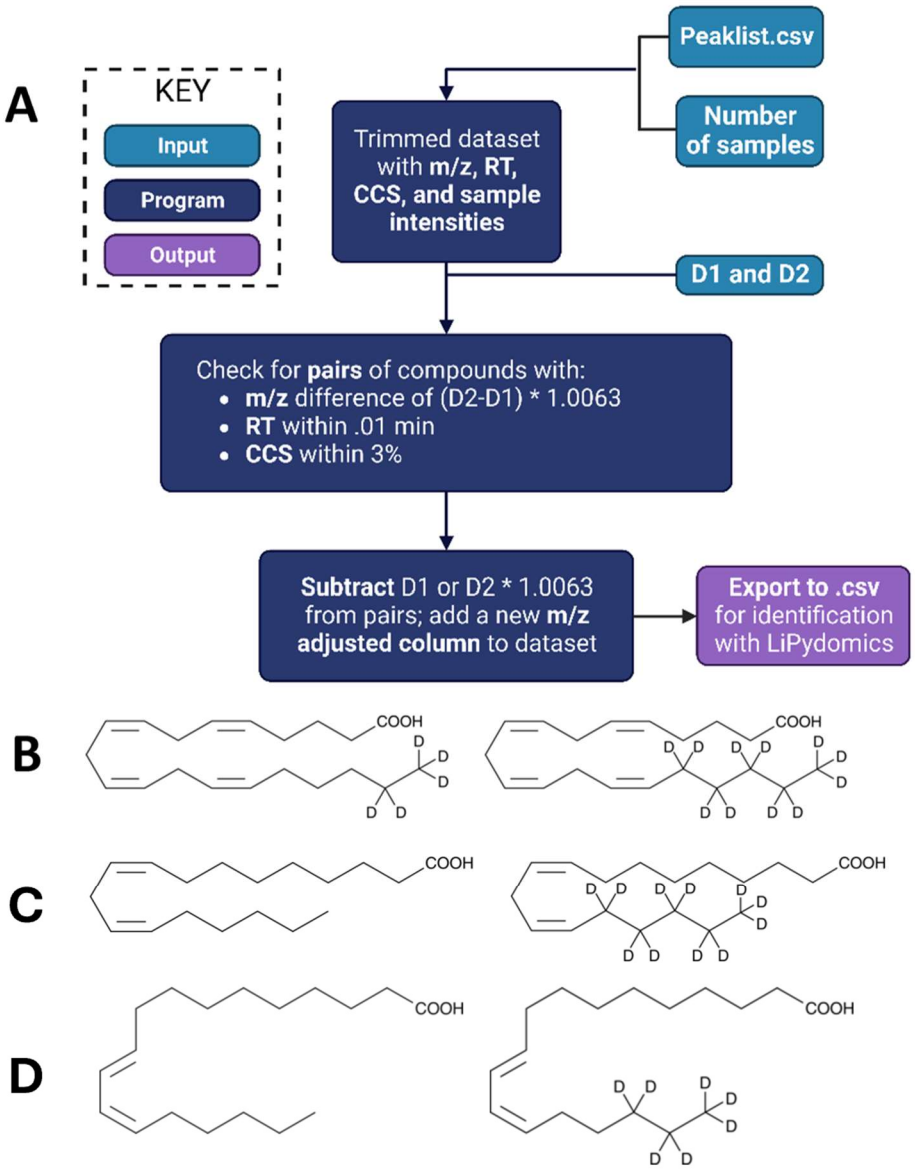

Figure 2.1: A) Schematic of the Python-based software D-Tracer. User inputs into the program are shown in light blue, functions are shown in dark blue, and outputs are shown in purple. Figure created using BioRender.com. B-D) **Structures of deuterated lipids used in this study**: d_5 and d_{11} arachidonic acid, d_0 and d_{11} nonconjugated linoleic acid, and d_0 and d_7 conjugated linoleic acid, respectively.

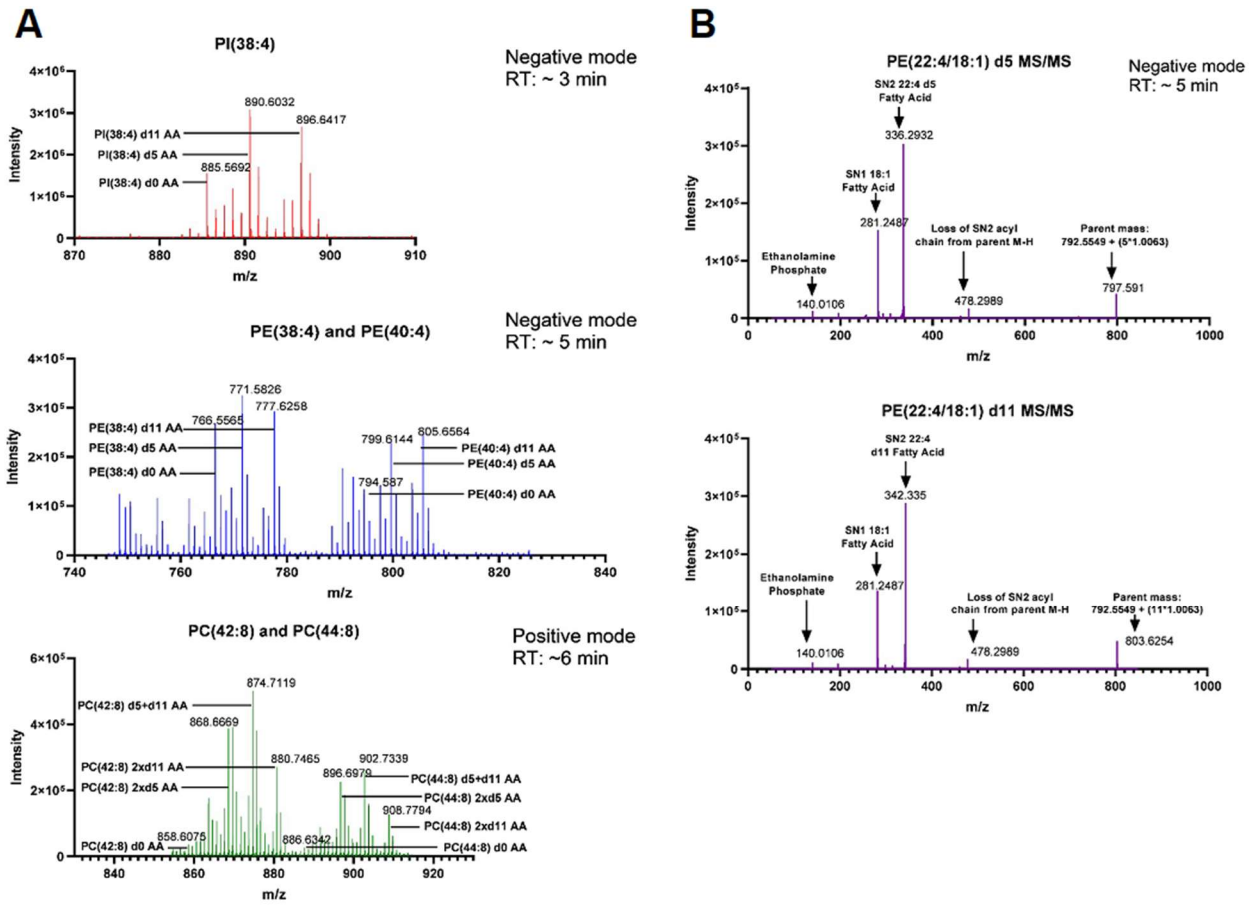

Figure 2.2: A) Examples of signature doublet and triplet peaks from lipids that incorporate d5 and d11 AA. Peaks labeled d0-AA represent the lipid incorporating unlabeled AA. PC 42:8 and 44:8 each incorporate two AA, so they form triplets corresponding to 2 x d5 AA, 1 d5 and 1 d11 AA, and 2 x d11 AA. B) Targeted MS/MS fragmentation of PE(22:4/18:0) incorporating d5 AA and d11 AA, respectively.

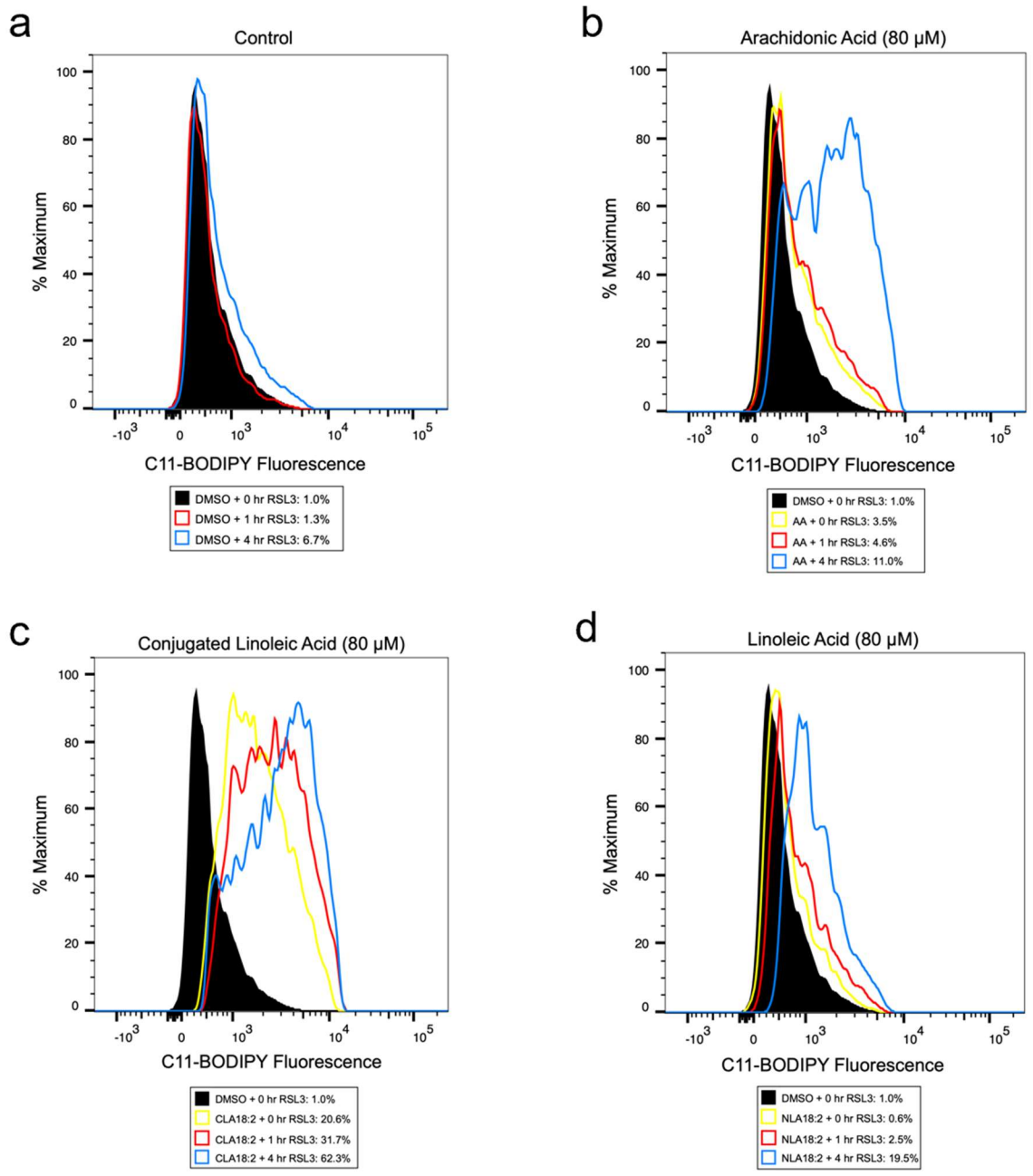

Figure 2.3: Flow cytometry with C11-BODIPY stained HT-1080 cells confirming increased levels of lipid peroxidation when AA (B), CLA (C), or NLA (D) is co-administered with RSL3.

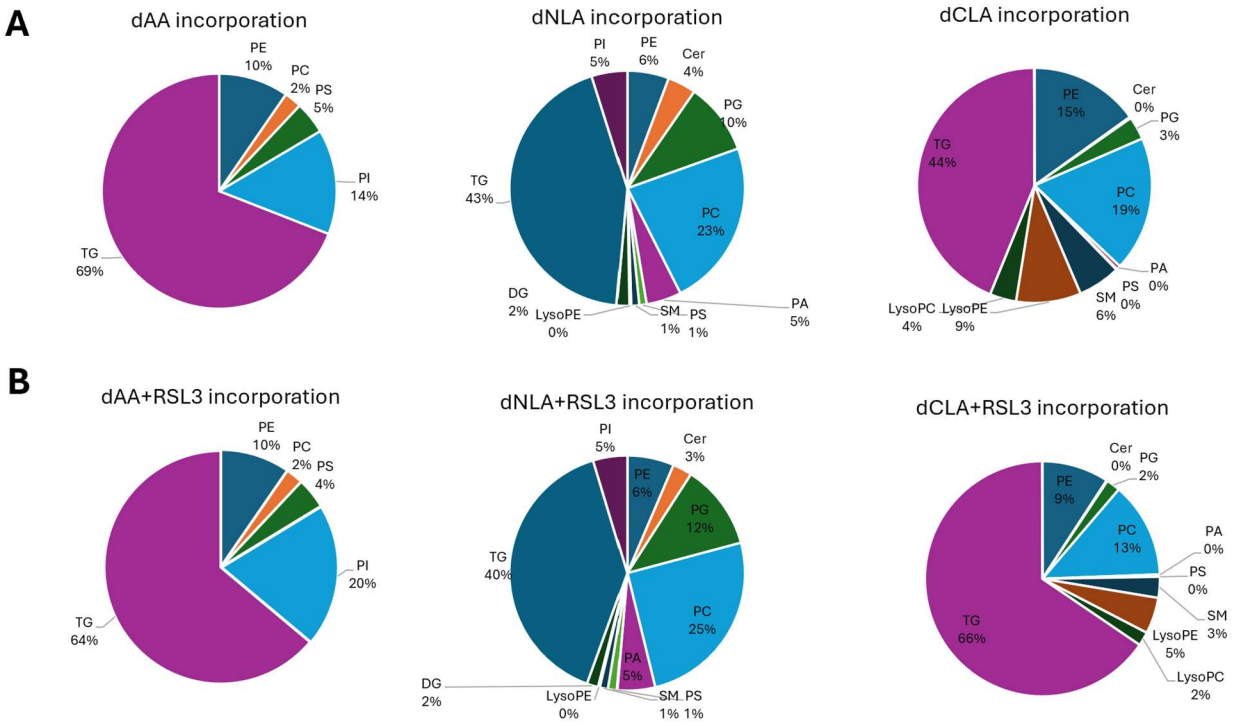

Figure 2.4: Pie charts representing the percent of each lipid class making up the total amount of deuterium-containing lipids identified in the absence (A) and presence (B) of RSL3 in cells treated with dAA, dCLA, or dCLA, respectively. Abbreviations: TG; triacylglycerol, PE; phosphatidylglycerol, PC; phosphatidylcholine, PS; phosphatidylserine, PI; phosphatidylinositol, Cer; ceramides, PG; phosphatidylglycerol, PA; phosphatidic acid, SM; sphingomyelin, DG; diacylglycerol.

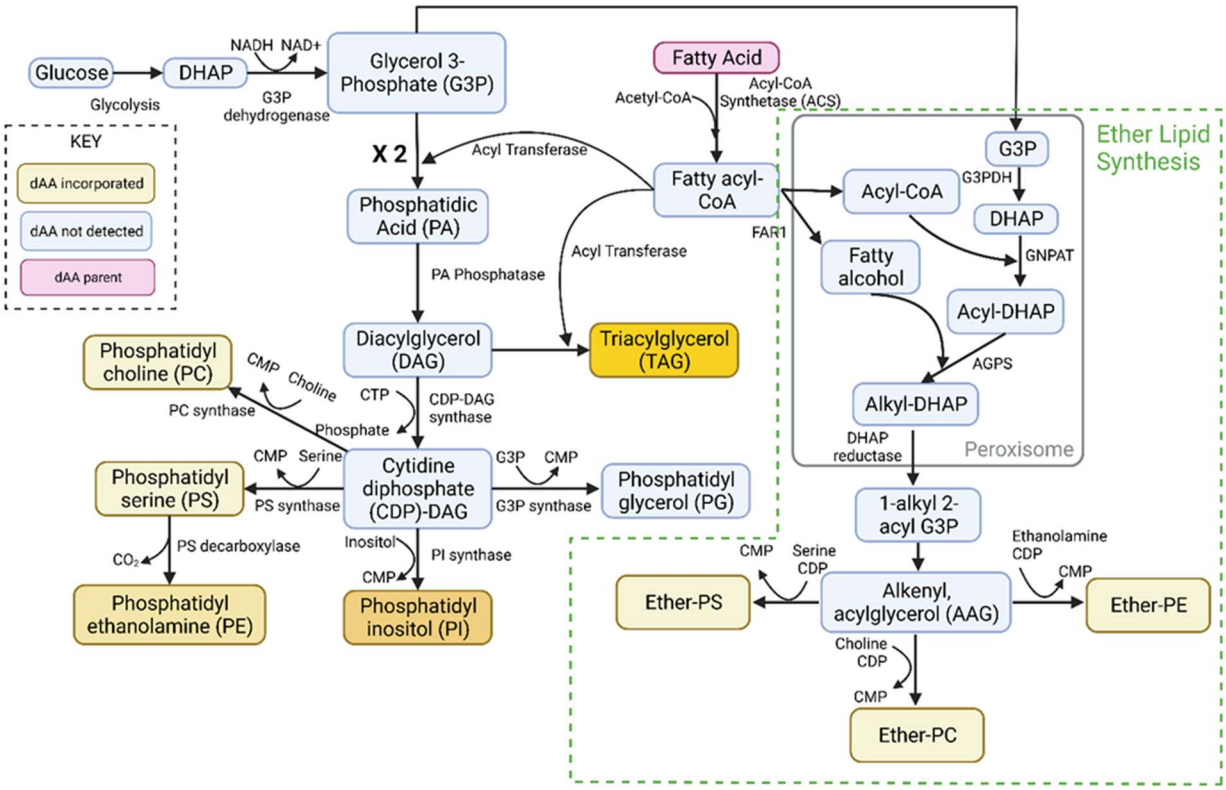

Figure 2.5: Scheme of the biosynthetic pathway of phospholipids via the cytidine diphosphate diacylglycerol (CDP-DAG) intermediate. Species found to incorporate dAA are shown in yellow. Darker yellow indicates more incorporation, lighter yellow indicates less incorporation as measured by quantitation. Abbreviations: DHAP; dihydroxyacetone phosphate, CMP; cytidine monophosphate, G3PDH; glycerol-3-phosphate dehydrogenase, GNPAT; glyceronephosphate O-acyltransferase, AGPS; alkylglycerone phosphate synthase, FAR1; fatty acyl-CoA reductase. Figure created using BioRender.com

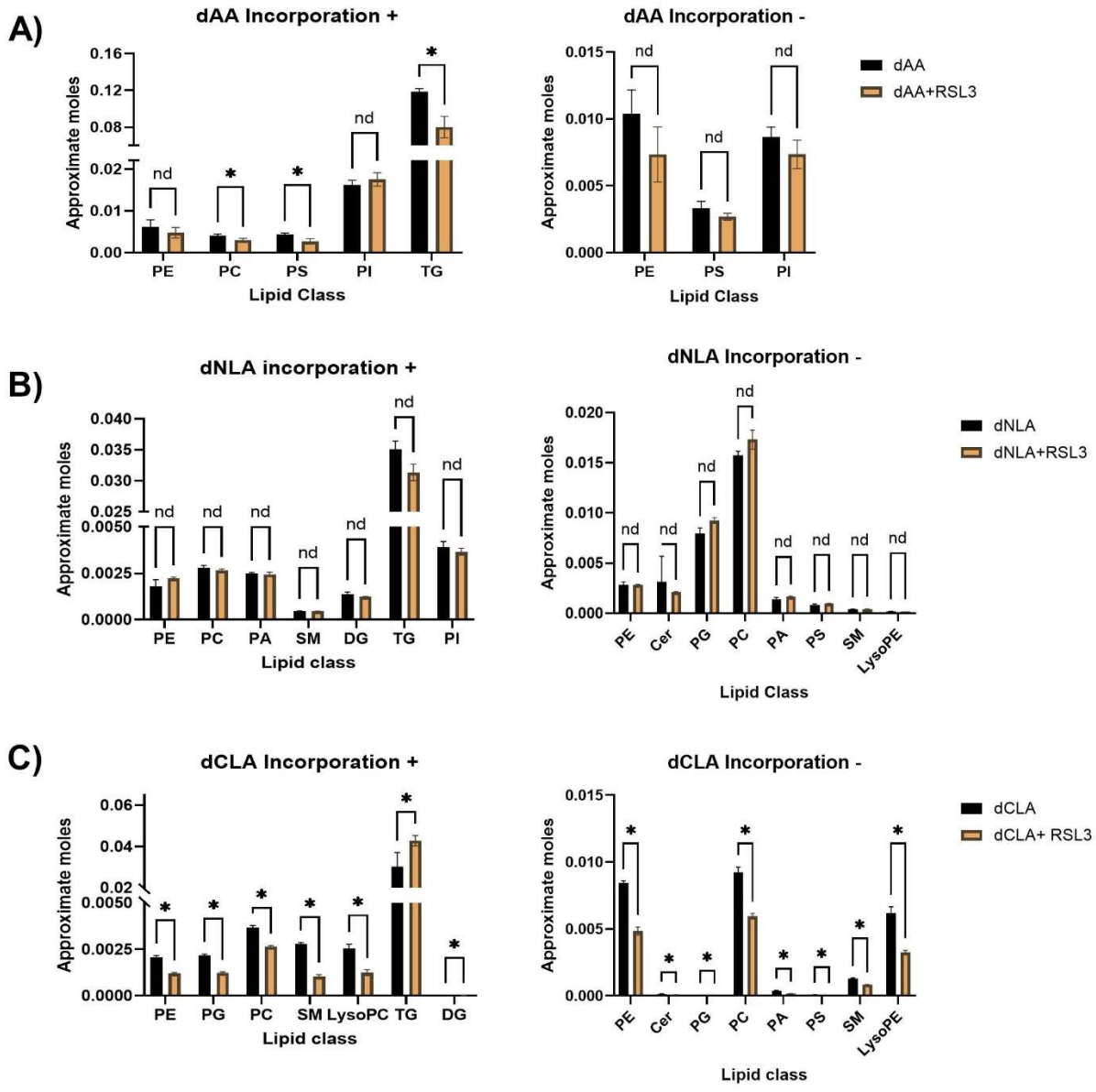

Figure 2.6: Bar charts representing the approximate moles (calculated by comparison with an internal standard from each lipid class) of deuterium-containing lipids identified in cells treated with dAA (A), dNLA (B), or dCLA (C) with and without RSL3. + and – in the chart title represents the ionization mode in which the data were collected. Abbreviations: TG; triacylglycerol, PE; phosphatidylglycerol, PC; phosphatidylcholine, PS; phosphatidylserine, PI; phosphatidylinositol, Cer; ceramides, PG; phosphatidylglycerol, PA; phosphatidic acid, SM; sphingomyelin, DG; diacylglycerol.

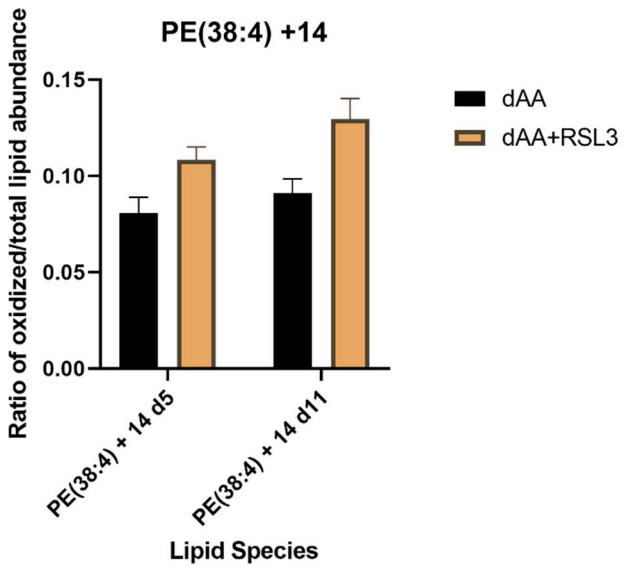

Figure 2.7: Ratio of oxidized (m+14 Da) to parent PE(38:4) incorporating d_5 and d_{11} AA lipid in cells treated with dAA alone or with RSL3.

Chapter 3: Development and application of an oxylipid LC-MS database

Introduction

The study of oxidized lipids, otherwise known as oxy-lipidomics or epilipidomics, is a relatively new branch of the lipidomics field. Interest in oxidized lipids is driven by multiple factors, including the discovery of ferroptosis and the implication of oxidized lipids in various disease states (Kodali et al., 2020). Cardiovascular disease is an example of a disease associated with lipid oxidation, in which the accumulation and subsequent oxidation of lipids within the arterial wall contribute to inflammation, vascular dysfunction, and the development of atherosclerosis (Gianazza et al., 2019). Lipid oxidation products, including isoprostanes and reactive aldehydes, as well as lipid-derived protein adducts, have been extensively characterized in cardiovascular disease, and the levels of these biomarkers are often associated with disease severity (Ho et al., 2013). Lipid oxidation products have also been observed to accumulate as cells undergo ferroptosis, both using direct measurement with tools including LC-MS/MS and indirect measurement with lipid peroxidation sensors including the fluorescent probe C11-BODIPY (Drummen et al., 2002; Kagan et al., 2017; Martinez et al., 2020; Samovich et al., 2024). Therefore, the detection and identification of lipid oxidation products is an area of interest for many applications of lipidomics research. While lipid oxidation sensors such as C11-BODIPY are helpful for determining whether lipid oxidation is present, mass spectrometry remains the gold standard for structural elucidation and identification of lipid oxidation products.

However, MS-based measurement and identification of lipid oxidation products is challenging for several reasons. Lipid oxidation products are highly reactive and subject to decomposition if proper precautions are not taken. In addition, they occur at an extremely low abundance relative to most of the other lipids present within a sample. For example, a study by Yoshida et al. found that the ratio of total

hydroxyoctadecadienoic acids (HODEs) to their parents, linoleates, in plasma samples was 194 μmol/mol of parent lipid (Yoshida et al., 2007). In other words, the concentration of oxidized linoleates was only about 0.0002% of the parent concentration in plasma. This low abundance makes them very difficult to detect when using untargeted MS acquisition methods such as data-independent and data-dependent acquisition (DIA and DDA), as they are easily lost to background noise. Furthermore, like all lipids, there are many isomeric and isobaric lipid oxidation products that are not possible to confidently identify without MS/MS fragmentation. Finally, there is a lack of reference data that can be used to confidently identify lipid oxidation products. While tools are developing for this purpose, including the LipidMaps oxylipid database and LPPTiger oxylipid identification software, more experimental data is needed to improve confidence and ease of identification for oxylipid products (*LIPID MAPS*, n.d.; Ni et al., 2017).

This study aims to address this gap in knowledge by generating an experimental oxylipid database including lipid identification, m/z, retention time (RT), collisional cross section (CCS), and fragment information for phospholipids from phosphatidylethanolamine (PE), phosphatidylcholine (PC), phosphatidic acid (PA), and phosphatidylglycerol (PG) lipid classes. To accomplish this, intact phospholipids were incubated in vitro with a radical initiator in the presence of oxygen to generate the oxidation products, then analyzed using targeted and untargeted methods on a Waters Synapt G2-XS mass spectrometer. The products were characterized and identified by spectral matching to a theoretical spectral library generated by LPPTiger in Skyline software. A Skyline-compatible target list in .csv format was then produced, containing the parent and product m/z, their identifications, retention times (RT), and CCS values, to facilitate the confident identification of lipid oxidation products in MS datasets.

Methods

In-vitro phospholipid oxidation: PLPC (PC(16:0/18:2)) in chloroform was dried down under argon and kept under vacuum for 10 minutes before being resuspended in 5× phosphate-buffered saline (PBS, Gibco) to a final concentration of 100 μM. Phospholipid mixtures (sunflower PA, soy PI, soy PC, soy PS,

sunflower PE, and sunflower PG (Avanti)) were mixed with neutral PC(14:0/14:0) in a ratio of 1:4 before drying and resuspension. Samples were sonicated for 5 mins, incubated at 37 ºC for 10 mins, and sonicated for 2 additional minutes to form liposomes. 10 µL of freshly prepared 0.02M 2,2'-Azobis[2-(2-imidazolin-2-yl)propane] Dihydrochloride in PBS (AIPH, TCI) was added to each sample, and they were incubated at 37 ºC for the desired time (0, 2, 4, or 24 hours). The incubation was quenched with 100 µL each of 0.1 M butylated hydroxytoluene (BHT) and 0.1 M triphenylphosphine (PPh_3) (Sigma) in ethanol and 4:1 ethanol:methylene chloride, respectively, and incubated for 30 minutes at room temperature. 1 mL of chilled Folch solution (2:1 chloroform:methanol) was added to each sample and vortexed. The lower organic layer was collected, dried under argon, and reconstituted in 2:1 methanol:acetonitrile for MS analysis.

MS analysis of oxylipid products: Oxidized lipid products were analyzed as previously described (Hines et al., 2017b). Briefly, samples were analyzed on a Waters Synapt G2-XS QTOF mass spectrometer with ion mobility and a Waters Acquity liquid chromatography system. Hydrophilic interaction liquid chromatography (HILIC) was used to separate the analytes with a HILIC Phenomenex Kinetex 2.1 x 100 mm, 1.7 µm column as the stationary phase. Mobile phase B was 95% acetonitrile, 5% water, and 5 mM ammonium acetate, while mobile phase A was 50% acetonitrile, 50% water, and 5 mM ammonium acetate across a 12-minute gradient. Samples were analyzed using an established data-independent acquisition scheme in negative ionization mode. A targeted fragmentation method was developed to confirm the identity of products found during the initial pilot study of PLPC oxidation using the precursor m/z for isolation and a collision energy ramp from 25 to 40 volts. Sodium formate was used for mass calibration, leucine enkephalin was used as a lockmass for all samples, and a standard mixture of PC and PE phospholipids was used for CCS calibration (Hines et al., 2016).

Generation of theoretical spectral libraries: Theoretical spectral libraries were created using LPPTiger software (Ni et al., 2017). Parent lipid lists were created for each headgroup containing all possible combinations of fatty acids that could be present in each phospholipid mixture (16:0, 18:0, 18:1, 18:2, 18:3, see Table 3.1 for fatty acid distributions) and input into LPPTiger under Refine epilipidome by unmodified lipids in the "in silico prediction" tab. A maximum of two modification sites were selected, with 3 max total oxygens, 2 max hydroxy groups, 1 max keto group, and 0 peroxyl or epoxy groups set as tolerances. Peroxyl and epoxy groups were excluded from the prediction because the antioxidant PPh_3 that was used to quench the oxidation would reduce these groups to hydroxyls. A script was written in Python to convert the resulting .json predicted epilipidome into a Skyline-compatible .msp spectral library file for each lipid class.

Creation of experimental oxylipid database using Skyline: Theoretical .msp spectral libraries were loaded into Skyline for each lipid class. Transition settings in Skyline were set to match the DIA data acquired on the Waters Synapt G2-XS mass spectrometer. Raw negative mode MS data was uploaded and matched automatically to the library. All transitions were manually reviewed and accepted or deleted based on the quality of the match. In order to be accepted, a match needed to have at least 3 precursor isotope peaks, the SN1 and SN2 fatty acid fragments, and the intensity of these peaks needed to be above the level of background noise. Accepted precursor and corresponding fragment peaks were exported from Skyline as a results file. CCS values were calculated using Progenesis software (Waters) and were manually added to each precursor peak. The final experimentally validated .csv transition list can be uploaded to Skyline as a transition list and used to search through DIA, DDA, or PRM/SRM MS datasets. The .csv library contains precursor m/z, name, and formula, as well as 3 isotope peaks and fragments with the expected area of each peak. The HILIC retention time and CCS are also included for all precursors. The complete .csv file will be included with publication and will also be available along with all raw data and Skyline files in the Massive data repository (**MSV000102924**, password: Oxylipids1).

Lipidomic analysis of HT-1080 cells: HT-1080 cells (ATCC) were seeded at a density of 500,000 cells into 10 cm culture dishes (Costar) in Dulbecco's high glucose modified eagle medium supplemented with 10% fetal bovine serum, 1% non-essential amino acids, and 1% penicillin-streptomycin (Gibco). Cells were allowed to adhere for 24 hours before the media was replaced with media containing DMSO as a vehicle control, 30 nM RSL3, 80 μM of an equimolar mixture of deuterated and unlabeled fatty acid, or both RSL3 and fatty acid. The fatty acids used in this study were conjugated linoleic acid (CLA) and nonconjugated linoleic acid (NLA). Both labeled (d_7-CLA and d_{11}-NLA) and unlabeled fatty acids were purchased from Cayman Chemical. The cells were incubated for 24 hours, and lipid extraction was completed as previously described (Hines et al., 2017b; Reimers et al., 2023). Samples were analyzed on a Waters Synapt G2-XS mass spectrometer using the same analytical and chromatographic methods as described above.

Results:

Detection and identification of oxylipids from in-vitro oxidation of PLPC: In an initial pilot study, PC(16:0/18:2) (PLPC) was formed into liposomes in aqueous solution and incubated with the radical initiator AIPH for 0, 2, 4, or 24 hours before quenching with antioxidants. The products were analyzed by untargeted LC-MS followed by targeted MS/MS to confirm their identities (Figure 3.1). Over the course of the oxidation, later eluting peaks were formed (Figure 3.2 A). These peaks corresponded to lipid oxidation products, whose identity was determined using targeted fragmentation (Figure 3.2). After 2 hours of incubation, we identified PC(16:0/18:2+1O) as the primary oxidation product that formed. After 4 hours, a later eluting peak was observed, which grew in magnitude by the 24-hour mark (Figure 3.2 C). This product was identified to be a truncation product, PC(16:0/9:0+1O); formed when the oxidized fatty acid undergoes Hock rearrangement and a carbon-carbon bond cleavage to release an aldehyde (Figure 3.3) (Williams et al., 2007). For the remainder of this study, we will refer to products resulting from the

addition of oxygen or hydroxy groups as oxygen addition products, and truncated products resulting from Hock rearrangement as truncation products. These were the two classes of oxylipids that were primarily identified in this study.

Oxidized lipids elute later than their parents proportionally to their degree of oxidation on a hydrophobic interaction liquid chromatography (HILIC) column. The retention time shift associated with oxidation is robust and expected; when using HILIC, more hydrophobic analytes elute first, and more hydrophilic analytes elute later. As the lipids are oxidized, they become more hydrophilic than their parents and elute later on the HILIC column. Across all PC oxidation products that we observed, we noted a consistent increase in retention time from parent to product that was proportional to the extent of oxidation (Figure 3.4 A). When products were averaged based on the extent of their oxidation, the retention time shift from the parent increases with the degree of oxidation (Figure 3.4 B). The distinct relationship between the degree of oxidation and retention time shift from the parent in PC lipid species could be used as a metric to increase confidence in the identification of lipid oxidation products.

Lipid oxidation products are not significantly compacted compared to the parents. CCS measures the three-dimensional conformation of analytes in the gas phase. It is calculated from drift time, which is the time it takes for the analyte to travel through a drift region filled with inert gas. Analytes that are larger will experience more collisions with the inert gas, causing them to take longer to traverse the drift tube and resulting in a larger CCS value (Figure 3.5 A). The compaction factor (C) of a product or metabolite represents the relationship between the m/z and gas-phase CCS of the parent and its product (Figure 3.5 B). Previous work from our lab has shown that the oxidative metabolism of certain xenobiotics results in them becoming more compact than their parents (Ross et al., 2019). We hypothesized that the oxidation of phospholipids could result in the same trend and therefore examined the CCS to m/z trend and compaction factors of the identified lipid oxidation products. The CCS to m/z

trend did not differ significantly between parents, oxygen addition products, and truncation products (Figure 3.6 A). While it appears that truncation products may be slightly more compact (lower CCS for the same m/z) than parent and addition products, calculation of the compaction factors for these products showed that the trend was not consistent (Figure 3.6 B). A compaction factor of greater than one indicates that a product is more compact than its parent, while a factor of less than one indicates less compaction than the parent. Neither the oxygen addition nor the truncation products showed a consistent trend in either direction, demonstrating that CCS and its resulting compaction factor are not a reliable metric to discern between oxidized and non-oxidized phospholipids.

LPPTiger software can be used to generate theoretical in-silico spectral libraries of lipid oxidation products. LPPTiger is an open-source software that was created by Dr. Zhixu Ni in the Maria Federova lab (Technische Universität Dresden) for the lipidome-specific prediction and identification of oxidized phospholipids from LC-MS DDA datasets (*GitHub - LMAI-TUD/Lpptiger2: LPPtiger2 · GitHub*, n.d.; Ni et al., 2017). It has multiple functions that are useful for identifying oxidized phospholipid products. Given a list of potential parent lipids present in a sample, it can generate an inclusion list containing the m/z, identity, formula, and fragment information for all possible oxidation products from each parent lipid (Figure 3.7 A). The information is stored in a .csv and in a .json file that can be exported from the software. The next function of the software is to search through DDA LC-MS datasets for these lipid oxidation products, producing 5 scores to quantify the quality of identification between the stored theoretical database and the user's actual experimental data. The scores are based on fragment spectra similarity, ranking of similar structures, chemical fingerprint, spectral specificity, and isotope distribution (Figure 3.7 B). It is important to note that this software is only compatible with negative mode DDA MS data that does not contain ion mobility. Given the utility of this tool, we first tried to apply it to our DDA data directly for identifying lipid oxidation products. However, under the DDA isolation scheme on the Waters Synapt G2-XS QTOF mass spectrometer, only the top 15 most

abundant peaks could be selected for fragmentation. Since lipid oxidation products have much lower abundance relative to non-oxidized parents, they were not being selected for fragmentation and therefore could not be matched on fragment spectra similarity.

Hence, we decided to use DIA acquisition in which precursor ions are fragmented according to isolation windows instead of intensity to maximize the number of precursors being fragmented in an acquisition. However, LPPTiger is not compatible with DIA MS data, so to circumvent this issue, we wrote a Python script to generate a standard .msp spectral library from the .json list of possible lipid oxidation produced by LPPTiger. We then imported this .msp library into Skyline to perform spectral matching and obtain accurate identifications of lipid oxidation products in DIA MS datasets (MacLean et al., 2010). Peak matches were individually reviewed, and any poor matches were removed from the dataset. The quality of the match was determined by 3 criteria: at least 3 precursor isotope peaks were identified, both the SN1 and SN2 fatty acid fragments were present, and the intensity of the precursors and fragments needed to be above the level of background signal. Matches passing the manual review process were exported from Skyline as a Molecule Results List and CCS values calculated from Progenesis software were manually added to each precursor. The resulting file was saved as a .csv, which can be imported back into Skyline as a target list. See Figure 3.8 for a schematic detailing this process. The resulting target list contains only experimentally validated lipid oxidation products as well as their fragments, m/z, CCS, retention time, and molecular formulas to facilitate accurate identification of lipid oxidation products in complex MS datasets.

Oxygen addition and truncated lipid oxidation products are formed from in-vitro oxidation of phospholipids. Phospholipid mixtures derived from soy (PC, PI, PS) and sunflower (PA, PG, PE) from Avanti Polar Lipids were used in this study (Table 3.1). Due to the nature of the mixtures being naturally derived, there is a range of fatty acids in each mixture from 16 to 18 carbons with anywhere from 0 to 3 desaturations. However, the most common (>50% for all classes) fatty acid is 18:2, commonly known as

linoleic acid. The PS and PI mixtures are not included in the final dataset because PS lipids did not oxidize, possibly due to adsorption to glass vials during incubation, and LPPTiger does not support the generation of PI lipid fragmentation spectra, so they could not be identified using the established workflow. A total of 65 lipid oxidation products were identified, along with 26 parent lipids (Table 3.2). PA, PC, and PG lipids produced 6, 3, and 4 truncation products, respectively, while no truncation products were detected from the oxidation of PE lipids. Various oxygen addition products, including +OH, +2OH, oxo (carbonyl), and +COOH were detected from all lipid classes, with 15, 11, 16, and 10 oxygen addition products being identified from PA, PC, PE, and PG lipid classes, respectively (Figure 3.9).

Application of the oxidized lipid library to HT-1080 cells treated with conjugated (CLA) and nonconjugated linoleic acid (NLA). Unlike typical polyunsaturated fatty acids, including NLA, the two double bonds in CLA are conjugated. Conjugated fatty acids typically undergo oxidation via peroxyl radical addition (PRA) rather than hydrogen atom abstraction (HAT), meaning that a reactive oxygen species can attack the conjugated double bond system directly instead of starting with the abstraction of a hydrogen atom, which is the rate-limiting step of lipid peroxidation (Figure 3.10). CLA undergoes peroxidation at a rate of 118 $M^{-1}s^{-1}$ and favors PRA, while NLA undergoes peroxidation at a rate of 62 $M^{-1}s^{-1}$ and favors HAT (Do et al., 2021; Howard & Ingold, 1967; Yin et al., 2011). CLA has been shown to promote ferroptosis in cells treated with RSL3 more so than its nonconjugated counterpart, NLA (Do et al., 2023). Therefore, we expected to observe more lipid oxidation products in cells treated with CLA than NLA. To investigate this hypothesis, we applied our oxidized lipid library to lipidomic datasets from HT-1080 cells treated with an equimolar mixture of unlabeled and d_7-labeled CLA or an equimolar mix of unlabeled and d_{11}-NLA with or without the ferroptosis inducer RSL3. The library is well-suited for this experiment in particular because the naturally derived phospholipid mixtures used in the creation of the library contained a high proportion of 18:2 fatty acids, and many 18:2 oxidation products were detected. It

is important to note that we cannot determine the double bond location or whether they are conjugated using our established LC-MS method, so while we assume that oxidation products observed were produced from the fatty acids that the cells were dosed with, we cannot definitively say whether the source fatty acid was conjugated or not. In addition, we acknowledge that the library is not equipped to handle isotopically labeled fatty acids, as the deuterium labeling produces a mass shift that is not accounted for in the library. Therefore, we are only able to identify oxidized lipids arising from the unlabeled proportion of the fatty acid mixture, and thus, the true amount of these products is likely higher than is reported here.

Linoleic acid-containing PC and PE parent lipids are detected and identified using the oxidized lipid library. In order for an oxidized lipid to be identified with confidence, the parent lipid first needs to be detected and identified. Since oxidized lipids occur at such a low abundance relative to their parents, the identification of an oxidized lipid would be unlikely if the parent lipid is not present in the dataset. Therefore, the parent lipids of all oxidation products included in the library are also included in the library. We identified four PC parent lipids and four PE parent lipids containing linoleic acid-derived fatty acids, including 16:0, 18:0, 18:1, and 18:2 fatty acids from both CLA and NLA-treated cells (Table 3.3). Lipid identifications were accepted based on the same criteria used for the library creation; at least 3 precursor isotope peaks are detected, the SN1 and SN2 fatty acid fragments are detected, and the signal from these peaks is well above background noise.

Lipid oxidation products derived from PE linoleic acid containing parents are detected and identified in CLA, but not NLA, treated cells using the oxidized lipid library. In cells treated with CLA and RSL3, two PE lipid oxidation products derived from the identified parent lipids were observed. Both observed oxidation products were oxygen addition products arising from the addition of one hydroxyl group to the polyunsaturated fatty acid chain. The products were identified as PE(16:0/18:2+OH) and

PE(18:0/18:2+OH). See Figure 3.11 for an example of Skyline chromatograms corresponding to identified PE(16:0/18:2) parent lipid (A) and its oxidation product (B, C) in CLA treated cells. Interestingly, even though the same linoleic acid-containing parent lipids were observed in NLA-treated cells, no oxidation products were successfully identified in cells treated with NLA and RSL3 (Table 3.3). This finding is consistent with the higher k_p of CLA compared to NLA, as well as the increased sensitization to ferroptosis in cells treated with CLA compared to NLA (Do et al., 2023). PC oxidized lipids did not produce large enough chromatographic peaks to be accepted. This could be due to a lower signal from PC lipids in negative ionization mode compared to PE lipids. PE lipids have been shown to be oxidized in cells undergoing ferroptosis (Kagan et al., 2017).

Discussion

Here, we report the development and application of a Skyline-compatible experimentally validated lipid oxidation product library containing m/z, RT, CCS, and fragmentation information for 65 lipid oxidation products produced from 26 unique parent lipids. The phospholipid oxidation products were formed via in vitro oxidation of unoxidized phospholipids using the radical initiator AIPH. The two main classes of products that were formed were oxygen-addition and truncation products. We showed that HILIC retention time shift is characteristic of lipid oxidation products relative to their parents, as the products become more polar as they are oxidized. Conversely, there was no discernible shift in CCS with respect to m/z or the compaction factor of oxidation products relative to parents, indicating that the 3-dimensional area of the lipids in the gas phase does not change significantly with oxidation.

After characterizing the oxidation products arising from in vitro phospholipid oxidation, we sought to assimilate the data into a Skyline-compatible library that could be used to identify lipid oxidation products in diverse datasets. To do this, we used LPPTiger to create theoretical spectral libraries of lipid oxidation products to confidently identify them from in vitro oxidation. We next compiled the identified lipids into an experimental library in .csv format that can be imported into Skyline as a

transition list and used to identify products based on m/z, RT, and fragmentation spectra. We then applied this library to a lipidomics dataset from HT-1080 cells treated with conjugated and nonconjugated linoleic acid. We were able to show that CLA treatment resulted in the formation of lipid oxidation products while NLA treatment did not. This finding is consistent with prior findings from our lab and others that have shown CLA to be more readily oxidizable than its nonconjugated counterpart.

While this library increases confidence in identifying lipid oxidation products in complex datasets, it has some limitations. First, the scope of the library is limited. It only contains oxidation products formed from 18:1, 18:2, and 18:3 unsaturated fatty acids. Many samples may contain oxidation products formed from more highly unsaturated fatty acids, including arachidonic acid (20:4), adrenic acid (22:4), and docosahexaenoic acid (22:6) (Kagan et al., 2017), and thus the use of the library is limited in cases where these fatty acids are expected to be oxidized. In addition, while the library contains CCS values for most of the identified lipids, Skyline is not able to use these values in the spectral matching of unknown analytes to the library. Therefore, if one wishes to use CCS as a parameter to identify oxidized lipids, it must be done manually or in a different program than Skyline. Further, the retention times included in the library were only measured once on the same column with the same LC system. Since retention times can vary due to a wide variety of factors, including the LC system used, mobile phase preparation, and temperature, they may not be consistent across different systems and labs. To address this issue, an internal or external retention time calibration system could be used to align measured retention times to a known reference value, similar to proteomics workflows that often use a set of peptides with known retention times to align the rest of the retention time values across a run. The retention time calibration strategy has been implemented in the Python package Lipydomics developed in our lab (Ross et al. 2020). Lastly, the library is still subject to manual review. Although Skyline will match peaks to transitions in the library, the user must still manually inspect all matches for accuracy before proceeding with the identification. This process can introduce subjectivity and human error in the identification of oxidized lipids.

To conclude, an experimental oxylipid library is now available for use in identifying oxidized lipids from multiple types of LC-MS datasets. This library will contribute to the growing selection of resources available for oxylipid identification and analysis, improving access to and understanding of the epilipidome. Future directions of this work include expanding the library to include a wider variety of lipid parents and their oxidation products, as well application of the library to more diverse types of lipidomic analyses, including targeted analyses and data-dependent acquisition. In addition, expanding the utility of Skyline to match experimental data to transition list libraries using CCS would improve the confidence of identity matches.

Figures:

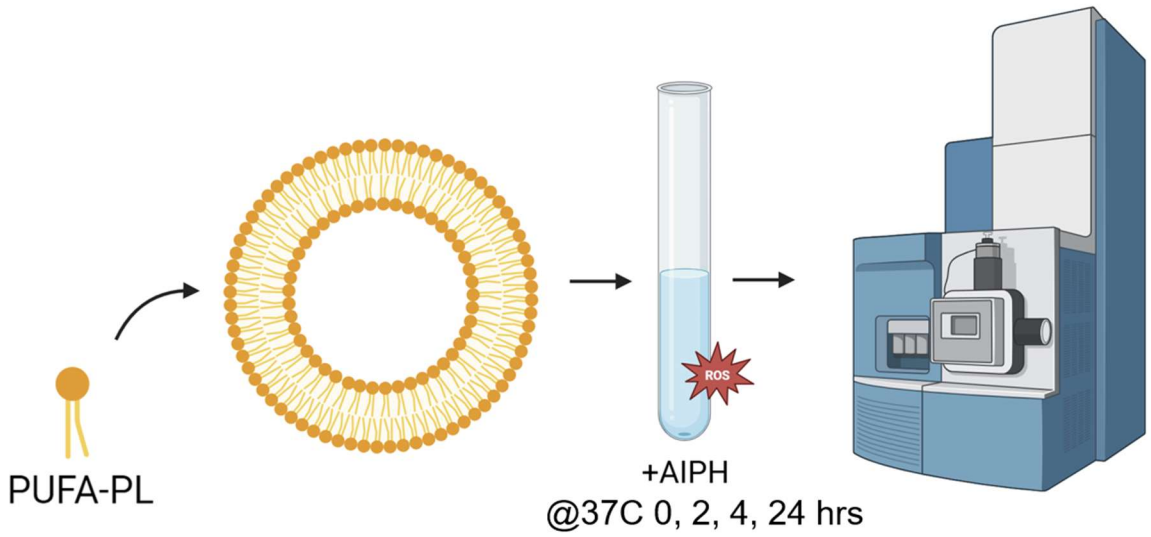

Figure 3.1: Schematic of in-vitro oxidation of polyunsaturated fatty acid containing phospholipids (PUFA-PLs). Figure created using Biorender.com.

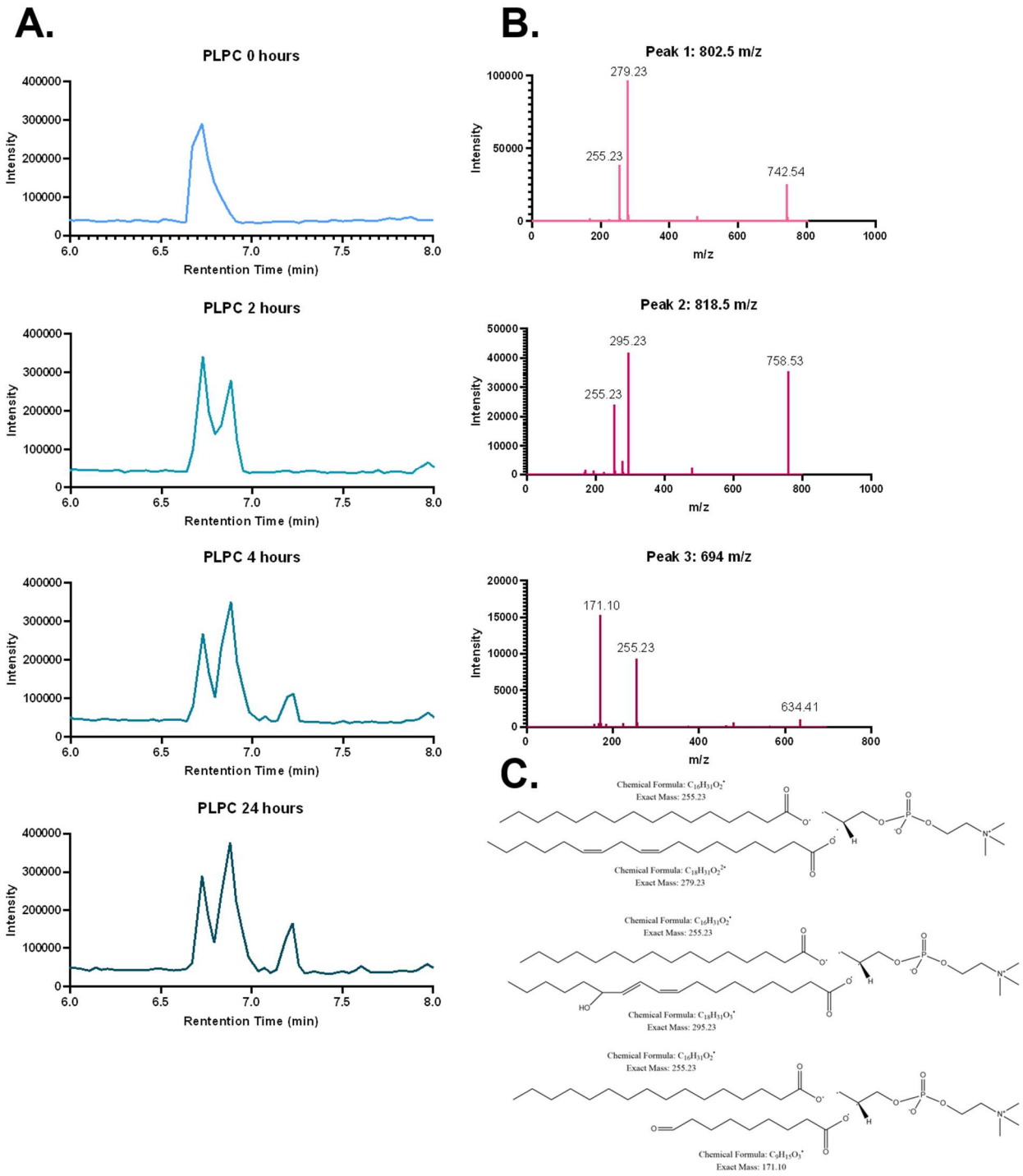

Figure 3.2: Results of in-vitro oxidation of palmitate-linoleate phosphatidylcholine (PLPC). A) chromatographic peaks of PLPC and oxidation products B) targeted fragmentation of each of the three chromatographic peaks C) possible structures corresponding to each of the three chromatographic peaks

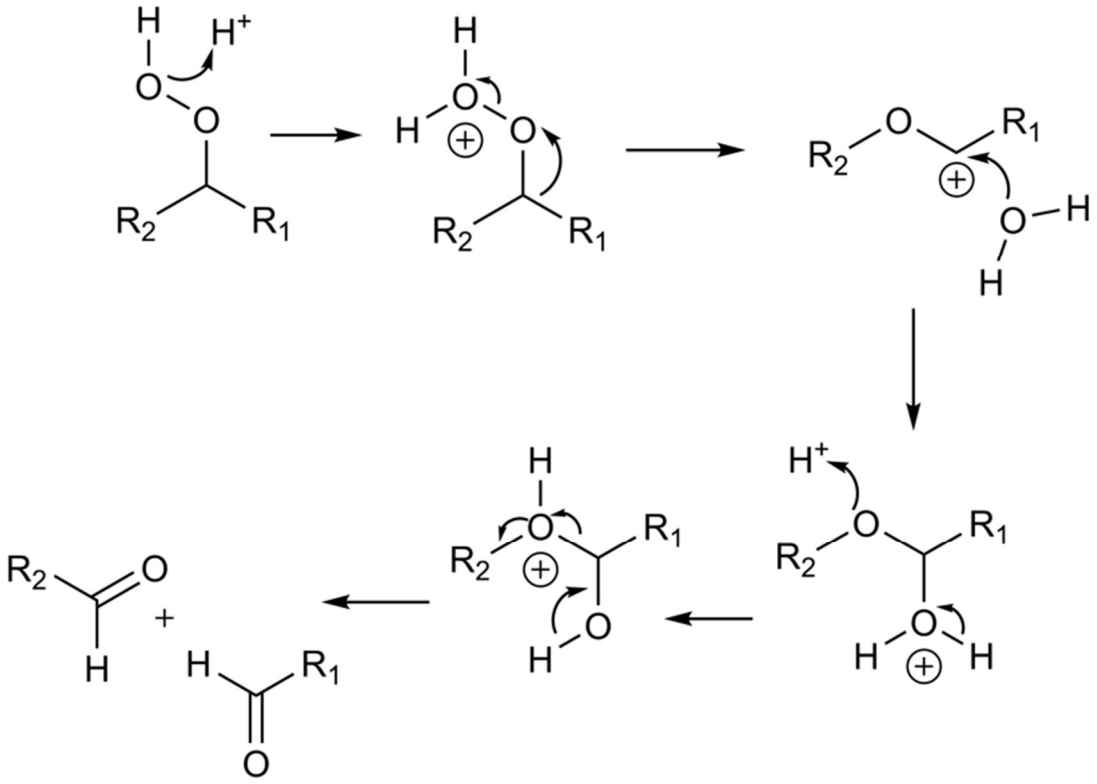

Figure 3.3: Mechanism of Hock rearrangement resulting in the formation of truncated lipid oxidation products.

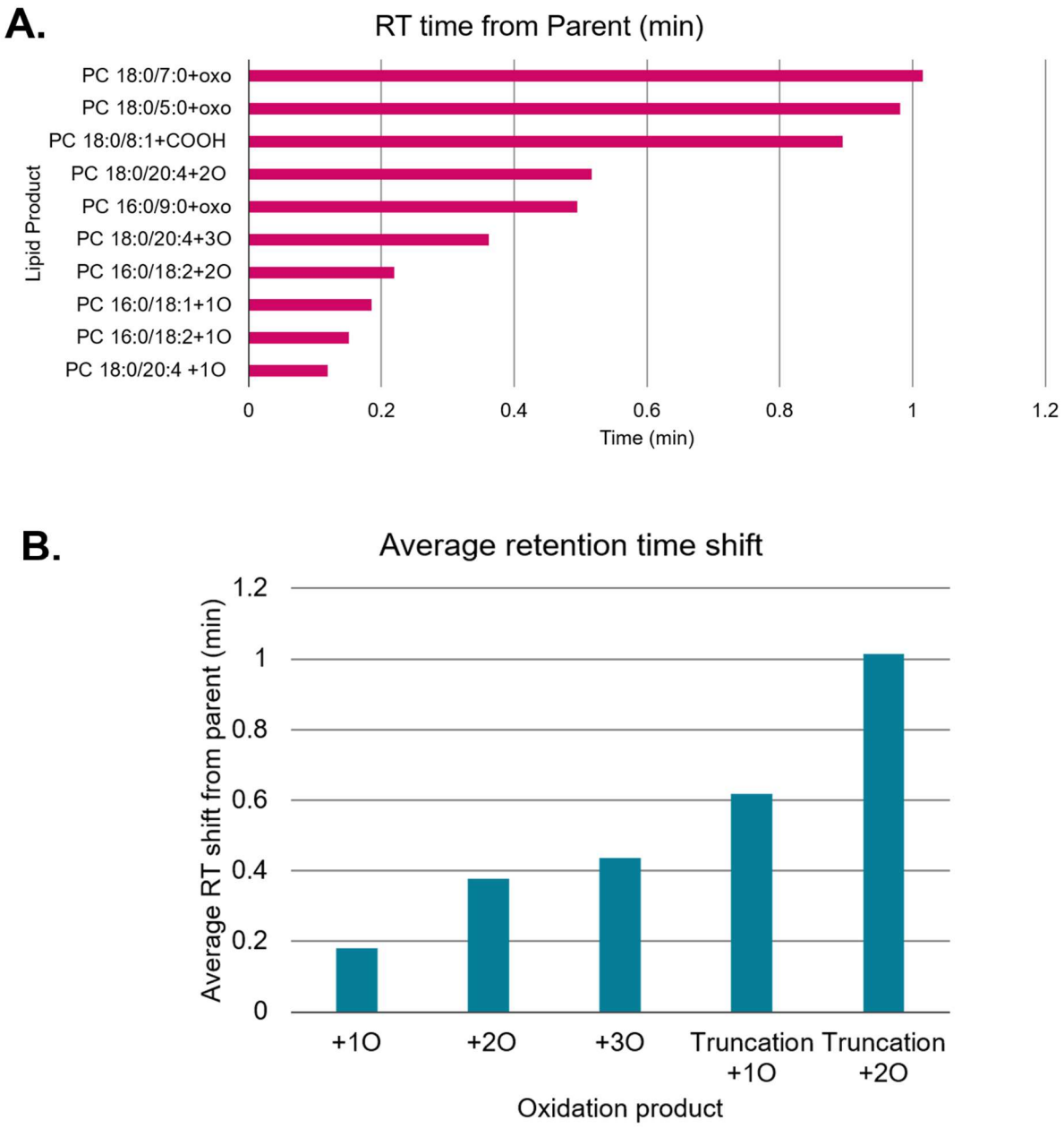

Figure 3.4: Observed retention time shift with oxidation of phosphatidylcholine (PC) lipid species. A) Retention time shift from parent for individual identified lipid oxidation products. B) Average retention time shift of increasingly oxidized PC lipid species from parent

A.

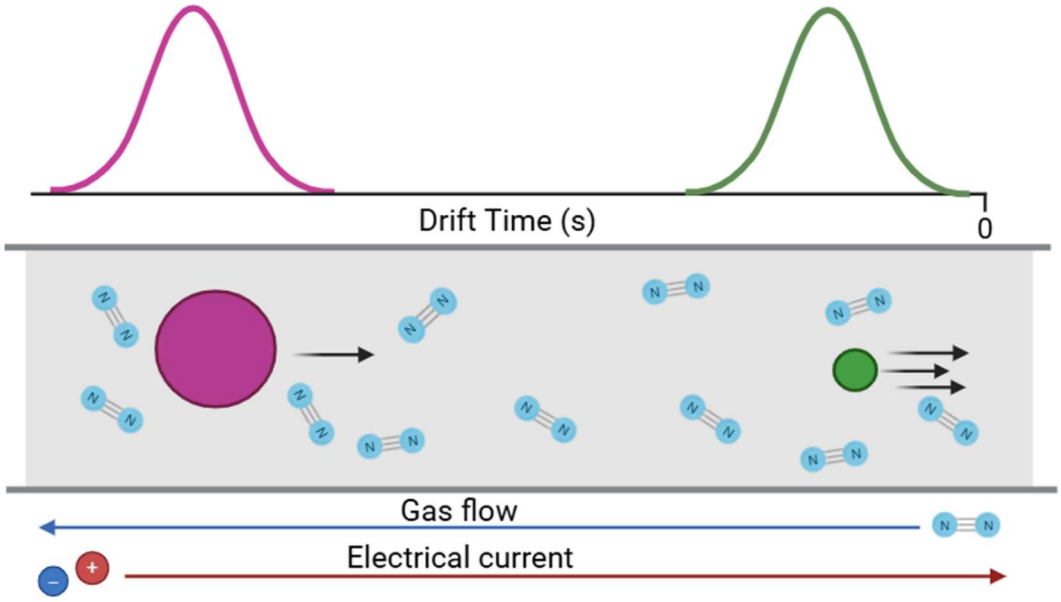

B.

$$\left(\frac{\mathrm{CCS}_{\mathrm{parent}}}{\mathrm{CCS}_{\mathrm{metab.}}}\right) = C \times \left(\frac{\mathrm{mass}_{\mathrm{parent}}}{\mathrm{mass}_{\mathrm{metab.}}}\right)^{2/3}$$

Figure 3.5: Depiction of collision cross section (CCS) and resulting compaction factor (C). A) Schematic of drift tube ion mobility used to calculate CCS values. B) Equation used to calculate compaction factor of a metabolite or oxidation product from its parent using CCS values.

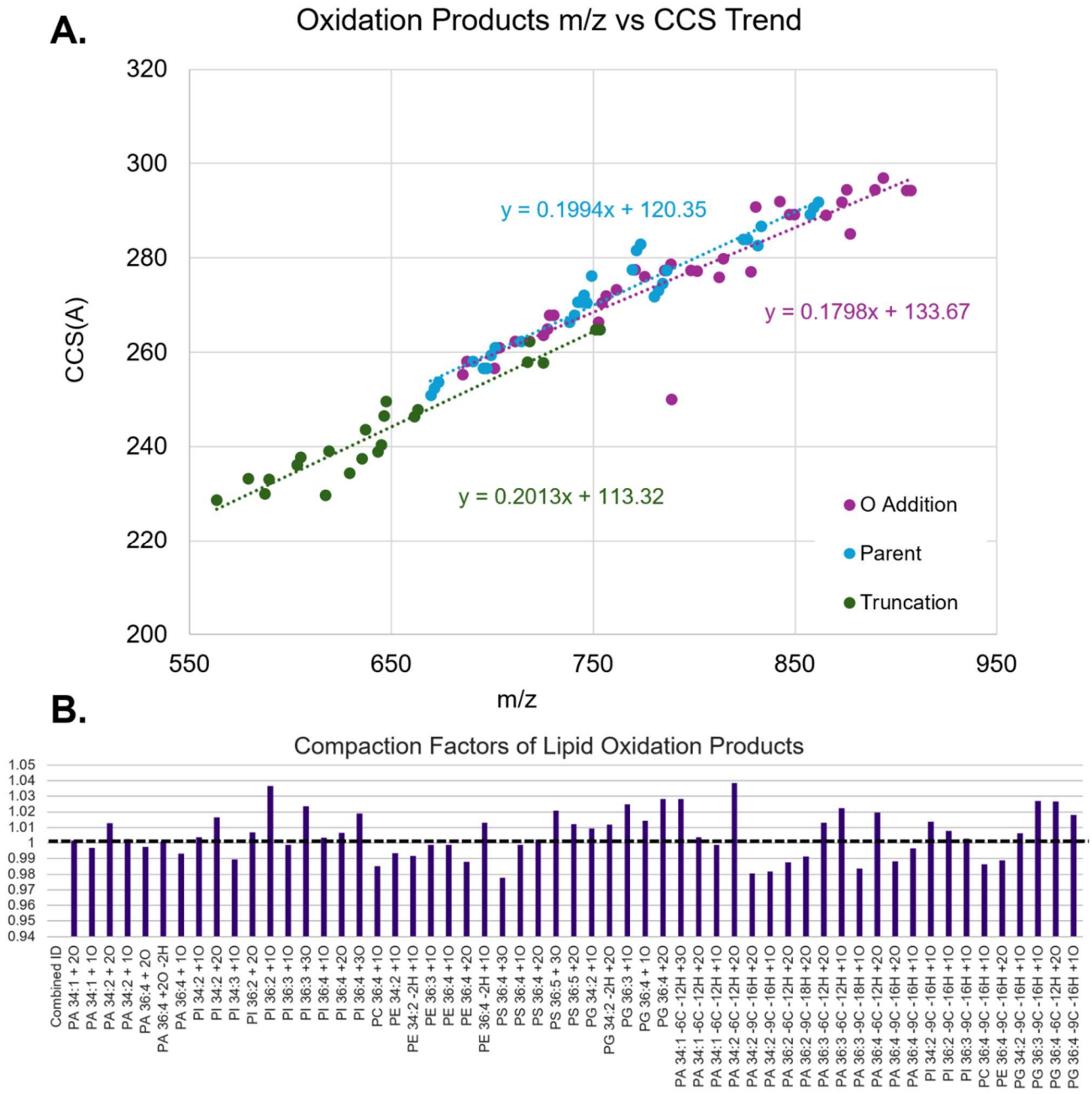

Figure 3.6: Conformational analysis of lipid oxidation products and parents using collision cross section (CCS). A) CCS vs m/z plot of lipid parents and oxidation products. B) Compaction factors of oxidation products compared to their parents

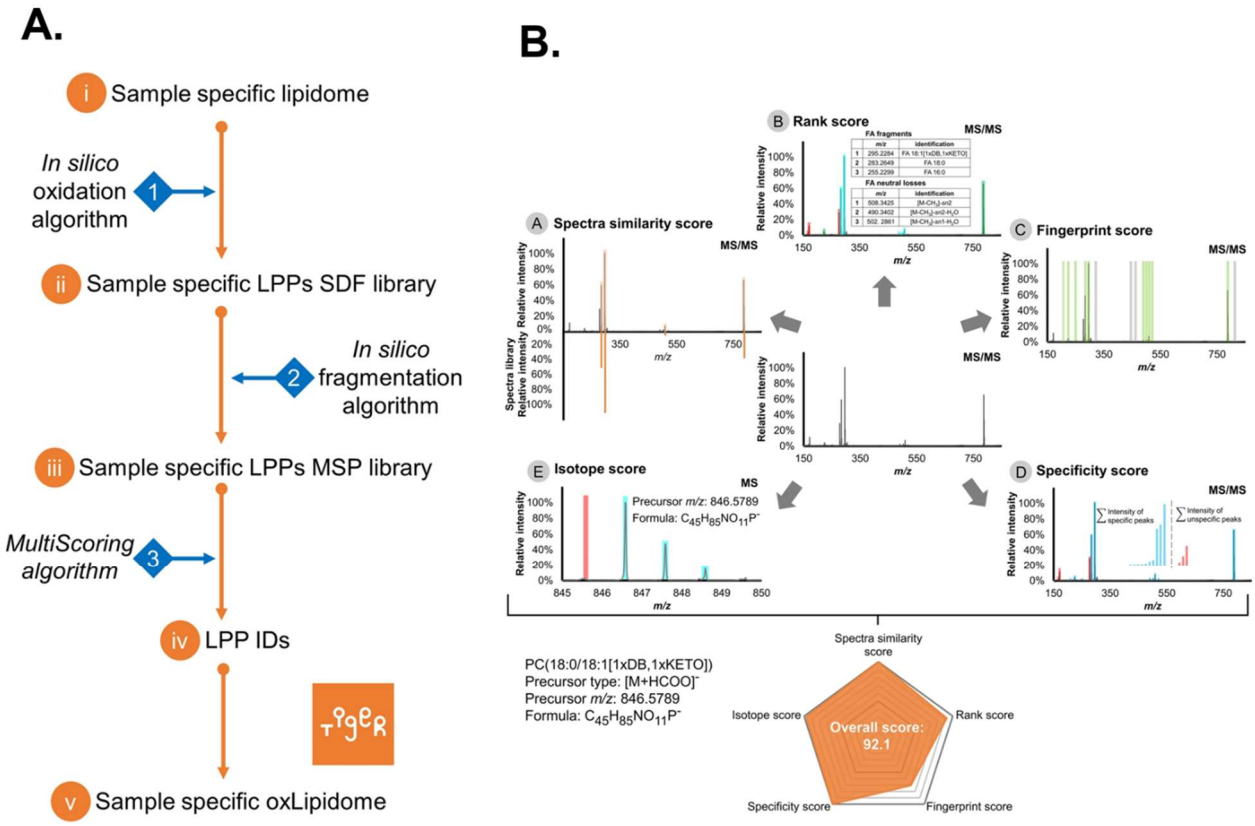

Figure 3.7: Schematic of LPPTiger software. A) overview of software functionality B) match scoring algorithm used by LPPTiger

Figures adapted with permission from: (Ni et al., 2017).

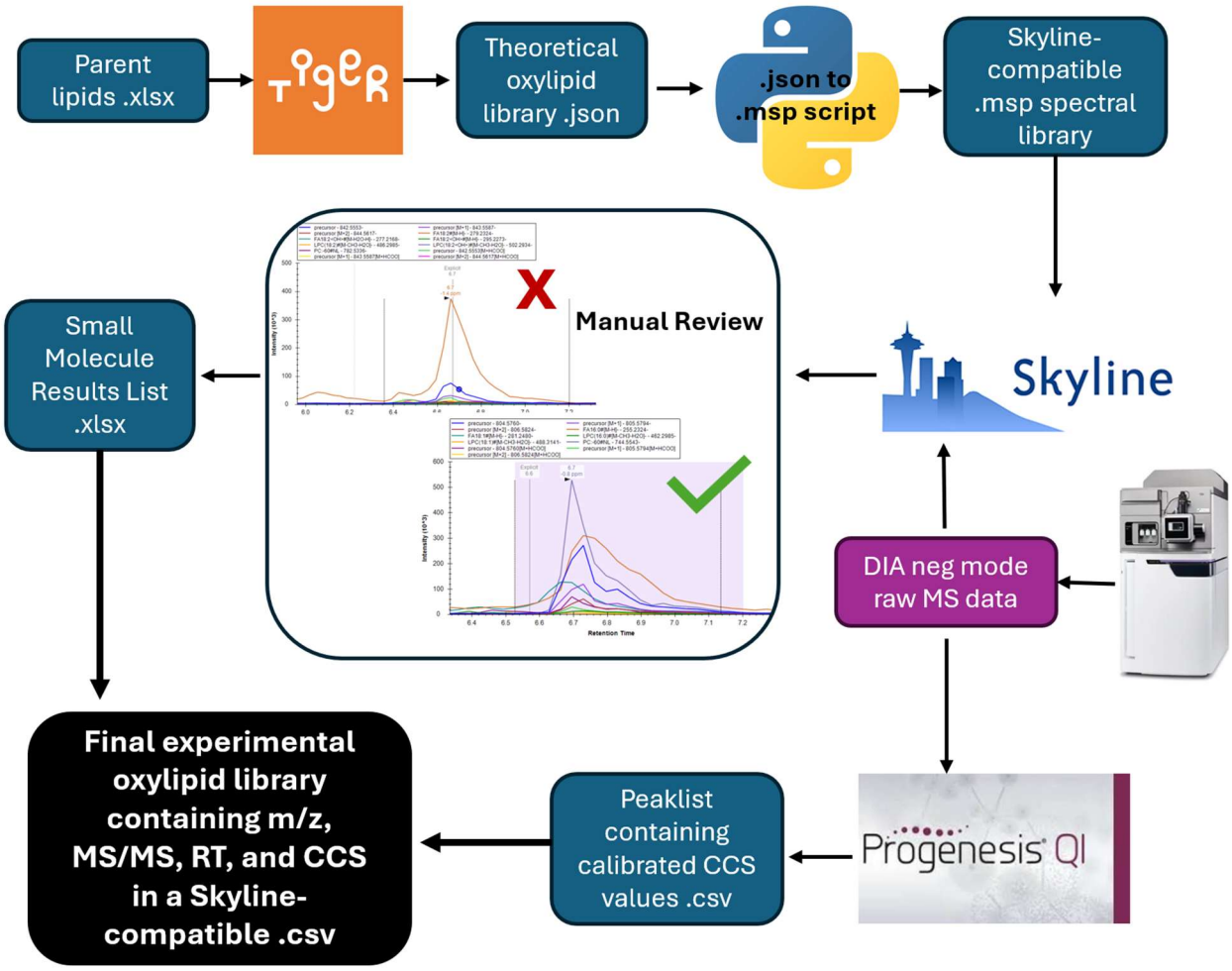

Figure 3.8: Schematic of the data analysis process used to create the oxylipid database.

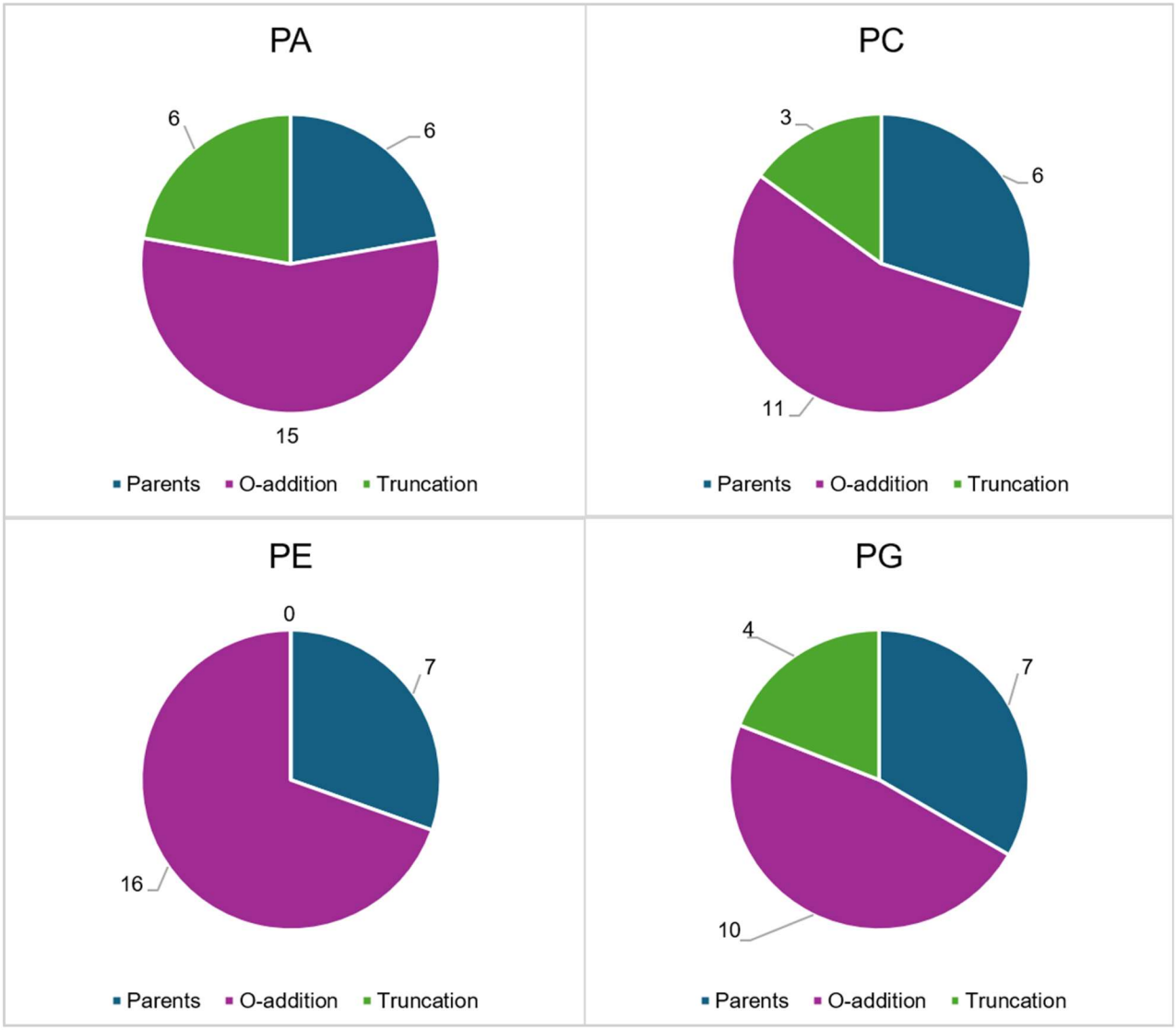

Figure 3.9: Overview of identified oxylipids and parents contained in the oxidized lipid library from phosphatidic acid (PA), phosphatidylcholine (PC), phosphatidylethanolamine (PE), and phosphatidylglycerol (PG) lipid classes.

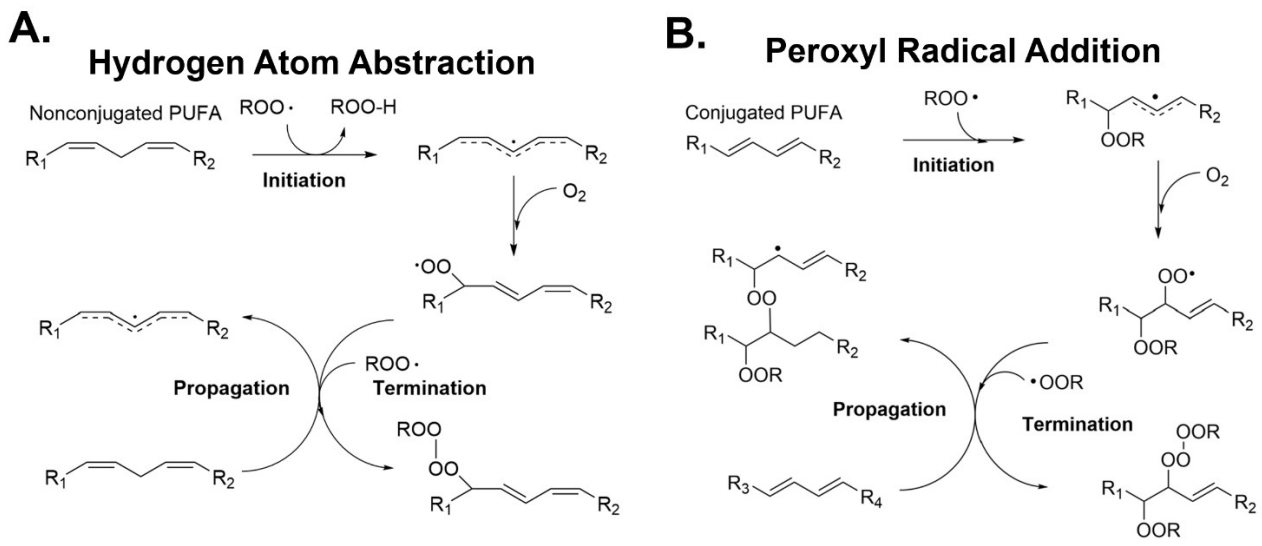

Figure 3.10: Mechanisms of lipid oxidation via hydrogen atom abstraction (A) and peroxyl radical addition (B).

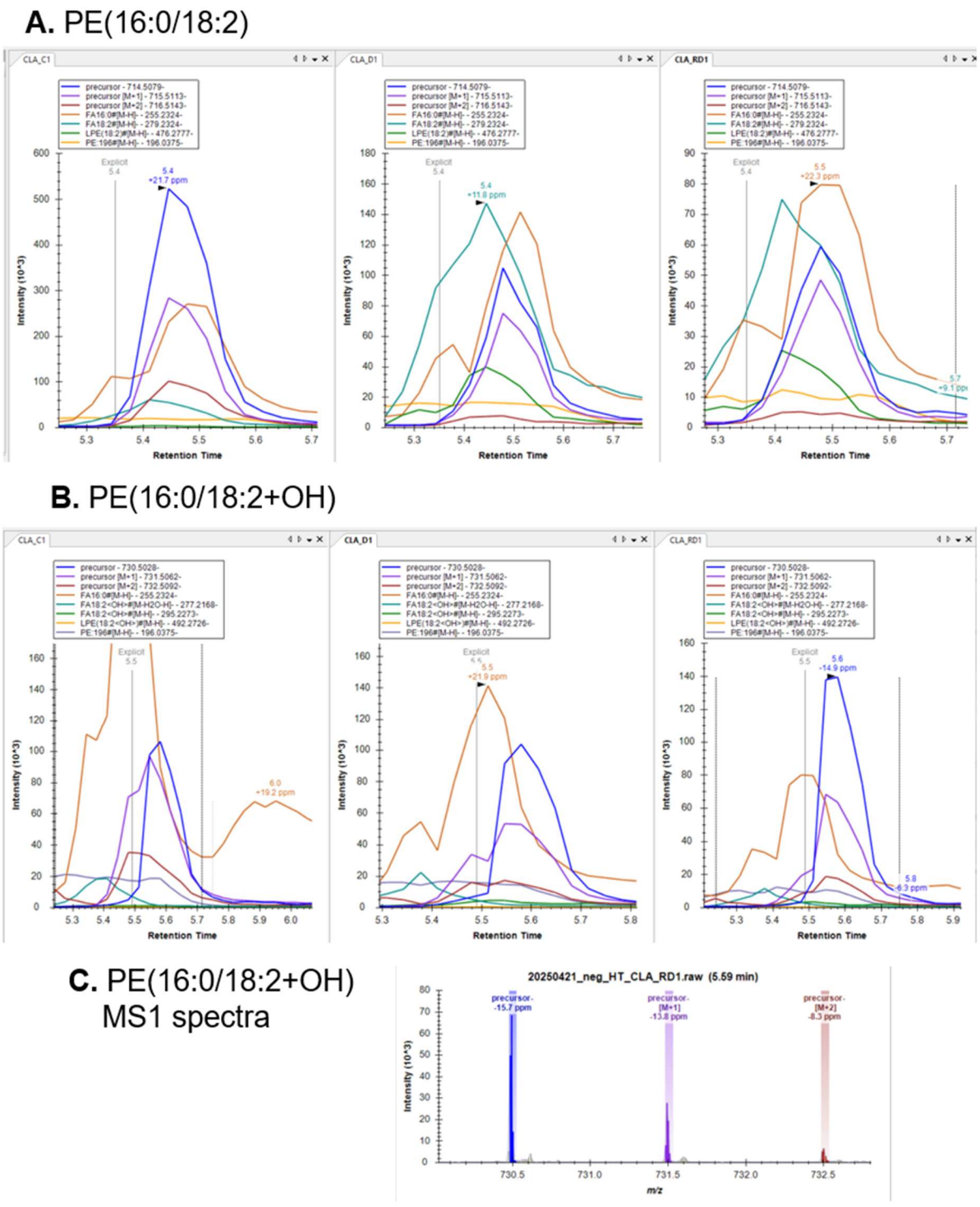

Figure 3.11: Identification of parent lipid PE(16:0/18:2) (A) and oxidation product PE(16:0/18:2+OH) (B) using the oxidized lipid library in Skyline from CLA-treated cells. C shows MS1 spectrum of PE(16:0/18:2+OH) in CLA RSL3 treated cells. C: control, D: deuterated CLA, RD: deuterated CLA and RSL3.

Table 3.1: Lipids used in this study

Lipid name	Source	Catalog	Fatty acid distribution	Avg MW
Sunflower PA	Avanti	181121C-25 mg	16:0 9.4%, 18:0 2.8%, 18:1 19.8%, 18:2 67.4%	718.916
Soy PI	Avanti	840044p-10mg	16:0 31%, 18:0 7%, 18:1 5%, 18:2 50%, 18:3 7%	866.647
Soy PC	Avanti	840054p-25mg	16:0 14.9%, 18:0 3.7%, 18:1 11.4%, 18:2 63%, 18:3 5.7%	775.037
Soy PS	Avanti	870336p-25mg	16:0 10%, 18:0 3%, 18:1 12%, 18:2 68%, 18:3 7%	801.632
Sunflower PE	Avanti	181101C-25mg	16:0 9.4%, 18:0 2.8%, 18:1 19.8 %, 18:2 67.4%	740.002
Sunflower PG	Avanti	181131C-25mg	16:0 9.4%, 18:0 2.8%, 18:1 19.8 %, 18:2 67.4%	792.994

Table 3.2: Oxidized lipids and parent precursors contained in the oxylipid database

Molecule	Precursor Ion Formula	Precursor Mz	Precursor Adduct	Retention Time	CCS
PA(16:0_18:1)	C37H70O8P	673.481381	[M-H]	7.19	243.9896
PA(16:0_18:1<OH>)	C37H70O9P	689.476295	[M-H]	6.15	242.4303
PA(16:0_18:1<oxo>)	C37H68O9P	687.460645	[M-H]	6.15	257.9142
PA(16:0_18:2)	C37H68O8P	671.46573	[M-H]	6.01	251.1147
PA(16:0_18:2<2OH>)	C37H68O10P	703.45556	[M-H]	6.18	260.5137
PA(16:0_18:2<OH>)	C37H68O9P	687.460645	[M-H]	6.15	257.9142
PA(16:0_9:0<COOH>)	C28H52O10P	579.330359	[M-H]	7.5	229.8543
PA(18:0_18:1)	C39H74O8P	701.512681	[M-H]	5.94	255.0706
PA(18:0_18:1<oxo>)	C39H72O9P	715.491945	[M-H]	6.11	264.4484
PA(18:0_18:2)	C39H72O8P	699.497031	[M-H]	5.94	261.8888
PA(18:0_18:2<OH,oxo>)	C39H70O10P	729.47121	[M-H]	6.21	264.3529
PA(18:0_18:2<OH>)	C39H72O9P	715.491945	[M-H]	6.11	264.4484
PA(18:0_18:2<oxo>)	C39H70O9P	713.476295	[M-H]	6.08	264.4642
PA(18:0_9:0<oxo>)	C30H56O9P	591.366745	[M-H]	6.32	235.825
PA(18:1_18:1)	C39H72O8P	699.497031	[M-H]	5.94	261.8888
PA(18:1_18:1<OH>)	C39H72O9P	715.491945	[M-H]	6.11	264.4484
PA(18:1_18:1<oxo>)	C39H70O9P	713.476295	[M-H]	6.08	264.4642
PA(18:1_9:0<COOH>)	C30H54O10P	605.346009	[M-H]	7.47	228.0829
PA(18:1_9:0<oxo>)	C30H54O9P	589.351095	[M-H]	6.28	231.2988
PA(18:2_18:1)	C39H70O8P	697.481381	[M-H]	5.94	257.8445
PA(18:2_18:1<OH>)	C39H70O9P	713.476295	[M-H]	7.8	249.4155
PA(18:2_18:1<oxo>)	C39H68O9P	711.460645	[M-H]	6.08	263.1428

PA(18:2_18:2)	C39H68O8P	695.46573	[M-H]	6.25	256.4871
PA(18:2_18:2<2OH>)	C39H68O10P	727.45556	[M-H]	6.21	265.6914
PA(18:2_18:2<OH>)	C39H68O9P	711.460645	[M-H]	7.8	263.1437
PA(18:2_9:0<COOH>)	C30H52O10P	603.330359	[M-H]	6.49	234.2151
PA(18:2_9:0<oxo>)	C30H52O9P	587.335445	[M-H]	6.32	223.5393
PC(16:0_18:1)	C43H83O10NP	804.576009	[M+HCOO]	6.57	284.3425
PC(16:0_18:1<oxo>)	C43H81O11NP	818.555273	[M+HCOO]	6.57	289.1477
PC(16:0_18:2)	C43H81O10NP	802.560359	[M+HCOO]	6.57	281.8786
PC(16:0_18:2<2OH>)	C43H81O12NP	834.550188	[M+HCOO]	6.94	286.6233
PC(16:0_18:2<OH>)	C43H81O11NP	818.555273	[M+HCOO]	6.57	289.1477
PC(16:0_18:2<oxo>)	C43H79O11NP	816.539623	[M+HCOO]	6.67	284.2718
PC(16:0_18:3)	C43H79O10NP	800.544709	[M+HCOO]	6.57	278.1358
PC(16:0_18:3<2OH>)	C43H79O12NP	832.534538	[M+HCOO]	6.98	290.2757
PC(16:0_18:3<2oxo>)	C43H75O12NP	828.503238	[M+HCOO]	6.91	282.9687
PC(16:0_18:3<OH>)	C43H79O11NP	816.539623	[M+HCOO]	6.67	284.2718
PC(16:0_18:3<oxo>)	C43H77O11NP	814.523973	[M+HCOO]	6.91	283.0486
PC(16:0_9:0<oxo>)	C34H65O11NP	694.430073	[M+HCOO]	7.04	260.5783
PC(18:1_9:0<oxo>)	C36H67O11NP	720.445723	[M+HCOO]	6.98	
PC(18:2_18:1)	C45H83O10NP	828.576009	[M+HCOO]	6.5	
PC(18:2_18:2)	C45H81O10NP	826.560359	[M+HCOO]	6.54	281.7396
PC(18:2_18:2<2OH>)	C45H81O12NP	858.550188	[M+HCOO]	6.87	
PC(18:2_18:2<OH>)	C45H81O11NP	842.555273	[M+HCOO]	6.67	287.7976
PC(18:2_18:3)	C45H79O10NP	824.544709	[M+HCOO]	6.54	
PC(18:2_18:3<OH>)	C45H79O11NP	840.539623	[M+HCOO]	6.54	287.8086
PC(18:2_9:0<oxo>)	C36H65O11NP	718.430073	[M+HCOO]	7.01	259.0566

PE(16:0_18:1)	C39H75O8NP	716.52358	[M-H]	5.35	261.7716
PE(16:0_18:1<OH>)	C39H75O9NP	732.518494	[M-H]	5.49	268.2916
PE(16:0_18:1<oxo>)	C39H73O9NP	730.502844	[M-H]	5.49	266.9909
PE(16:0_18:2)	C39H73O8NP	714.50793	[M-H]	5.35	263.1224
PE(16:0_18:2<2OH>)	C39H73O10NP	746.497759	[M-H]	5.55	266.8853
PE(16:0_18:2<OH>)	C39H73O9NP	730.502844	[M-H]	5.49	268.3011
PE(16:0_18:2<oxo>)	C39H71O9NP	728.487194	[M-H]	5.49	
PE(18:0_18:1)	C41H79O8NP	744.55488	[M-H]	5.28	272.112
PE(18:0_18:1<OH>)	C41H79O9NP	760.549794	[M-H]	5.45	
PE(18:0_18:1<oxo>)	C41H77O9NP	758.534144	[M-H]	5.45	274.5873
PE(18:0_18:2)	C41H77O8NP	742.53923	[M-H]	5.28	273.41
PE(18:0_18:2<2OH>)	C41H77O10NP	774.529059	[M-H]	5.52	
PE(18:0_18:2<OH>)	C41H77O9NP	758.534144	[M-H]	5.45	274.5873
PE(18:0_18:2<oxo>)	C41H75O9NP	756.518494	[M-H]	5.42	272.0309
PE(18:1_18:1)	C41H77O8NP	742.53923	[M-H]	5.28	272.1254
PE(18:1_18:1<OH>)	C41H77O9NP	758.534144	[M-H]	5.45	274.5873
PE(18:1_18:1<oxo>)	C41H75O9NP	756.518494	[M-H]	5.42	272.0348
PE(18:2_18:1)	C41H75O8NP	740.52358	[M-H]	5.28	266.9274
PE(18:2_18:1<OH>)	C41H75O9NP	756.518494	[M-H]	5.42	272.0348
PE(18:2_18:1<oxo>)	C41H73O9NP	754.502844	[M-H]	5.45	269.4518
PE(18:2_18:2)	C41H73O8NP	738.50793	[M-H]	5.32	265.6177
PE(18:2_18:2<2OH>)	C41H73O10NP	770.497759	[M-H]	5.59	274.5113
PE(18:2_18:2<OH>)	C41H73O9NP	754.502844	[M-H]	5.45	269.4518
PG(16:0_18:1)	C40H76O10P	747.51816	[M-H]	1.93	275.9382
PG(16:0_18:1<OH>)	C40H76O11P	763.513075	[M-H]	2.17	271.9871

PG(16:0_18:1<oxo>)	C40H74O11P	761.497425	[M-H]	2.17	277.1122
PG(16:0_18:2)	C40H74O10P	745.50251	[M-H]	1.97	277.2184
PG(16:0_18:2<2OH>)	C40H74O12P	777.492339	[M-H]	2.3	277.0118
PG(16:0_18:2<OH>)	C40H74O11P	761.497425	[M-H]	2.17	277.1122
PG(16:0_9:0<oxo>)	C31H58O11P	637.372224	[M-H]	2.61	239.8923
PG(18:0_18:1)	C42H80O10P	775.54946	[M-H]	1.73	288.1993
PG(18:0_18:1<oxo>)	C42H78O11P	789.528725	[M-H]	2.1	291.738
PG(18:0_18:2)	C42H78O10P	773.53381	[M-H]	1.73	289.4257
PG(18:0_18:2<OH>)	C42H78O11P	789.528725	[M-H]	2.1	291.738
PG(18:0_9:0<oxo>)	C33H62O11P	665.403524	[M-H]	2.51	248.3401
PG(18:1_18:1)	C42H78O10P	773.53381	[M-H]	1.73	289.4257
PG(18:1_18:1<OH>)	C42H78O11P	789.528725	[M-H]	2.1	291.738
PG(18:1_18:1<oxo>)	C42H76O11P	787.513075	[M-H]	2.07	290.5469
PG(18:1_9:0<oxo>)	C33H60O11P	663.387874	[M-H]	2.51	245.5009
PG(18:2_18:1)	C42H76O10P	771.51816	[M-H]	1.76	288.2228
PG(18:2_18:1<OH>)	C42H76O11P	787.513075	[M-H]	2.07	290.5469
PG(18:2_18:2)	C42H74O10P	769.50251	[M-H]	1.86	284.56
PG(18:2_18:2<OH>)	C42H74O11P	785.497425	[M-H]	2.1	280.7352
PG(18:2_9:0<oxo>)	C33H58O11P	661.372224	[M-H]	2.54	244.0778

Table 3.3: Parents and oxidation products detected in NLA and CLA treated HT-1080 cells

Molecule	Precursor Ion Formula	Replicate Name	Precursor Mz	Precursor Adduct	Retention Time	Area
PC(16:0_18:2)	C43H81O10NP	CLA_C1	802.560359	[M+HCOO]	6.76	222228
PC(16:0_18:2)	C43H81O10NP	CLA_D1	802.560359	[M+HCOO]	6.86	553116
PC(16:0_18:2)	C43H81O10NP	CLA_RD1	802.560359	[M+HCOO]	5.88	515703
PC(16:0_18:2)	C43H81O10NP	NLA_C1	802.560359	[M+HCOO]	6.7	774742
PC(16:0_18:2)	C43H81O10NP	NLA_D1	802.560359	[M+HCOO]	6.7	872756
PC(16:0_18:2)	C43H81O10NP	NLA_RD1	802.560359	[M+HCOO]	6.71	962154
PC(18:2_18:2)	C45H81O10NP	CLA_C1	826.560359	[M+HCOO]	6.66	193859
PC(18:2_18:2)	C45H81O10NP	CLA_D1	826.560359	[M+HCOO]	6.73	409404
PC(18:2_18:2)	C45H81O10NP	CLA_RD1	826.560359	[M+HCOO]	6.73	263217
PC(18:2_18:2)	C45H81O10NP	NLA_C1	826.560359	[M+HCOO]	6.59	351542
PC(18:2_18:2)	C45H81O10NP	NLA_D1	826.560359	[M+HCOO]	6.66	454169
PC(18:2_18:2)	C45H81O10NP	NLA_RD1	826.560359	[M+HCOO]	6.65	427638
PE(16:0_18:2)	C39H73O8NP	CLA_C1	714.507929	[M-H]	5.45	2838857
PE(16:0_18:2)	C39H73O8NP	CLA_D1	714.507929	[M-H]	5.51	659114
PE(16:0_18:2)	C39H73O8NP	CLA_RD1	714.507929	[M-H]	5.48	393094
PE(16:0_18:2)	C39H73O8NP	NLA_C1	714.507929	[M-H]	5.45	4034750
PE(16:0_18:2)	C39H73O8NP	NLA_D1	714.507929	[M-H]	5.45	5506723
PE(16:0_18:2)	C39H73O8NP	NLA_RD1	714.507929	[M-H]	5.46	5596439
PE(16:0_18:2<OH>)	C39H73O9NP	CLA_C1	730.502844	[M-H]	5.58	387384
PE(16:0_18:2<OH>)	C39H73O9NP	CLA_D1	730.502844	[M-H]	5.58	350612
PE(16:0_18:2<OH>)	C39H73O9NP	CLA_RD1	730.502844	[M-H]	5.58	503193
PE(18:0_18:2)	C41H77O8NP	CLA_C1	742.539229	[M-H]	5.41	5127675
PE(18:0_18:2)	C41H77O8NP	CLA_D1	742.539229	[M-H]	5.41	1513646
PE(18:0_18:2)	C41H77O8NP	CLA_RD1	742.539229	[M-H]	5.41	905765

PE(18:0_18:2)	C41H77O8NP	NLA_C1	742.539229	[M-H]	5.38	9663131
PE(18:0_18:2)	C41H77O8NP	NLA_D1	742.539229	[M-H]	5.41	11085638
PE(18:0_18:2)	C41H77O8NP	NLA_RD1	742.539229	[M-H]	5.39	11505036
PE(18:2_18:2)	C41H73O8NP	CLA_C1	738.507929	[M-H]	5.34	1591297
PE(18:2_18:2)	C41H73O8NP	CLA_D1	738.507929	[M-H]	5.41	2413978
PE(18:2_18:2)	C41H73O8NP	CLA_RD1	738.507929	[M-H]	5.41	1324766
PE(18:2_18:2)	C41H73O8NP	NLA_C1	738.507929	[M-H]	5.34	2533840
PE(18:2_18:2)	C41H73O8NP	NLA_D1	738.507929	[M-H]	5.34	2134366
PE(18:2_18:2)	C41H73O8NP	NLA_RD1	738.507929	[M-H]	5.36	2136606
PE(18:2_18:2<OH>)	C41H73O9NP	CLA_C1	754.502844	[M-H]	5.51	79115
PE(18:2_18:2<OH>)	C41H73O9NP	CLA_D1	754.502844	[M-H]	5.51	239320
PE(18:2_18:2<OH>)	C41H73O9NP	CLA_RD1	754.502844	[M-H]	5.51	140734

Chapter 4: Detection of Lipid Peroxidation in Cells Undergoing Ferroptosis Using Stimulated Raman Scattering Microscopy and Confocal Microscopy

This specific aim was completed in collaboration with Fiona Xi Xu, PhD, in the lab of Dan Fu, PhD, from the University of Washington Department of Chemistry, and Angela Guo, research technician in the Department of Medicinal Chemistry. Fiona Xi Xu completed all the SRS imaging, data analysis, and figure creation. Dan Fu and Libin Xu contributed to conceptualizing and planning of experiments. Angela Guo contributed to sample preparation, completed all confocal microscopy, and all flow cytometry included in this study. I acknowledge and sincerely appreciate their many contributions to this chapter. I contributed to the design and planning of the experiments, the preparation of the cell culture samples for SRS imaging, analysis of confocal microscopy data, and supervision of Angela Guo.

Introduction:

Ferroptosis is a form of regulated cell death dependent on the iron-mediated peroxidation of lipids within the cell. In this process, iron catalyzes the formation of reactive oxygen species (ROS) that drive the peroxidation of polyunsaturated fatty acids (PUFAs) within cellular phospholipids. While lipid peroxidation has been observed on a global level in ferroptosis using fluorescent probes, mass spectrometry, and flow cytometry, the subcellular distribution of PUFAs and their peroxidation products within the cell remains unclear. Many organelles have been shown to play important roles in ferroptosis. The endoplasmic reticulum (ER) is the primary site for phospholipid synthesis, and it has been shown that polyunsaturated fatty acids (PUFAs) accumulate in and around the ER preceding ferroptosis (von Krusenstiern et al., 2023b). In addition, lipid droplets serve as storage sites for neutral lipids including triglycerides, diglycerides, and cholesterol esters. It has been shown that PUFA-containing neutral lipids

stored within lipid droplets are oxidized in the absence of ferroptosis suppressor protein 1 (FSP1), and that FSP1 knockout can lead to the induction of ferroptosis in cells (Lange et al., 2025b). Moreover, the mitochondria have been implicated in cysteine-deprivation-induced ferroptosis, as it naturally produces reactive oxygen species (ROS) during ATP production (Gao et al., 2019a). In a state of cysteine, and thus glutathione, deprivation, these ROS can accumulate and contribute to the production of oxidized phospholipids. Furthermore, the peroxisome is another organelle that has been shown to contribute to ferroptosis by synthesizing PUFA-containing ether lipids (Zou et al., 2020). Ether lipids are phospholipids in which the SN1 fatty acid is attached to the headgroup by an ether or vinyl-ether bond rather than the typical ester bond. PUFA-containing ether lipids have been shown to contribute to the sensitivity of certain cell types to ferroptosis under conditions of lipid remodeling (Sokol et al., 2025). Finally, plasma membrane rupture is the terminal step of ferroptosis, and lipid peroxide buildup at the plasma membrane has been observed prior to ferroptotic death, rendering the plasma membrane an indispensable site for lipid accumulation and peroxidation during ferroptosis (Dixon & Olzmann, 2024; Magtanong et al., 2019).

Given the diverse organelles implicated in ferroptosis, one prominent hypothesis is that lipid peroxidation is initiated at discrete intracellular membrane sites before spreading throughout the cell to eventually disrupt the plasma membrane (X. Chen et al., 2021; Yang, 2023). Although this model is supported by accumulating evidence, the mechanisms by which PUFA accumulation and peroxidation propagate throughout the cell remain unclear (Dixon & Olzmann, 2024). This study aims to employ stimulated Raman scattering (SRS) and confocal microscopy to observe the progress and location of lipid peroxidation in HT-1080 cells as they undergo ferroptosis induced by RSL3. SRS is a label-free imaging technique that measures the stimulated vibrations of specific chemical bonds within a sample. It is a powerful tool for imaging of biological samples without perturbing the morphology and nature of the sample, and has recently demonstrated its great potential in the detection of lipid localization in cells (von Krusenstiern et al., 2023b). Confocal microscopy is used as an orthogonal technique to SRS to confirm

specific sites using organelle-specific fluorescent dyes. Together, SRS and confocal microscopy were used in this study to distinguish oxidation products, mechanisms, and sites of accumulation of conjugated linoleic acid (CLA), nonconjugated linoleic acid (NLA), and arachidonic acid (AA) in HT-1080 fibrosarcoma cells undergoing RSL3-induced ferroptosis.

Methods:

Cell Culture: HT-1080 wild-type (WT) cells were a generous gift from the Dixon lab at Stanford University. HT-1080 WT cells were cultured in DMEM high glucose media containing 10% fetal bovine serum (Gibco), 1% penicillin-streptomycin (10,000 U/mL; Gibco), and 1% MEM nonessential amino acids (Gibco). Cells were incubated at 37 °C and 5% CO_2 in a HERA cell 150i carbon dioxide incubator. Cells were passaged at 80% confluency for maintenance. All cell culture materials were obtained from Thermo Fisher Scientific.

Stimulated Raman Scattering Microscopy Sample Preparation: HT-1080 WT cells were harvested by trypsinization and seeded in 8-well chamber slides (Thermo Fisher Scientific) at 4,800 cells per well in 300 µL media. Cells were treated with DMSO or 80 µM conjugated linoleic acid, linoleic acid, linoleic acid-^{13}C, arachidonic acid, arachidonic acid-d_8, or arachidonic acid-d_{11} (Cayman Chemical). The cells were then incubated at 37 °C/5% CO_2 for 24 hours. The next day, the media was aspirated, and the cells were treated with DMSO or 0.05 µM RSL3 and 80 µM of the indicated lipids in 300 µL of media per well. After incubating for 4, 3, 2, 1, 0.5, or 0 hours, the cells were washed with PBS and fixed with 4% paraformaldehyde for 15 minutes. 100 µL of PBS was added to each well until imaging to prevent morphological changes associated with drying.

Flow Cytometry: Following the protocol described by (Martinez et al., 2020), HT-1080 WT cells were seeded in 6-well plates at 2.0 × 105 cells per well, treated with 80 μM of the indicated lipids in 2 mL media per well, and incubated at 37 °C/5% CO_2. After 24 hours, the media was removed and replaced with media containing DMSO (control) or 0.05 μM RSL3 with or without 80 μM of the indicated lipids in 2 mL of media per well. After incubating for 4, 1, or 0 hours, 2 μL of 1.5 mM BODIPY581/591 C11 dye was added to each test well. The cells were incubated for 20 minutes and then washed with PBS. They were then harvested by trypsinization, resuspended in 500 μL PBS, and passed through 40 μm cell strainers. Flow cytometry data were collected on a BD FACSymphony A3 Cell Analyzer and analyzed using FlowJo at the University of Washington Department of Pathology Flow Cytometry Core facility.

Hyperspectral SRS microscopy: The hyperspectral SRS microscopy setup has been reported in detail in our previous work (Su et al., 2022). Briefly, a broadband femtosecond dual beam laser system (Spectra-Physics Insight DS+) outputs a wavelength-tunable beam (pump) and a fixed beam at 1040 nm (Stokes) at an 80 MHz repetition rate. The pump beam is chirped to approximately 3 ps with high-dispersion SF11 dense flint glass rods (GR, Newlight Photonics). The Stokes beam is modulated at 20 MHz with an electro-optical modulator (EOM, Thorlabs) and coupled into a 4-m polarization-maintaining Yb-doped fiber (YB1200-10/125 DC-PM, Thorlabs) for parabolic amplification22, then chirped to match that of the pump beam using a grating stretcher (GS, LightSmyth). The two beams are combined with a 1000 nm short pass (SP) dichroic mirror (Thorlabs) and temporally overlapped using a motorized delay stage (DS, Zaber X-DMQ-AE).

The synchronized laser beams are directed into a home-built upright laser scanning microscope equipped with a 40× water immersion objective (Nikon N40XLWD-NIR, NA = 1.15) and an oil immersion condenser (Nikon MEL41410, NA = 1.4). The pump beam is isolated with a 1000 nm SP filter (Thorlabs) and detected by an amplified Si photodiode (PD). The signal is then demodulated with a lock-in amplifier (LIA, Zurich Instruments H2FLI) with a time constant of 4 μs to generate 512 × 512-pixel SRS images.

For SRS imaging of the HT-1080 cells, 40 mW of the pump beam at 800 nm for C–H, 851 nm for C–D, and 887 nm for the fingerprint region, and 72 mW of the Stokes beam were used. All SRS imaging and data analysis were completed by Fiona Xi Xu in the Dan Fu lab at the University of Washington Department of Chemistry.

Laser Scanning Confocal Microscopy: HT-1080 WT cells were harvested by trypsinization and seeded in 8-well chambered coverslips (Ibidi) at 4,800 cells per well in 300 μL media. Cells were treated with DMSO or 80 μM conjugated linoleic acid, linoleic acid, or arachidonic acid. The cells were then incubated at 37 °C/5% CO2 for 24 hours. The next day, the media was aspirated, and the cells were treated with DMSO or 0.05 μM RSL3 and 80 μM of the indicated lipids in 300 μL of media per well. After incubating for 4, 2, 1, or 0 hours, the cells were washed with PBS and stained with 10 μM BODIPY581/591 C11. After incubating for 20 minutes, the cells were washed with PBS and fixed with 4% paraformaldehyde for 15 minutes. After washing with PBS, 50 μL of Fluoromount-G Mounting Medium (SouthernBiotech) was added to each well. The cells were imaged on the Leica SP8X Confocal Microscope at the University of Washington's W. M. Keck Microscopy Center. Image analysis was carried out using Imaris software in the W. M. Keck Microscopy Center.

Results:

SRS imaging reveals morphological changes associated with ferroptosis. HT-1080 cells were incubated with RSL3 and imaged at 0, 0.5, 1, 2, 3, and 4 hours after treatment. See Figure 4.1A for a diagram of the SRS imaging apparatus that was used. Even in the absence of exogenous PUFA treatment, multiple morphological changes were noted. First, cell size decreased significantly over the course of RSL3 treatment (Figure 4.1B, C). Meanwhile, the intensity of the lipid C-H signal increased in cells during treatment (Figure 4.1D). We hypothesize that this is due to the shrinking of cells resulting in a

higher density of C-H lipid signal in the cell region, as both the C-H spectra and amide spectra (corresponding to protein content) increased over the course of RSL3 treatment when normalized to cell size (Figure 4.1 E,F). Increasing cell density has been observed with other cell death processes such as apoptosis (W. Wu et al., 2025). The increase in C-H signal corresponding to lipids could also be due to the formation of lipid droplets, which is a known phenomenon that can occur during ferroptotic death (Bai et al., 2019). Another interesting morphological trait that was noted in a small subset of cells was the appearance of cytoplasmic holes in the perinuclear region (Figure 4.1 B). The holes increased in size and quantity over the course of RSL3 treatment. We hypothesize that the appearance of these holes could indicate membrane damage as cells undergo lipid peroxidation.

Confocal microscopy shows appearance of lipid droplets with exogenous fatty acid treatment. To complement the SRS imaging and confirm specific subcellular compartments, we performed confocal microscopy on HT-1080 cells treated with exogenous fatty acid and RSL3. We used fluorescent dyes Nile Red and C11-BODIPY to stain lipid-rich areas of the cell. C11-BODIPY and oxidized C11-BODIPY fluoresce at two different wavelengths, so it is a commonly used fluorescent probe to measure lipid peroxidation, as lipid peroxidation leads to a higher proportion of its oxidized form (Drummen et al., 2002). We observed that cells treated with exogenous fatty acid (AA, NLA, and CLA) had bright puncta of lipid-rich regions in the perinuclear space, which were absent in the control group (Figure 4.2, A-D). Due to the colocalization with Nile Red and C11-BODIPY, we believe these puncta to be lipid droplets. As incubation time with RSL3 increases, the C11-BODIPY signal shifts from red (non-oxidized) to green (oxidized), indicating the presence of lipid oxidation in the perinuclear region. Interestingly, while some areas of oxidized lipids colocalize with Nile red, others do not. In particular, the puncta with the brightest emission in the oxidized BODIPY region tend not to colocalize with Nile Red. See arrows and boxes in Figure 4.2B for examples of this phenomenon in AA-treated cells. The same phenomenon can also be seen in cells treated with CLA and NLA (Figures 4.2 C and D, respectively). The converse is also true; not all areas of Nile Red emission colocalize with oxidized BODIPY. This could indicate that the

oxidation is not occurring in lipid droplets, but rather in the perinuclear space surrounding the lipid droplets, which could correspond to the ER. However, it could also be due to oxidation of lipids within the lipid droplets changing the lipophilicity or structural integrity of the droplets, causing a lack of Nile Red accumulation and fluorescence. More investigation is needed to determine the cause of this phenomenon. Nonetheless, the accumulation of oxidized BODIPY is consistently more apparent in the cells treated with exogenous fatty acid (Figure 4.2 B-D) than the control cells (Figure 4.2 A), which is consistent with prior work showing that exogenous PUFA treatment sensitizes cells to ferroptosis (Do et al., 2023). The accumulation is also more apparent in cells that have begun to shrink in size, supporting our earlier observations that cells undergoing ferroptosis shrink in size and become denser as they approach death.

Isotopically labeling fatty acids does not affect their ferroptosis-inducing potential. We next sought to use isotopically labeled fatty acids, specifically ^{13}C-labeled linoleic acid (^{13}C-NLA), terminally labeled d_{11} arachidonic acid (d_{11}-AA), and internally labeled d_8 arachidonic acid (d_8-AA) in SRS experiments to increase specificity (Figure 4.3). Isotopically labeling certain positions of fatty acids can render them non-oxidizable, as a deuterium will not be abstracted by ROS as readily as a hydrogen (von Krusenstiern et al., 2023b). Therefore, we first needed to confirm that the isotopic labeling did not interfere with the ferroptosis-inducing activity of the fatty acids. To do this, we employed flow cytometry with the lipid oxidation probe, C11-BODIPY (Martinez et al., 2020). Indeed, we were able to confirm that isotopic labeling of NLA and AA did not affect their propensity towards oxidation (Figure 4.4 A-D). As expected, all fatty acids resulted in a greater degree of lipid peroxidation with RSL3 treatment than the control cells (Figure 4.4 A). NLA and ^{13}C-NLA had very similar lipid oxidation profiles, with 4 hours of RSL3 treatment resulting in 31.1% and 29.4% oxidized cells, respectively (Figure 4.4 C). CLA is far more potent at inducing ferroptosis as it undergoes peroxidation at a faster rate than its nonconjugated counterpart (Do et al., 2021). This is confirmed with C11-BODIPY showing 62.3% of cells with lipid peroxidation after 4 hours of RSL3 exposure (Figure 4.4 B). An isotopic label was not needed for CLA

because the conjugated double bond vibration occurs in a unique region of the SRS spectrum, as opposed to the nonconjugated double bond region, which contains signal from many different biomolecules. As with NLA, isotopic labeling of AA did not significantly affect its ferroptosis-inducing potential. Unlabeled AA resulted in 46% of cells showing lipid peroxidation after 4 hours of RSL3 treatment while d_{11} AA resulted in 44% of cells showing peroxidation (Figure 4.4 D). Interestingly, d_8-AA resulted in a higher number of cells showing oxidation at 79%, so it is possible that it is more prone to oxidation than unlabeled or d_{11}-labeled arachidonic acid. However, the degree of oxidation at the 1-hour timepoint remained consistent across all three isoforms, and all three isoforms resulted in increased lipid peroxidation, as expected, so we chose to proceed with using these isotopically labeled analogs in future SRS experiments.

SRS imaging shows loss of C-D signal in terminally labeled fatty acids, possibly indicating truncation. Truncation products are downstream products of lipid oxidation resulting from Hock rearrangement and cleavage of a carbon-carbon bond, producing reactive aldehyde byproducts (McIntyre, 2012). They have been observed in the context of ferroptosis and are indicative of significant lipid peroxidation (Do & Xu, 2023; Qiu et al., 2024a; Sokol et al., 2025). We hypothesized that we could observe differences in the C-D SRS signal over the course of RSL3 treatment between internally labeled d_8 AA and terminally labeled d_{11} AA (See Figure 4.3 for structures). Due to their unique labeling patterns, d_8 AA and d_{11} AA have distinct SRS spectra in both C-D region (2050 – 2265 cm^{-1}) and fingerprint region (1600 – 1700 cm^{-1}). Figure 4.5A shows the average spectra of no lipid, d_8-AA, and d_{11}-AA labeled cells in the C-H stretching, C-D, and amide /C=C bond region. In the C-D region, d_8-AA shows a prominent peak at 2250 cm^{-1}, resulting from C-D stretching, whereas d_{11}-AA displays multiple peaks center around 2125 cm^{-1}, due to C-D_2 and C-D_3 stretching vibrations. In the fingerprint region, d_8-AA exhibits a red-shifted C=C peak (~1635 cm^{-1}) due to the proximity of the C-D bonds to the C=C bonds, while d_{11}-AA retains the typical nonconjugated PUFA C=C peak at 1656 cm^{-1}, overlapping with the amide I band.

Upon RSL3 treatment, we observed different spectral and intensity changes between the two isotopically labeled fatty acids. As shown in Figure 4.5 B, in d_8-AA-treated cells, the C-D signal remained relatively stable with a slight increase during the first 2 hours of treatment before undergoing a rapid decline in the final 2 hours. This initial increase may reflect lipid droplet accumulation and cell shrinkage, which enhance local lipid density and thus SRS intensity. The subsequent decline likely corresponds to lipid degradation and the onset of ferroptotic cell death. In contrast, d_{11}-AA-treated cells exhibited an overall more dramatic decrease in C-D signal with the RSL3 treatment, starting at the 30-minute timepoint (Figure 4.5 C). The increase in C-D signal at the two-hour timepoint is still observed in d_{11} AA-treated cells, however it is lower in magnitude compared to in d_8 AA-treated cells. The peak of C-D signal in d_{11} AA-treated cells occurs at the 0-hour timepoint, whereas for d_8 AA-treated cells, it occurs at the two-hour timepoint. Overall, these trends indicate a more rapid and precipitous drop in C-D signal from terminally labeled d_{11} AA than from internally labeled d_8 AA.

We propose that this difference is due to the loss of C-D bonds during oxidative truncation of the fatty acid. Since the d_{11} AA is terminally labeled, truncation at any of the four double bond locations would result in complete loss of the deuterium label. In contrast, for the internally labeled d_8 AA, truncation at the distal double bond locations would result in a loss of some, but not all, deuterium labels. Therefore, we would expect to see a more dramatic loss of C-D signal from the d_{11}-AA treated cells as opposed to the d_8-AA treated cells during the formation of truncation products. This is consistent with the pattern of C-D signal loss that was observed in the differentially treated cells.

SRS spectral shift indicates differential oxidation mechanisms between conjugated and nonconjugated linoleic acid. As discussed previously, conjugated linoleic acid is more cytotoxic than its nonconjugated counterpart because it is more prone to oxidation (Do et al., 2023). Conjugated PUFAs are preferentially oxidized through peroxyl radical addition (PRA), in which ROS attack the conjugated double bond system directly, whereas nonconjugated PUFAs primarily undergo oxidation through

hydrogen atom transfer (HAT), in which a hydrogen atom is first abstracted from an allylic carbon to leave a vulnerable site for ROS attack (Do et al., 2021). Peroxidation of CLA has contribution from both the PRA and HAT mechanisms. Therefore, the oxidation of CLA occurs faster than NLA, rendering it more prone to inducing ferroptosis in cells. We hypothesized that the spectral shift associated with these distinct forms of oxidation could be distinguished using SRS.

To assess this, we first incubated HT-1080 cells with NLA or CLA overnight before adding RSL3 for 0 to 4 hours. The cells were fixed with formaldehyde prior to SRS imaging. As expected, cotreatment with CLA and RSL3 was highly toxic to the cells and resulted in significant shrinkage and loss of cellular content by the 4-hour mark (Figure 4.6 A). The Raman spectrum of pure CLA and NLA is distinct, as conjugated carbon-carbon double bonds produce a different vibrational pattern than nonconjugated carbon-carbon double bonds (Figure 4.6 B). The NLA peak is notably less intense than the CLA peak, and slightly right-shifted. As CLA becomes oxidized via PRA, the double bond system would become nonconjugated, and we hypothesized that this process could cause a right shift of the CLA peak. Cells treated with CLA produced a distinct peak compared to control cells, demonstrating that they have successfully incorporated the CLA (Figure 4.6 C, left panel). Figure 4.6 C, center panel shows the lipid-to-protein ratio in CLA-treated cells, which decreases with RSL3 treatment. This indicates that lipids are being depleted, likely through oxidation, as the cells undergo RSL3 treatment. We also observed a right shift of the CLA C=C peak over the course of RSL3 treatment, suggesting that the C=C bonds are lost as the CLA is oxidized (Figure 4.6 C, right panel). This is consistent with our hypothesis based on the PRA mechanism of CLA peroxidation, shown in Figure 4.6 D.

Our next step was to investigate the oxidation mechanism and products of CLA's nonconjugated counterpart, NLA 18:2. As expected, NLA was significantly less cytotoxic than CLA and resulted in less notable cell shrinkage and loss of cellular contents after 4 hours of incubation with RSL3 (Figure 4.7 A) One challenge of monitoring NLA oxidation using SRS microscopy is that its C=C peak overlaps with the cellular amide peak at 1656 cm^{-1} (Figure 4.7 B), hindering spectral interpretation and intensity

quantification. In order to differentiate the effects of peroxidation on NLA from the contribution of amide spectral information, we employed ^{13}C-NLA, which introduces a red shift in the C=C peak to ~1598 cm^{-1}, spectrally well-separated from the amide peak at 1656 cm^{-1} (Figure 4.7 C, left panel). As with CLA treatment, a decrease in the lipid-to-protein ratio with RSL3 treatment was observed, indicating that lipids are being diminished over the course of RSL3 treatment (Figure 4.7 C, center panel). The spectral shift associated with NLA was less clear than that associated with CLA (Figure 4.7 C, right panel). While the primary hydroperoxide product formed via HAT could initially introduce conjugation and cause a red shift, subsequent oxidation via PRA may result in the disruption of conjugation and formation of a more complicated hydroperoxide product (Figure 4.7 D). This combination of spectral effects could explain the unclear spectral shift associated with oxidation of NLA-treated cells.

Discussion

Here, we demonstrated the utility of SRS and confocal microscopy to explore the location and mechanisms of lipid peroxidation in HT-1080 cells undergoing RSL3-induced ferroptosis. While many organelles have been implicated in ferroptotic death, the subcellular location and progression of lipid peroxidation in cells remains unclear. Using confocal microscopy, we showed that oxidizable lipids and their oxidation products accumulate in perinuclear puncta that we believe to be lipid droplets due to their colocalization with the neutral lipid stain, Nile Red. We noted that some areas of lipid oxidation did not colocalize with Nile Red, indicating that oxidation could be occurring elsewhere in the perinuclear space, such as the ER, which is in agreement with a recent publication from the Stockwell lab (von Krusenstiern et al., 2023b). Alternatively, the oxidation could alter the nature of the lipid droplets such that Nile Red was no longer localized to that area. Additionally, using SRS, we highlighted significant morphological changes occurring during ferroptosis, including cell shrinkage, increased density, and the appearance of cytoplasmic holes in the perinuclear area. We also identified multiple potential mechanisms of lipid peroxidation using SRS, including the formation of truncated lipid oxidation products, PRA, and HAT.

We showed that conjugated and nonconjugated fatty acids produce distinct spectral patterns as they undergo oxidation in cells, hinting at their different mechanisms of oxidation.

Several limitations of this study exist. Due to the need to use fluorescent dyes for confocal microscopy that could interfere with SRS spectral intensity, we were not able to image the same samples using both modalities. Overlaying the confocal and SRS images would increase our confidence in the location of lipid accumulation and peroxidation. In addition, we had access to a limited number of stains for confocal microscopy. Including a nuclear stain, such as DAPI, and an ER stain, such as ER tracker green, would increase our confidence in identifying subcellular regions and enable quantification of fluorescent signals. Lastly, while we created timepoints by treating different samples with RSL3 for varying times, it would be advantageous to employ live cell imaging to probe how the same subset of cells progresses through RSL3-induced ferroptosis.

Nonetheless, this study highlights the role of lipid droplets and the ER as sites for the accumulation of lipids and their oxidation products during ferroptosis. It also demonstrates a novel application of SRS to discriminate between different mechanisms of lipid oxidation that occur in vitro during ferroptosis. This application could be explored in other contexts of lipid peroxidation, such as inflammation and tissue damage, to probe how lipids are being oxidized in different contexts.

Figures:

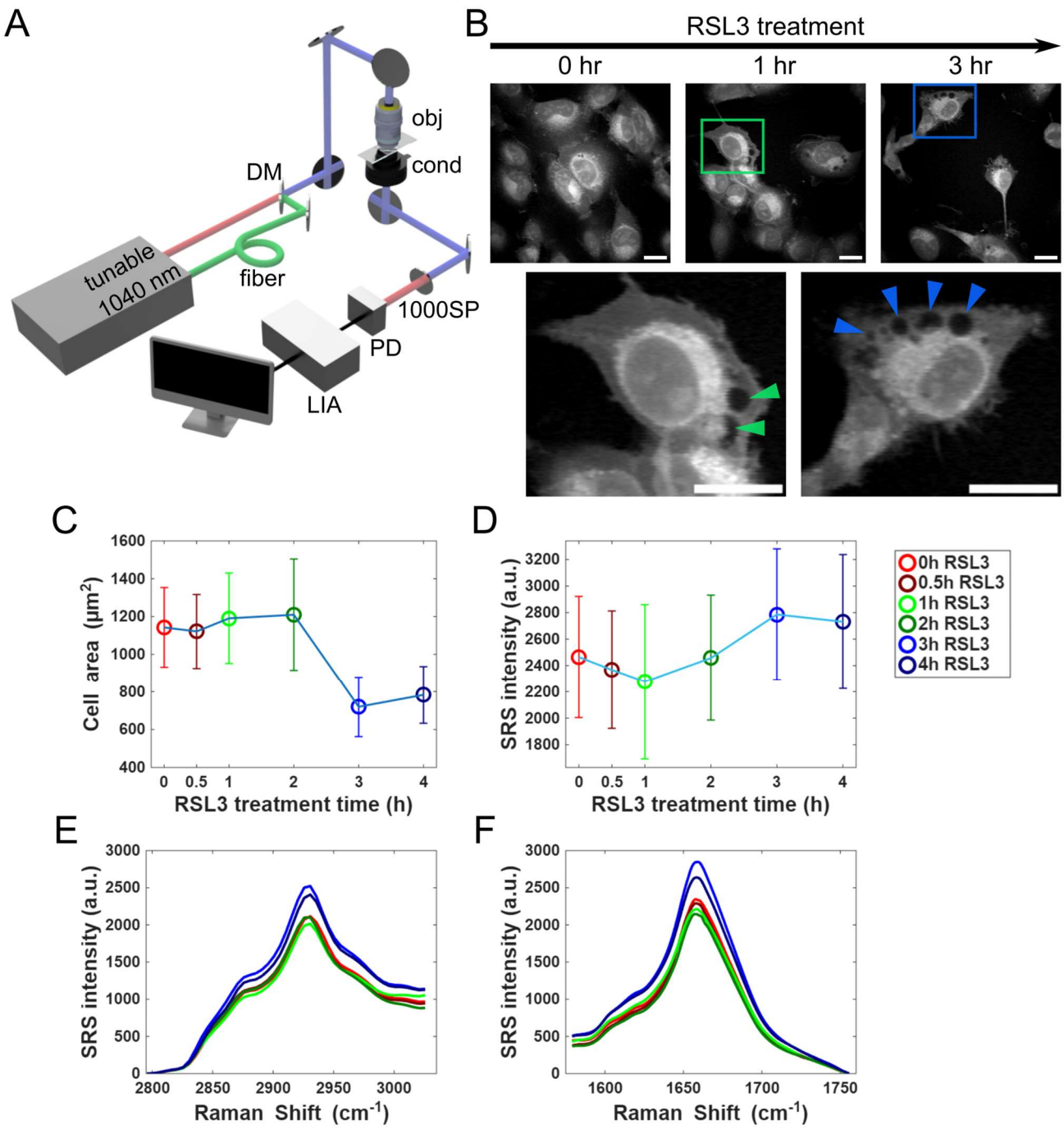

Figure 4.1: SRS imaging of HT-1080 cells during RSL3-induced ferroptosis. (A) Schematic diagram of the SRS microscopy system. Abbreviations: DM: dichroic mirror; obj: objective; cond: condenser;

1000SP: 1000nm short pass filter; PD: photodiode; LIA: lock-in amplifier. (B) SRS images show the morphological changes during ferroptosis, with arrows indicating holes formed in the cell cytoplasm. (C-D) Cell area change (C) and 2930 cm^{-1} C-H SRS intensity change (D) during RSL3 treatment, with error bars showing standard deviations. (E-F) Averaged SRS spectra of cell cytoplasm in the C-H stretching (E) and amide I (F) regions. Scale bars: 20 μm.

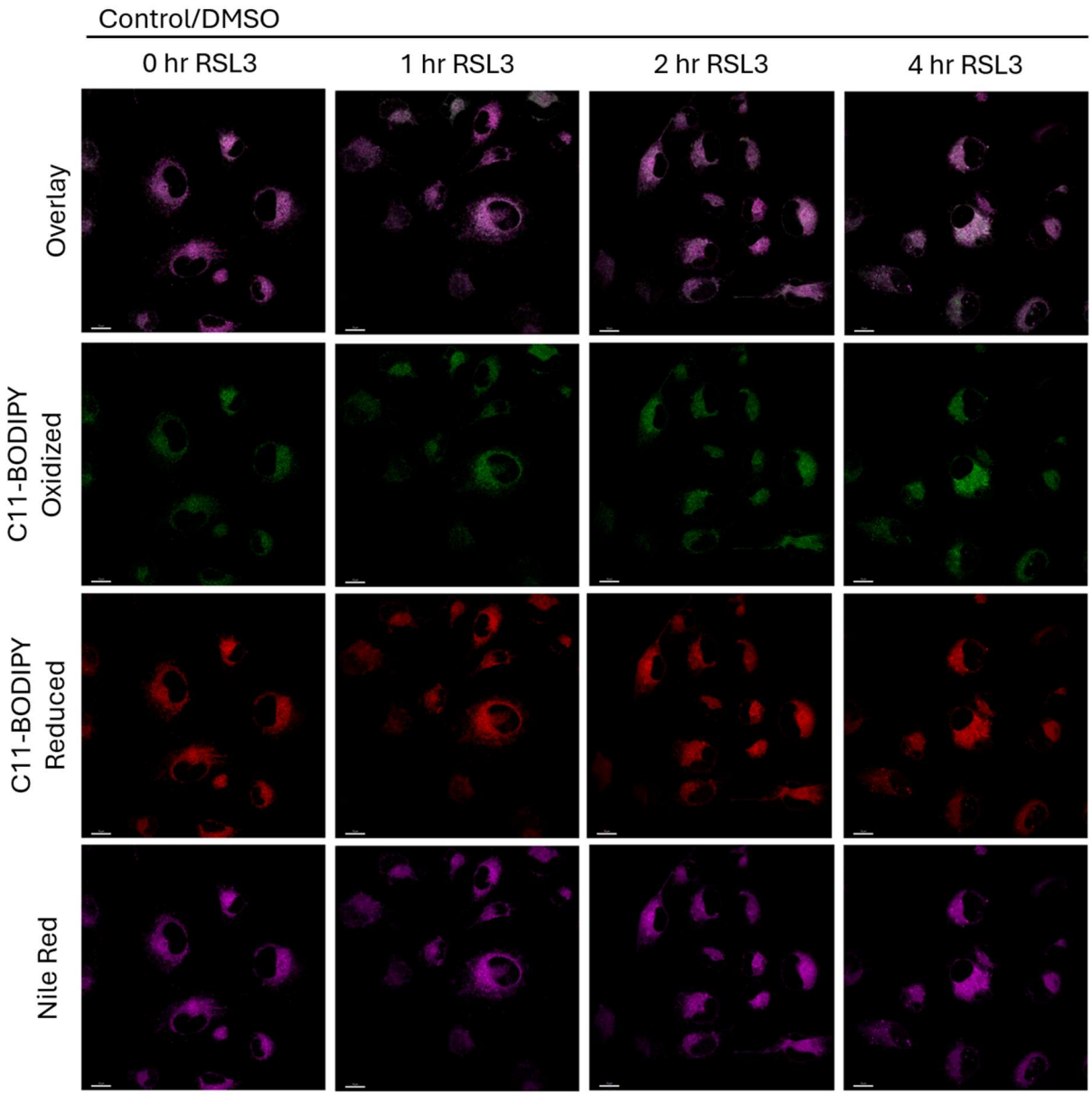

Figure 4.2 A: Confocal imaging of HT-1080 cells treated with vehicle no lipid control (DMSO) and RSL3 for 0, 1, 2, and 4 hours. Scale bar: 10 µm

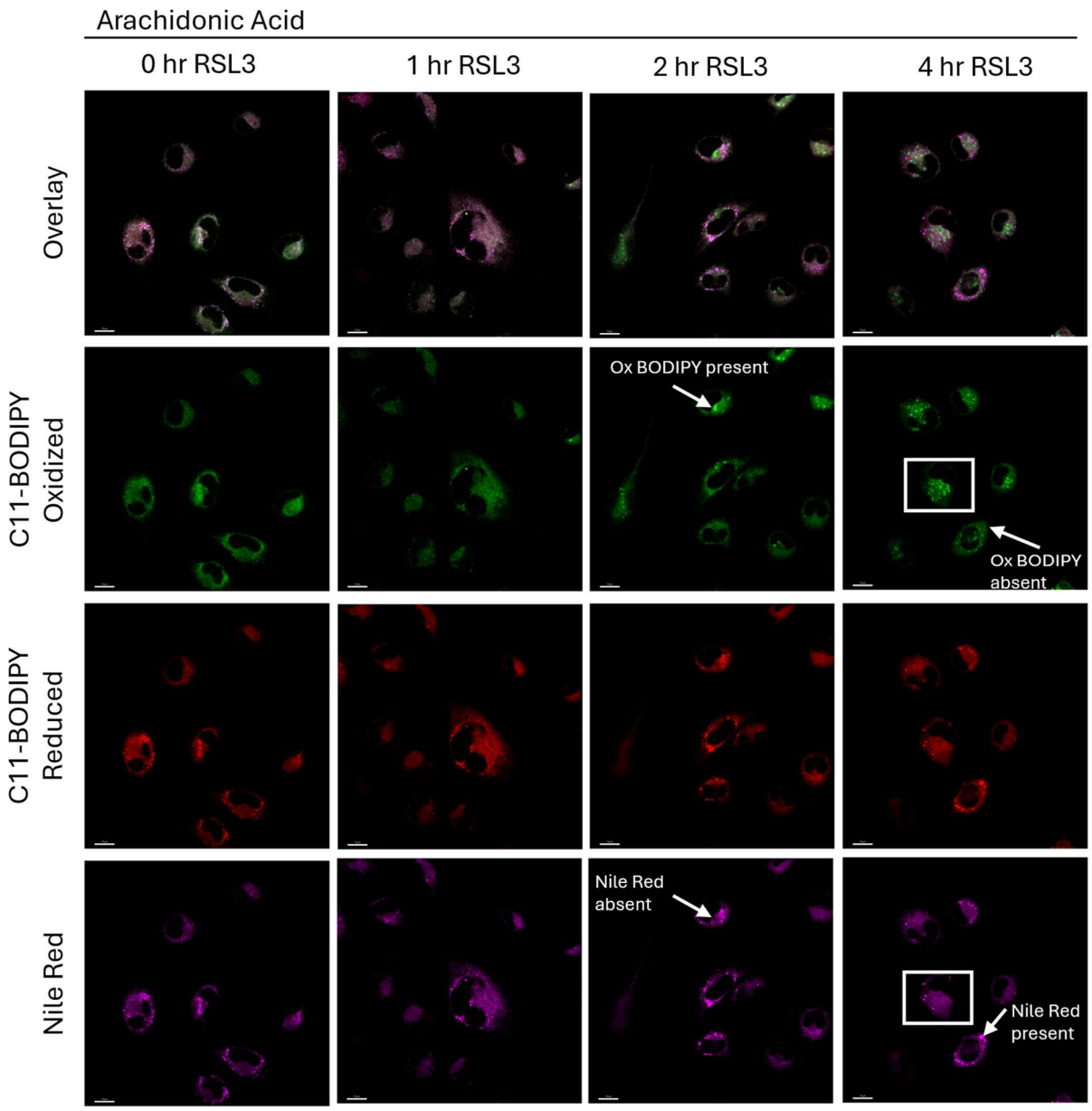

Figure 4.2 B: Confocal imaging of HT-1080 cells treated with 80 µM arachidonic acid overnight, followed by RSL3 for 0, 1, 2, and 4 hours. Arrows and boxes indicate areas where Nile Red and oxidized BODIPY do not colocalize. Scale bar: 10 µm

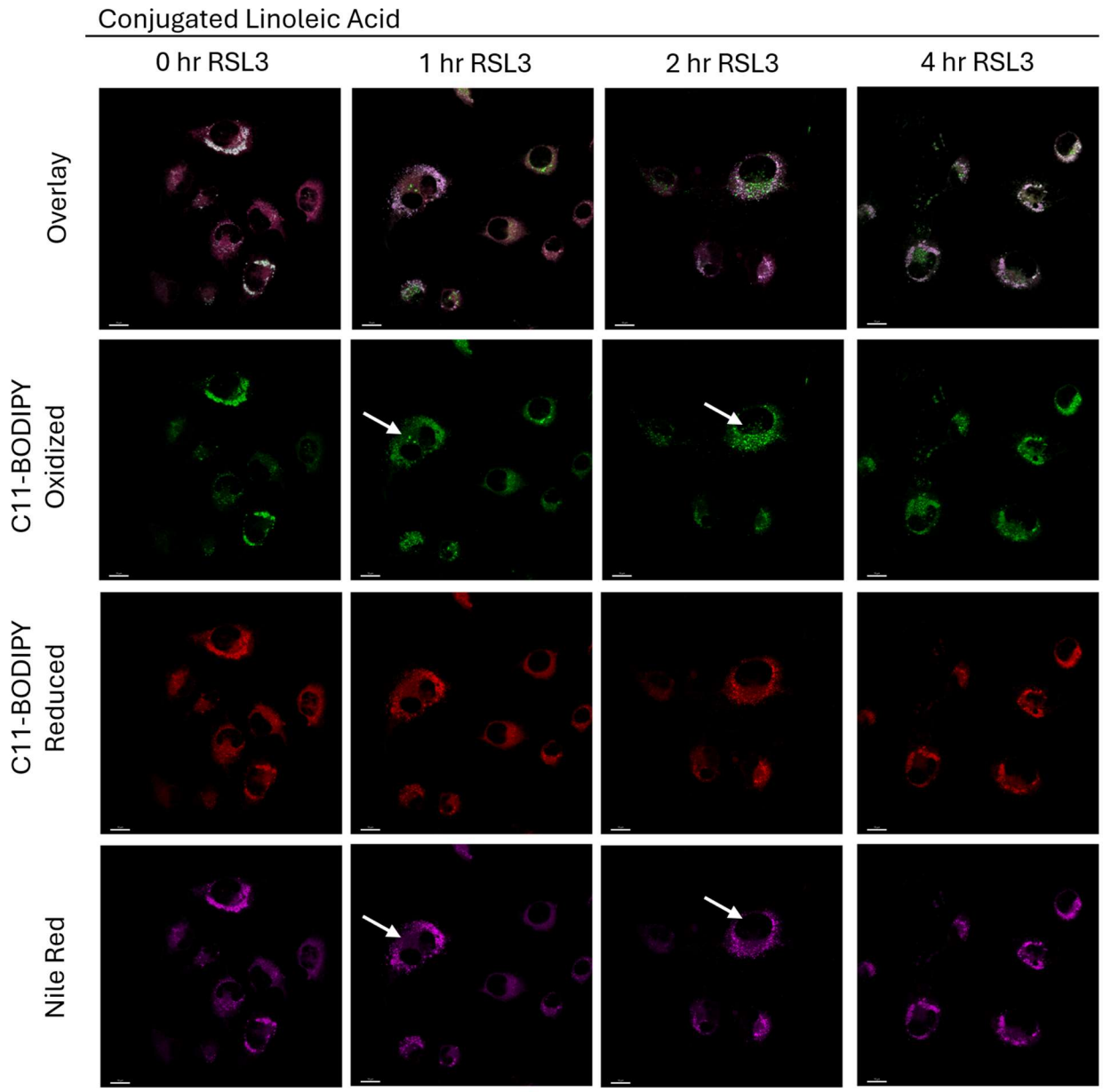

Figure 4.2 C: Confocal imaging of HT-1080 cells treated with 80 µM conjugated linoleic acid overnight, followed by RSL3 for 0, 1, 2, and 4 hours. Arrows indicate areas where Nile Red and oxidized BODIPY do not colocalize. Scale bar: 10 µm

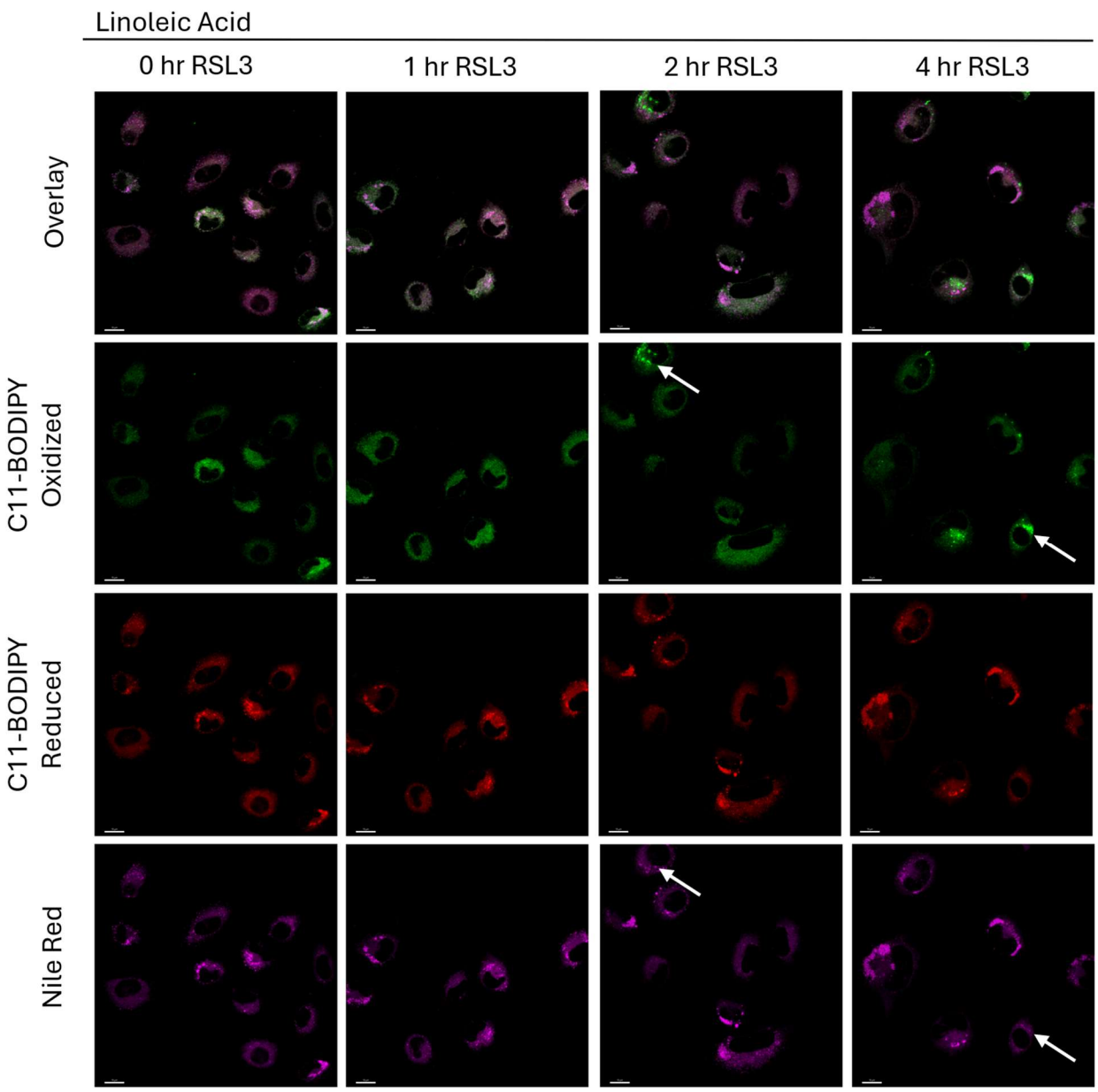

Figure 4.2 D: Confocal imaging of HT-1080 cells treated with 80 µM nonconjugated linoleic acid overnight, followed by RSL3 for 0, 1, 2, and 4 hours. Arrows indicate areas where Nile Red and oxidized BODIPY do not colocalize. Scale bar: 10 µm

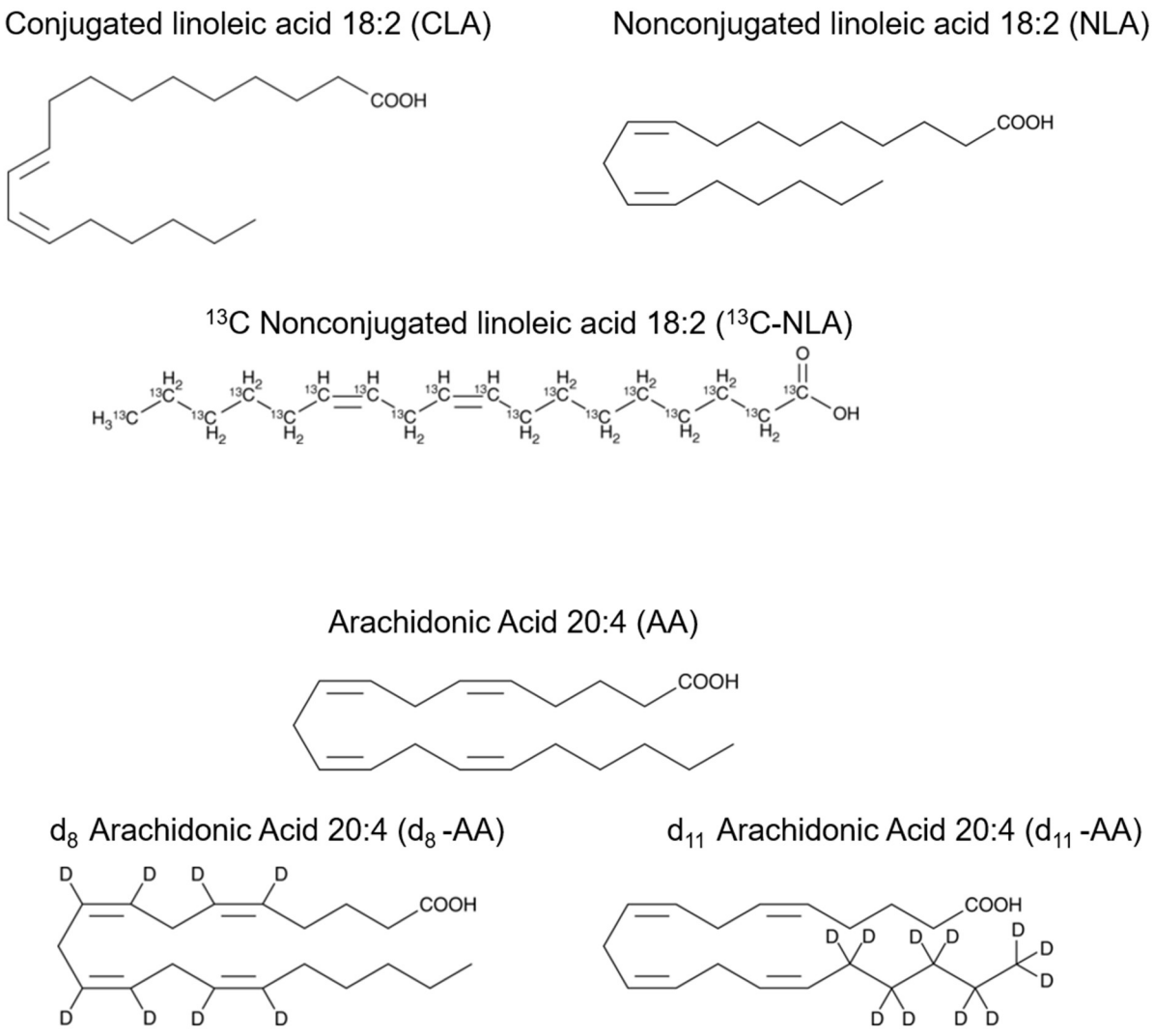

Figure 4.3: Structures of fatty acids used in this study and their isotopically labeled analogs.

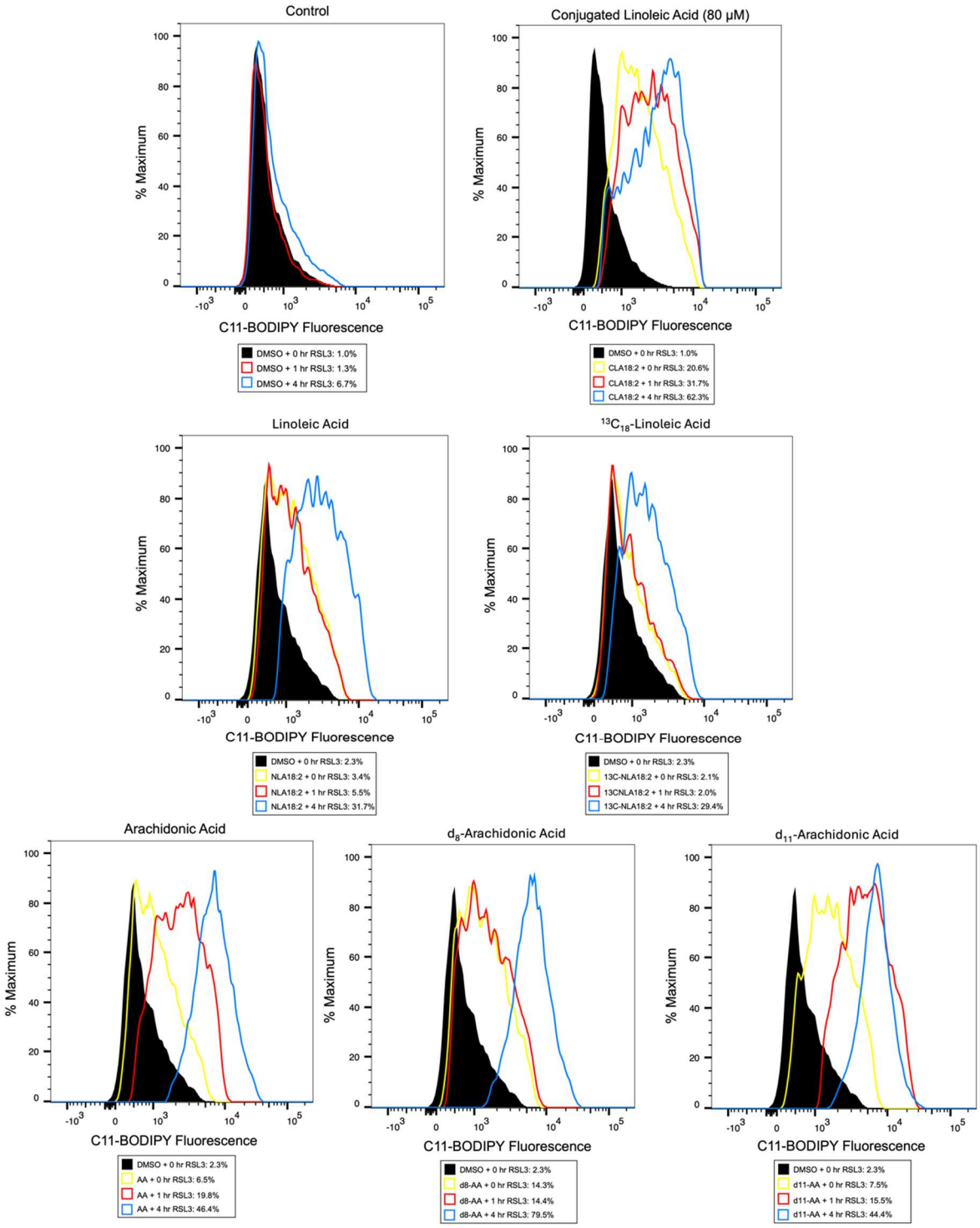

Figure 4.4: Assessment of lipid peroxidation in HT-1080 cells treated with the indicated fatty acid overnight followed by RSL3 for 0-4 hours using flow cytometry with the probe C11-BODIPY. Right shift indicates greater peroxidation.

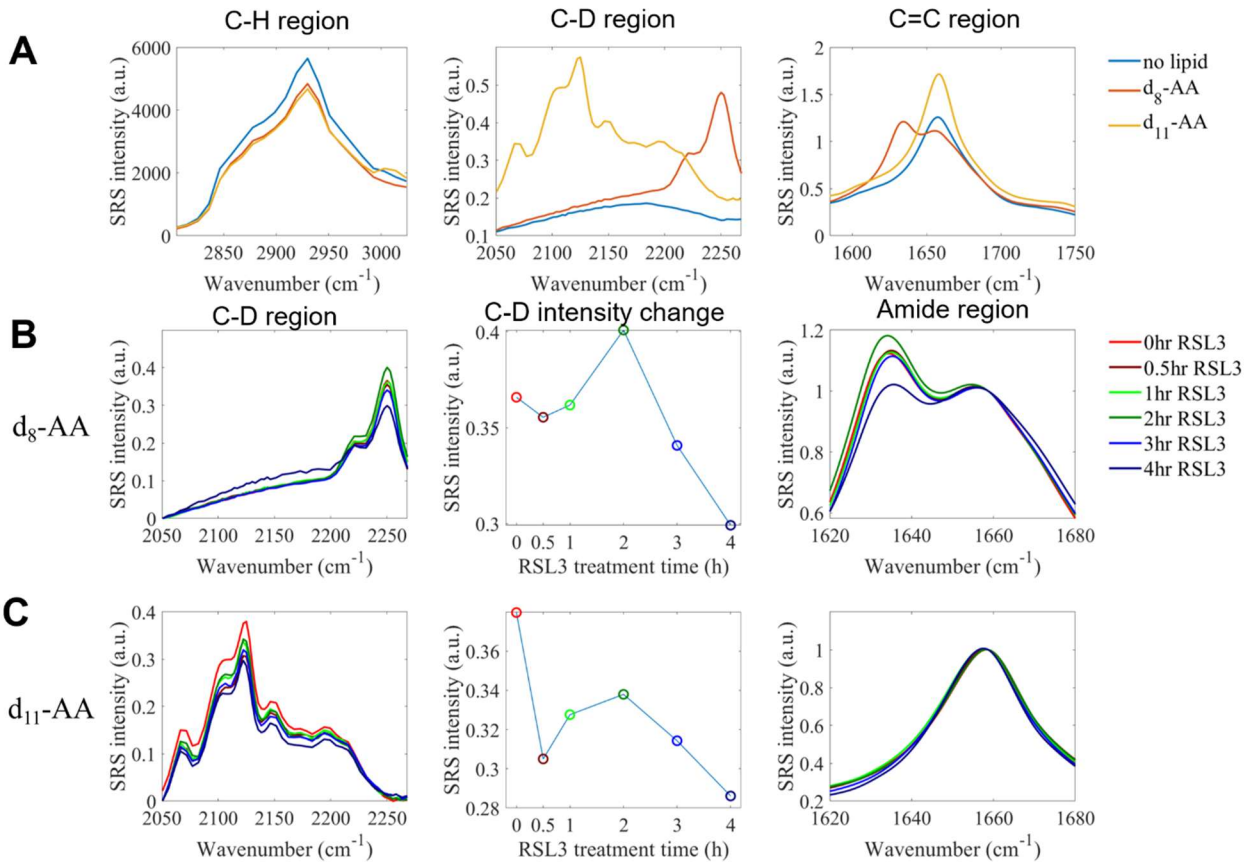

Figure 4.5: SRS spectral and signal intensity changes in cells incorporated with deuterated arachidonic acid (AA) during lipid peroxidation. A) SRS spectra of cells incorporated with d8-AA or d11-AA in the C-H stretching, C-D, and C=C/amide I regions. (B-C) SRS spectral and intensity changes in cells incorporated with d8-AA (B) or d11-AA (C). Left: SRS spectra in the C-D region. Middle: C-D peak SRS intensity change. Right: SRS spectra in the amide I region, with normalization by the amide I peak.

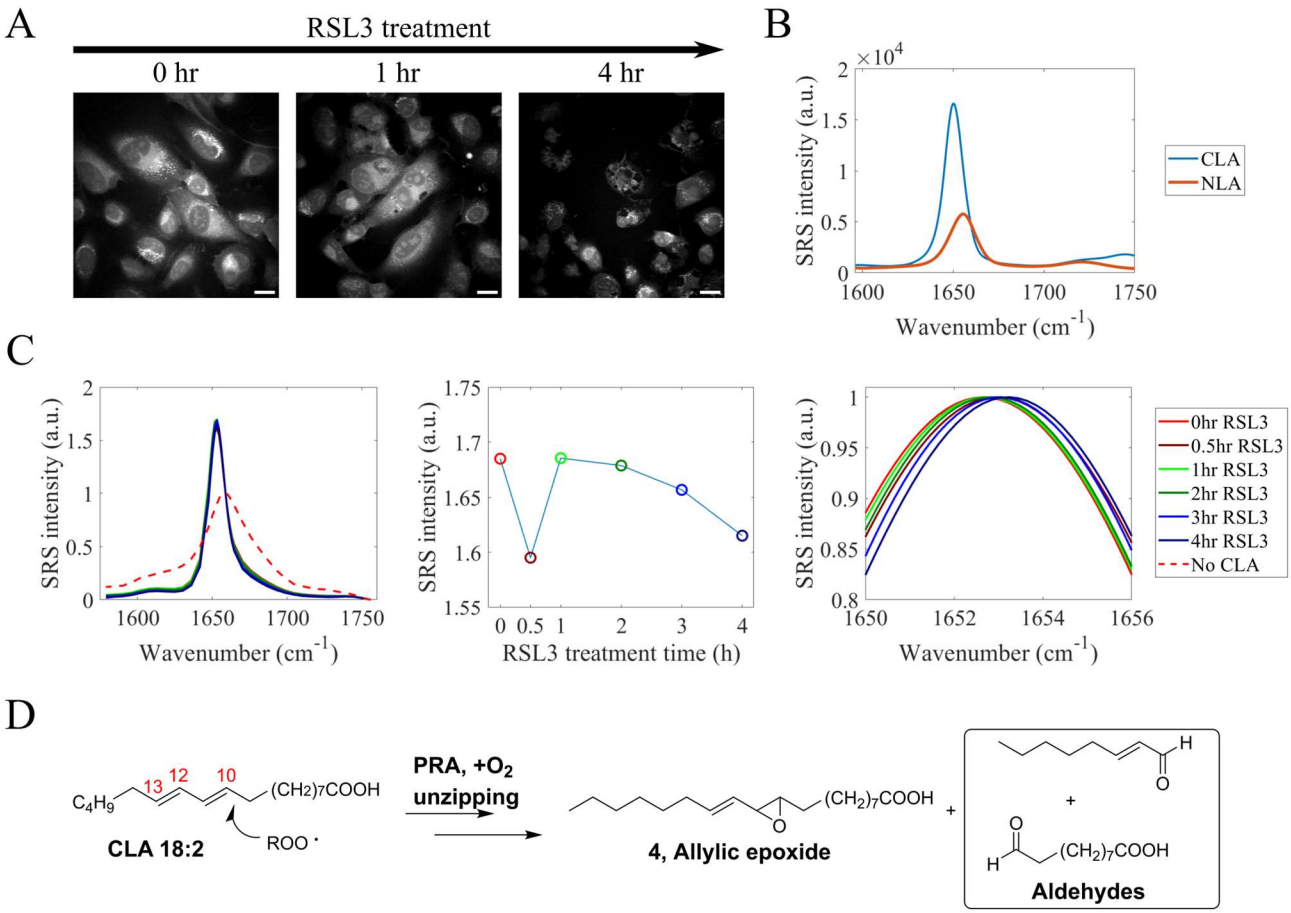

Figure 4.6: SRS imaging of lipid peroxidation of conjugated linoleic acid (CLA 18:2). (A) SRS images of CLA-incorporated cells during RSL3 treatment. (B) SRS spectra of pure CLA and nonconjugated linoleic acid (NLA). (C) Normalized SRS spectra of cell cytoplasm in the C=C/amide I region. Left: SRS spectra normalized by the amide I peak. Middle: CLA peak intensity change normalized to protein level to visualize lipid to protein ratio. Right: Normalized lipid peak with Lorentzian fitting to visualize the spectral shift induced by lipid peroxidation. (D) Proposed oxidation mechanisms and products of CLA.

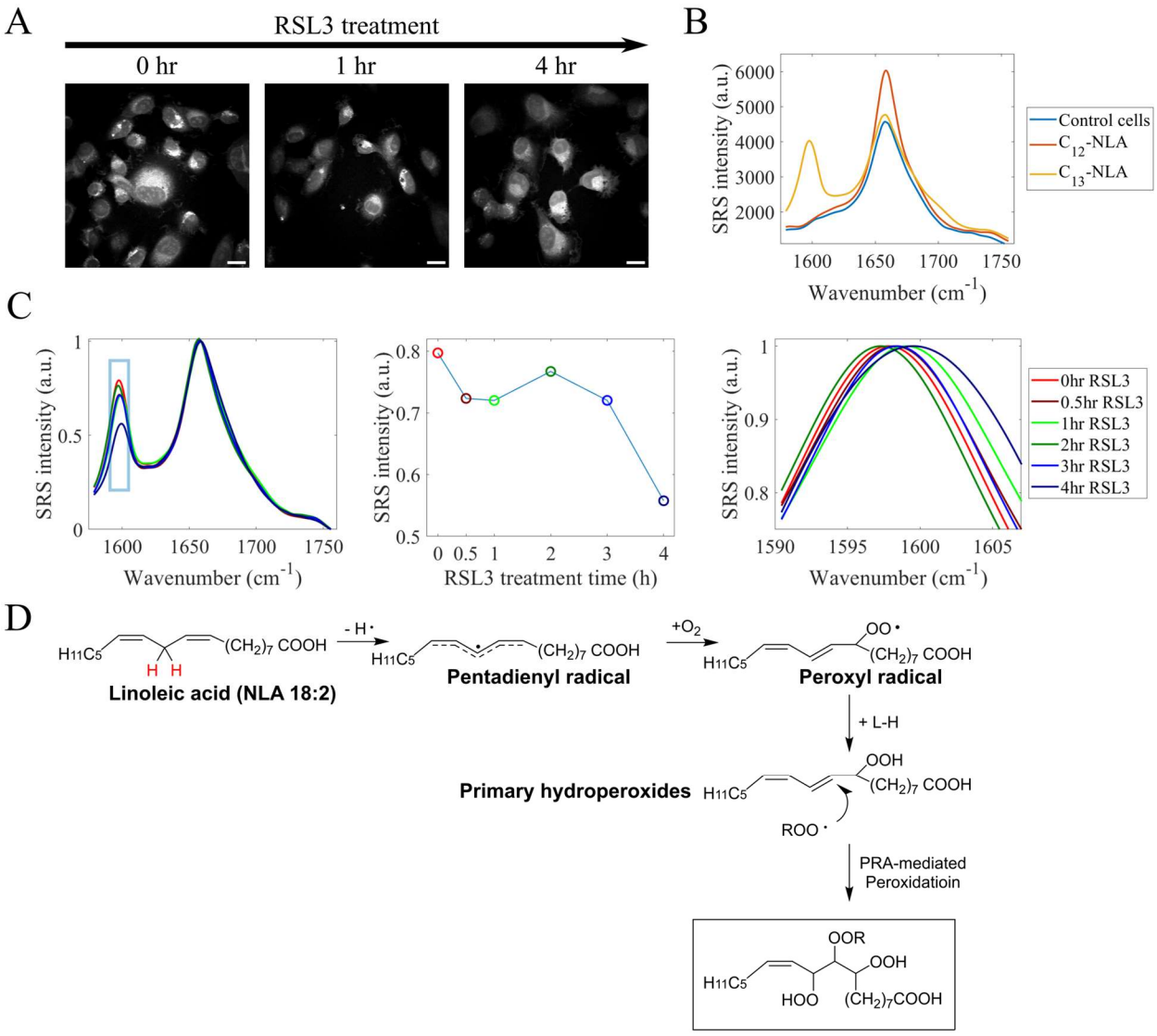

Figure 4.7: SRS imaging of lipid peroxidation of nonconjugated linoleic acid (NLA 18:2). (A) SRS images of C_{13}-NLA-incorporated cells during RSL3 treatment. (B) Spectral difference of cells incorporating C_{12} or C_{13}-NLA. (C) Normalized SRS spectra of cell cytoplasm in the C=C/amide I region. Left: SRS spectra normalized by the amide I peak. Middle: C_{13}-NLA peak intensity change with amide I peak normalization for visualizing lipid to protein ratio. Right: Normalized lipid peak with Lorentzian fitting to visualize the spectral shift induced by lipid peroxidation. (D) Proposed oxidation mechanisms and products of NLA.

Chapter 5: Multi-omic Characterization of *ACSL4* Knockout in the Context of Ferroptosis

Introduction

Ferroptosis is an iron-dependent form of regulated cell death that was first coined by Dixon and others in 2012 (Dixon et al., 2012). In ferroptosis, a buildup of lipid peroxides in the cell results in membrane permeabilization, protein damage, and cell death (Conrad et al., 2016; Stockwell et al., 2017). Since its discovery, ferroptosis has been implicated in many different physiological processes, including neurodegeneration, ischemia-reperfusion injury, and cancer (Stockwell, 2022). As such, it has garnered significant interest in its potential as a therapeutic target. However, this potential remains largely untapped as the regulatory pathways of ferroptosis remain poorly understood. Many studies have attempted to address this gap in knowledge through large-scale genetic screening efforts. Ultimately, the regulation of ferroptosis appears to be context dependent, meaning that the genes that are important to the execution of ferroptosis is dependent on the cell type and its environment (Magtanong et al., 2022). However, the gene acyl-coenzyme A (CoA) synthetase long chain family member 4 *(ACSL4*) has been identified as a key regulator of ferroptosis induced by direct GPX4 inhibition by multiple screens (Dixon et al., 2015; Doll et al., 2017) and has been shown to reduce ferroptotic death in disease models (Y. Xu et al., 2020; Zhao et al., 2024).

ACSL4 is a member of the *ACSL* enzyme family, which catalyzes the addition of a coenzyme A (CoA) group to free fatty acids in the cell. This activation step allows the fatty acid to be ligated to various glycerophospholipid headgroups by enzymes of the lysophospholipid acyl transferase (LPLAT) family. Once attached to a headgroup by ACSL and LPLAT, fatty acids can be incorporated into membranes throughout the cell. Each of the 4 ASCL isoforms has a substrate preference. ACSL4 prefers polyunsaturated fatty acids (PUFAs), specifically arachidonic acid (20:4) (Klett et al., 2017). PUFAs are

relevant to ferroptosis because they have multiple sites where peroxidation can occur, rendering them highly susceptible to peroxidation (Do et al., 2021; Kagan et al., 2017; L. Xu et al., 2009). Indeed, co-treating cells with a ferroptosis inducer and various PUFAs decreases the IC_{50} of RSL3 and erastin, and increases cellular lipid peroxidation as measured by the lipid peroxidation probe C11-BODIPY (Do et al., 2023; Martinez et al., 2020). Taken together, this evidence demonstrates that PUFA treatment sensitizes cells to ferroptosis by increasing the amount of oxidizable substrate within the lipidome.

ACSL4 knockout (KO) has been shown to protect cells from ferroptosis by altering cellular lipid composition. In reducing the amount of oxidizable PUFAs that are incorporated into cellular lipids, the lipidome becomes less prone to oxidation and ferroptosis (Doll et al., 2017; Magtanong et al., 2022). However, the impact of *ACSL4* KO on the lipidome has not been elucidated. We sought to better understand the effect of *ACSL4* KO on lipid metabolism and ferroptosis sensitivity using global and targeted MS-based lipidomics. Through these experiments, we show that *ACSL4* KO HT-1080 cells can still incorporate exogenous arachidonic acid into phospholipids, although at a lower level that is observed in wild-type HT-1080 cells. We identified a unique group of lipids that were especially reduced in ACSL4-KO cells relative to wild-type cells, called diPUFAs. DiPUFAs are phospholipids in which both of the fatty acids attached to the headgroup are polyunsaturated, as opposed to the majority of PUFA-containing phospholipids in which one fatty acid is saturated and the other is mono- or polyunsaturated. Recently, the Stockwell Group showed that DiPUFAs increase cell susceptibility to ferroptosis in a manner that cannot be replicated by the same total PUFA content present in phospholipids containing only one PUFA acyl chain, indicating that this unique class of lipids plays an important role in mediating ferroptosis (Qiu et al., 2024b). We also observed widespread changes in expression of lipid metabolic genes and proteins between wild-type and *ACSL4*-KO cells, including SREBF2 and PPARγ, as well as lipid transport genes such as FABP5. Downstream effects of these gene expression changes were observed, as sterol abundance was significantly higher in *ACSL4*-KO cells than in wild-type cells. Furthermore, assessment of lipid-carbonyl modified proteins showed significant enrichment of lipid-

adducted proteins in WT endoplasmic reticulum, mitochondria, and the outer membrane relative to KO cells, suggesting heightened lipid peroxidation in these areas. We hypothesize that the protective effect of ASCL4 knockout against ferroptosis is multifaceted and mediated by complex changes to the lipidome, including alterations to specific lipid species such as diPUFAs and sterols.

Methods:

Cell culture: ACSL4-KO and wild-type (WT) HT-1080 cells were received as a generous gift from the Scott Dixon laboratory (Doll et al., 2017; Magtanong et al., 2022). Both cell lines were cultured in high-glucose DMEM media supplemented with 10% fetal bovine serum, 1% penicillin-streptomycin antibiotics, and 1% non-essential amino acids (all materials obtained from Gibco). Cells were maintained at 80% confluency for up to 10 passages. For long-term storage, cells were stored in a liquid nitrogen dewar in growth media supplemented with 10% DMSO.

C11-BODIPY flow cytometry: Lipid peroxidation was measured using the probe C11-BODIPY (Thermo) as previously described (Martinez et al., 2020). Briefly, WT and *ACSL4*-KO HT-1080 cells were seeded in 6-well plates (Costar) and allowed to adhere for 24 hours. The following day, media was aspirated and replaced with media containing DMSO (vehicle control), 50 nM RSL3, 80 μM
, or both RSL3 and AA and incubated for 3 hours. Flow cytometry data were collected on a BD FACSymphony A3 Cell Analyzer and analyzed using FlowJo at the University of Washington Department of Pathology Flow Cytometry Core facility.

Cell viability dose response assay: WT and *ACSL4*-KO HT-1080 cells were seeded in 96-well plates (Costar) at a density of 5,000 cells/well. They were allowed to adhere for 24 hours before the media was replaced with media containing 80 μM AA and increasing concentrations of RSL3 from 0.001 to 3 μM in triplicate. After 24 hours of incubation with the treatment media, cell viability was assessed using

CellTiter 96 MTT dye (Promega) according to the manufacturer's instructions. Absorbance values were read on a BioTek Synergy HTX Multimode Microplate Reader. Total percent viability was calculated by subtracting background absorbance of empty wells and averaging three replicates per condition. Results were graphed in GraphPad Prism 9 against the log of RSL3 concentration. IC50 values were determined by non-linear regression analysis.

Dual-isotope labeling lipidomics: Dual-isotope labeling lipidomics was carried out as previously described (Reimers et al., 2023). Briefly, WT and KO cells were seeded at a density of 500,000 cells/10 cm dish. After 24 hours, they were treated with 80 μM of an equimolar mix of d_5- and d_{11}- arachidonic acid (dAA) (Cayman Chemical), 50 nM RSL3, both dAA and RSL3, or an equivalent amount of DMSO as a vehicle control for 24 hours. Lipidomic analysis was completed as previously described (A. Li et al., 2020). Samples were analyzed in positive and negative ionization mode using a data-independent acquisition (DIA) method on a Waters Synapt XS mass spectrometer with a Waters Acquity LC stack and a Phenomenex 100 mm x 1.8 Å HILIC column. Retention time alignment, collision cross section (CCS) calibration, and peak picking were completed using Waters Progenesis software. Deuterated lipids were picked and mass-adjusted using D-Tracer software (nreimers99, 2022/2023; Reimers et al., 2023), and lipids were identified using LiPydomics software (Ross, Cho, Zhang, et al., 2020). Doubly-labeled lipids (diPUFAs) were identified manually, and ID was confirmed using targeted fragmentation.

Targeted diPUFA lipid analysis: Lipid extracts were prepared as above, except that unlabeled arachidonic acid (AA) was used in place of dAA. Antioxidants butylated hydroxytoluene (BHT) and triphenylphosphine ($TPPh_3$) were included in the Folch solution to prevent atmospheric oxidation of lipid samples. A targeted multiple reaction monitoring (MRM) method was created on a Waters Xevo XS triple quadrupole mass spectrometer in negative ionization mode using a di-arachidonoyl phosphatidylcholine

(DAPC) standard (Avanti) to tune collision parameters. MS parameters, including transitions, are listed in Table 5.0. Samples were separated using a Waters Acquity LC stack and a Phenomenex 100 mm x 1.8 Å HILIC column. Peak areas were calculated using TargetLynx software (Waters). Peak smoothing and ApexTrack were enabled during peak integration. GraphPad Prism was used for graphing and significance analysis of the results.

Transcriptomics: WT and ACSL4-KO HT-1080 cells were seeded at a density of 500,000 cells/10 cm dish in quadruplicate. After 24 hours, they were treated with DMSO as a vehicle control or 80 uM AA overnight. Total RNA was isolated from cells using the Rneasy Mini Kit (Qiagen). RNA quantity was confirmed by measuring absorbance on a Synergy HTX Multimode Microplate Reader (BioTek). RNA integrity was confirmed by measuring A260/A280 on a Nanodrop spectrophotometer. Samples were sent to Novogene for cDNA library construction and sequencing on the Illumina NovaSeq 6000 platform (150 base pairs with sequencing depth above 20 million reads per sample). All samples met Novogene requirements for quantity and quality, confirmed using the Agilent 2100 BioAnalyzer (Agilent). Raw sequencing FASTQ files were mapped to the human genome (hg38) using HISAT2 in R (Kim et al., 2019). Format conversions were completed using SAMtools (H. Li et al., 2009). DESeq2 was used in R to determine differentially expressed genes (DEGs) (Liao et al., 2014; Love et al., 2014). Pathways analysis of DEGs was completed by the EDGE Center at the University of Washington.

Global Proteomics: WT and ACSL4-KO HT-1080 cells were treated with DMSO (control), 80 uM AA, or AA with 30 nM RSL3 (RA, Sigma) for 24 hours. Cells were rinsed and collected in an SDS-based lysis buffer with Halt Protease Inhibitor Cocktail (Thermo). Cells were sonicated, then centrifuged at 4 °C at 3000×G for 10 mins. Supernatant was collected, and protein was quantified using a BCA assay (BioRad). 1 mg of each sample was adjusted to the same volume, and samples were incubated with 1 µg each sequencing-grade trypsin and glu-c (Promega) overnight at 37 °C. The next day, digestion was quenched

with formic acid, and samples were desalted using the Pierce Peptide Cleanup Plate (Thermo) according to the manufacturer's instructions. Final peptide yield was determined using the Pierce Quantitative Colorimetric Peptide assay kit (Thermo). 10 µg worth of peptides was dried in a Savant SpeedVac Vacuum Concentrator and reconstituted in 10 µL Optima LCMS-grade water with 0.1% formic acid. 1 µL of iRT internal standards were added to each sample prior to analysis. Samples were analyzed on a Thermo Lumos Orbitrap mass spectrometer with a Thermo Vanquish nano-LC system on a packed 30 cm C18 column. Pooled samples were analyzed in data-dependent acquisition mode to build a spectral library. Other samples were analyzed using data-independent acquisition (DIA) mode. MSConvert was used for demultiplexing of DIA data prior to spectral library building and alignment using Skyline 26.1 (Adusumilli & Mallick, 2017; MacLean et al., 2010). Advaita iPathwayGuide was used for pathway enrichment analysis by the University of Washington EDGE Center.

Sterolomics: Analysis of sterols was completed as previously described (Herron et al., 2018). Briefly, WT and *ACSL4*-KO HT-1080 cells seeded at 80% confluency in 10 cm dishes were collected in PBS by scraping. The cells were lysed, and lipids were extracted using Folch solution. Deuterated (d_7 cholesterol and d_7 7-DHC) were added and the lipid fraction of the sample was dried in a Savant SpeedVac. Samples were reconstituted in 90% methanol (Optima LCMS grade, FisherSci) prior to MS analysis using a Waters Xevo XS triple quadrupole mass spectrometer with an atmospheric pressure chemical ionization (APCI) source and Waters Aquity liquid chromatography stack. A Phenomenex C18 100 mm × 2.1 mm, 1.7 µm column was used with an isocratic gradient of mobile phase B, consisting of 90% methanol, 10% water with 0.1% formic acid (all materials Optima LCMS grade, sourced from Fisher Scientific). Data was acquired using a previously developed multiple reaction monitoring method (Herron et al., 2018) and peak integrations were carried out using TargetLynx software (Waters). Analyte peaks were compared with internal standards to obtain a concentration for each analyte. Plotting and statistical analysis was carried out using GraphPad Prism software.

Pulldown proteomics: Analysis of lipid carbonylated proteins was completed based on previously published studies (Y. Chen et al., 2018a; Kallemeijn et al., 2021a). WT and ACSL4-KO HT-1080 cells were treated with DMSO (control), 80 uM arachidonic acid (AA, Cayman), or AA with 30 nM RSL3 (RA, Sigma) for 24 hours. Cells were rinsed and collected in an SDS-based lysis buffer with Halt Protease Inhibitor Cocktail (Thermo). Universal Nuclease (Thermo) was added, and cells were sonicated, then centrifuged at 4 °C at 3000×G for 10 mins. Supernatant was collected, and protein was quantified using a BCA assay (BioRad). Samples were diluted to 1mg/mL, adjusted to pH 5 with 1M hydrochloric acid, and meta-aminophenylacetylene (mAPA) was added to a final concentration of 500 µM. Sodium cyanoborohydride was added to a final concentration of 60 mM, and samples were incubated by vortexing at room temperature for 1 hour. Samples were then precipitated in acetone overnight at -20 °C to remove excess reagent. Copper-catalyzed click chemistry was used to conjugate mAPA-labeled proteins to biotin using a dialkoxydiphenylsilane (DADPS) biotin azide probe. After clicking, samples were precipitated in acetone at 20 °C overnight to remove excess reagents. Clicked proteins were then attached to Neutravidin beads (Thermo) and purified according to a previously published protocol (Kallemeijn et al., 2021a). Once attached to beads and purified, samples were incubated with sequencing-grade trypsin and glu-c (Promega), shaking overnight at 37 °C. The next day, digestion was quenched, and labeled proteins were released from the beads by adding formic acid to a pH of 4. Samples were desalted using Thermo C18 spin columns, and peptides were quantified using the Pierce Quantitative Colorimetric Peptide assay kit (Thermo). An aliquot of the peptides (10 µg) was dried in a Savant SpeedVac Vacuum Concentrator and reconstituted in 10 µL Optima LCMS-grade water with 0.1% formic acid. iRT internal standards (1 µL) were added to each sample prior to analysis. Samples were analyzed on a Thermo Astral Orbitrap mass spectrometer with a Thermo Neo nano-LC system on a packed 30 cm C18 column. Pooled samples were analyzed in data-dependent acquisition mode to build a spectral library. Other samples were analyzed using data-independent acquisition (DIA) mode. MSConvert was used for demultiplexing of DIA data prior to spectral library building and alignment using Skyline 26.1 (Adusumilli & Mallick, 2017; MacLean et al., 2010).

Click-chemistry Western Blot: Invitrogen Sample Loading Dye and freshly prepared 1M dithiothreitol were added to clicked protein samples, and they were incubated for 5 minutes at 90 ºC. 20 µL of the sample mixture was added to each well of a Nu-PAGE 12-well precast 4-12% bis-tris gel (Invitrogen). The gel was run on the Invitrogen Nu-PAGE system at 200V for 25 minutes using Invitrogen MES running buffer. The gel was transferred to a nitrocellulose membrane using the iBlot dry blotting system (Thermo Fisher). The membrane was incubated shaking for 1 hour in LiCor Odyssey TBS Blocking Buffer (LiCor). 4 uL Streptavidin IRDye 800 CW and 10 uL goat anti-beta actin (Abcam) antibodies were added to the blocked buffer and incubated overnight. The next day, the membrane was washed with 1x Tris-Buffered Saline with Tween 20 and imaged on the LiCor Odyssey Gel Imager. Background subtraction and band quantification was carried out using ImageJ.

Results:

ACSL4 knockout reduces ferroptosis sensitivity in HT-1080 cells. To confirm that *ACSL4* KO produced the expected phenotype in our model system, we used a dose-response assay and flow cytometry to assess the ferroptosis sensitivity of wild-type (WT) and *ACSL4*-KO HT-1080 cells. As expected, the dose response curve showed that *ASCL4* KO significantly increased the IC_{50} of RSL3 (Figure 5.1A). In addition, the cotreatment of both RSL3 and AA decreased the IC_{50} of RSL3. This is consistent with prior work showing that the addition of PUFAs to RSL3 treatment sensitizes cells to ferroptosis (Do et al., 2023). To further confirm that ASCL4 knockout reduces lipid peroxidation in cells, we used the lipid peroxidation probe C11-BODIPY that changes in fluorescence when in the presence of lipid peroxides (Drummen et al., 2002; Martinez et al., 2020). Fluorescence of cells was determined using multi-color flow cytometry. Indeed, KO cells showed fewer cells with lipid peroxidation when treated with RSL3 or RSL3 and AA than their WT counterparts (Figure 5.1B). Taken together, this evidence

confirms that ACSL4 knockout does reduce RSL3-mediated ferroptosis sensitivity in HT1080 cells, with or without exogenous PUFA cotreatment.

ACSL4 knockout reduces but does not completely ablate arachidonic acid incorporation into phospholipids. Using a dual-isotope labeling lipidomics strategy that was previously developed in our lab (Reimers et al., 2023), we sought to elucidate the metabolic fate of arachidonic acid in WT and KO HT-1080 cells. As expected, the total amount of dAA-containing phospholipids was significantly lower in KO cells in TG, PC, PA, and PG lipid classes than in WT cells (Figure 5.2A), meaning that *ACSL4* KO cells do not incorporate as much exogenous PUFA into phospholipids as WT cells do. The difference was largest in the TG lipid class. Differences between WT and KO in the PE and PI lipid classes were not significant. This is consistent with other studies that have shown a reduction in PUFA-containing phospholipids in KO cells relative to WT cells (Doll et al., 2017). Notably, the KO cells were still able to incorporate a significant amount of dAA into phospholipids, as all the lipid classes detected in KO cells had dAA-containing lipids. We hypothesized that this incorporation could be due to compensatory upregulation of other ACSL isoforms and performed RNA sequencing as well as proteomics to assess this possibility. The results of these analyses will be discussed in a later section.

The lipidomes of KO and WT cells differ significantly in their response to RSL3. In WT HT-1080 cells treated with 80 μM dAA and 50 nM RSL3 for 24 hours, we observed a reduction in the overall abundance of dAA-containing phospholipids compared with cells treated with dAA alone (Figure 5.2B). The difference in abundance was significant for TG, PC, and PA lipid classes. This is consistent with our previous study, and we hypothesized that the loss of this lipid abundance could be due to the lipids being oxidized as the cells undergo ferroptosis (Reimers et al., 2023). Notably, the same trend was not present in KO cells treated with RSL3. There were no significant changes in the abundance of dAA-containing phospholipids in any of the lipid classes in KO cells between RSL3+dAA-treated and dAA-only-treated

groups (Figure 5.2C). While the abundance of dAA-containing lipids was higher in the WT dAA treated than the KO dAA treated cells, the abundance was lower in the WT RSL3+dAA than in the KO RSL3+dAA, indicating that the lack of response to RSL3 observed in KO cells is not simply due to a lower starting level of dAA-containing phospholipids. These results indicate that although *ACSL4*-KO cells can still incorporate some dAA into phospholipids, it is not being depleted during RSL3 treatment as it is in the WT cells, meaning that the KO cells are not responding in the same way to RSL3 treatment as are the WT cells. We hypothesized that this difference in response could be driven by a certain subclass of highly oxidizable lipids that is more abundant in the WT than the KO cells.

DiPUFAs are significantly lower in abundance in KO than in WT cells. DiPUFAs are phospholipids that contain a PUFA in both the SN1 and SN2 positions, whereas a typical PUFA-PL contains a PUFA at only the SN2 position. Lipids containing multiple dAA species produce signature triplet peaks in the lipidomics mass spectra (Figure 5.3 A,B). These peaks form when the lipid has two d5, one d5 and one d11, or two d11 AA moieties attached to a phosphate headgroup, adding 10, 16, or 22 Da to the unlabeled m/z, respectively. From a global lipidomics study of WT and KO cells treated with dAA that was acquired using data independent acquisition (DIA) mode, we identified multiple species producing these triplet peaks (Figure 5.2D). Their fatty acid chain composition was confirmed using targeted fragmentation of the parent species (Figure 5.3C). The doubly-deuterated lipids were identified as being PC, PE, and PI headgroups attached to labeled AA (20:4) or labeled adrenic acid (AdA, 22:4), which is the elongation product of AA. We then sought to quantify these species using a targeted multiple reaction monitoring (MRM) method on a triple quadrupole mass spectrometer. In order to increase the signal of the diPUFA species for more robust quantification, cells were treated with unlabeled arachidonic acid instead of deuterated arachidonic acid for the MRM quantification study.

The most abundant of these diPUFA species in each class we identified (PC, PE, and PI) are lipids containing one AA and one AdA (20:4-22:4). We identified all three possible combinations of AA

and AdA (20:4-20:4, 20:4-22:4, 22:4-22:4) in PC and PI classes, but only (20:4-20:4) and (20:4-22:4) in PE. It is important to note that because we cannot determine the location (sn1 or sn2) of each fatty acid chain on the phospholipid headgroup using targeted fragmentation alone, the composition of the fatty acid chains is denoted as (XX-XX) instead of (XX/XX). The observation of PC and PE AA and AdA containing lipids is consistent with the recent study from the Stockwell lab that identified diPUFA PC lipids as being particularly important to the induction of ferroptosis, as well as a previous paper from Kegan et al. that identified AA- and AdA-containing lipids as drivers of ferroptosis and a more recent paper from the same group highlighting the role of PE-diPUFAs in enzymatically mediated lipid peroxidation (Kagan et al., 2017; Qiu et al., 2024b; Samovich et al., 2024).

Notably, all the diPUFA species that were identified in our study had significantly lower abundance in KO than in WT cells treated with AA only, with the exception of PE(20:4/20:4), which was lower but not significant (Figure 5.4). The same trend is true for cells treated with AA+RSL3, with the exception of PE(20:4/20:4), which was also lower in KO than WT but was not significant (Figure 5.4). This finding is consistent with our hypothesis that *ACSL4* KO cells produce less diPUFAs than WT cells when treated with exogenous AA. To determine if the oxidation of these diPUFAs could be driving the difference in ferroptosis sensitivity observed between WT and KO cells, we next sought to identify and quantify products formed from the oxidation of the identified diPUFA products in cell extracts.

Oxidation products of diPUFAs are identified and are more abundant in WT than in KO cells when treated with AA and RSL3. To determine which oxidation products are readily formed from diPUFA oxidation, we performed an in vitro oxidation of a pure diPUFA standard, diarachidonoyl phosphatidylcholine (DAPC, PC(20:4/20:4)) (Figure 5.5A). After 4 hours of incubation with the radical initiator 2,2'-Azobis[2-(2-imidazolin-2-yl) propane] Dihydrochloride (AIPH) in liposomes, we identified +1O, +3O, +5O, and Δ5 truncated products as being the most abundant from in vitro oxidation (Figure 5.5B). Identities were verified with targeted fragmentation (Figure 5.5C). Truncation products are formed

from Hock rearrangement of lipid peroxides, resulting in carbon-carbon bond cleavage and the production of reactive aldehydes, including 4-HNE (Ayala et al., 2014) (Figure 5.5 D). See Chapter 3 Figure 3.3 for a mechanism of Hock rearrangement.

We then sought to identify these oxidation products in cell extracts from WT and *ACSL4*-KO cells treated with AA in the presence and absence of RSL3. A targeted MRM method was developed using the m/z of the parent diPUFA for Q1 isolation and the m/z of the oxidized fatty acid product for Q3 isolation. By using the mass of the oxidized fatty acid chain for Q3 isolation, we avoided isolating isomeric or isobaric non-oxidized lipids. While the method was developed using DAPC, we adjusted the parent m/z values to search for diPUFA products with PE and PI headgroups in addition to PC, because we previously identified diPUFAs from each of these classes in WT and KO lipidomics datasets.

We identified +1O, +3O, and Δ5 truncation products from PC, PI, and PE AA and AdA-containing diPUFAs in the cell extracts (Figure 5.6). +1O oxidation products were significantly higher in WT than KO RSL3+AA-treated cells for all diPUFAs with the exception of PI(22:4/22:4), which was higher in WT, though not significant, and PE(20:4/20:4), which did not follow a clear trend (Figure 5.6A). +3O oxidation products were lower in abundance than +1O oxidation products, leading to more variability in the quantification and lower overall statistical significance. The +3O product was significantly higher in WT than in KO RSL3+AA-treated cells for PC(20:4/22:4) and (22:4/22:4) parents and followed the same trend for (20:4/20:4) but did not reach significance. PI +3O products were higher in WT than KO RSL3-treated cells for all 3 parent diPUFAs, although (22:4/22:4) did not reach significance. PE(20:4/20:4)+3O did not follow the same trend as the other oxylipids, leading us to believe that it may be a different isomeric lipid or formed through enzymatic rather than non-enzymatic oxidation (Figure 5.6B). Lastly, we identified multiple Δ5 truncation products, both with 20:4 and 22:4 fatty acids attached in the other position on the headgroup. These truncation products followed the same trend as the other oxidized lipids, in which they were significantly higher in WT than KO cells, particularly in the RSL3+AA-treated groups (Figure 5.6C)

ACSL1 is upregulated in ACSL4 KO cells relative to WT but is not further induced by AA treatment. We next sought to determine whether the dAA incorporation into phospholipids could be due to compensatory action by another lipid metabolic enzyme by performing RNA sequencing on WT and KO HT-1080 cells in the presence and absence of AA treatment. The screening revealed a significant +0.36- and +0.38-Log_2(fold-change) increase in *ACSL1* expression in *ACSL4* KO cells relative to the WT cells, in the untreated and treated groups, respectively (Table 5.1). The fold change in the gene expression was nearly the same in untreated cells and in cells treated with AA, indicating that the enzyme is not induced by excess exogenous fatty acids. The upregulation of *ACSL1* could represent an alternative pathway by which exogenous fatty acids are incorporated into membrane phospholipids in the absence of ACSL4 expression. While each of the ACSL enzymes has a unique substrate preference, they are promiscuous and can still activate non-preferential fatty acids at a substantial rate (Klett et al., 2017).

Transcriptomics reveals altered expression of lipid metabolism regulator genes in *ACSL4* KO relative to WT cells. *SREBF2*, or sterol regulatory element binding transcription factor 2, is a master regulator of many lipid metabolic genes, most notably those along the pathway of cholesterol biosynthesis (Madison, 2016). RNA sequencing revealed a modest but significant downregulation of *SREBF2* in both WT and KO AA-treated cells compared to Control cells (log_2FC=-0.454, p = $1.0e^{-6}$ and log_2FC=-0.434, p = $1.0e^{-6}$, respectively) (Table 5.1). Consequently, many of the genes regulated by SREBF2 were downregulated in both WT and KO cells when treated with AA (Figure 5.7 A,B), including DHCR7, SQLE, and HMGCR, which are critical enzymes in the cholesterol biosynthesis pathway (Table 5.1). We hypothesized that the changes to the expression of sterol synthesis genes lead to differences in sterol abundance between the WT and KO cells. We performed sterolomics analysis to assess this hypothesis, and the results of this study are discussed in a later section. All the genes regulated by SREBF2 that were detected and differentially expressed showed lower expression in AA-treated versus control cells for both

WT and KO cells, meaning that the regulator and the affected genes were consistently downregulated together.

Another crucial lipid metabolic regulator is PPARγ, or peroxisome proliferator-activated receptor gamma. PPARγ has been implicated in regulating ferroptosis, particularly in Alzheimer's disease (AD) (L. Tang et al., n.d.). This regulator was significantly less expressed in KO AA-treated cells than in WT AA-treated cells (log_2FC=-6.494, p=1.0e^{-6}) (Table 5.1). This regulator controls the transcription of many lipid metabolic and survival genes. Even though PPARG was downregulated overall, many of these individual genes were upregulated in KO AA-treated cells compared to WT, including *ACSL1*, *APOE*, and *HMOX1* (Figure 5.7C). We have seen that the upregulation of *ACSL1* may be a compensatory mechanism for the ACSL4 KO cells to incorporate exogenous AA into phospholipids. APOE, or apolipoprotein E, is a lipid transport protein that incorporates cholesterol and other lipids into lipoproteins that can be effectively transported throughout the body. Variants of APOE can influence an individual's risk for developing AD (Corder et al., 1993). It has been shown that APOE can act as an inhibitor of ferroptosis by preventing the buildup of free iron in the brain. Interestingly, the variant associated with increased risk of AD, APOE4, is associated with lower levels of the protective APOE protein and higher levels of highly oxidizable PUFAs, which could implicate ferroptosis as a form of cell death contributing to AD pathology (Belaidi et al., 2024). APOE was significantly upregulated in KO control and KO AA-treated cells relative to their WT counterparts (log_2FC=+1.172, p=2.163e^{-4}, log_2FC=+1.128, p=0.014, respectively) (Table 5.1). HMOX1, or heme-oxygenase 1, catalyzes the breakdown of heme into carbon monoxide, iron, and biliverdin. Its role in ferroptosis is multifaceted, because it produces pro-ferroptotic free iron, but also anti-ferroptotic biliverdin, which has antioxidant properties (D. Tang et al., 2021). It was significantly upregulated in AA-treated versus control cells for both WT and KO (log_2FC=+1.856, p=1.000e^{-6}, log_2FC=+1.246, p=1.000e^{-6}, respectively), as well as in KO AA-treated and control cells versus WT counterparts (log_2FC=+0.832, p=1.000e^{-6}, log_2FC=+1.444, p=1.000e^{-6}, respectively)(Table 5.1). The role of HMOX1 in ferroptosis is not fully understood; however, most studies indicate that

upregulation of HMOX1 can sensitize cells to ferroptosis by increasing the amount of free iron in the cell (Souza et al., 2025; Y. Sun & Zhang, 2024; D. Tang et al., 2021). While transcriptomics is a good representation of acute cell state and stress responses, many gene transcripts can be post-transcriptionally modified or degraded before being transcribed into protein. Therefore, gene expression does not always directly correspond to protein expression. Therefore, we next performed a global proteomics analysis on ACSL4-KO HT-1080 cells and WT HT-1080 cells treated with DMSO (control), AA, RSL3, and AA+RSL3.

Global proteomics reveals differential responses to ferroptosis by WT and ACSL4-KO cells. Differential expression analysis revealed many differentially expressed proteins (DEPs) between WT and KO cells (Table 5.2). Interestingly, the greatest number of DEPs resulted from the KO RSL3 versus WT RSL3-treated groups, with over 1000 DEPs. Upstream regulator analysis revealed that the master regulators TP53 (tumor suppressor protein 53) and SRSF10 (serine and arginine rich splicing factor 10) were significantly upregulated in KO RSL3-treated cells compared to WT RSL3-treated cells (Figure 5.8, A, B, respectively). SRSF10 primarily regulates RNA splicing. Interestingly, all the proteins regulated by SRSF10 that were identified in this screening were downregulated in KO cells even though SRSF10 itself was upregulated, meaning that SRSF10 is negatively regulating these downstream proteins (Figure 5.8A). Most of the proteins regulated by SRSF10 are involved in gene transcription, splicing, and cell division, suggesting that KO cells are not actively transcribing as many genes as the WT cells. This is expected, as the WT cells are undergoing ferroptosis; they may upregulate transcription of stress response genes to mitigate the effects of RSL3 treatment. Since KO cells are less susceptible to RSL3-induced ferroptosis, they may not need to transcribe as many stress response genes, thus resulting in lower expression of these transcriptional regulators. The trend was less consistent with genes regulated by TP53; while some were upregulated, others were downregulated (Figure 5.8B). However, TP53 expression is typically induced by

stress, which indicates that the KO cells were experiencing some type of oxidative stress induced by RSL3 treatment.

Lipid transport protein FABP5 is upregulated in ACSL4 KO cells relative to WT. FABP5, or fatty acid binding protein 5, is a cytoplasmic lipid transport protein that is responsible for the uptake, transport, and metabolism of long-chain fatty acids within cells. It has been implicated as a potential biomarker for ferroptosis, as its expression increases on the cell surface during ferroptosis (Peng et al., 2024). It is hypothesized that the role of FABP5 in ferroptosis is in response to the cells' increased need for fatty acids, as they need to replace oxidatively damaged phospholipids with newly synthesized intact phospholipids. We were initially surprised to see upregulation of FABP5 in KO AA, RSL3, and RSL3+AA-treated cells compared to their WT counterparts ($log_2FC=+1.810$, $p=0.024$, $log_2FC=+1.697$, $p=4.000e^{-4}$, $log_2FC=+1.103$, $p=0.015$, respectively) (Figure 5.8 C,D). However, we hypothesize that this upregulation in KO cells could be in response to their having a limited capacity to uptake fatty acids, particularly in the context of exogenous AA treatment. KO cells could upregulate FABP5 in order to increase their uptake of fatty acids.

KO cells have increased sterol abundance relative to WT, suggesting an alternative protective mechanism of ASCL4 KO. As discussed earlier, transcriptomics revealed downregulation of *SREBF2*, a master regulator of sterol synthesis, in KO AA-treated cells relative to WT. We hypothesized that this differential expression could lead to differences in sterol abundance between WT and KO cells. Sterols, including cholesterol and its immediate precursor, 7-dehydrocholesterol (7-DHC), have recently been shown to be protective against ferroptosis and thus could represent a novel mechanism of *ACSL4*-mediated ferroptosis resistance (Freitas et al., 2024; Y. Li et al., 2024; C. Liu et al., 2023; Q. Sun et al., 2023b). Indeed, sterolomics analysis revealed that *ACSL4*-KO cells have higher overall sterol abundance than WT, in AA-treated and AA+RSL3-treated cells (Figure 5.9A). Notably, 7-DHC was significantly

higher in the KO than in the WT when treated with AA and AA+RSL3 (Figure 5.9B). 7-DHC is highly oxidizable and has been shown to protect cells against ferroptosis by acting in a sacrificial manner to prevent the peroxidation of phospholipids (Freitas et al., 2024; Y. Li et al., 2024). The oxidation of 7-DHC results in the formation of an oxysterol called 3β,5α-dihydroxycholest-7-en-6-one, or DHCEO. The abundance of DHCEO was significantly higher in KO than WT AA+RSL3-treated cells, indicating that the oxidation of 7-DHC may be contributing to the ferroptosis resistance observed in *ACSL4*-KO cells (Figure 5.9C).

These results may seem contradictory given that sterol synthesis genes were downregulated overall in KO cells relative to WT. However, sterol synthesis is regulated via a negative feedback loop, such that high levels of cholesterol in a cell will 'turn down' or negatively regulate upstream sterol synthesis genes to maintain consistent levels of sterols. We hypothesize that the increased levels of sterols in KO cells compared to WT could be due to shuttling excess precursors to fatty acids, such as acetate, into sterol synthesis rather than into phospholipids. The overall higher levels of sterols in *ACSL4*-KO cells relative to WT could represent another mechanism of ferroptosis resistance afforded by ACSL4 knockout.

Pulldown proteomics reveals enrichment of lipid-carbonyl-modified ER and mitochondrial membrane proteins in WT compared to ACSL4-KO HT-1080 cells. Protein modification is a well-known phenomenon as a result of lipid peroxidation (Fritz & Petersen, 2011). Protein modification occurs when lipid-derived electrophiles, such as 4-hydroxynonenal and malondialdehyde, adduct to nucleophilic sites on proteins, commonly cysteine, histidine, and lysine (LoPachin et al., 2009). Protein carbonylation as an effect of lipid peroxidation has been observed in many models, including alcoholic liver disease, breast cancer, and ferroptosis (Y. Chen et al., 2018b; Galligan et al., 2012; Madian et al., 2011). Due to the differences in ferroptosis susceptibility between WT and *ACSL4* KO HT-1080 cells, we hypothesized that

we would observe differences in protein adduction between these two cell types upon treatment with arachidonic acid and the ferroptosis inducer RSL3.

Following the protocols by Chen et al. and Kallemeijin, et al., we used the probe meta-aminophenylacetylene (m-APA) and copper-catalyzed click chemistry to isolate lipid-carbonylated proteins from WT and *ACSL4*-KO protein extracts (Y. Chen et al., 2018b; Kallemeijn et al., 2021b). The pulldown proteins were assessed by Western blot and mass spectrometry-based proteomics. Western blot showed significantly higher levels of carbonylated protein in WT compared to KO cells when normalized to GAPDH signal (Figure 5.10 A, B). Since the same quantity of peptides were injected for each sample, the relative abundance changes of WT proteins relative to KO proteins were obtained, and those enriched in WT samples were used for pathway analysis, as visualized by volcano plot (Figure 5.10 C). Mass spectrometry-based proteomics revealed a higher number of proteins identified as carbonylated in WT cells than KO cells with RSL3 and AA treatment (1488 versus 1094 unique proteins, respectively and 3423 shared). WT and KO control groups had a similar amount of carbonylated proteins (782 versus 756 unique proteins, respectively). However, WT RSL3+AA and AA groups had more unique carbonylated proteins than KO (1043 and 687 versus 840 and 543, respectively) (Figure 5.11).

Pathway analysis of proteins enriched in WT RSL3+AA treated cells compared to their *ACSL4*-KO counterparts revealed specific enrichment of endoplasmic reticulum and mitochondrial proteins as well as some plasma membrane proteins. The top cellular compartment gene ontology (GO) terms (ranked by smallest p-value) were endoplasmic reticulum membrane, endoplasmic reticulum, membrane, blood microparticle, and mitochondrion (Table 5.3). KEGG pathway analysis revealed similar findings, with protein processing in endoplasmic reticulum as being the most significantly upregulated pathway (Table 5.4, Figure 5.12). The endoplasmic reticulum is the primary site for phospholipid synthesis and has been identified as an important site for lipid peroxidation during ferroptosis (von Krusenstiern et al., 2023b). Cholesterol metabolism was the second most significantly enriched pathway; however, the enriched proteins were not the main proteins along the cholesterol synthesis pathway. Rather, enriched

proteins were lipid transport proteins (NPC1, LRP1, APOH) and mitochondrial membrane proteins (VDAC1, VDAC2, VDAC3, TSPO) (Table 5.4, Figure 5.13).

The mitochondria have been shown to be relevant to ferroptosis, particularly for cysteine-deprivation mediated ferroptosis, due in part to ROS production as a byproduct of naturally occurring oxidative metabolism in the mitochondria (Gao et al., 2019b). The Stockwell lab recently identified the mitochondria as a site for accumulation of highly oxidizable diPUFAs, which we identified as enriched in WT cells relative to KO (Qiu et al., 2024a). VDAC (voltage-dependent anion channel) proteins are expressed on the outer mitochondrial membrane and are responsible for regulating mitochondrial metabolism through controlling transport of metabolites between the cytosol and mitochondria (Colombini, 2012). The opening of VDAC channels has been shown to increase mitochondrial metabolism and consequent ROS production, promoting ferroptosis in cancer cells (DeHart et al., 2018).

Taken together, these findings indicate increased lipid peroxidation in the endoplasmic reticulum and mitochondrial regions in WT cells undergoing RSL3-induced ferroptosis relative to *ACSL4*-KO cells. This finding is in agreement with recent works highlighting the ER and mitochondria as important sites of lipid peroxidation in ferroptosis. It is also consistent with the ferroptosis-resistant phenotype observed in KO cells, as well as the decreased expression of oxidizable PUFAs and their oxidation products in KO cells relative to WT that was described earlier in the chapter.

Discussion:

In this study, we identified that the ferroptosis resistance afforded by *ACSL4* KO is complex and multifaceted. *ACSL4* KO in HT-1080 cells resulted in widespread changes in the cellular lipidome, as well as in the expression of critical lipid metabolic regulatory genes and proteins. First, we confirmed that *ACSL4* KO does reduce sensitivity to ferroptosis induced by RSL3 but does not completely ablate the incorporation of arachidonic acid into major phospholipid classes.

We identified a specific subclass of lipids, called diPUFAs, that were significantly more abundant in WT cells than in *ACSL4*-KO. Recent work by the Stockwell, Kagan, and Bayir labs has highlighted the importance of PC and PE diPUFAs in moderating ferroptosis sensitivity (Qiu et al., 2024b; Samovich et al., 2024). Importantly, the Stockwell lab demonstrated that the ferroptosis-inducing effect of diPUFA treatment could not be recapitulated by adding an equivalent amount of monoPUFA phospholipid species. They hypothesized that the diPUFAs could occupy a specific subcellular location that heightens their propensity to undergo peroxidation, such as near the mitochondria. We identified a number of oxidation products produced from these diPUFAs, including +1O, +3O, and truncation products. Nearly all of the parents and oxidation products that we identified were higher in WT cells than in KO, particularly with exogenous arachidonic acid (AA) and RSL3 treatment. This indicates that the oxidation products we observed were produced during RSL3-induced lipid peroxidation, and, once again, highlights that PC, PE, and PI diPUFAs play an important role in ferroptosis. Importantly, PI diPUFAs have not previously been reported in the context of ferroptosis, so the identification of PI diPUFAs and their oxidation products in this study represents a novel finding that merits further research. In addition, this work highlights the potential of phospholipid remodeling via the Lands cycle to contribute to ferroptosis sensitivity. diPUFAs are synthesized by the remodeling of existing monoPUFA phospholipids, in which the saturated fatty acid located in the SN1 position is cleaved by phospholipase A2 and replaced with a PUFA-CoA. This pathway is activated in response to excess fatty-acyl-CoA substrate. In KO cells, PUFA-CoAs are being generated to a much lesser extent than in WT cells, because ACSL4 is the most efficient enzyme to activate free PUFAs into PUFA-CoAs. We hypothesize that this discrepancy in PUFA-CoA content between WT and KO cells is driving the observed difference in diPUFA content in this study.

In order to characterize the effect of *ACSL4* KO on gene and protein expression, we performed transcriptomics and global proteomics to compare gene and protein expression between WT and ACSL4-KO cells in the context of ferroptosis. We initially hypothesized that we would observe upregulation of other ACSL isoforms to compensate for the loss of ACSL4, since we still observed incorporation of AA

in *ACSL4*-KO cells. Indeed, transcriptomics revealed a significant upregulation of *ACSL1* in *ACSL4*-KO cells relative to their WT counterparts. While each ACSL isoform has a substrate preference, they are promiscuous enzymes and will activate non-preferential fatty acids into fatty acyl-CoAs to some extent (Klett et al., 2017). Transcriptomics also revealed significant changes to various lipid metabolic regulator genes, including *SREBF2* and *PPARγ*. Genes regulated by SREBF2 were consistently downregulated in both WT and KO AA-treated cells relative to control cells. These genes include *DHCR7*, *DCHR24*, and *HMGCR*, which are critical enzymes in the pathway of cholesterol synthesis. Genes regulated by PPARγ were not consistently downregulated; some genes were more expressed in KO than WT, while others were not, even though PPARγ expression was lower in KO than WT AA-treated cells. Genes regulated by PPARγ with relevance to ferroptosis include *APOE* and *HMOX1*, which were both more highly expressed in KO than WT cells. *APOE* has been shown to have a protective effect against ferroptosis in the brain by reducing the quantity of highly oxidizable PUFAs (L. Tang et al., n.d.). The role of *HMOX1* in ferroptosis is less clear; however, it is known to be responsible for the breakdown of heme into free iron, which produces both pro-ferroptotic free iron and anti-ferroptotic antioxidants, including biliverdin. Their increased expression in KO cells relative to WT could contribute to the decreased susceptibility of *ACSL4*-KO cells to undergo RSL3-induced ferroptosis.

Global proteomics analysis revealed further changes to transcriptional regulators dictating cell cycle, gene expression, and cell division. SRSF10, an RNA splicing regulator, was significantly downregulated in KO compared to WT RSL3-treated cells. All of the detected proteins downstream of SRSF10 were consistently downregulated in KO cells as well. We hypothesize that this could be due to lower overall transcription occurring in KO than WT cells, as the WT cells are undergoing death induced by RSL3, they likely upregulate transcription of stress response and survival genes. TP53, a well-known tumor suppressor protein, was upregulated in KO cells relative to WT. The role of TP53 is to control cell division and prevent the division of genetically compromised cells that could lead to cancer in an organism. Importantly, not all of the proteins downstream of TP53 were consistently upregulated in KO

cells, indicating that the role of TP53 in KO RSL3-treated cells may be complex and multifaceted. We also identified an individual lipid metabolic protein in our screening, FABP5, that has been implicated as a ferroptosis biomarker when expressed on the surface of cells (Peng et al., 2024). Interestingly, it was upregulated in KO cells across all treatment groups (Control, RSL3, AA, and RSL3+AA) relative to their WT counterparts. This protein is responsible for the transport of PUFAs and PUFA-containing phospholipids around the cell. We hypothesize that its upregulation in KO cells could be a response to their lack of PUFA-containing phospholipids.

To evaluate if the changes observed in the expression of sterol synthesis genes impacted the downstream levels of sterols in WT and *ACSL4*-KO cells, we performed MS-based targeted sterolomics and found that the total sterol amount, as well as the amount of 7-DHC and its oxidation product, DCHEO, were significantly higher in KO than WT cells, particularly with exogenous AA treatment. We hypothesize that the higher sterol abundance in KO cells could be due to an alternative route of metabolism of exogenous AA. Since it is not efficiently incorporated into phospholipids by the KO cells, its precursor, acetyl Co-A, may be used to synthesize sterols. This could represent another mechanism of ferroptosis protection afforded by *ACSL4* KO, because sterols including cholesterol and 7-DHC have been shown to be protective against ferroptosis (Y. Li et al., 2024; Q. Sun et al., 2023b).

Finally, we performed pulldown proteomics to evaluate differences in protein carbonylation between WT and *ACSL4*-KO cells undergoing ferroptosis. The overall amount of carbonylated proteins was higher in WT than KO cells, as assessed by Western blot. Using quantitative proteomics, we observed significant enrichment in endoplasmic reticulum and mitochondrial proteins in WT treated with RSL3 and AA compared to the corresponding KO cells. This indicates increased levels of lipid peroxidation in these cellular regions in WT cells compared to KO, and is in agreement with recent studies identifying the mitochondria and endoplasmic reticulum as important sites of lipid peroxidation in ferroptosis (Gao et al., 2019b; Qiu et al., 2024a; von Krusenstiern et al., 2023b). Multiple lipid transport proteins were also identified, highlighting the potential role of oxidized lipid trafficking in ferroptosis.

In conclusion, we have shown that *ACSL4*-mediated ferroptosis suppression may depend on multiple mechanisms, including decreased synthesis of highly oxidizable diPUFA species, alterations to lipid metabolic gene and protein expression, increased synthesis of sterols, and reduced protein-lipid adduction. This work demonstrates that the ferroptosis protection induced by *ACSL4* knockout is far more complex than was previously appreciated. It highlights potential new avenues for the therapeutic modulation of ferroptosis, including phospholipid remodeling by the Lands cycle, lipid metabolic and transport genes *APOE, HMOX1*, and *FABP5*, and sterol synthesis, as well as the role of the endoplasmic reticulum and mitochondria as sites for lipid peroxidation. Further work is warranted to continue the exploration of these pathways in the context of ferroptosis.

Figures:

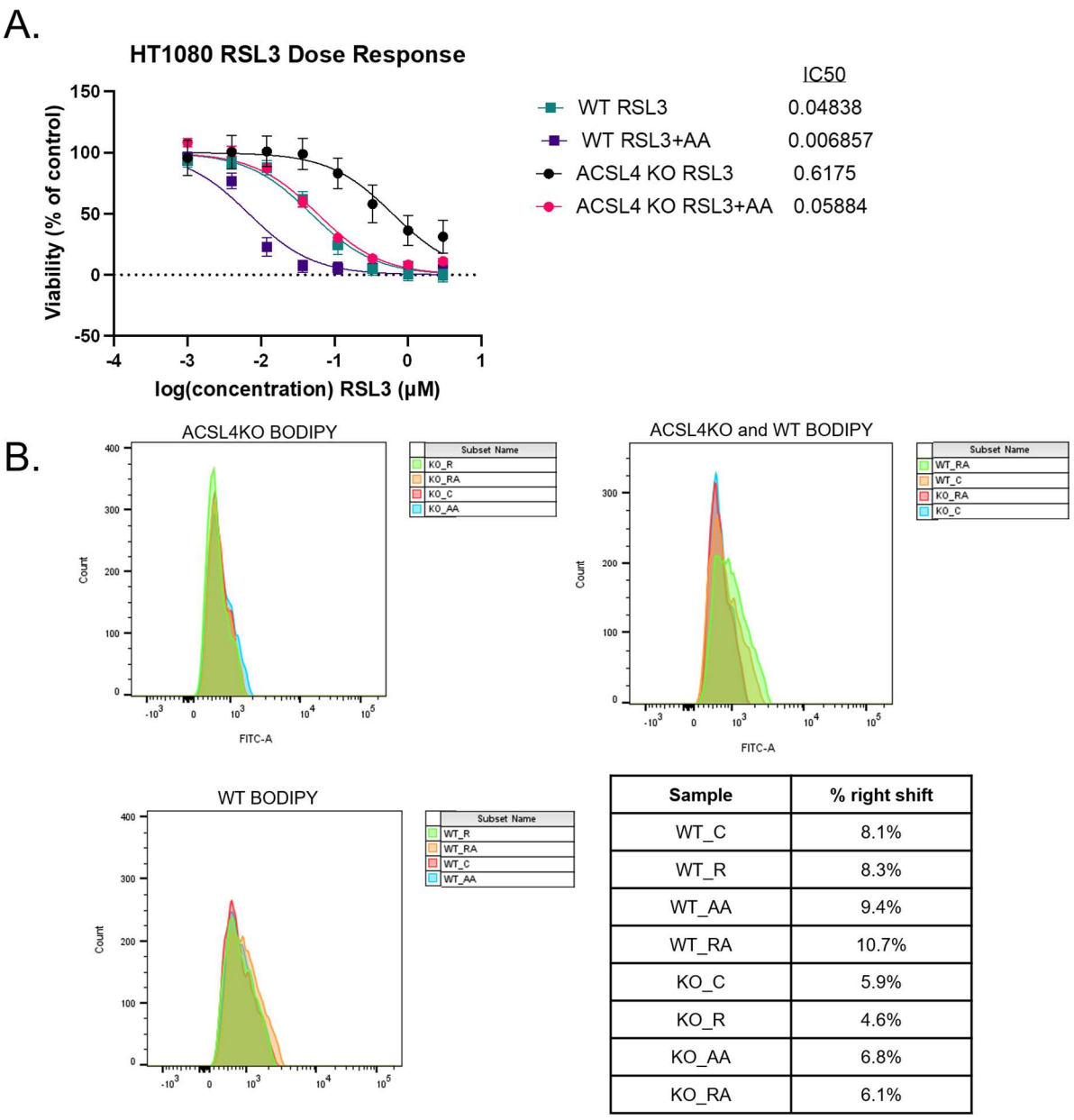

Sample	% right shift
WT_C	8.1%
WT_R	8.3%
WT_AA	9.4%
WT_RA	10.7%
KO_C	5.9%
KO_R	4.6%
KO_AA	6.8%
KO_RA	6.1%

Figure 5.1: ACSL4 knockout confers ferroptosis resistance in HT-1080 cells. A) Dose response curve and IC50 values of WT and ACSL4-KO cells treated with RSL3 with and without exogenous AA. B) Quantification of lipid peroxidation measured by C11 BODIPY and multicolor flow cytometry in ACSL4-KO and WT cells treated with RSL3 (R), RSL3+AA (RA), AA (AA), or DMSO (C). Higher % right shift corresponds to higher lipid peroxidation in cells.

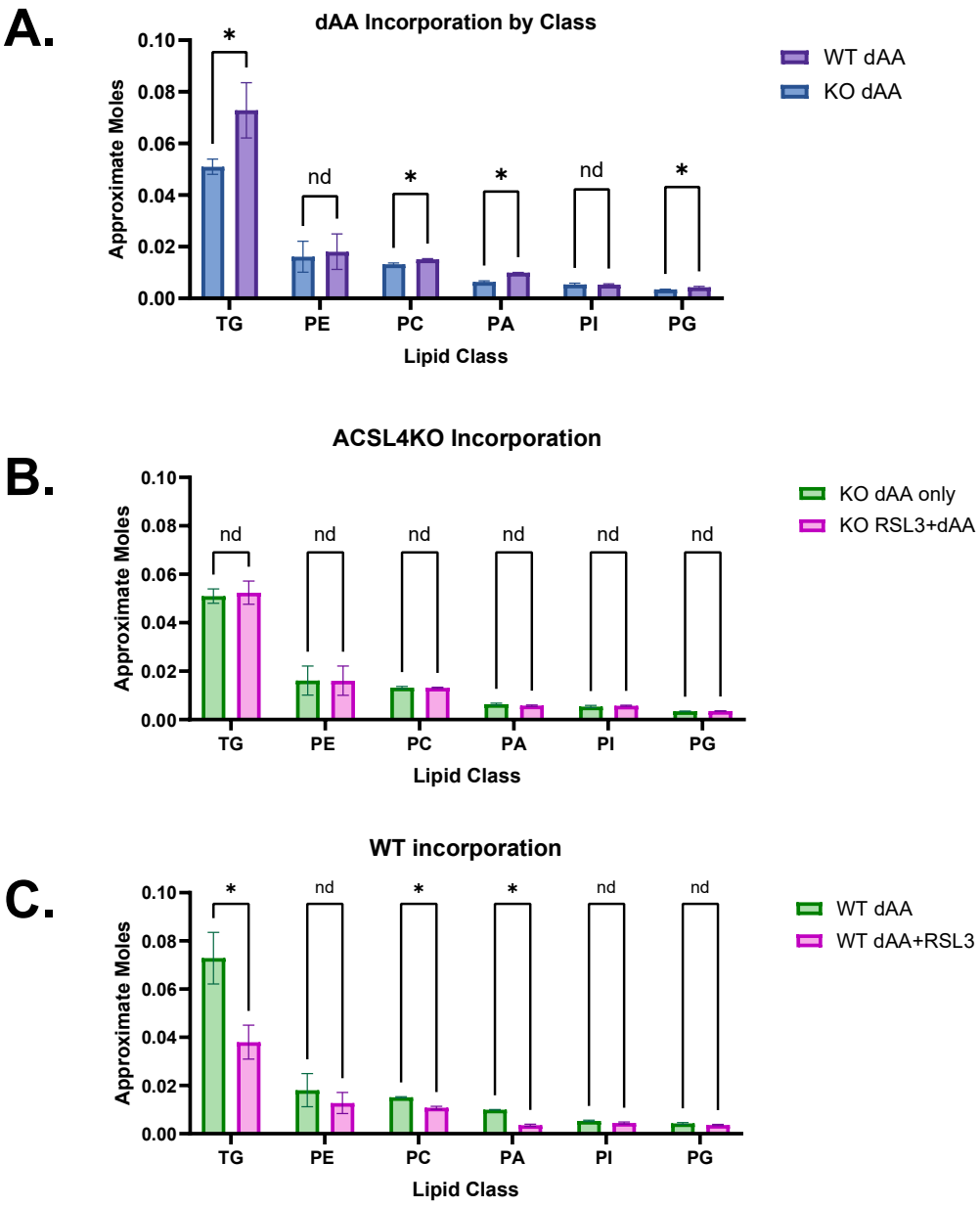

Figure 5.2: Incorporation of dAA into phospholipids in WT and ACSL4-KO cells. A) Approximate moles of dAA-containing phospholipids in WT (purple) and ACSL4-KO (blue) cells. B) Approximate moles of dAA-containing phospholipids in KO dAA-treated (green) and KO dAA+RSL3-treated (pink) cells. C) Approximate moles of dAA-containing phospholipids in WT dAA-treated (green) and WT dAA+RSL3-treated (pink) cells.

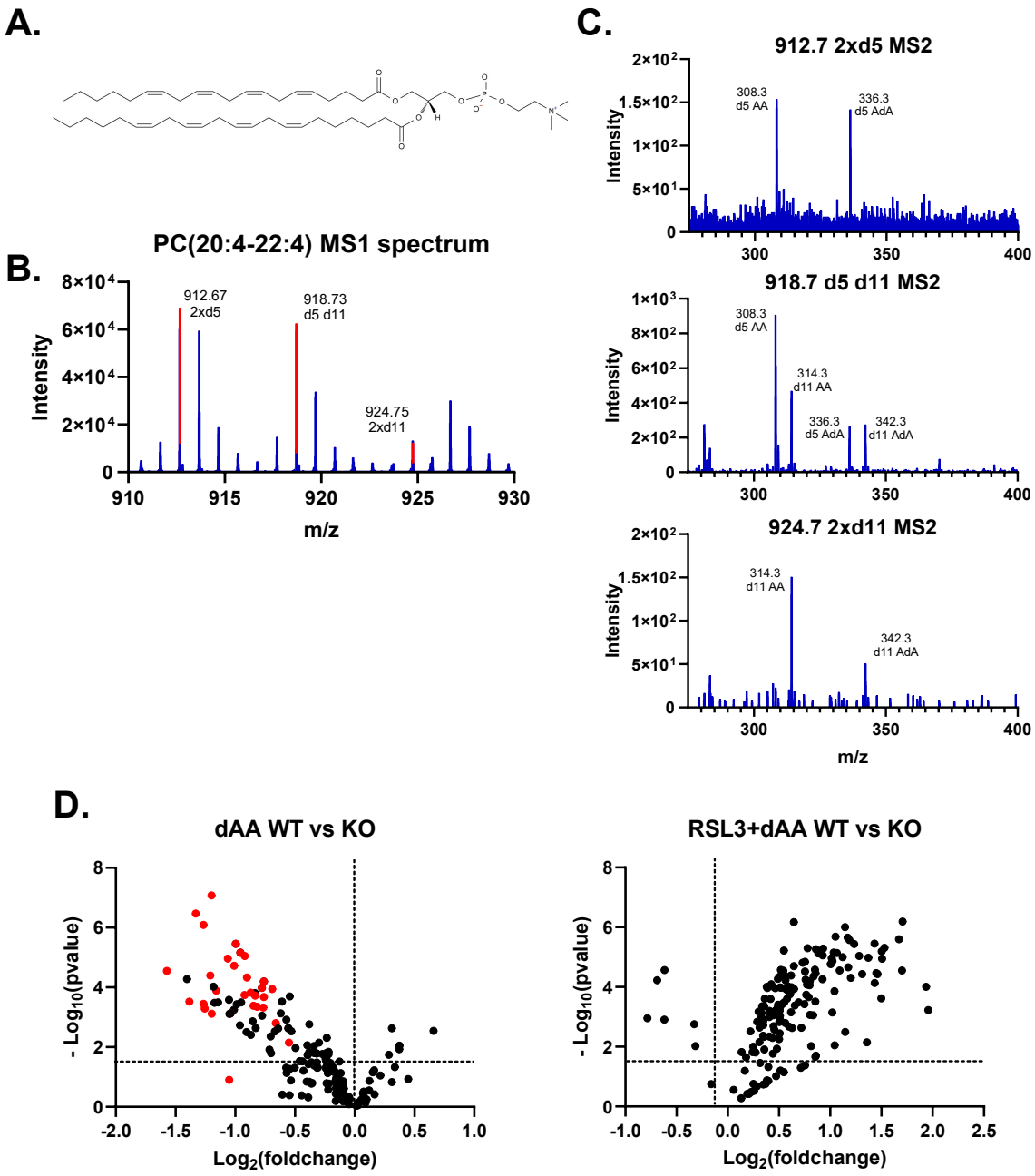

Figure 5.3: Characterization of diPUFA lipid species. A) Structure of diPUFA PC(20:4/22:4) B) Characteristic triplet MS1 spectrum resulting from diPUFA species incorporating d_5 and d_{11} labeled arachidonic acid. C) Targeted fragmentation of each characteristic triplet diPUFA peak showing the incorporation of 2 d_5, 1 d_5 and 1 d_{11}, and 2 d_{11} arachidonoyl fatty acids. D) Volcano plots of differentially expressed lipids between WT and ACSL4 KO cells treated with dAA and RSL3+dAA. Red dots correspond to diPUFAs.

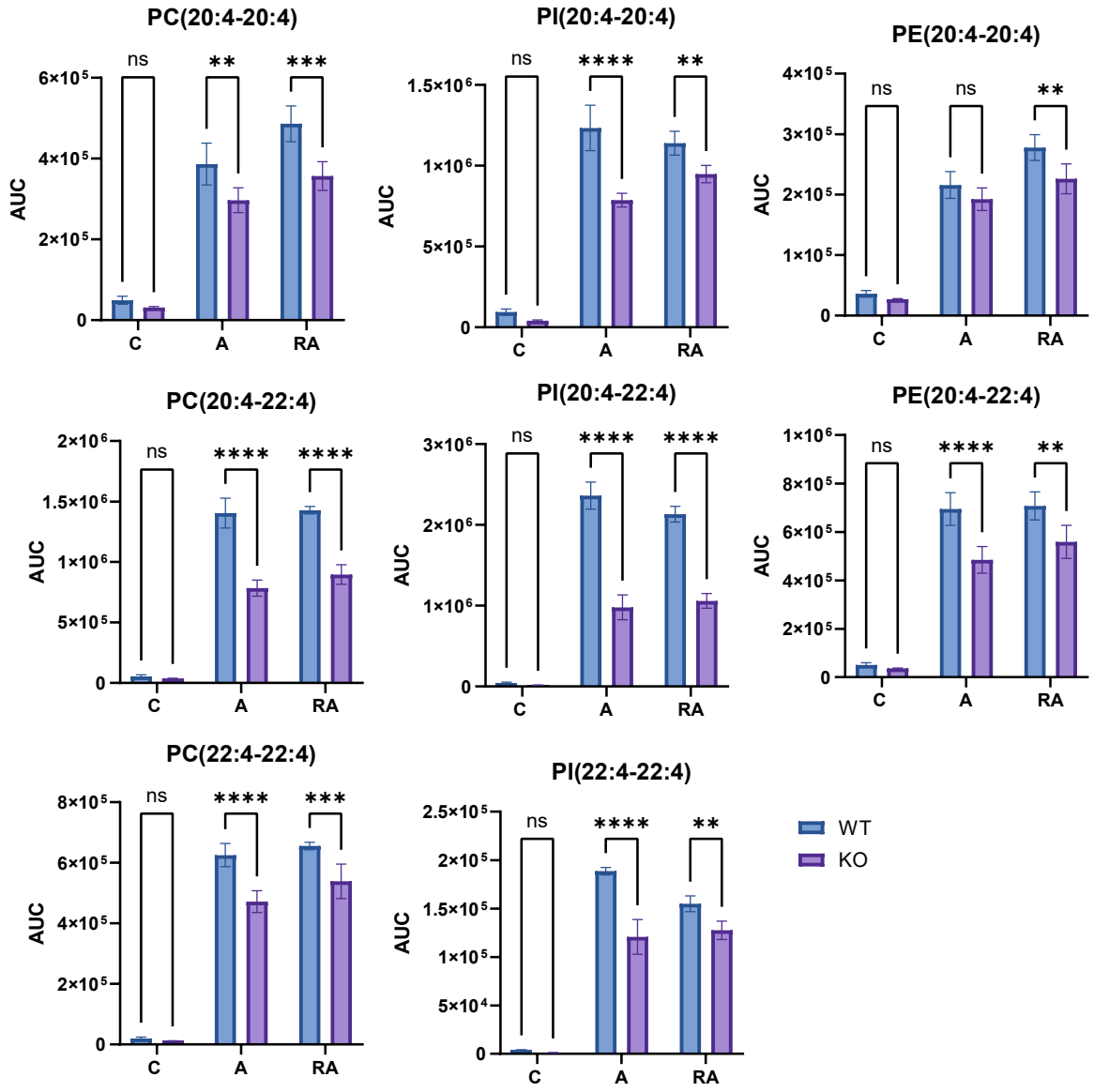

Figure 5.4: Targeted analysis of diPUFA parent species in WT and ACSL4-KO cells. PC: phosphatidylcholine, PI: phosphatidylinositol, PE: phosphatidylethanolamine, C: control, A: arachidonic acid, RA: RSL3 + arachidonic acid. AUC: peak area. WT shown in blue, KO shown in purple. ns: not significant (P>0.05), *: P<0.05, **:P<0.01, ***: P<0.001, ****: P<0.0001. Significance calculated using unpaired AVOVA in GraphPad Prism.

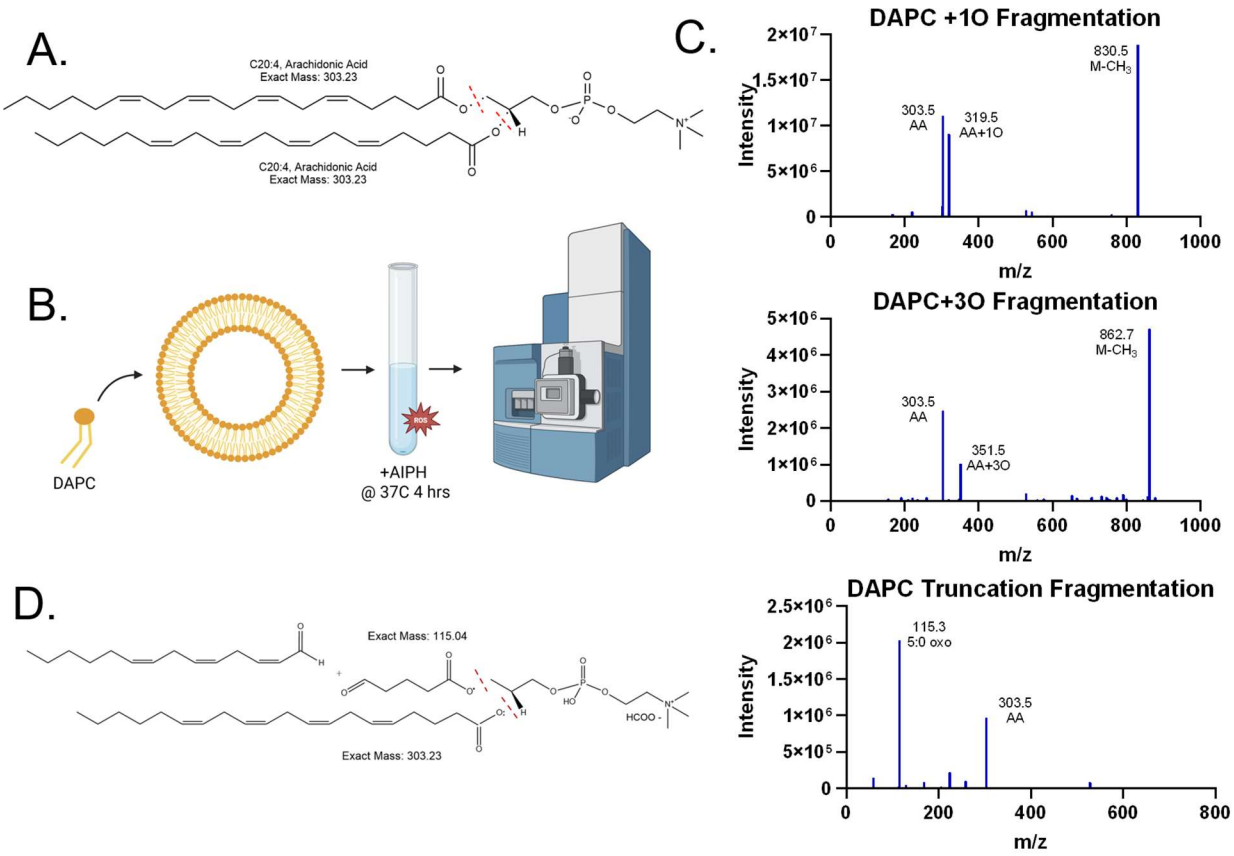

Figure 5.5: Identification of DAPC oxidation products. A) Structure of di-arachidonoyl phosphatidylcholine (DAPC). B) Schematic of in-vitro oxidation of DAPC C) Targeted fragmentation of primary DAPC oxidation products. D) Potential structure of Δ5 truncation product.

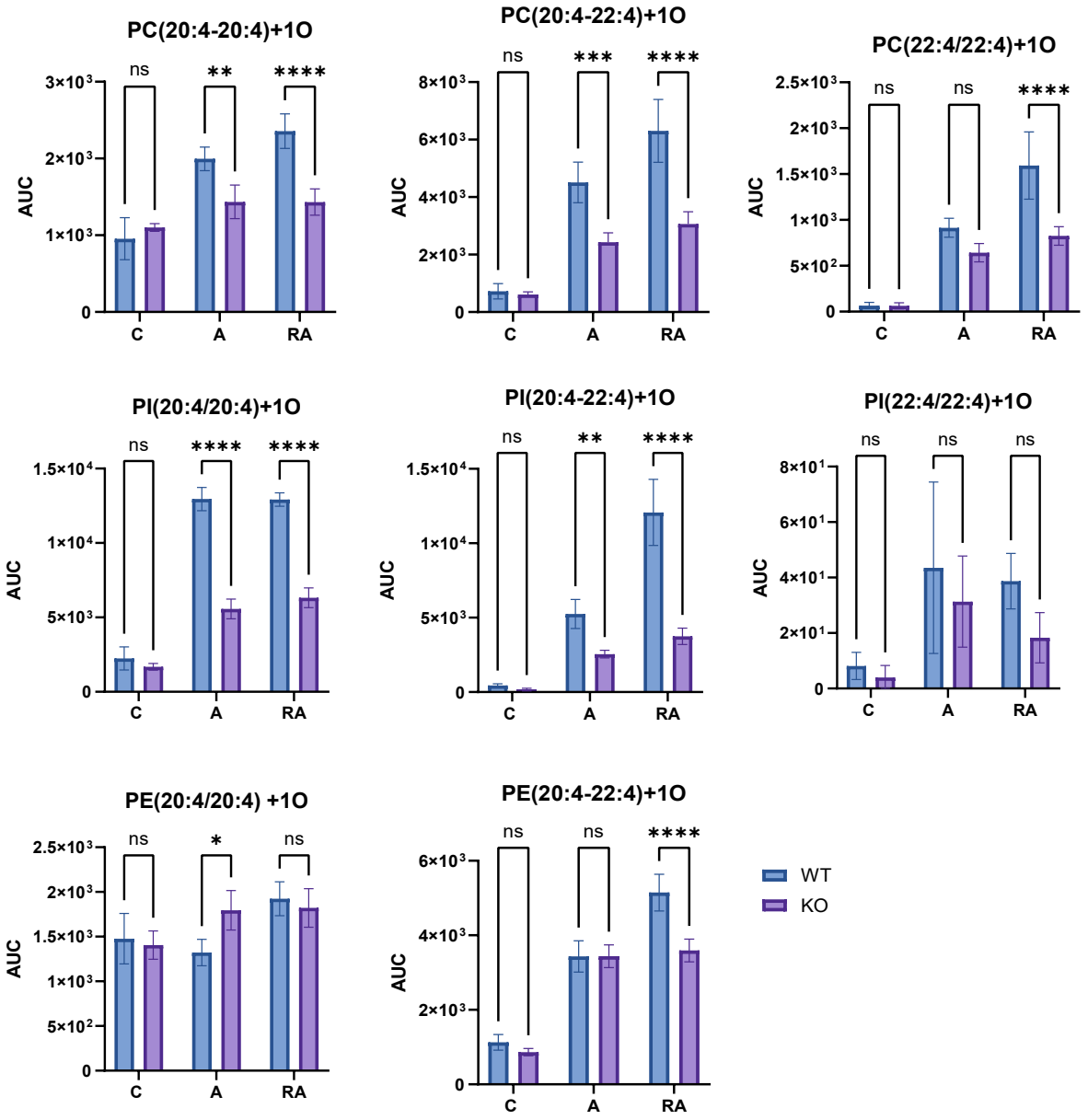

Figure 5.6A: Targeted analysis of +1O diPUFA oxidation products. PC: phosphatidylcholine, PI: phosphatidylinositol, PE: phosphatidylethanolamine, C: control, A: arachidonic acid, RA: RSL3 + arachidonic acid. AUC: peak area. WT shown in blue, KO shown in purple. ns: not significant (P>0.05), *: P<0.05, **:P<0.01, ***: P<0.001, ****: P<0.0001. Significance calculated using unpaired AVOVA in GraphPad Prism.

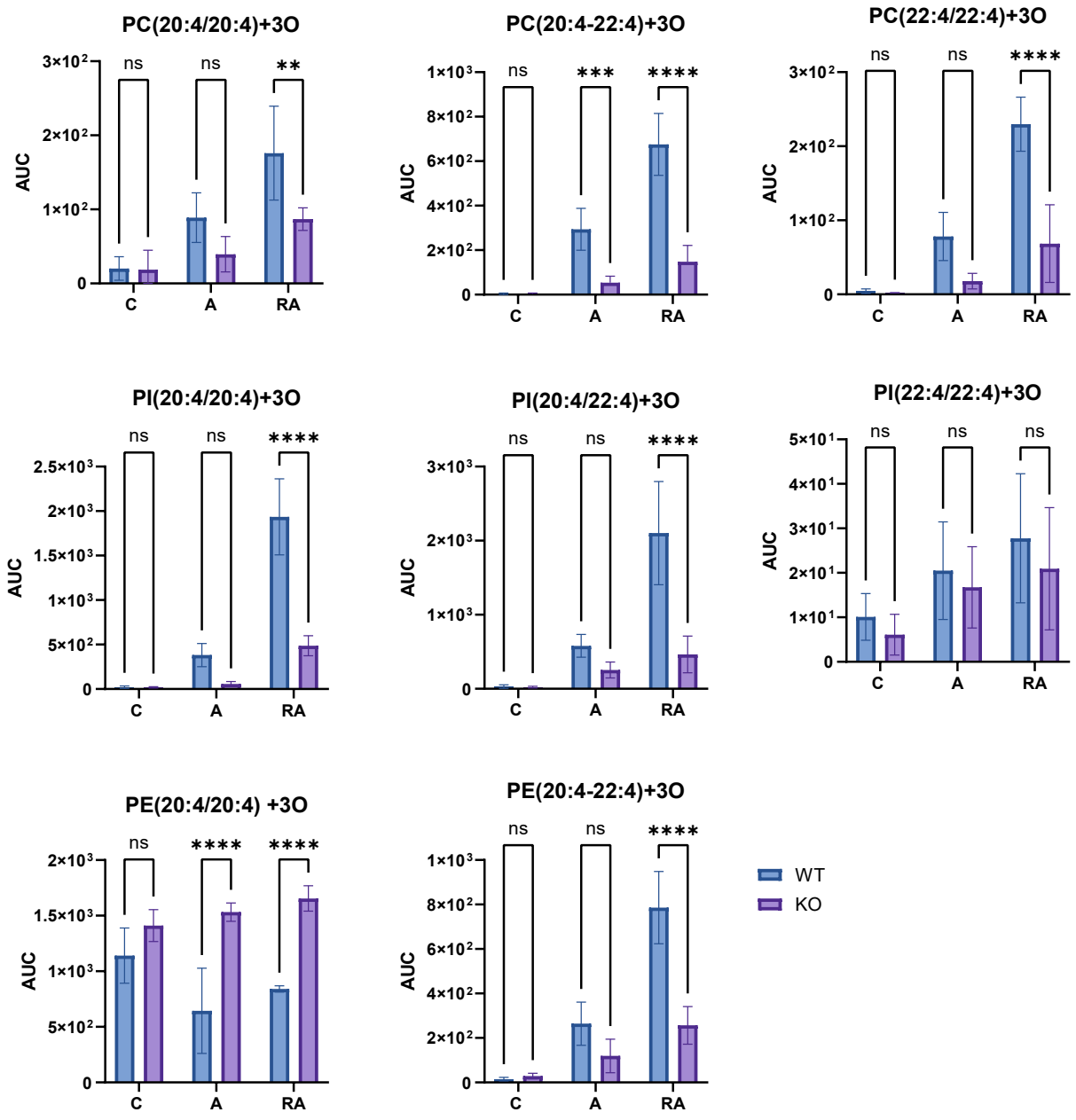

Figure 5.6B: Targeted analysis of +3O diPUFA oxidation products. PC: phosphatidylcholine, PI: phosphatidylinositol, PE: phosphatidylethanolamine, C: control, A: arachidonic acid, RA: RSL3 + arachidonic acid. AUC: peak area. WT shown in blue, KO shown in purple. ns: not significant (P>0.05), *: P<0.05, **:P<0.01, ***: P<0.001, ****: P<0.0001. Significance calculated using unpaired AVOVA in GraphPad Prism.

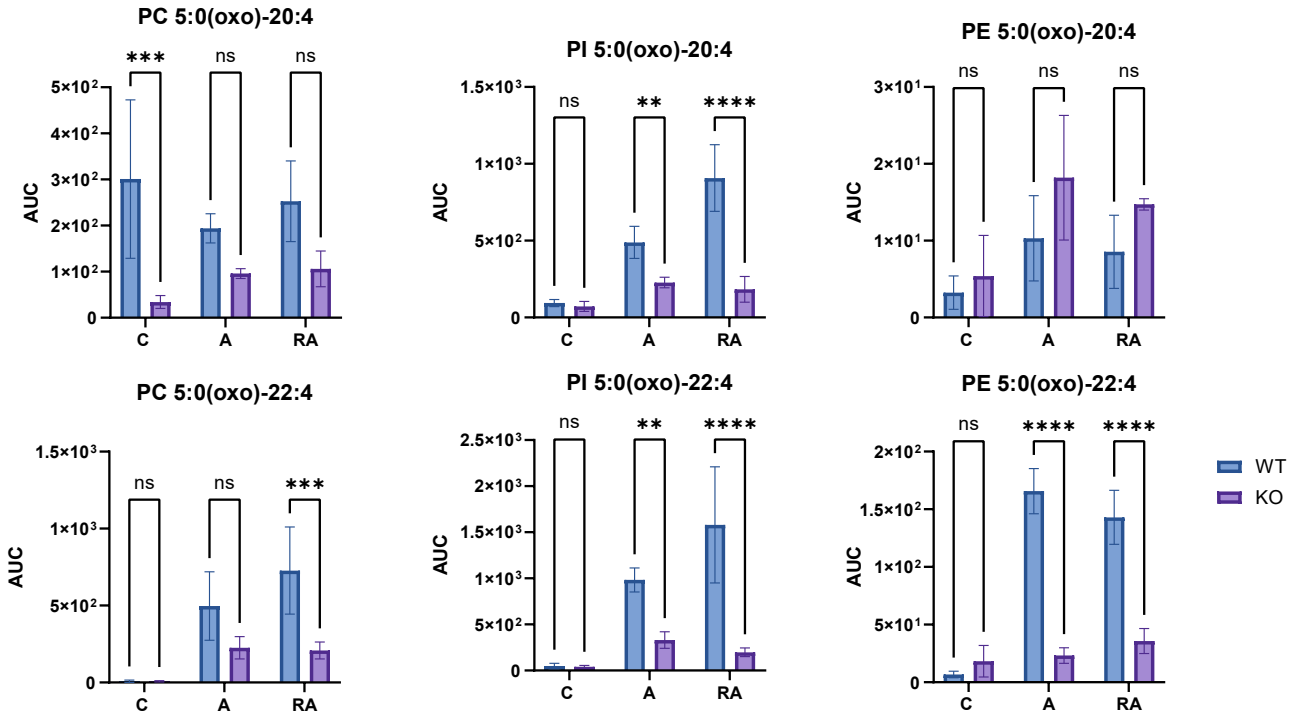

Figure 5.6C: Targeted analysis of truncated diPUFA oxidation products. PC: phosphatidylcholine, PI: phosphatidylinositol, PE: phosphatidylethanolamine, oxo: aldehyde. C: control, A: arachidonic acid, RA: RSL3 + arachidonic acid. AUC: peak area. WT shown in blue, KO shown in purple. ns: not significant (P>0.05), *: P<0.05, **:P<0.01, ***: P<0.001, ****: P<0.0001. Significance calculated using unpaired AVOVA in GraphPad Prism

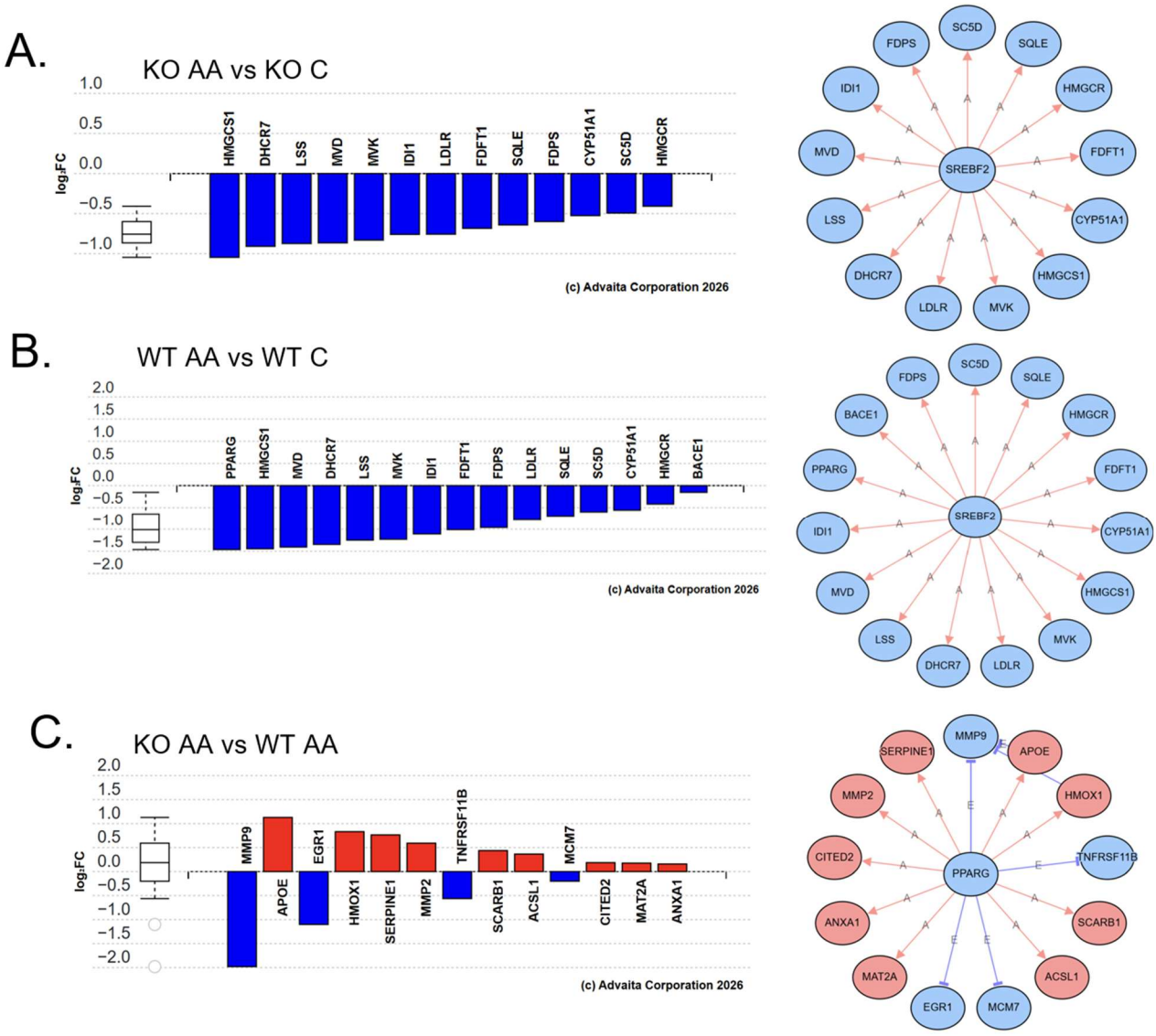

Figure 5.7: Differential expression of lipid metabolic regulator genes between WT and ACSL4-KO cells. A) Expression of genes regulated by SREBF2 in KO AA-treated cells versus KO control cells. B) Expression of genes regulated by SREBF2 in WT AA-treated cells versus WT control cells. C) Expression of genes regulated by PPARγ in KO AA-treated versus WT AA-treated cells. Figures from Advaita iPathway Guide (2026).

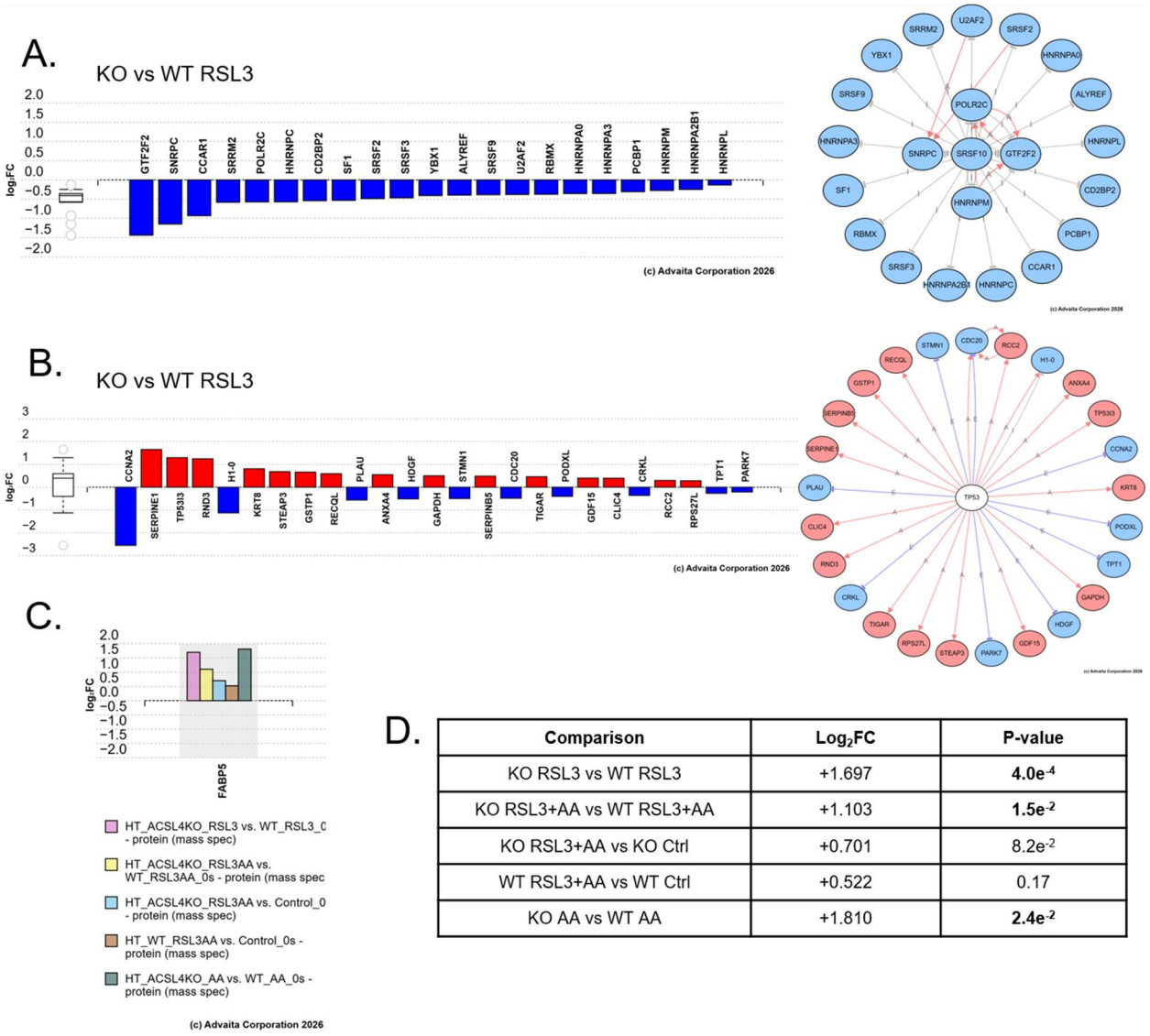

D.

Comparison	Log_2FC	P-value
KO RSL3 vs WT RSL3	+1.697	**$4.0e^{-4}$**
KO RSL3+AA vs WT RSL3+AA	+1.103	**$1.5e^{-2}$**
KO RSL3+AA vs KO Ctrl	+0.701	$8.2e^{-2}$
WT RSL3+AA vs WT Ctrl	+0.522	0.17
KO AA vs WT AA	+1.810	**$2.4e^{-2}$**

Figure 5.8: Differential expression of protein regulators in WT and ACSL4-KO cells. A) Expression of proteins regulated by SRSF10 in KO RSL3-treated cells versus WT RSL3-treated cells. B) Expression of proteins regulated by TP53 in KO RSL3-treated cells versus WT RSL3-treated cells. C) Bar graph showing Log_2(fold change) of FABP5 expression. D) Table showing Log_2(fold change) values and p-values of differential FABP5 expression between treatment groups.

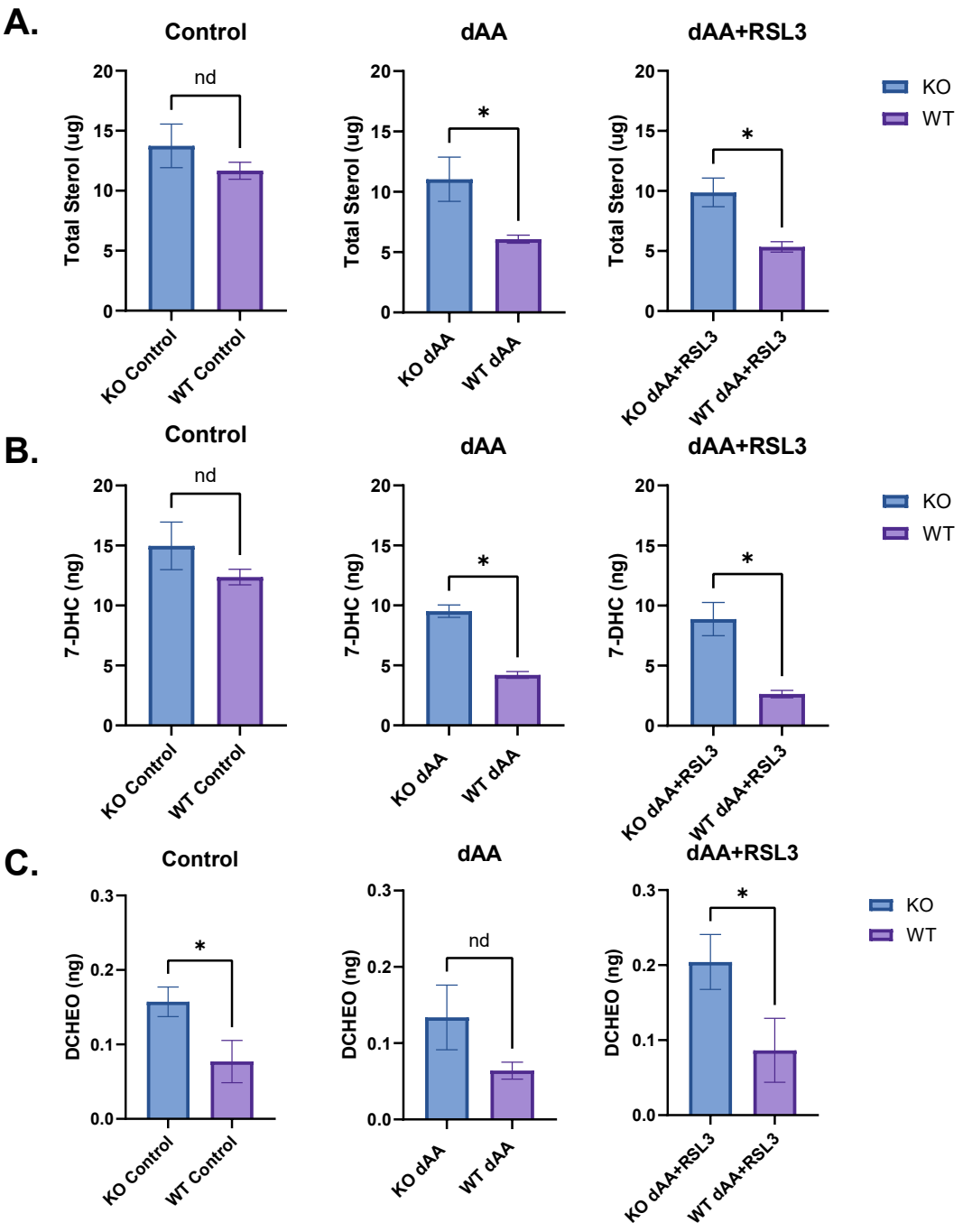

Figure 5.9: Sterolomics analysis of WT and ACSL4-KO cells. A) Total sterol amount in KO (blue) and WT (purple) control, dAA, and dAA+RSL3 treated cells. B) 7-dehydrocholesterol (7-DHC) amount in KO (blue) and WT (purple) control, dAA, and dAA+RSL3 treated cells. C) DHCEO amount in KO (blue) and WT (purple) control, dAA, and dAA+RSL3 treated cells. Significance calculated using students t-test in GraphPad Prism.

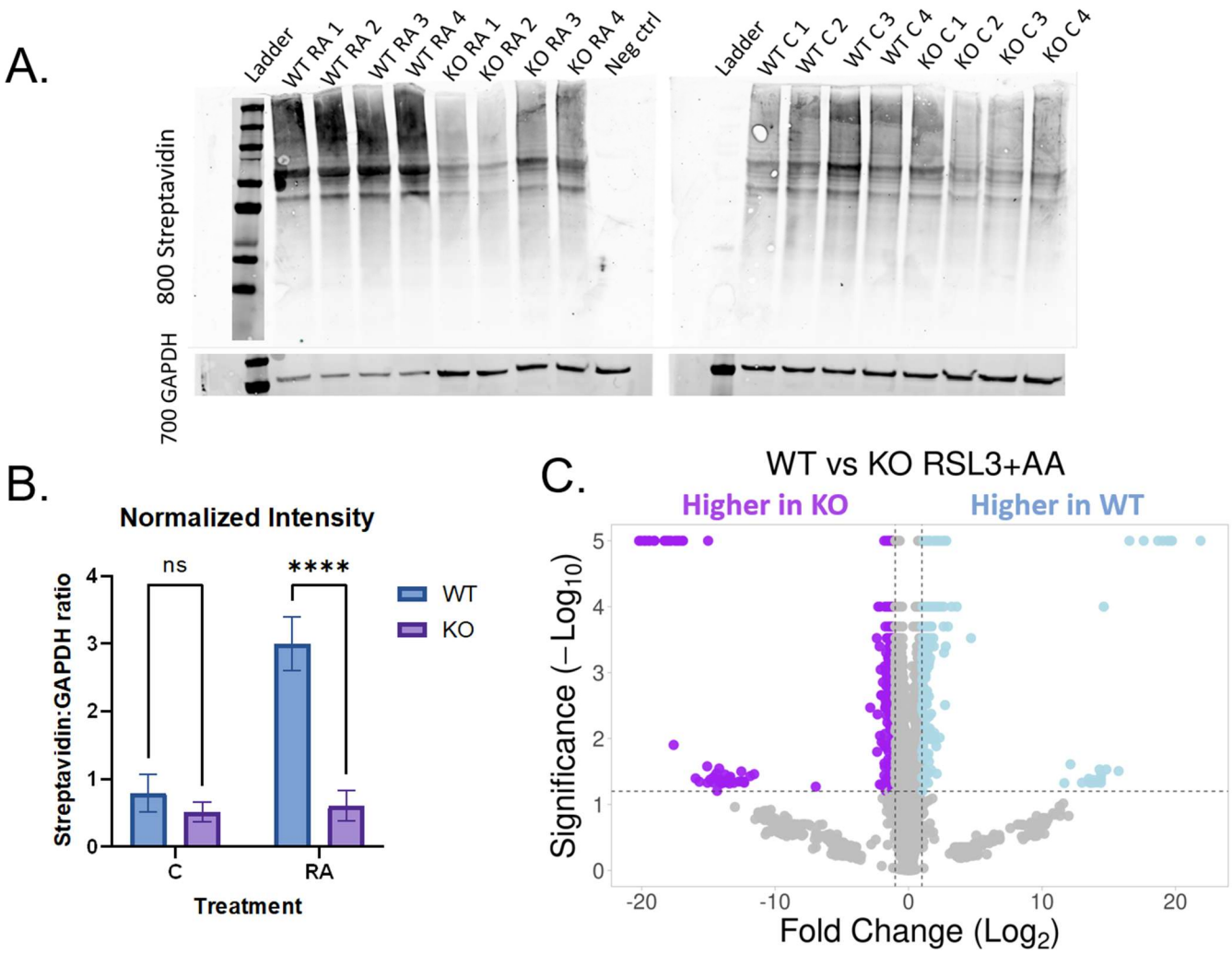

Figure 5.10: Western blot assessment of lipid-adducted proteins in WT and ACSL4-KO cells by protein pulldown. A) Western blot of carbonylated proteins (C: control, RA: RSL3+arachidonic acid, neg: unclicked negative control). B) Quantification of western blot bands using ImageJ. Intensity of streptavidin signal corresponding to carbonylated proteins was normalized to GAPDH as a loading control. C) Volcano plot showing significantly altered carbonylated proteins in WT and KO RA-treated cells using KO as the reference.

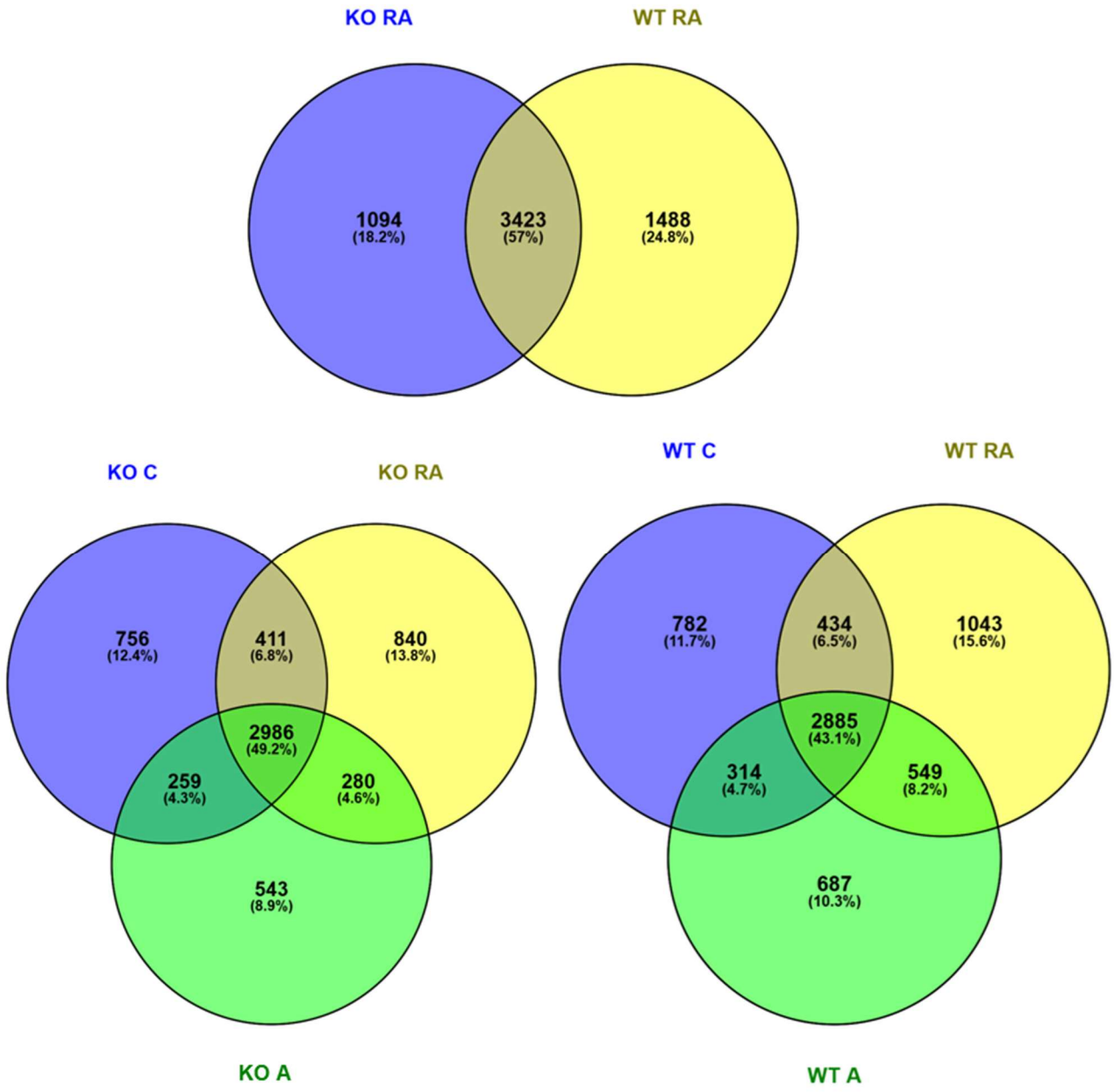

Figure 5.11: Venn diagrams of the identified carbonylated proteins in WT and ACSL4-KO cells. (C: control, A: arachidonic acid, RA: RSL3+arachidonic acid)

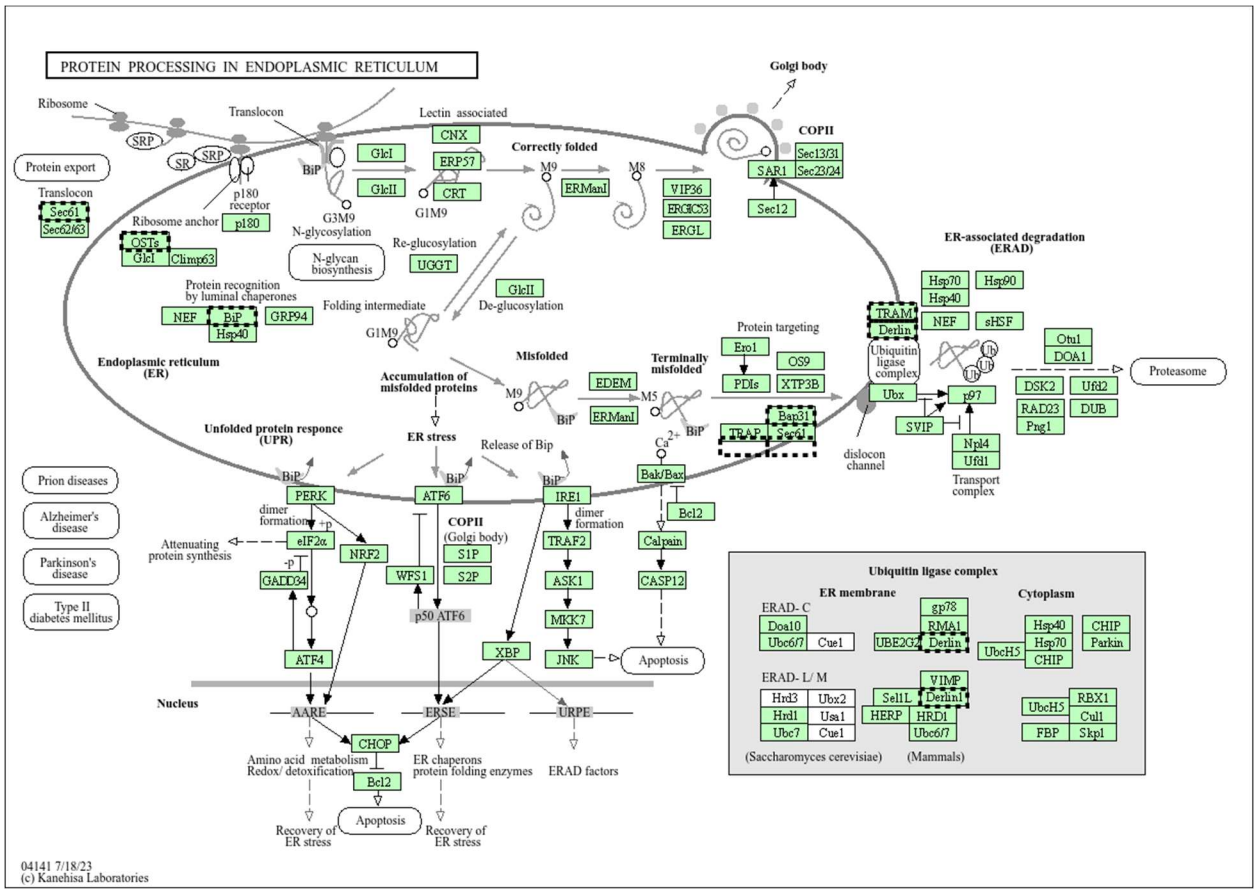

Figure 5.12: KEGG endoplasmic reticulum proteins enriched in WT compared to KO RSL3+AA treated cells. Black boxes around proteins indicate their identification in the dataset. Figure obtained from pathway analysis using DAVID Bioinformatics (NIH).

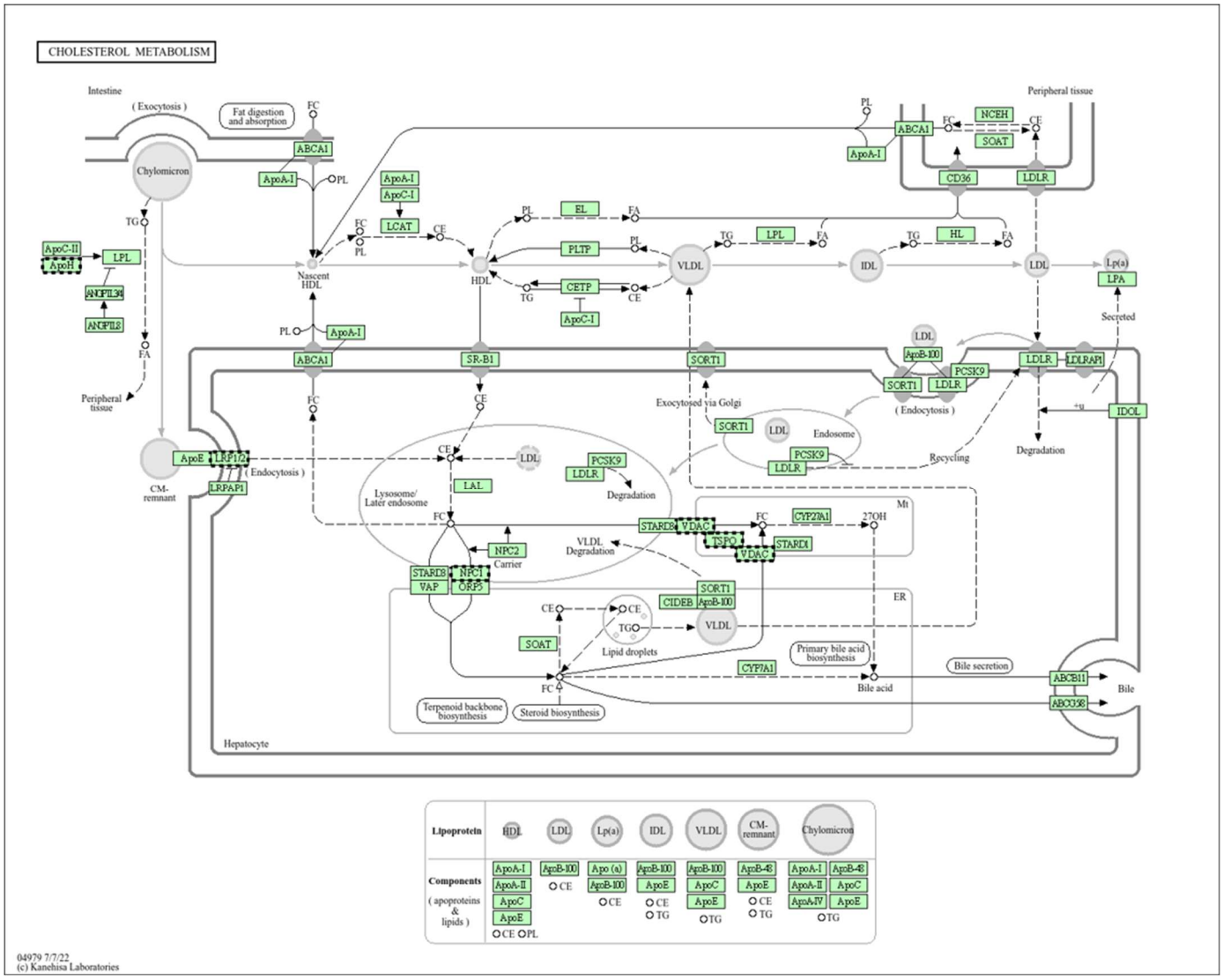

Figure 5.13: KEGG cholesterol metabolism proteins enriched in WT compared to KO RSL3+AA treated cells. Black boxes around proteins indicate their identification in the dataset. Note involvement of VDAC and TSPO proteins in the mitochondrial membrane. Figure obtained from pathway analysis using DAVID Bioinformatics (NIH).

Tables

Table 5.0: DiPUFA MRM MS parameters

Function 1					
Scans in function: 396					
Cycle time (secs): Automatic					
Inter Scan Delay (secs): Automatic					
Inter Channel Delay (secs):Automatic					
Span (Da): 1.000					
Start and End Time(mins): 3.800 to 6.500					
Ionization mode: ES-					
Data type: Enhanced SIR or MRM					
Function type: MRM of 10 channels					
Chan Reaction	Dwell(secs)	Cone Volt.	Col.Energy	Delay(secs)	Compound
1 : 598.24 > 115.33	0.025	Tune	35.0	Auto	PE(20:4/20:4) trunc
2 : 626.27 > 115.33	0.025	Tune	35.0	Auto	PE(20:4/22:4) trunc
3 : 786.51 > 303.24	0.025	Tune	35.0	Auto	PE(20:4/20:4)
4 : 802.51 > 319.50	0.025	Tune	35.0	Auto	PE(20:4/20:4) +1O
5 : 814.54 > 303.24	0.025	Tune	35.0	Auto	PE(20:4/22:4)
6 : 830.54 > 319.50	0.025	Tune	35.0	Auto	PE(20:4/22:4) +1O AA
7 : 830.54 > 347.53	0.025	Tune	35.0	Auto	PE(20:4/22:4) +1O Ad
8 : 834.51 > 351.14	0.025	Tune	35.0	Auto	PE(20:4/20:4) +3O
9 : 862.54 > 351.14	0.025	Tune	35.0	Auto	PE(20:4/22:4) +3O AA
10 : 862.54 > 379.17	0.025	Tune	35.0	Auto	PE(20:4/22:4) +3O Ad
Function 2					
Scans in function: 348					
Cycle time (secs): Automatic					
Inter Scan Delay (secs): Automatic					
Inter Channel Delay (secs):Automatic					
Span (Da): 1.000					
Start and End Time(mins): 5.300 to 8.000					
Ionization mode: ES-					
Data type: Enhanced SIR or MRM					
Function type: MRM of 13 channels					
Chan Reaction	Dwell(secs)	Cone Volt.	Col.Energy	Delay(secs)	Compound
1 : 700.31 > 115.30	0.025	Tune	35.0	Auto	PC(20:4/20:4) trunc
2 : 728.34 > 115.30	0.025	Tune	35.0	Auto	PC(22:4/22:4) trunc
3 : 888.58 > 303.24	0.025	Tune	35.0	Auto	PC(20:4/20:4)
4 : 904.58 > 319.50	0.025	Tune	35.0	Auto	PC(20:4/20:4) +1O
5 : 916.61 > 303.24	0.025	Tune	35.0	Auto	PC(20:4/22:4)

6 : 932.61 > 319.50	0.025	Tune	35.0	Auto	PC(20:4/22:4) +1O AA
7 : 932.61 > 347.53	0.025	Tune	35.0	Auto	PC(20:4/22:4) +1O Ad
8 : 936.58 > 351.14	0.025	Tune	35.0	Auto	PC(20:4/20:4) +3O
9 : 944.64 > 331.27	0.025	Tune	35.0	Auto	PC(22:4/22:4)
10 : 960.64 > 347.53	0.025	Tune	35.0	Auto	PC(22:4/22:4) +1O
11 : 964.61 > 351.14	0.025	Tune	35.0	Auto	PC(20:4/22:4) +3O AA
12 : 964.61 > 379.17	0.025	Tune	35.0	Auto	PC(20:4/22:4) +3O Ad
13 : 992.64 > 351.14	0.025	Tune	35.0	Auto	PC(22:4/22:4) +3O
Function 3					
Scans in function: 336					
Cycle time (secs): Automatic					
Inter Scan Delay (secs): Automatic					
Inter Channel Delay (secs):Automatic					
Span (Da): 1.000					
Start and End Time(mins): 1.800 to 4.000					
Ionization mode: ES-					
Data type: Enhanced SIR or MRM					
Function type: MRM of 13 channels					
Chan Reaction	Dwell(secs)	Cone Volt.	Col.Energy	Delay(secs)	Compound
1 : 717.25 > 115.30	0.025	Tune	35.0	Auto	PI(20:4/20:4) trunc
2 : 745.28 > 115.30	0.025	Tune	35.0	Auto	PI(22:4/22:4) trunc
3 : 905.52 > 303.24	0.025	Tune	35.0	Auto	PI(20:4/20:4)
4 : 921.52 > 319.50	0.025	Tune	35.0	Auto	PI(20:4/20:4) +1O
5 : 933.55 > 303.24	0.025	Tune	35.0	Auto	PI(20:4/22:4)
6 : 949.55 > 319.50	0.025	Tune	35.0	Auto	PI(20:4/22:4) +1O AA
7 : 949.55 > 347.53	0.025	Tune	35.0	Auto	PI(20:4/22:4) +1O Ad
8 : 953.52 > 351.14	0.025	Tune	35.0	Auto	PI(20:4/20:4) +3O
9 : 961.58 > 331.27	0.025	Tune	35.0	Auto	PI(22:4/22:4)
10 : 977.58 > 347.53	0.025	Tune	35.0	Auto	PI(22:4/22:4) +1O
11 : 981.55 > 351.14	0.025	Tune	35.0	Auto	PI(20:4/22:4) +3O AA
12 : 981.55 > 379.17	0.025	Tune	35.0	Auto	PI(20:4/22:4) +3O Ad
13 : 1009.58 > 379.17	0.025	Tune	35.0	Auto	PI(22:4/22:4) +3O

Table 5.1: Differential expression of selected genes of interest from RNA sequencing. adjpv: adjusted p-value, logfc: $\log_2$(fold change). Comparisons are listed as test_vs_control, meaning that the second treatment listed in each comparison is the denominator for fold change calculations. Bolded p-value indicates statistical significance. WT: wild-type HT-1080 cells, KO: ACSL4 HT-1080 cells, AA: arachidonic acid-treated, Ctrl: untreated.

Gene	adjpv WT_AA vs. WT_Ctrl	logfc WT_AA vs. WT_Ctrl	adjpv KO_Ctrl vs. WT_Ctrl	logfc KO_Ctrl vs. WT_Ctrl	adjpv KO_AA vs. WT_AA	logfc KO_AA vs. WT_AA	adjpv KO_AA vs. KO_Ctrl	logfc KO_AA vs. KO_Ctrl
ACSL1	8.38E-01	-0.026	**1.85E-05**	0.379	**1.13E-03**	0.364	8.38E-01	-0.028
ACSL3	**1.00E-06**	-0.707	**1.00E-06**	-0.164	2.59E-01	0.079	**1.00E-06**	-0.451
ACSL4	**3.38E-05**	-0.139	**1.00E-06**	-4.609	**1.00E-06**	-4.508	9.08E-01	-0.018
SREBF1	**1.00E-06**	-1.374	**1.00E-06**	-0.380	2.95E-01	-0.087	**1.00E-06**	-1.075
SREBF2	**1.00E-06**	-0.454	**1.00E-06**	-0.207	**2.52E-03**	-0.194	**1.00E-06**	-0.434
PPARG	**1.00E-06**	-1.463	**1.00E-06**	-5.980	**1.00E-06**	-6.494	nd	nd
PPARA	7.07E-01	0.045	**5.36E-04**	0.329	9.40E-01	0.017	1.94E-01	-0.166
PPARD	4.83E-01	-0.041	**1.00E-06**	0.370	**1.00E-06**	0.477	3.71E-01	0.062
APOE	7.50E-02	-0.133	**2.16E-04**	1.172	**1.38E-02**	1.128	**3.02E-02**	-0.658
HMOX1	**1.00E-06**	1.856	**1.00E-06**	1.444	**1.00E-06**	0.832	1.00E-06	1.246
DHCR24	**1.00E-06**	-0.393	**1.00E-06**	0.163	**1.36E-02**	0.156	**1.00E-06**	-0.390
DHCR7	**1.00E-06**	-1.347	**2.35E-05**	-0.136	**1.00E-06**	0.290	**1.00E-06**	-0.907

HMGCR	**1.00E-06**	-0.419	**3.90E-05**	-0.125	8.28E-02	-0.122	**1.00E-06**	-0.407
FABP5	1.95E-01	0.119	**1.00E-06**	1.177	**1.00E-06**	1.218	2.44E-01	0.136
FADS1	**1.00E-06**	-0.637	**1.00E-06**	0.122	9.88E-02	0.152	**1.00E-06**	-0.582
FADS2	**1.00E-06**	-1.342	**1.00E-06**	0.268	**1.00E-06**	0.662	**1.00E-06**	-0.940
FADS3	**1.00E-06**	0.514	**1.18E-06**	0.286	3.23E-01	0.094	**2.26E-05**	0.311
TP53	**1.00E-06**	-0.475	**1.00E-06**	-0.504	**1.00E-06**	-0.417	**1.00E-06**	-0.384
TP53I11	1.19E-01	-0.149	**1.00E-06**	1.436	**1.00E-06**	2.010	6.15E-01	-0.055
TP53I3	6.38E-02	-0.128	**1.00E-06**	0.576	**1.00E-06**	0.703	9.99E-01	0.000

Table 5.2: Global proteomics differential expression analysis. Comparisons are listed as test vs control, meaning that the second treatment listed in each comparison is the denominator for differential expression calculations.

Treatment comparison	**Number of differentially expressed proteins**
WT RSL3+AA vs WT Control	378
KO RSL3+AA vs KO Control	244
KO RSL3+AA vs WT RSL3+AA	79
KO RSL3 vs WT RSL3	1,159
KO AA vs WT AA	28
KO AA vs KO C	0
WT AA vs WT C	14

Table 5.3: Top ten cellular compartment (CC) GO terms corresponding to carbonylated proteins enriched in WT versus KO RSL3+AA treated cells. Table obtained using DAVID bioinformatics software (NIH). Entries are ranked by p-value.

GO CC term	Count	P-Value	FDR	Protein Ids
endoplasmic reticulum membrane	63	1.64E-26	4.98E-24	POMT2,SCARB2,NOMO3,SLC35B2,MCFD2,TRAM1,PIGT,LPGAT1,GPAA1,ATP2A2,MSMO1,MAGT1,ABHD12,SEC61A1,SPTLC1,SMPD4,SPTLC2,BCAP29,NOMO1,NOMO2,VKORC1,JAGN1,CERS6,ELOVL5,SSR2,SIGMAR1,SSR3,SLC30A1,DDOST,TMEM33,RFT1,ERGIC2,CERS2,AGPAT5,MGST3,EI24,HM13,DERL1,TOR1AIP2,ITPR3,HACD3,ZMPSTE24,PTDSS1,SSR1,HMOX1,SEC11A,MPDU1,ERAP2,HSPA5,GALNT1,MBOAT7,CAV1,SURF4,SLC33A1,ERLIN2,YIF1A,VMP1,SPCS2,STT3A,DEGS1,CLPTM1L,PLP2,STT3B
endoplasmic reticulum	61	5.14E-24	7.81E-22	POMT2,MCFD2,TRAM1,SERPINA1,LPGAT1,GPAA1,ATP2A2,MSMO1,MAGT1,SEC61A1,SPTLC1,SMPD4,SPTLC2,BCAP29,NOMO1,VKORC1,JAGN1,CERS6,ELOVL5,SSR2,SIGMAR1,SSR3,P3H1,CNPY2,SLC30A1,DDOST,RCN3,RCN2,NPC1,TMEM33,ERGIC2,CERS2,AGPAT5,MGST3,EI24,HM13,DERL1,TOR1AIP2,ITPR3,HACD3,HSPA13,VTN,PRDX4,SSR1,HMOX1,MPDU1,AMBP,ERAP2,HSPA5,MBOAT7,CAV1,SURF4,ERLIN2,VMP1,GLUD1,ALB,STT3A,DEGS1,CLPTM1L,PLP2,STT3B
membrane	124	1.01E-19	1.03E-17	SCARB2,NOMO3,SLC35B2,MTCH1,MT-ND5,LPGAT1,NRM,MSMO1,ABHD12,LAPTM4A,HERC1,

				BCAP29,NOMO1,NOMO2,FNDC3B,P3H1,RPSA,SLC30A1,ATP1B1,OXA1L,SPINT1,MYADM,VDAC3,ADAM9,VDAC2,VDAC1,CD151,COX15,MGST3,TOR1AIP2,ITPR3,SLC1A5,AAAS,ZMPSTE24,PTDSS1,SSR1,HMOX1,MDN1,MPDU1,SURF1,CADM1,HSPA5,CAV1,SURF4,SLC33A1,SLC75A1,DNAJC11,LNPEP,STT3A,SFXN3,DEGS1,STT3B,CLPTM1L,MT-CYB,POMT2,ITGB1,SLC25A3,TRAM1,PIGT,GPAA1,SLC2A1,ATP2A2,MAGT1,SEC61A1,SPTLC1,SMPD4,SPTLC2,NNT,C1QBP,FLOT1,TSPO,ME2,CERS6,ANXA3,ELOVL5,ITGA2,SSR2,SIGMAR1,SSR3,HBA1,SLC39A14,DDOST,F5,SLC7A5,SLC7A6,SLC7A7,NPC1,TMEM33,RFT1,NDUFS3,SLC25A10,KIF2C,CD46,SLC29A1,ERGIC2,CERS2,AGPAT5,CD63,TOMM40,LRP1,EI24,LAMA4,HM13,DERL1,DLST,NOL9,SLC3A2,TM9SF4,TMEM165,TM9SF3,SAMM50,RAB24,BPNT2,SEC11A,SLC16A1,F10,CD70,GALNT1,MBOAT7,VMP1,TM9SF2,TM9SF1,SPCS2,PLP2
blood microparticle	15	3.30E-10	2.51E-08	ITIH4,ITIH2,GSN,AMBP,AFM,SLC2A1,HBB,HBD,HBA1,F2,C3,VTN,ALB,GC
mitochondrion	44	2.92E-08	1.78E-06	AGPAT5,MTCH1,SLC25A3,MT-ND4,TOMM40,MT-ND5,COX15,GPAA1,MGST3,MRPL38,DLST,ECSIT,TMEM70,GCSH,SAMM50,PDPR,NNT,C1QBP,RAB24,TSPO,DLAT,ME2,SLC25A22,PAK5,MPDU1,SURF1,HSPA5,APOOL,MCCC1,MTUS1,DNAJC11,COQ7,OXA1L,GLUD1,DNAJA3,NDUFS3,VDAC3,SFXN3,VDAC2,DEGS1,VDAC1,SLC25A10,MT-CYB,DLD

extracellular exosome	50	1.15E-07	5.81E-06	SCARB2,ITGB1,SLC25A3,SERPINA1,SLC2A1,HBB,FLOT1,TSPO,ANXA3,KRT8,P3H1,RPSA,HBA1,ATP1B1,F2,SLC7A5,NPC1,SPINT1,VDAC3,ADAM9,VDAC1,CD46,LTF,CD63,ITIH4,ITIH3,ITIH2,LAMA4,AFM,SLC3A2,SLC1A5,HSPA13,ZMPSTE24,C3,VTN,PRDX4,SAMM50,TTR,APOH,GC,SLC16A1,GSN,AMBP,HSPA5,CD70,HRNR,TM9SF2,KRT18,ALB,VIM
basolateral plasma membrane	15	9.24E-07	4.01E-05	SLC16A1,LRP1,CADM1,CAV1,ERBIN,SLC2A1,SLC30A1,SLC3A2,ATP1B1,SLC39A14,SLC7A5,SLC7A7,FLOT1,ITGA6,SLC29A1
mitochondrial inner membrane	19	6.84E-06	2.60E-04	SLC25A3,SURF1,MT-ND4,TOMM40,MT-ND5,AMBP,APOOL,COX15,MRPL38,ECSIT,COQ7,TMEM70,OXA1L,NNT,NDUFS3,SFXN3,SLC25A10,MT-CYB,SLC25A22
cytoplasmic side of endoplasmic reticulum membrane	6	1.16E-05	3.92E-04	SPTLC1,SPTLC2,HM13,DEGS1,ITPR3,CERS2
endoplasmic reticulum-Golgi intermediate compartment membrane	8	2.45E-05	7.45E-04	VMP1,MCFD2,SERPINA1,GALNT1,SURF4,ERGIC2,YIF1A,F5

Table 5.4: KEGG enriched pathways in carbonylated proteins from WT versus KO RSL3+AA treated cells. Table obtained using DAVID bioinformatics software (NIH). Entries are ranked by p-value.

KEGG Pathway	Count	P-Value	FDR	Protein Ids
Protein processing in endoplasmic reticulum	12	2.62E-05	5.48E-03	SEC61A1,TRAM1,HSPA5,SSR2,SSR3,DERL1,STT3A,BCAP29,SSR1,STT3B,MAGT1,DDOST
Cholesterol metabolism	7	7.32E-05	7.65E-03	NPC1,LRP1,APOH,VDAC3,TSPO,VDAC2,VDAC1
Complement and coagulation cascades	8	2.00E-04	1.39E-02	C3,VTN,SERPINA1,SERPINE2,F10,CD46,F2,F5
Protein export	5	8.07E-04	3.69E-02	SEC61A1,OXA1L,SPCS2,HSPA5,SEC11A
Sphingolipid metabolism	6	9.15E-04	3.69E-02	CERS6,SMPD4,SPTLC1,SPTLC2,DEGS1,CERS2
Metabolic pathways	37	1.06E-03	3.69E-02	POMT2,AGPAT5,MT-ND4,PIGT,MT-ND5,COX15,GPAA1,MGST3,DLST,MSMO1,HACD3,GCSH,PTDSS1,SMPD4,SPTLC1,SPTLC2,NNT,BPNT2,HMOX1,DLAT,VKORC1,GALNT5,CERS6,ELOVL5,GALNT1,MCCC1,SLC33A1,COQ7,DDOST,GLUD1,NDUFS3,STT3A,DEGS1,STT3B,MT-CYB,DLD,CERS2
Lipoic acid metabolism	4	2.10E-03	6.27E-02	GCSH,DLST,DLAT,DLD

Ferroptosis	5	2.56E-03	6.68E-02	VDAC3,VDAC2,HMOX1,SLC3A2,SLC39A14
Focal adhesion	9	6.87E-03	1.52E-01	ITGB1,VTN,LAMA4,ITGA2,CAV1,XIAP,ITGA6,PAK5,PAK4
Diabetic cardiomyopathy	9	7.27E-03	1.52E-01	MT-ND4,MT-ND5,SLC2A1,NDUFS3,VDAC3,ATP2A2,VDAC2,VDAC1,MT-CYB
Parkinson disease	10	1.16E-02	2.17E-01	MT-ND4,MT-ND5,HSPA5,NDUFS3,VDAC3,VDAC2,VDAC1,ITPR3,MT-CYB,SLC39A14
Chemical carcinogenesis - reactive oxygen species	9	1.30E-02	2.17E-01	MT-ND4,MT-ND5,MGST3,NDUFS3,VDAC3,VDAC2,HMOX1,VDAC1,MT-CYB
Prion disease	10	1.35E-02	2.17E-01	MT-ND4,MT-ND5,HSPA5,CAV1,NDUFS3,VDAC3,VDAC2,VDAC1,ITPR3,MT-CYB
Thyroid hormone synthesis	5	1.96E-02	2.92E-01	TTR,HSPA5,ALB,ITPR3,ATP1B1
Carbon metabolism	6	2.18E-02	2.92E-01	GCSH,GLUD1,DLST,ME2,DLAT,DLD

Various types of N-glycan biosynthesis	4	2.24E-02	2.92E-01	STT3A,STT3B,MAGT1,DDOST
Virion - Rotavirus	2	2.73E-02	3.36E-01	ITGB1,ITGA2
Pathways of neurodegeneration - multiple diseases	13	3.24E-02	3.75E-01	MT-ND4,TOMM40,MT-ND5,HSPA5,SIGMAR1,DERL1,ATP2A2,ITPR3,NDUFS3,VDAC3,VDAC2,VDAC1,MT-CYB
ECM-receptor interaction	5	3.41E-02	3.75E-01	ITGB1,VTN,LAMA4,ITGA2,ITGA6
Small cell lung cancer	5	3.91E-02	3.78E-01	ITGB1,LAMA4,ITGA2,XIAP,ITGA6
Proximal tubule bicarbonate reclamation	3	3.94E-02	3.78E-01	GLUD1,SLC25A10,ATP1B1
Alzheimer disease	11	4.11E-02	3.78E-01	MT-ND4,MT-ND5,LRP1,NDUFS3,VDAC3,ATP2A2,VDAC2,VDAC1,ITPR3,MT-CYB,SLC39A14
N-Glycan biosynthesis	4	4.16E-02	3.78E-01	STT3A,STT3B,MAGT1,DDOST
Integrin signaling	6	6.11E-02	5.32E-01	ITGB1,C3,VTN,LAMA4,ITGA2,ITGA6

Citrate cycle (TCA cycle)	3	6.36E-02	5.32E-01	DLST,DLAT,DLD
Amyotrophic lateral sclerosis	10	6.70E-02	5.39E-01	MT-ND4,TOMM40,MT-ND5,HSPA5,SIGMAR1,NDUFS3,DERL1,VDAC1,ITPR3,MT-CYB
2-Oxocarboxylic acid metabolism	3	7.52E-02	5.82E-01	DLST,DLAT,DLD
cGMP-PKG signaling pathway	6	7.88E-02	5.88E-01	VDAC3,ATP2A2,VDAC2,VDAC1,ITPR3,ATP1B1
Platinum drug resistance	4	8.43E-02	6.07E-01	TOP2A,TOP2B,MGST3,XIAP
African trypanosomiasis	3	9.16E-02	6.31E-01	LAMA4,HBB,HBA1
Sphingolipid signaling pathway	5	9.35E-02	6.31E-01	CERS6,SPTLC1,SPTLC2,DEGS1,CERS2

Chapter 6: Summary and Future Directions

It is well known in the field that the regulation of ferroptosis is highly complex and dependent on many factors, including cell type, environment, gene regulation, and lipid composition (Magtanong et al., 2022). This thesis focuses on the lipid metabolism aspect of ferroptosis regulation, and we found that it is also highly complex and multifaceted. We showed that ferroptosis sensitivity is dependent on the type, location, oxidation mechanism, downstream products, and genetic regulation of lipids within a cell. Despite the inherent complexity of these results, the study does highlight some important aspects of lipid metabolism that contribute more to ferroptosis sensitivity than others and merit further investigation.

Chapter 1 introduced the different types of lipids and sterols and discussed their susceptibility to peroxidation, and how this reactivity may dictate their role in ferroptosis. It is known that PUFAs are highly relevant to ferroptosis due to their high propensity to undergo peroxidation, as determined by linoleate radical clock. The ferroptosis-protective effects of MUFAs are also discussed, as well as the enzymes that produce PUFA, MUFA, and SFA containing phospholipids. We highlighted the importance of ACSL4, the enzyme responsible for the incorporation of PUFAs into phospholipids, and reviewed studies showing that *ACSL4*-knockout is protective against ferroptosis in many cell types. We also discussed the recent studies showing the protective effects of some highly oxidizable sterols, particularly 7-DHC, that can act as sacrificial substrates to protect phospholipids from oxidation. Finally, we presented the impetus for this work, which is to further elucidate the role that these lipids and others contribute to ferroptotic death in vitro.

Chapter 2 presented a novel strategy to trace the metabolic fate of arachidonic acid (AA), a PUFA, in cells undergoing ferroptosis. To circumvent the difficulty of differentiating exogenous AAs from endogenous AAs in a global untargeted lipidomics LC-MS dataset, we employed a dual-isotope strategy to improve the robustness of identification of exogenous AAs. When using two different isotope labels, lipids incorporating isotopically labeled lipids will produce a signature doublet peak in the mass

spectra that is easy to discriminate from other lipids in the region of the spectrum. We developed a software, D-Tracer, to automatically pick and identify these isotopically labeled lipids, improving the speed and fidelity of labeled lipid identification. We applied this strategy to a study of HT-1080 fibrosarcoma cells treated with the isotopically labeled AA mixture in the presence and absence of a ferroptosis inducer, RSL3. This study showed that isotopically labeled AA was incorporated into all major lipid classes, with the highest levels of incorporation into triglycerides, which are neutral lipids used primarily for storing excess lipids for later use. Interestingly, we observed that RSL3 treatment resulted in a loss of abundance of these isotopically labeled lipids, suggesting that they could be undergoing oxidation and being exported from the cell during ferroptosis. Triglycerides are stored in lipid droplets within the cell, and later in this work we identify a similar trend in which lipid droplets first appear robustly and then decrease with RSL3 treatment.

Chapter 3 discussed the development and application of an oxidized phospholipid LC-IM-MS database. The identification of oxidized lipids in lipidomic datasets is very challenging due to their low abundance, high reactivity, and lack of high-quality experimental reference data that can be used for identification. To address this shortcoming, we sought to create an oxidized lipid database containing m/z, retention time, CCS, and fragmentation spectra of oxidized lipids. We employed in vitro oxidation of pure phospholipid standards with a radical initiator to produce the lipid oxidation products, and analyzed them via LC-IM-MS. We used the software LPPTiger to generate theoretical spectral libraries for each oxidation product that was possible given the parent lipids included and then used Skyline to match our experimental data with the theoretical spectra to identify the lipid oxidation products. We then exported the experimental library as a .csv that can be re-imported to Skyline as a transition list to search for matches in a diverse range of datasets. Finally, we applied the new database to a lipidomics study of HT-1080 cells treated with conjugated and nonconjugated linoleic acid (CLA and NLA, respectively) in the presence and absence of RSL3. We were able to identify oxidized PE lipids in the CLA, but not the NLA, treated cells, which is consistent with the higher ferroptosis inducing potential of CLA compared to NLA.

Chapter 4 explored the subcellular distribution of lipids and lipid oxidation in cells undergoing ferroptosis using stimulated Raman scattering (SRS) and confocal microscopy. The location of lipid peroxidation in ferroptosis is not fully understood, though recent studies have highlighted the endoplasmic reticulum (ER), mitochondria, and lipid droplets as potential sites. Our study sought not only to identify sites of lipid peroxidation in cells, but also to use SRS spectral shifts to elucidate the mechanism of peroxidation of different types of lipids in cells undergoing ferroptosis. Confocal microscopy showed that lipids accumulated initially in bright perinuclear puncta that we believe to be lipid droplets. These puncta tend to diminish over the course of RSL3 treatment, suggesting again that lipids are being oxidized and exported from the cell during ferroptosis. This is consistent with our findings in Chapter 2 that showed a significant decrease in PUFA-containing triglycerides over the course of RSL3 treatment. We also noted that the signal corresponding to oxidized lipids (using C11-BODIPY as a probe) did not always colocalize with the lipid droplet stain, suggesting that the oxidation could be occurring in another subcellular compartment such as the ER. SRS imaging with terminally labeled deuterated AA revealed that the deuterium signal diminished greatly over the course of RSL3 treatment. However, the trend was significantly less dramatic when using an internally labeled AA isotope, suggesting that oxidation of the fatty acid could result in lipid truncation and consequent loss of the isotope label. We also noted a distinct spectral shift between cells treated with CLA and NLA over the course of RSL3 treatment, which we believe to be due to the different oxidation mechanisms preferred by each of these fatty acids.

Chapter 5 sought to further explore the ferroptosis-protective effect of *ACSL4*-knockout (KO) in HT-1080 cells utilizing a multi-omics approach. First, we employed the dual-isotope tracing strategy presented in Chapter 2 to evaluate the differences in AA incorporation between KO and wild-type (WT) cells with and without RSL3. We observed that KO cells were still able to incorporate AA into all major classes of phospholipids, although to a lesser extent than WT cells. Interestingly, unlike in WT cells where RSL3 treatment results in a reduction in the abundance of AA-containing lipids, the abundance of

AA-containing lipids in KO cells did not decrease in responding to RSL3 treatment. We identified a unique class of lipids, called diPUFAs, which were highly enriched in WT cells relative to KO. DiPUFAs are highly oxidizable phospholipids that contain two polyunsaturated fatty acids and have recently been shown by the Stockwell group to play an important role in mediating ferroptosis susceptibility. We developed a targeted MS method to search for and quantify these diPUFAs and their oxidation products in WT and KO cells, and found PE, PI, and PC diPUFAs and their +1O, +3O, and truncation oxidation products to be significantly higher in WT than KO cells. We hypothesize that the reduction in this class of lipids in KO cells contributes significantly to the observed ferroptosis protective effect of *ACSL4*-knockout.

We also hypothesized that the incorporation of AA in KO cells could be mediated by a different ACSL isoform, so we performed RNA sequencing to examine the expression of genes in WT and KO cells treated with AA and/or RSL3. We observed a significant upregulation of ACSL1 in KO cells, as well as a decrease in expression of sterol synthesis genes. We next performed sterolomics analysis, which revealed that KO cells had a higher abundance of sterols than WT cells. This could represent another ferroptosis-protective mechanism of *ACSL4*-knockout, as it has recently been shown that many sterols are protective against ferroptosis. To corroborate the results of RNA sequencing and examine any post-translational regulation, we next performed global proteomics analysis. Global proteomics revealed changes in expression of various lipid metabolic regulators that have been shown to play a role in ferroptosis, including APOE and HMOX1. We also noted significant upregulation of FABP5 in KO cells, which is a lipid transport protein whose expression on the surface of cells has been proposed as a biomarker for ferroptosis. We believe this upregulation in KO is due to their reduced levels of PUFAs relative to WT, as they could upregulate FABP5 to increase uptake of PUFAs from the environment.

Lastly, we performed pulldown proteomics to assess differences in protein lipid carbonylation between WT and KO cells undergoing ferroptosis. Protein lipid carbonylation occurs when lipid peroxidation-derived electrophilic aldehydes, such as 4-HNE and malondialdehyde, react with

nucleophilic sites on protein residues. The resulting adduction of proteins can result in protein dysfunction and may contribute to ferroptotic cell death. We observed a greater abundance of carbonylated proteins in WT cells, which was expected given the higher abundance of lipid oxidation products and ferroptosis sensitivity in WT compared to KO cells. Notably, pathway analysis revealed significant upregulation of adducted proteins in the ER and mitochondria in WT cells compared to KO. This suggests that peroxidation is likely enriched in these organelles in WT cells. This finding is consistent with recent studies highlighting the importance of the ER and mitochondria as sites for lipid peroxidation during ferroptosis (Gao et al., 2019b; Qiu et al., 2024b; von Krusenstiern et al., 2023b).

This study led to several important results and findings. First, a method was developed to trace the metabolism of PUFAs in vitro using LC-MS, including a software program to facilitate robust data analysis practices. An LC-IM-MS database was also developed to enable the identification of oxidized phospholipids in lipidomics MS datasets. These methods were applied to trace the metabolism of various PUFAs and showed that the abundance of PUFAs decreases as cells undergo ferroptosis, as well as identifying several oxidation products that are produced during RSL3 treatment. We hope these methods can be applied by other research groups to study different contexts of lipid metabolism and oxidation. In addition, using imaging techniques, we identified that exogenous fatty acids initially accumulate in lipid droplets, but these droplets diminish over the course of RSL3 treatment. We also observed that lipid oxidation may not be occurring in these droplets, but rather in a different organelle, such as the ER, in the perinuclear region of cells. SRS imaging was able to detect subtle differences in lipid peroxidation mechanisms in cells, including spectral differences between conjugated and nonconjugated fatty acids and the formation of truncation products during lipid oxidation. Lastly, we showed that the ferroptosis-protective effect afforded by *ACSL4*-knockout is dependent on many factors. While less PUFAs are incorporated into phospholipids in KO cells, there was a striking difference in the abundance of diPUFAs and their oxidation products between WT and KO cells. These diPUFAs are formed through the Lands cycle of phospholipid remodeling, and this study highlights the potential of the Lands cycle as a target for

mediating ferroptosis in cells. In addition, we observed widespread changes to gene and protein expression between WT and KO cells, including lipid metabolic genes ACSL1, SREBF2, APOE, and FABP5, suggesting that *ACSL4*-KO produces widespread changes to the lipid metabolic state of cells. We also observed increased protein lipid carbonylation in WT cells relative to KO, particularly in the ER and mitochondria regions. This finding shows that there is likely more lipid peroxidation occurring in the ER and mitochondria of WT cells as they undergo ferroptosis

To summarize, we have shown that the role of lipid metabolism in ferroptosis is a crucial aspect of this form of cell death. It depends on many factors, including the type of fatty acids incorporated into main phospholipid classes, the location of these phospholipids in cells, the transcriptome and proteome changes of the cells, as well as the mechanisms of lipid peroxidation. Future directions of this study will involve further exploration of the epilipidome using the LC-MS tools developed, as well as continued exploration of the role of lipid droplets, the ER, and the mitochondria in ferroptotic regulation. In addition, it is important to note that this study used only one cell type, HT-1080, for all experiments. The results identified in this study should be verified using other ferroptosis-susceptible cell types. The observation of the importance of diPUFAs in ferroptosis warrants further exploration, in particular the Lands cycle, which produces these diPUFAs, should certainly be further explored in the context of ferroptosis. In addition, the methods used to analyze oxidized lipids in this thesis are likely to only capture a subset of all possible oxidized lipids within a cell. These methods should be expanded to include a broader range of oxidized lipids, including those that may be adducted to glutathione or other thiol moieties and those that may be too reactive to capture using the methods outlined here, including peroxides, epoxides, and cross-linked fatty acids. Moreover, it appears that lipid transport and shuttling around the cell is an important aspect of ferroptotic death; while lipids initially accumulate in lipid droplets, they appear to be oxidized in other subcellular compartments such as the ER and mitochondria, and then the oxidation reaction spreads to the outer membrane, eventually leading to cell death. Further study of the mechanisms behind this shuttle of oxidized lipids is warranted. Although the regulation of

this type of cell death is proving to be increasingly complex, every new discovery and observation is a step closer to understanding ferroptosis and being able to harness its significant therapeutic potential. I look forward to the continued advancement in this field and am grateful to have been able to contribute to the growing body of research regarding ferroptosis.

References

Abdelmagid, S. A., Clarke, S. E., Nielsen, D. E., Badawi, A., El-Sohemy, A., Mutch, D. M., & Ma, D. W. L. (2015). Comprehensive Profiling of Plasma Fatty Acid Concentrations in Young Healthy Canadian Adults. *PLOS ONE*, *10*(2), e0116195. https://doi.org/10.1371/journal.pone.0116195

Acosta, M. J., Vazquez Fonseca, L., Desbats, M. A., Cerqua, C., Zordan, R., Trevisson, E., & Salviati, L. (2016). Coenzyme Q biosynthesis in health and disease. *Biochimica et Biophysica Acta (BBA) - Bioenergetics, EBEC 2016: 19th European Bioenergetics Conference*, *1857*(8), 1079–1085. https://doi.org/10.1016/j.bbabio.2016.03.036

Adibhatla, R. M., & Hatcher, J. F. (2008). Altered Lipid Metabolism in Brain Injury and Disorders. In P. J. Quinn & X. Wang (Eds.), *Lipids in Health and Disease* (pp. 241–268). Springer Netherlands. https://doi.org/10.1007/978-1-4020-8831-5_9

Adusumilli, R., & Mallick, P. (2017). Data Conversion with ProteoWizard msConvert. In L. Comai, J. E. Katz, & P. Mallick (Eds.), *Proteomics: Methods and Protocols* (pp. 339–368). Springer. https://doi.org/10.1007/978-1-4939-6747-6_23

Arroyo, A., Navarro, F., Navas, P., & Villalba, J. M. (1998). Ubiquinol regeneration by plasma membrane ubiquinone reductase. *Protoplasma*, *205*(1), 107–113. https://doi.org/10.1007/BF01279300

Ayala, A., Muñoz, M. F., & Argüelles, S. (2014). Lipid Peroxidation: Production, Metabolism, and Signaling Mechanisms of Malondialdehyde and 4-Hydroxy-2-Nonenal. *Oxidative Medicine and Cellular Longevity*, *2014*, 360438. https://doi.org/10.1155/2014/360438

Bacellar, I. O. L., Oliveira, M. C., Dantas, L. S., Costa, E. B., Junqueira, H. C., Martins, W. K., Durantini, A. M., Cosa, G., Di Mascio, P., Wainwright, M., Miotto, R., Cordeiro, R. M., Miyamoto, S., & Baptista, M. S. (2018). Photosensitized Membrane Permeabilization Requires Contact-Dependent Reactions between Photosensitizer and Lipids. *Journal of the American Chemical Society*, *140*(30), 9606–9615. https://doi.org/10.1021/jacs.8b05014

Bai, Y., Meng, L., Han, L., Jia, Y., Zhao, Y., Gao, H., Kang, R., Wang, X., Tang, D., & Dai, E. (2019). Lipid storage and lipophagy regulates ferroptosis. *Biochemical and Biophysical Research Communications*, *508*(4), 997–1003. https://doi.org/10.1016/j.bbrc.2018.12.039

Beatty, A., Singh, T., Tyurina, Y. Y., Tyurin, V. A., Samovich, S., Nicolas, E., Maslar, K., Zhou, Y., Cai, K. Q., Tan, Y., Doll, S., Conrad, M., Subramanian, A., Bayır, H., Kagan, V. E., Rennefahrt, U., & Peterson, J. R. (2021). Ferroptotic cell death triggered by conjugated linolenic acids is mediated by ACSL1. *Nature Communications*, *12*(1), 2244. https://doi.org/10.1038/s41467-021-22471-y

Belaidi, A. A., Masaldan, S., Southon, A., Kalinowski, P., Acevedo, K., Appukuttan, A. T., Portbury, S., Lei, P., Agarwal, P., Leurgans, S. E., Schneider, J., Conrad, M., Bush, A. I., & Ayton, S. (2024). Apolipoprotein E potently inhibits ferroptosis by blocking ferritinophagy. *Molecular Psychiatry*, *29*(2), 211–220. https://doi.org/10.1038/s41380-022-01568-w

Bell, R. M., Ballas, L. M., & Coleman, R. A. (1981). Lipid topogenesis. *Journal of Lipid Research*, *22*(3), 391–403.

Bentinger, M., Brismar, K., & Dallner, G. (2007). The antioxidant role of coenzyme Q. *Mitochondrion, The Role of Coenzyme Q in Cellular Metabolism: Current Biological and Clinical Aspects*, *7*, S41–S50. https://doi.org/10.1016/j.mito.2007.02.006

Bersuker, K., Hendricks, J. M., Li, Z., Magtanong, L., Ford, B., Tang, P. H., Roberts, M. A., Tong, B., Maimone, T. J., Zoncu, R., Bassik, M. C., Nomura, D. K., Dixon, S. J., & Olzmann, J. A. (2019). The CoQ oxidoreductase FSP1 acts parallel to GPX4 to inhibit ferroptosis. *Nature*, *575*(7784), Article 7784. https://doi.org/10.1038/s41586-019-1705-2

Birge, R. B., Boeltz, S., Kumar, S., Carlson, J., Wanderley, J., Calianese, D., Barcinski, M., Brekken, R. A., Huang, X., Hutchins, J. T., Freimark, B., Empig, C., Mercer, J., Schroit, A. J., Schett, G., & Herrmann, M. (2016). Phosphatidylserine is a global immunosuppressive signal in efferocytosis, infectious disease, and cancer. *Cell Death & Differentiation*, *23*(6), 962–978. https://doi.org/10.1038/cdd.2016.11

Blanksby, S. J., & Mitchell, T. W. (2010). Advances in Mass Spectrometry for Lipidomics. *Annual Review of Analytical Chemistry*, *3*(1), 433–465. https://doi.org/10.1146/annurev.anchem.111808.073705

Burton, G. W., Doba, T., Gabe, E., Hughes, L., Lee, F. L., Prasad, L., & Ingold, K. U. (1985). Autoxidation of biological molecules. 4. Maximizing the antioxidant activity of phenols. *Journal of the American Chemical Society*, *107*(24), 7053–7065. https://doi.org/10.1021/ja00310a049

Chen, X., Kang, R., Kroemer, G., & Tang, D. (2021). Organelle-specific regulation of ferroptosis. *Cell Death & Differentiation*, *28*(10), 2843–2856. https://doi.org/10.1038/s41418-021-00859-z

Chen, Y., Liu, Y., Lan, T., Qin, W., Zhu, Y., Qin, K., Gao, J., Wang, H., Hou, X., Chen, N., Friedmann Angeli, J. P., Conrad, M., & Wang, C. (2018a). Quantitative Profiling of Protein Carbonylations in Ferroptosis by an Aniline-Derived Probe. *Journal of the American Chemical Society*, *140*(13), 4712–4720. https://doi.org/10.1021/jacs.8b01462

Chen, Y., Liu, Y., Lan, T., Qin, W., Zhu, Y., Qin, K., Gao, J., Wang, H., Hou, X., Chen, N., Friedmann Angeli, J. P., Conrad, M., & Wang, C. (2018b). Quantitative Profiling of Protein Carbonylations in Ferroptosis by an Aniline-Derived Probe. *Journal of the American Chemical Society*, *140*(13), 4712–4720. https://doi.org/10.1021/jacs.8b01462

Cockcroft, S. (2021). Mammalian lipids: Structure, synthesis and function. *Essays in Biochemistry*, *65*(5), 813–845. https://doi.org/10.1042/EBC20200067

Colombini, M. (2012). VDAC Structure, Selectivity, and Dynamics. *Biochimica et Biophysica Acta*, *1818*(6), 1457–1465. https://doi.org/10.1016/j.bbamem.2011.12.026

Conrad, M., Angeli, J. P. F., Vandenabeele, P., & Stockwell, B. R. (2016). Regulated necrosis: Disease relevance and therapeutic opportunities. *Nature Reviews Drug Discovery*, *15*(5), 348–366. https://doi.org/10.1038/nrd.2015.6

Corder, E. H., Saunders, A. M., Strittmatter, W. J., Schmechel, D. E., Gaskell, P. C., Small, G. W., Roses, A. D., Haines, J. L., & Pericak-Vance, M. A. (1993). Gene dose of apolipoprotein E type 4 allele and the risk of Alzheimer's disease in late onset families. *Science*, *261*(5123), 921–923. https://doi.org/10.1126/science.8346443

Corvera, E., Mouritsen, O. G., Singer, M. A., & Zuckermann, M. J. (1992). The permeability and the effect of acyl-chain length for phospholipid bilayers containing cholesterol: Theory and experiment. *Biochimica Et Biophysica Acta*, *1107*(2), 261–270. https://doi.org/10.1016/0005-2736(92)90413-g

Craig, M., Yarrarapu, S. N. S., & Dimri, M. (2025). Biochemistry, Cholesterol. In *StatPearls*. StatPearls Publishing. http://www.ncbi.nlm.nih.gov/books/NBK513326/

da Silva, R. R., Dorrestein, P. C., & Quinn, R. A. (2015). Illuminating the dark matter in metabolomics. *Proceedings of the National Academy of Sciences*, *112*(41), 12549–12550. https://doi.org/10.1073/pnas.1516878112

Damiani, T., Bonciarelli, S., Thallinger, G. G., Koehler, N., Krettler, C. A., Salihoğlu, A. K., Korf, A., Pauling, J. K., Pluskal, T., Ni, Z., & Goracci, L. (2023a). Software and Computational Tools for LC-MS-Based Epilipidomics: Challenges and Solutions. *Analytical Chemistry*, *95*(1), 287–303. https://doi.org/10.1021/acs.analchem.2c04406

Damiani, T., Bonciarelli, S., Thallinger, G. G., Koehler, N., Krettler, C. A., Salihoğlu, A. K., Korf, A., Pauling, J. K., Pluskal, T., Ni, Z., & Goracci, L. (2023b). Software and Computational Tools for LC-MS-Based Epilipidomics: Challenges and Solutions. *Analytical Chemistry*, *95*(1), 287–303. https://doi.org/10.1021/acs.analchem.2c04406

de Carvalho, C. C. C. R., & Caramujo, M. J. (2018). The Various Roles of Fatty Acids. *Molecules : A Journal of Synthetic Chemistry and Natural Product Chemistry*, *23*(10), 2583. https://doi.org/10.3390/molecules23102583

DeHart, D. N., Fang, D., Heslop, K., Li, L., Lemasters, J. J., & Maldonado, E. N. (2018). Opening of voltage dependent anion channels promotes reactive oxygen species generation, mitochondrial dysfunction and cell death in cancer cells. *Biochemical Pharmacology*, *148*, 155–162. https://doi.org/10.1016/j.bcp.2017.12.022

Deng, X., Luo, Y., Gao, Y., & Wu, T. (2025). Long-chain acyl-CoA synthetases: Biological functions, diseases and therapeutic targets. *Molecular Biomedicine*, *6*, 117. https://doi.org/10.1186/s43556-025-00366-4

Di Paolo, G., & De Camilli, P. (2006). Phosphoinositides in cell regulation and membrane dynamics. *Nature*, *443*(7112), 651–657. https://doi.org/10.1038/nature05185

Dixon, S. J., Lemberg, K. M., Lamprecht, M. R., Skouta, R., Zaitsev, E. M., Gleason, C. E., Patel, D. N., Bauer, A. J., Cantley, A. M., Yang, W. S., Morrison, B., & Stockwell, B. R. (2012). Ferroptosis: An Iron-Dependent Form of Nonapoptotic Cell Death. *Cell*, *149*(5), 1060–1072. https://doi.org/10.1016/j.cell.2012.03.042

Dixon, S. J., & Olzmann, J. A. (2024). The cell biology of ferroptosis. *Nature Reviews Molecular Cell Biology*, *25*(6), 424–442. https://doi.org/10.1038/s41580-024-00703-5

Dixon, S. J., Patel, D. N., Welsch, M., Skouta, R., Lee, E. D., Hayano, M., Thomas, A. G., Gleason, C. E., Tatonetti, N. P., Slusher, B. S., & Stockwell, B. R. (2014). Pharmacological inhibition of cystine–glutamate exchange induces endoplasmic reticulum stress and ferroptosis. *eLife*, *3*, e02523. https://doi.org/10.7554/eLife.02523

Dixon, S. J., Winter, G. E., Musavi, L. S., Lee, E. D., Snijder, B., Rebsamen, M., Superti-Furga, G., & Stockwell, B. R. (2015). Human Haploid Cell Genetics Reveals Roles for Lipid Metabolism Genes in Nonapoptotic Cell Death. *ACS Chemical Biology*, *10*(7), 1604–1609. https://doi.org/10.1021/acschembio.5b00245

Do, Q., Lee, D. D., Dinh, A. N., Seguin, R. P., Zhang, R., & Xu, L. (2021). Development and Application of a Peroxyl Radical Clock Approach for Measuring Both Hydrogen-Atom Transfer and Peroxyl Radical Addition Rate Constants. *The Journal of Organic Chemistry*, *86*(1), 153–168. https://doi.org/10.1021/acs.joc.0c01920

Do, Q., & Xu, L. (2023). How do different lipid peroxidation mechanisms contribute to ferroptosis? *Cell Reports. Physical Science*, *4*(12), 101683. https://doi.org/10.1016/j.xcrp.2023.101683

Do, Q., Zhang, R., Hooper, G., & Xu, L. (2023). Differential Contributions of Distinct Free Radical Peroxidation Mechanisms to the Induction of Ferroptosis. *JACS Au*, jacsau.2c00681. https://doi.org/10.1021/jacsau.2c00681

Doll, S., Freitas, F. P., Shah, R., Aldrovandi, M., da Silva, M. C., Ingold, I., Goya Grocin, A., Xavier da Silva, T. N., Panzilius, E., Scheel, C. H., Mourão, A., Buday, K., Sato, M., Wanninger, J., Vignane, T., Mohana, V., Rehberg, M., Flatley, A., Schepers, A., … Conrad, M. (2019). FSP1 is a glutathione-independent ferroptosis suppressor. *Nature*, *575*(7784), 693–698. https://doi.org/10.1038/s41586-019-1707-0

Doll, S., Proneth, B., Tyurina, Y. Y., Panzilius, E., Kobayashi, S., Ingold, I., Irmler, M., Beckers, J., Aichler, M., Walch, A., Prokisch, H., Trümbach, D., Mao, G., Qu, F., Bayir, H., Füllekrug, J., Scheel, C. H., Wurst, W., Schick, J. A., … Conrad, M. (2017). ACSL4 dictates ferroptosis sensitivity by shaping cellular lipid composition. *Nature Chemical Biology*, *13*(1), 91–98. https://doi.org/10.1038/nchembio.2239

Dolma, S., Lessnick, S. L., Hahn, W. C., & Stockwell, B. R. (2003). Identification of genotype-selective antitumor agents using synthetic lethal chemical screening in engineered human tumor cells. *Cancer Cell*, *3*(3), 285–296. https://doi.org/10.1016/S1535-6108(03)00050-3

Donnelly, K. L., Smith, C. I., Schwarzenberg, S. J., Jessurun, J., Boldt, M. D., & Parks, E. J. (2005). Sources of fatty acids stored in liver and secreted via lipoproteins in patients with nonalcoholic fatty liver disease. *The Journal of Clinical Investigation*, *115*(5), 1343–1351. https://doi.org/10.1172/JCI23621

Drummen, G. P. C., van Liebergen, L. C. M., Op den Kamp, J. A. F., & Post, J. A. (2002). C11-BODIPY(581/591), an oxidation-sensitive fluorescent lipid peroxidation probe: (Micro)spectroscopic characterization and validation of methodology. *Free Radical Biology & Medicine*, *33*(4), 473–490. https://doi.org/10.1016/s0891-5849(02)00848-1

Du, Y., & Guo, Z. (2022). Recent progress in ferroptosis: Inducers and inhibitors. *Cell Death Discovery*, *8*(1), 1–10. https://doi.org/10.1038/s41420-022-01297-7

Ducker, G. S., Chen, L., Morscher, R. J., Ghergurovich, J. M., Esposito, M., Teng, X., Kang, Y., & Rabinowitz, J. D. (2016). Reversal of Cytosolic One-Carbon Flux Compensates for Loss of the Mitochondrial Folate Pathway. *Cell Metabolism*, *23*(6), 1140–1153. https://doi.org/10.1016/j.cmet.2016.04.016

Epilipidome as a New Level of Cellular Regulation. (n.d.). Retrieved July 16, 2026, from https://www.frontiersin.org/research-topics/13062/epilipidome-as-a-new-level-of-cellular-regulation/magazine

Fahy, E., Subramaniam, S., Murphy, R. C., Nishijima, M., Raetz, C. R. H., Shimizu, T., Spener, F., van Meer, G., Wakelam, M. J. O., & Dennis, E. A. (2009). Update of the LIPID MAPS comprehensive classification system for lipids. *Journal of Lipid Research*, *50 Suppl*(Suppl), S9-14. https://doi.org/10.1194/jlr.R800095-JLR200

Fedorova, M., Bendt, A. K., Bertrand-Michel, J., Fiehn, O., Godzien, J., Goracci, L., Gruber, F., Guan, X. L., Han, X., Holčapek, M., Kuligowski, J., Meikle, P. J., Nepachalovich, P., O'Donnell, V. B., Orešič, M., Penkov, S., Petrović, S., Potapov, A., Prabutzki, P., … Domingues, M. R. (2026). A lipidomics roadmap: From basic research to societal challenges. *Nature Communications*, *17*(1), 4778. https://doi.org/10.1038/s41467-026-73797-4

Fiorentini, D., Cipollone, M., Galli, M. C., & Landi, L. (1997). Antioxidant activity of reduced menadione in solvent solution and in model membranes. *Free Radical Research*, *26*(5), 419–429. https://doi.org/10.3109/10715769709084478

Freitas, F. P., Alborzinia, H., dos Santos, A. F., Nepachalovich, P., Pedrera, L., Zilka, O., Inague, A., Klein, C., Aroua, N., Kaushal, K., Kast, B., Lorenz, S. M., Kunz, V., Nehring, H., Xavier da Silva, T. N., Chen, Z., Atici, S., Doll, S. G., Schaefer, E. L., … Friedmann Angeli, J. P. (2024). 7-Dehydrocholesterol is an endogenous suppressor of ferroptosis. *Nature*, *626*(7998), Article 7998. https://doi.org/10.1038/s41586-023-06878-9

Fritz, K. S., & Petersen, D. R. (2011). Exploring the Biology of Lipid Peroxidation-Derived Protein Carbonylation. *Chemical Research in Toxicology*, *24*(9), 1411–1419. https://doi.org/10.1021/tx200169n

Galligan, J. J., Smathers, R. L., Fritz, K. S., Epperson, L. E., Hunter, L. E., & Petersen, D. R. (2012). Protein Carbonylation in a Murine Model for Early Alcoholic Liver Disease. *Chemical Research in Toxicology*, *25*(5), 1012–1021. https://doi.org/10.1021/tx300002q

Gao, M., Yi, J., Zhu, J., Minikes, A. M., Monian, P., Thompson, C. B., & Jiang, X. (2019a). Role of Mitochondria in Ferroptosis. *Molecular Cell*, *73*(2), 354-363.e3. https://doi.org/10.1016/j.molcel.2018.10.042

Gao, M., Yi, J., Zhu, J., Minikes, A. M., Monian, P., Thompson, C. B., & Jiang, X. (2019b). Role of Mitochondria in Ferroptosis. *Molecular Cell*, *73*(2), 354-363.e3. https://doi.org/10.1016/j.molcel.2018.10.042

Garcia-Bermudez, J., Baudrier, L., Bayraktar, E. C., Shen, Y., La, K., Guarecuco, R., Yucel, B., Fiore, D., Tavora, B., Freinkman, E., Chan, S. H., Lewis, C., Min, W., Inghirami, G., Sabatini, D. M., & Birsoy, K. (2019). Squalene accumulation in cholesterol auxotrophic lymphomas prevents oxidative cell death. *Nature*, *567*(7746), 118–122. https://doi.org/10.1038/s41586-019-0945-5

Gerhardtova, I., Jankech, T., Majerova, P., Piestansky, J., Olesova, D., Kovac, A., & Jampilek, J. (2024). Recent Analytical Methodologies in Lipid Analysis. *International Journal of Molecular Sciences*, *25*(4), 2249. https://doi.org/10.3390/ijms25042249

Gianazza, E., Brioschi, M., Fernandez, A. M., & Banfi, C. (2019). Lipoxidation in cardiovascular diseases. *Redox Biology*, *23*, 101119. https://doi.org/10.1016/j.redox.2019.101119

Gibellini, F., & Smith, T. K. (2010). The Kennedy pathway—De novo synthesis of phosphatidylethanolamine and phosphatidylcholine. *IUBMB Life*, *62*(6), 414–428. https://doi.org/10.1002/iub.337

Gill, S., Stevenson, J., Kristiana, I., & Brown, A. J. (2011). Cholesterol-Dependent Degradation of Squalene Monooxygenase, a Control Point in Cholesterol Synthesis beyond HMG-CoA Reductase. *Cell Metabolism*, *13*(3), 260–273. https://doi.org/10.1016/j.cmet.2011.01.015

GitHub—LMAI-TUD/lpptiger2: LPPtiger2 · GitHub. (n.d.). Retrieved June 30, 2026, from https://github.com/LMAI-TUD/lpptiger2

Glade, M. J., & Smith, K. (2015). Phosphatidylserine and the human brain. *Nutrition*, *31*(6), 781–786. https://doi.org/10.1016/j.nut.2014.10.014

Goldberg, I. J., Trent, C. M., & Schulze, P. C. (2012). Lipid Metabolism and Toxicity in the Heart. *Cell Metabolism*, *15*(6), 805–812. https://doi.org/10.1016/j.cmet.2012.04.006

Goracci, L., Tortorella, S., Tiberi, P., Pellegrino, R. M., Di Veroli, A., Valeri, A., & Cruciani, G. (2017). Lipostar, a Comprehensive Platform-Neutral Cheminformatics Tool for Lipidomics. *Analytical Chemistry*, *89*(11), 6257–6264. https://doi.org/10.1021/acs.analchem.7b01259

Han, X. (2016). Lipidomics for studying metabolism. *Nature Reviews Endocrinology*, *12*(11), 668–679. https://doi.org/10.1038/nrendo.2016.98

Han, X., & Gross, R. W. (2003). Global analyses of cellular lipidomes directly from crude extracts of biological samples by ESI mass spectrometry: A bridge to lipidomics. *Journal of Lipid Research*, *44*(6), 1071–1079. https://doi.org/10.1194/jlr.R300004-JLR200

Herron, J., Hines, K. M., & Xu, L. (2018). Assessment of Altered Cholesterol Homeostasis by Xenobiotics Using Ultra-High Performance Liquid Chromatography-Tandem Mass Spectrometry. *Current Protocols in Toxicology*, *78*(1), e65. https://doi.org/10.1002/cptx.65

Hines, K. M., Herron, J., & Xu, L. (2017a). Assessment of altered lipid homeostasis by HILIC-ion mobility-mass spectrometry-based lipidomics. *Journal of Lipid Research*, *58*(4), 809–819. https://doi.org/10.1194/jlr.D074724

Hines, K. M., Herron, J., & Xu, L. (2017b). Assessment of altered lipid homeostasis by HILIC-ion mobility-mass spectrometry-based lipidomics. *Journal of Lipid Research*, *58*(4), 809–819. https://doi.org/10.1194/jlr.D074724

Hines, K. M., May, J. C., McLean, J. A., & Xu, L. (2016). Evaluation of Collision Cross Section Calibrants for Structural Analysis of Lipids by Traveling Wave Ion Mobility-Mass Spectrometry. *Analytical Chemistry*, *88*(14), 7329–7336. https://doi.org/10.1021/acs.analchem.6b01728

Hinnenkamp, V., Klein, J., Meckelmann, S. W., Balsaa, P., Schmidt, T. C., & Schmitz, O. J. (2018). Comparison of CCS Values Determined by Traveling Wave Ion Mobility Mass Spectrometry and Drift Tube Ion Mobility Mass Spectrometry. *Analytical Chemistry*, *90*(20), 12042–12050. https://doi.org/10.1021/acs.analchem.8b02711

Hinz, C., Liggi, S., & Griffin, J. L. (2018). The potential of Ion Mobility Mass Spectrometry for high-throughput and high-resolution lipidomics. *Current Opinion in Chemical Biology*, *42*, 42–50. https://doi.org/10.1016/j.cbpa.2017.10.018

Ho, E., Karimi Galougahi, K., Liu, C.-C., Bhindi, R., & Figtree, G. A. (2013). Biological markers of oxidative stress: Applications to cardiovascular research and practice. *Redox Biology*, *1*(1), 483–491. https://doi.org/10.1016/j.redox.2013.07.006

Howard, J. A., & Ingold, K. U. (1967). Absolute rate constants for hydrocarbon autoxidation. VI. Alkyl aromatic and olefinic hydrocarbons. *Canadian Journal of Chemistry*, *45*(8), 793–802. https://doi.org/10.1139/v67-132

Howe, V., Chua, N. K., Stevenson, J., & Brown, A. J. (2015). The Regulatory Domain of Squalene Monooxygenase Contains a Re-entrant Loop and Senses Cholesterol via a Conformational Change *. *Journal of Biological Chemistry*, *290*(46), 27533–27544. https://doi.org/10.1074/jbc.M115.675181

Hu, L., Zeng, Z., Xia, Q., Liu, Z., Feng, X., Chen, J., Huang, M., Chen, L., Fang, Z., Liu, Q., Zeng, H., Zhou, X., & Liu, J. (2019). Metformin attenuates hepatoma cell proliferation by decreasing glycolytic flux through the HIF-1α/PFKFB3/PFK1 pathway. *Life Sciences*, *239*, 116966. https://doi.org/10.1016/j.lfs.2019.116966

Huang, X., Chen, Y.-J., Cho, K., Nikolskiy, I., Crawford, P. A., & Patti, G. J. (2014). X13CMS: Global Tracking of Isotopic Labels in Untargeted Metabolomics. *Analytical Chemistry*, *86*(3), 1632–1639. https://doi.org/10.1021/ac403384n

Huynh, K., Lim, W. L. F., Giles, C., Jayawardana, K. S., Salim, A., Mellett, N. A., Smith, A. A. T., Olshansky, G., Drew, B. G., Chatterjee, P., Martins, I., Laws, S. M., Bush, A. I., Rowe, C. C., Villemagne, V. L., Ames, D., Masters, C. L., Arnold, M., Nho, K., … Meikle, P. J. (2020). Concordant peripheral lipidome signatures in two large clinical studies of Alzheimer's disease. *Nature Communications*, *11*(1), 5698. https://doi.org/10.1038/s41467-020-19473-7

Isotope Distribution Calculator, Mass Spec Plotter, Isotope Abundance Graphs. (n.d.). Retrieved April 19, 2023, from https://www.sisweb.com/mstools/isotope.htm

Jang, C., Chen, L., & Rabinowitz, J. D. (2018). Metabolomics and Isotope Tracing. *Cell*, *173*(4), 822–837. https://doi.org/10.1016/j.cell.2018.03.055

Jun-Mei Yi, Yi, J., Zhu, J., Jiajun Zhu, Zhu, J., Jiao Wu, Wu, J., Craig B. Thompson, Thompson, C. B., Xuejun Jiang, & Jiang, X. (2020). Oncogenic activation of PI3K-AKT-mTOR signaling suppresses ferroptosis via SREBP-mediated lipogenesis. *Proceedings of the National Academy of Sciences of the United States of America*, *117*(49), 31189–31197. https://doi.org/10.1073/pnas.2017152117

Kagan, V. E., Mao, G., Qu, F., Angeli, J. P. F., Doll, S., Croix, C. S., Dar, H. H., Liu, B., Tyurin, V. A., Ritov, V. B., Kapralov, A. A., Amoscato, A. A., Jiang, J., Anthonymuthu, T., Mohammadyani, D., Yang, Q., Proneth, B., Klein-Seetharaman, J., Watkins, S., … Bayır, H. (2017). Oxidized arachidonic and adrenic PEs navigate cells to ferroptosis. *Nature Chemical Biology*, *13*(1), 81–90. https://doi.org/10.1038/nchembio.2238

Kallemeijn, W. W., Lanyon-Hogg, T., Panyain, N., Goya Grocin, A., Ciepla, P., Morales-Sanfrutos, J., & Tate, E. W. (2021a). Proteome-wide analysis of protein lipidation using chemical probes: In-gel fluorescence visualization, identification and quantification of N-myristoylation, N- and S-

acylation, O-cholesterylation, S-farnesylation and S-geranylgeranylation. *Nature Protocols*, *16*(11), 5083–5122. https://doi.org/10.1038/s41596-021-00601-6

Kallemeijn, W. W., Lanyon-Hogg, T., Panyain, N., Goya Grocin, A., Ciepla, P., Morales-Sanfrutos, J., & Tate, E. W. (2021b). Proteome-wide analysis of protein lipidation using chemical probes: In-gel fluorescence visualization, identification and quantification of N-myristoylation, N- and S-acylation, O-cholesterylation, S-farnesylation and S-geranylgeranylation. *Nature Protocols*, *16*(11), 5083–5122. https://doi.org/10.1038/s41596-021-00601-6

Kamphorst, J. J., Cross, J. R., Fan, J., De Stanchina, E., Mathew, R., White, E. P., Thompson, C. B., & Rabinowitz, J. D. (2013). Hypoxic and Ras-transformed cells support growth by scavenging unsaturated fatty acids from lysophospholipids. *Proceedings of the National Academy of Sciences*, *110*(22), 8882–8887. https://doi.org/10.1073/pnas.1307237110

KEGG PATHWAY: Steroid biosynthesis—Reference pathway. (n.d.). Retrieved December 16, 2025, from https://www.kegg.jp/pathway/map00100

Kennedy, E. P., & Weiss, S. B. (1956). THE FUNCTION OF CYTIDINE COENZYMES IN THE BIOSYNTHESIS OF PHOSPHOLIPIDES. *Journal of Biological Chemistry*, *222*(1), 193–214. https://doi.org/10.1016/S0021-9258(19)50785-2

Kent, C. (1995). EUKARYOTIC PHOSPHOLIPID BIOSYNTHESIS. *Annual Review of Biochemistry*, *64*(Volume 64, 1995), 315–343. https://doi.org/10.1146/annurev.bi.64.070195.001531

Kim, D., Paggi, J. M., Park, C., Bennett, C., & Salzberg, S. L. (2019). Graph-based genome alignment and genotyping with HISAT2 and HISAT-genotype. *Nature Biotechnology*, *37*(8), Article 8. https://doi.org/10.1038/s41587-019-0201-4

Kind, T., Liu, K.-H., Lee, D. Y., DeFelice, B., Meissen, J. K., & Fiehn, O. (2013). LipidBlast in silico tandem mass spectrometry database for lipid identification. *Nature Methods*, *10*(8), 755–758. https://doi.org/10.1038/nmeth.2551

Kishimoto, K., Urade, R., Ogawa, T., & Moriyama, T. (2001). Nondestructive Quantification of Neutral Lipids by Thin-Layer Chromatography and Laser-Fluorescent Scanning: Suitable Methods for

"Lipidome" Analysis. *Biochemical and Biophysical Research Communications*, *281*(3), 657–662. https://doi.org/10.1006/bbrc.2001.4404

Klett, E. L., Chen, S., Yechoor, A., Lih, F. B., & Coleman, R. A. (2017). Long-chain acyl-CoA synthetase isoforms differ in preferences for eicosanoid species and long-chain fatty acids. *Journal of Lipid Research*, *58*(5), 884–894. https://doi.org/10.1194/jlr.M072512

Kodali, S. T., Kauffman, P., Kotha, S. R., Yenigalla, A., Veeraraghavan, R., Pannu, S. R., Hund, T. J., Satoskar, A. R., McDaniel, J. C., Maddipati, R. K., & Parinandi, N. L. (2020). Oxidative Lipidomics: Analysis of Oxidized Lipids and Lipid Peroxidation in Biological Systems with Relevance to Health and Disease. In L. J. Berliner & N. L. Parinandi (Eds.), *Measuring Oxidants and Oxidative Stress in Biological Systems*. Springer. http://www.ncbi.nlm.nih.gov/books/NBK566435/

Kopczynski, D., Ejsing, C. S., McDonald, J. G., Bamba, T., Baker, E. S., Bertrand-Michel, J., Brügger, B., Coman, C., Ellis, S. R., Garrett, T. J., Griffiths, W. J., Guan, X. L., Han, X., Höring, M., Holčapek, M., Hoffmann, N., Huynh, K., Lehmann, R., Jones, J. W., … Liebisch, G. (2024). The lipidomics reporting checklist a framework for transparency of lipidomic experiments and repurposing resource data. *Journal of Lipid Research*, *65*(9). https://doi.org/10.1016/j.jlr.2024.100621

Koundouros, N., & Poulogiannis, G. (2020). Reprogramming of fatty acid metabolism in cancer. *British Journal of Cancer*, *122*(1), 4–22. https://doi.org/10.1038/s41416-019-0650-z

Kurotaki, A., Kuwata, H., & Hara, S. (2021). Substrate Specificity of Human Long-Chain Acyl-CoA Synthetase ACSL6 Variants. *Biological and Pharmaceutical Bulletin*, *44*(10), 1571–1575. https://doi.org/10.1248/bpb.b21-00551

Kyle, J. E., Zhang, X., Weitz, K. K., Monroe, M. E., Ibrahim, Y. M., Moore, R. J., Cha, J., Sun, X., Lovelace, E. S., Wagoner, J., Polyak, S. J., Metz, T. O., Dey, S. K., Smith, R. D., Burnum-Johnson, K. E., & Baker, E. S. (2016). Uncovering biologically significant lipid isomers with

liquid chromatography, ion mobility spectrometry and mass spectrometry. *Analyst*, *141*(5), 1649–1659. https://doi.org/10.1039/C5AN02062J

Lai, Y., Gao, Y., Lin, J., Liu, F., Yang, L., Zhou, J., Xue, Y., Li, Y., Chang, Z., Li, J., Chao, T., Chen, J., Cheng, X., Gao, X., Li, X., Lu, F., Chu, Q., & Wang, W. (2024). Dietary elaidic acid boosts tumoral antigen presentation and cancer immunity via ACSL5. *Cell Metabolism*, *36*(4), 822-838.e8. https://doi.org/10.1016/j.cmet.2024.01.012

Lamberson, C. R., Muchalski, H., McDuffee, K. B., Tallman, K. A., Xu, L., & Porter, N. A. (2017). Propagation rate constants for the peroxidation of sterols on the biosynthetic pathway to cholesterol. *Chemistry and Physics of Lipids, Oxysterols and Phytosterols in Human Health*, *207*, 51–58. https://doi.org/10.1016/j.chemphyslip.2017.01.006

Landi, L., Cabrini, L., Fiorentini, D., Stefanelli, C., & Pedulli, G. F. (1992). The antioxidant activity of ubiquinol-3 in homogeneous solution and in liposomes. *Chemistry and Physics of Lipids*, *61*(2), 121–130. https://doi.org/10.1016/0009-3084(92)90004-9

Lange, M., Wölk, M., Li, V. W., Doubravsky, C. E., Hendricks, J. M., Kato, S., Otoki, Y., Styler, B., Johnson, S. L., Harris, C. A., Nakagawa, K., Snodgrass, I. F., Kim, D., Newman, J. W., Fedorova, M., & Olzmann, J. A. (2025a). FSP1-mediated lipid droplet quality control prevents neutral lipid peroxidation and ferroptosis. *Nature Cell Biology*, *27*(11), 1902–1913. https://doi.org/10.1038/s41556-025-01790-y

Lange, M., Wölk, M., Li, V. W., Doubravsky, C. E., Hendricks, J. M., Kato, S., Otoki, Y., Styler, B., Johnson, S. L., Harris, C. A., Nakagawa, K., Snodgrass, I. F., Kim, D., Newman, J. W., Fedorova, M., & Olzmann, J. A. (2025b). FSP1-mediated lipid droplet quality control prevents neutral lipid peroxidation and ferroptosis. *Nature Cell Biology*, *27*(11), 1902–1913. https://doi.org/10.1038/s41556-025-01790-y

Leaptrot, K. L., May, J. C., Dodds, J. N., & McLean, J. A. (2019). Ion mobility conformational lipid atlas for high confidence lipidomics. *Nature Communications*, *10*(1), Article 1. https://doi.org/10.1038/s41467-019-08897-5

Li, A., Hines, K. M., & Xu, L. (2020). Lipidomics by HILIC-Ion Mobility-Mass Spectrometry. In G. Paglia & G. Astarita (Eds.), *Ion Mobility-Mass Spectrometry* (Vol. 2084, pp. 119–132). Springer US. https://doi.org/10.1007/978-1-0716-0030-6_7

Li, H., Handsaker, B., Wysoker, A., Fennell, T., Ruan, J., Homer, N., Marth, G., Abecasis, G., Durbin, R., & 1000 Genome Project Data Processing Subgroup. (2009). The Sequence Alignment/Map format and SAMtools. *Bioinformatics*, *25*(16), 2078–2079. https://doi.org/10.1093/bioinformatics/btp352

Li, Y., Ran, Q., Duan, Q., Jin, J., Wang, Y., Yu, L., Wang, C., Zhu, Z., Chen, X., Weng, L., Li, Z., Wang, J., Wu, Q., Wang, H., Tian, H., Song, S., Shan, Z., Zhai, Q., Qin, H., … Wang, P. (2024). 7-Dehydrocholesterol dictates ferroptosis sensitivity. *Nature*, *626*(7998), 411–418. https://doi.org/10.1038/s41586-023-06983-9

Liao, Y., Smyth, G. K., & Shi, W. (2014). featureCounts: An efficient general purpose program for assigning sequence reads to genomic features. *Bioinformatics*, *30*(7), 923–930. https://doi.org/10.1093/bioinformatics/btt656

Liebisch, G., Fahy, E., Aoki, J., Dennis, E. A., Durand, T., Ejsing, C. S., Fedorova, M., Feussner, I., Griffiths, W. J., Köfeler, H., Merrill, A. H., Murphy, R. C., O'Donnell, V. B., Oskolkova, O., Subramaniam, S., Wakelam, M. J. O., & Spener, F. (2020). Update on LIPID MAPS classification, nomenclature, and shorthand notation for MS-derived lipid structures. *Journal of Lipid Research*, *61*(12), 1539–1555. https://doi.org/10.1194/jlr.s120001025

LIPID MAPS. (n.d.). Retrieved June 29, 2026, from https://www.lipidmaps.org/resources/tools/ms/gp-ox-search

Liu, C., Liao, W., Chen, J., Yu, K., Wu, Y., Zhang, S., Chen, M., Chen, F., Wang, S., Cheng, T., Wang, J., & Du, C. (2023). Cholesterol confers ferroptosis resistance onto myeloid-biased hematopoietic stem cells and prevents irradiation-induced myelosuppression. *Redox Biology*, *62*, 102661. https://doi.org/10.1016/j.redox.2023.102661

Liu, H., Forouhar, F., Lin, A. J., Wang, Q., Polychronidou, V., Soni, R. K., Xia, X., & Stockwell, B. R. (2022). Small-molecule allosteric inhibitors of GPX4. *Cell Chemical Biology*, *29*(12), 1680-1693.e9. https://doi.org/10.1016/j.chembiol.2022.11.003

LoPachin, R. M., Gavin, T., Petersen, D. R., & Barber, D. S. (2009). Molecular Mechanisms of 4-Hydroxy-2-nonenal and Acrolein Toxicity: Nucleophilic Targets and Adduct Formation. *Chemical Research in Toxicology*, *22*(9), 1499–1508. https://doi.org/10.1021/tx900147g

Lordan, R., Tsoupras, A., & Zabetakis, I. (2017). Phospholipids of Animal and Marine Origin: Structure, Function, and Anti-Inflammatory Properties. *Molecules : A Journal of Synthetic Chemistry and Natural Product Chemistry*, *22*(11), 1964. https://doi.org/10.3390/molecules22111964

Louie, S. M., Roberts, L. S., Mulvihill, M. M., Luo, K., & Nomura, D. K. (2013). Cancer cells incorporate and remodel exogenous palmitate into structural and oncogenic signaling lipids. *Biochimica et Biophysica Acta (BBA) - Molecular and Cell Biology of Lipids*, *1831*(10), 1566–1572. https://doi.org/https://doi.org/10.1016/j.bbalip.2013.07.008

Love, M. I., Huber, W., & Anders, S. (2014). Moderated estimation of fold change and dispersion for RNA-seq data with DESeq2. *Genome Biology*, *15*(12), 550. https://doi.org/10.1186/s13059-014-0550-8

Luo, J., Yang, H., & Song, B.-L. (2020). Mechanisms and regulation of cholesterol homeostasis. *Nature Reviews Molecular Cell Biology*, *21*(4), 225–245. https://doi.org/10.1038/s41580-019-0190-7

MacLean, B., Tomazela, D. M., Shulman, N., Chambers, M., Finney, G. L., Frewen, B., Kern, R., Tabb, D. L., Liebler, D. C., & MacCoss, M. J. (2010). Skyline: An open source document editor for creating and analyzing targeted proteomics experiments. *Bioinformatics*, *26*(7), 966–968. https://doi.org/10.1093/bioinformatics/btq054

Madian, A. G., Diaz-Maldonado, N., Gao, Q., & Regnier, F. E. (2011). Oxidative stress induced carbonylation in human plasma. *Journal of Proteomics, Redox Proteomics*, *74*(11), 2395–2416. https://doi.org/10.1016/j.jprot.2011.07.014

Madison, B. B. (2016). Srebp2: A master regulator of sterol and fatty acid synthesis1. *Journal of Lipid Research*, *57*(3), 333–335. https://doi.org/10.1194/jlr.C066712

Magtanong, L., Ko, P.-J., To, M., Cao, J. Y., Forcina, G. C., Tarangelo, A., Ward, C. C., Cho, K., Patti, G. J., Nomura, D. K., Olzmann, J. A., & Dixon, S. J. (2019). Exogenous Monounsaturated Fatty Acids Promote a Ferroptosis-Resistant Cell State. *Cell Chemical Biology*, *26*(3), 420-432.e9. https://doi.org/10.1016/j.chembiol.2018.11.016

Magtanong, L., Mueller, G. D., Williams, K. J., Billmann, M., Chan, K., Armenta, D. A., Pope, L. E., Moffat, J., Boone, C., Myers, C. L., Olzmann, J. A., Bensinger, S. J., & Dixon, S. J. (2022). Context-dependent regulation of ferroptosis sensitivity. *Cell Chemical Biology*, *29*(9), 1409-1418.e6. https://doi.org/10.1016/j.chembiol.2022.06.004

Marsh, D. (2007). Lateral pressure profile, spontaneous curvature frustration, and the incorporation and conformation of proteins in membranes. *Biophysical Journal*, *93*(11), 3884–3899. https://doi.org/10.1529/biophysj.107.107938

Martinez, A. M., Kim, A., & Yang, W. S. (2020). Detection of Ferroptosis by BODIPY™ 581/591 C11. In I. Vancurova & Y. Zhu (Eds.), *Immune Mediators in Cancer* (Vol. 2108, pp. 125–130). Springer US. https://doi.org/10.1007/978-1-0716-0247-8_11

Mashek, D. G., Bornfeldt, K. E., Coleman, R. A., Berger, J., Bernlohr, D. A., Black, P., DiRusso, C. C., Farber, S. A., Guo, W., Hashimoto, N., Khodiyar, V., Kuypers, F. A., Maltais, L. J., Nebert, D. W., Renieri, A., Schaffer, J. E., Stahl, A., Watkins, P. A., Vasiliou, V., & Yamamoto, T. T. (2004). Revised nomenclature for the mammalian long-chain acyl-CoA synthetase gene family. *Journal of Lipid Research*, *45*(10), 1958–1961. https://doi.org/10.1194/jlr.E400002-JLR200

Mason, E. A., & Schamp, H. W. (1958). Mobility of gaseous lons in weak electric fields. *Annals of Physics*, *4*(3), 233–270. https://doi.org/10.1016/0003-4916(58)90049-6

McDonald, J. G., Ejsing, C. S., Kopczynski, D., Holčapek, M., Aoki, J., Arita, M., Arita, M., Baker, E. S., Bertrand-Michel, J., Bowden, J. A., Brügger, B., Ellis, S. R., Fedorova, M., Griffiths, W. J., Han, X., Hartler, J., Hoffmann, N., Koelmel, J. P., Köfeler, H. C., … Ekroos, K. (2022). Introducing the

Lipidomics Minimal Reporting Checklist. *Nature Metabolism*, *4*(9), 1086–1088. https://doi.org/10.1038/s42255-022-00628-3

McIntyre, T. M. (2012). Bioactive Oxidatively Truncated Phospholipids in Inflammation and Apoptosis: Formation, Targets, and Inactivation. *Biochimica et Biophysica Acta*, *1818*(10), 2456–2464. https://doi.org/10.1016/j.bbamem.2012.03.004

Millard, P., Letisse, F., Sokol, S., & Portais, J.-C. (2012). IsoCor: Correcting MS data in isotope labeling experiments. *Bioinformatics (Oxford, England)*, *28*(9), 1294–1296. https://doi.org/10.1093/bioinformatics/bts127

Mishima, E., Ito, J., Wu, Z., Nakamura, T., Wahida, A., Doll, S., Tonnus, W., Nepachalovich, P., Eggenhofer, E., Aldrovandi, M., Henkelmann, B., Yamada, K., Wanninger, J., Zilka, O., Sato, E., Feederle, R., Hass, D., Maida, A., Mourão, A. S. D., … Conrad, M. (2022). A non-canonical vitamin K cycle is a potent ferroptosis suppressor. *Nature*, *608*(7924), 778–783. https://doi.org/10.1038/s41586-022-05022-3

Mukai, K., Kikuchi, S., & Urano, S. (1990). Stopped-flow kinetic study of the regeneration reaction of tocopheroxyl radical by reduced ubiquinone-10 in solution. *Biochimica et Biophysica Acta (BBA) - General Subjects*, *1035*(1), 77–82. https://doi.org/10.1016/0304-4165(90)90176-W

Ni, Z., Angelidou, G., Hoffmann, R., & Fedorova, M. (2017). LPPtiger software for lipidome-specific prediction and identification of oxidized phospholipids from LC-MS datasets. *Scientific Reports*, *7*, 15138. https://doi.org/10.1038/s41598-017-15363-z

nreimers99. (2023). *D-Tracer* [Jupyter Notebook]. https://github.com/nreimers99/d-tracer (Original work published 2022)

Peng, H., Xin, S., Pfeiffer, S., Müller, C., Merl-Pham, J., Hauck, S. M., Harter, P. N., Spitzer, D., Devraj, K., Varynskyi, B., Arzberger, T., Momma, S., & Schick, J. A. (2024). Fatty acid-binding protein 5 is a functional biomarker and indicator of ferroptosis in cerebral hypoxia. *Cell Death & Disease*, *15*(4), 286. https://doi.org/10.1038/s41419-024-06681-y

Pratt, D. A., DiLabio, G. A., Brigati, G., Pedulli, G. F., & Valgimigli, L. (2001). 5-Pyrimidinols: Novel Chain-Breaking Antioxidants More Effective than Phenols. *Journal of the American Chemical Society*, *123*(19), 4625–4626. https://doi.org/10.1021/ja005679l

Qiu, B., Zandkarimi, F., Bezjian, C. T., Reznik, E., Soni, R. K., Gu, W., Jiang, X., & Stockwell, B. R. (2024a). Phospholipids with two polyunsaturated fatty acyl tails promote ferroptosis. *Cell*, *187*(5), 1177-1190.e18. https://doi.org/10.1016/j.cell.2024.01.030

Qiu, B., Zandkarimi, F., Bezjian, C. T., Reznik, E., Soni, R. K., Gu, W., Jiang, X., & Stockwell, B. R. (2024b). Phospholipids with two polyunsaturated fatty acyl tails promote ferroptosis. *Cell*, *187*(5), 1177-1190.e18. https://doi.org/10.1016/j.cell.2024.01.030

Reddy, J. K., & Sambasiva Rao, M. (2006). Lipid Metabolism and Liver Inflammation. II. Fatty liver disease and fatty acid oxidation. *American Journal of Physiology-Gastrointestinal and Liver Physiology*, *290*(5), G852–G858. https://doi.org/10.1152/ajpgi.00521.2005

Reimers, N., Do, Q., Zhang, R., Guo, A., Ostrander, R., Shoji, A., Vuong, C., & Xu, L. (2023). Tracking the Metabolic Fate of Exogenous Arachidonic Acid in Ferroptosis Using Dual-Isotope Labeling Lipidomics. *Journal of the American Society for Mass Spectrometry*. https://doi.org/10.1021/jasms.3c00181

Reimers, N., & Xu, L. (2025). Peroxidation rate constants and mechanisms of isoprenoid-derived lipids and their roles in ferroptosis. *Redox Biochemistry and Chemistry*, *13*, 100058. https://doi.org/10.1016/j.rbc.2025.100058

Roschek, B., Tallman, K. A., Rector, C. L., Gillmore, J. G., Pratt, D. A., Punta, C., & Porter, N. A. (2006). Peroxyl Radical Clocks. *The Journal of Organic Chemistry*, *71*(9), 3527–3532. https://doi.org/10.1021/jo0601462

Ross, D. H., Cho, J. H., & Xu, L. (2020). Breaking Down Structural Diversity for Comprehensive Prediction of Ion-Neutral Collision Cross Sections. *Analytical Chemistry*, *92*(6), 4548–4557. https://doi.org/10.1021/acs.analchem.9b05772

Ross, D. H., Cho, J. H., Zhang, R., Hines, K. M., & Xu, L. (2020). LiPydomics: A Python Package for Comprehensive Prediction of Lipid Collision Cross Sections and Retention Times and Analysis of Ion Mobility-Mass Spectrometry-Based Lipidomics Data. *Analytical Chemistry*, *92*(22), 14967–14975. https://doi.org/10.1021/acs.analchem.0c02560

Ross, D. H., Seguin, R. P., & Xu, L. (2019). Characterization of the Impact of Drug Metabolism on the Gas-Phase Structures of Drugs Using Ion Mobility-Mass Spectrometry. *Analytical Chemistry*, *91*(22), 14498–14507. https://doi.org/10.1021/acs.analchem.9b03292

Samovich, S. N., Mikulska-Ruminska, K., Dar, H. H., Tyurina, Y. Y., Tyurin, V. A., Souryavong, A. B., Kapralov, A. A., Amoscato, A. A., Beharier, O., Karumanchi, S. A., St Croix, C. M., Yang, X., Holman, T. R., VanDemark, A. P., Sadovsky, Y., Mallampalli, R. K., Wenzel, S. E., Gu, W., Bunimovich, Y. L., … Bayir, H. (2024). Strikingly High Activity of 15-Lipoxygenase Towards Di-Polyunsaturated Arachidonoyl/Adrenoyl-Phosphatidylethanolamines Generates Peroxidation Signals of Ferroptotic Cell Death. *Angewandte Chemie International Edition*, *63*(9), e202314710. https://doi.org/10.1002/anie.202314710

Schwalbe-Herrmann, M., Willmann, J., & Leibfritz, D. (2010). Separation of phospholipid classes by hydrophilic interaction chromatography detected by electrospray ionization mass spectrometry. *Journal of Chromatography A*, *1217*(32), 5179–5183. https://doi.org/10.1016/j.chroma.2010.05.014

Seiler, A., Schneider, M., Förster, H., Roth, S., Wirth, E. K., Culmsee, C., Plesnila, N., Kremmer, E., Rådmark, O., Wurst, W., Bornkamm, G. W., Schweizer, U., & Conrad, M. (2008). Glutathione Peroxidase 4 Senses and Translates Oxidative Stress into 12/15-Lipoxygenase Dependent- and AIF-Mediated Cell Death. *Cell Metabolism*, *8*(3), 237–248. https://doi.org/10.1016/j.cmet.2008.07.005

Shindou, H., Hishikawa, D., Harayama, T., Yuki, K., & Shimizu, T. (2009). Recent progress on acyl CoA: Lysophospholipid acyltransferase research. *Journal of Lipid Research*, *50*(Suppl), S46–S51. https://doi.org/10.1194/jlr.R800035-JLR200

Sokol, K. H., Lee, C. J., Rogers, T. J., Waldhart, A., Ellis, A. E., Madireddy, S., Daniels, S. R., House, R. (Rae) J., Ye, X., Olesnavich, M., Johnson, A., Furness, B. R., Sheldon, R. D., & Lien, E. C. (2025). Lipid availability influences ferroptosis sensitivity in cancer cells by regulating polyunsaturated fatty acid trafficking. *Cell Chemical Biology*, *32*(3), 408-422.e6. https://doi.org/10.1016/j.chembiol.2024.09.008

Souza, I. de, Andrade, I. A. M., Freitas, F. P., Teixeira, A. B. da S., Ramalho, M. C. C., Lima, K. A., Santos, A. F. dos, Schmitz, W., Fazeli, G., Rocha, C. R. R., & Angeli, J. P. F. (2025). *HMOX1 controls a heme–ferritin switch that protects cells from ferroptosis* (p. 2025.10.14.682408). bioRxiv. https://doi.org/10.1101/2025.10.14.682408

Spanova, M., Zweytick, D., Lohner, K., Klug, L., Leitner, E., Hermetter, A., & Daum, G. (2012). Influence of squalene on lipid particle/droplet and membrane organization in the yeast Saccharomyces cerevisiae. *Biochimica Et Biophysica Acta*, *1821*(4), 647–653. https://doi.org/10.1016/j.bbalip.2012.01.015

Stahl, A. (2004). A current review of fatty acid transport proteins (SLC27). *Pflugers Archiv: European Journal of Physiology*, *447*(5), 722–727. https://doi.org/10.1007/s00424-003-1106-z

Steinberg, S. J., Morgenthaler, J., Heinzer, A. K., Smith, K. D., & Watkins, P. A. (2000). Very Long-chain Acyl-CoA Synthetases: HUMAN "BUBBLEGUM" REPRESENTS A NEW FAMILY OF PROTEINS CAPABLE OF ACTIVATING VERY LONG-CHAIN FATTY ACIDS *. *Journal of Biological Chemistry*, *275*(45), 35162–35169. https://doi.org/10.1074/jbc.M006403200

Stockwell, B. R. (2022). Ferroptosis turns 10: Emerging mechanisms, physiological functions, and therapeutic applications. *Cell*, *185*(14), 2401–2421. https://doi.org/10.1016/j.cell.2022.06.003

Stockwell, B. R., Angeli, J. P. F., Bayir, H., Bush, A. I., Conrad, M., Dixon, S. J., Fulda, S., Gascón, S., Hatzios, S. K., Kagan, V. E., Noel, K., Jiang, X., Linkermann, A., Murphy, M. E., Overholtzer, M., Oyagi, A., Pagnussat, G. C., Park, J., Ran, Q., … Zhang, D. D. (2017). Ferroptosis: A Regulated Cell Death Nexus Linking Metabolism, Redox Biology, and Disease. *Cell*, *171*(2), 273–285. https://doi.org/10.1016/j.cell.2017.09.021

Su, D., Wang, X., Zhang, W., Li, P., & Tang, B. (2022). Fluorescence imaging for visualizing the bioactive molecules of lipid peroxidation within biological systems. *TrAC Trends in Analytical Chemistry*, *146*, 116484. https://doi.org/10.1016/j.trac.2021.116484

Sud, M., Fahy, E., Cotter, D., Brown, A., Dennis, E. A., Glass, C. K., Merrill, A. H., Murphy, R. C., Raetz, C. R. H., Russell, D. W., & Subramaniam, S. (2007a). LMSD: LIPID MAPS structure database. *Nucleic Acids Research*, *35*(Database issue), D527-532. https://doi.org/10.1093/nar/gkl838

Sud, M., Fahy, E., Cotter, D., Brown, A., Dennis, E. A., Glass, C. K., Merrill, A. H., Murphy, R. C., Raetz, C. R. H., Russell, D. W., & Subramaniam, S. (2007b). LMSD: LIPID MAPS structure database. *Nucleic Acids Research*, *35*(Database), D527–D532. https://doi.org/10.1093/nar/gkl838

Sun, Q., Liu, D., Cui, W., Cheng, H., Huang, L., Zhang, R., Gu, J., Liu, S., Zhuang, X., Lu, Y., Chu, B., & Li, J. (2023a). Cholesterol mediated ferroptosis suppression reveals essential roles of Coenzyme Q and squalene. *Communications Biology*, *6*(1), 1–15. https://doi.org/10.1038/s42003-023-05477-8

Sun, Q., Liu, D., Cui, W., Cheng, H., Huang, L., Zhang, R., Gu, J., Liu, S., Zhuang, X., Lu, Y., Chu, B., & Li, J. (2023b). Cholesterol mediated ferroptosis suppression reveals essential roles of Coenzyme Q and squalene. *Communications Biology*, *6*(1), 1–15. https://doi.org/10.1038/s42003-023-05477-8

Sun, Y., & Zhang, J. (2024). HMOX1 regulates ferroptosis via mic14 and its impact on chemotherapy resistance in small-cell lung cancer. *Anti-Cancer Drugs*, *35*(5), 397–411. https://doi.org/10.1097/CAD.0000000000001588

Suthers, P. F., Burgard, A. P., Dasika, M. S., Nowroozi, F., Van Dien, S., Keasling, J. D., & Maranas, C. D. (2007). Metabolic flux elucidation for large-scale models using 13C labeled isotopes. *Metabolic Engineering*, *9*(5), 387–405. https://doi.org/10.1016/j.ymben.2007.05.005

Takahashi, T., Okamoto, T., Mori, K., Sayo, H., & Kishi, T. (1993). Distribution of ubiquinone and ubiquinol homologues in rat tissues and subcellular fractions. *Lipids*, *28*(9), 803–809. https://doi.org/10.1007/BF02536234

Tang, D., Chen, X., Kang, R., & Kroemer, G. (2021). Ferroptosis: Molecular mechanisms and health implications. *Cell Research*, *31*(2), 107–125. https://doi.org/10.1038/s41422-020-00441-1

Tang, L., Wu, N., Xu, H., & Mo, Y. (n.d.). PPARG as a central regulator of ferroptosis in Alzheimer's disease: Integrated transcriptomic, single-cell, and experimental evidence. *Frontiers in Aging Neuroscience*, *18*, 1759279. https://doi.org/10.3389/fnagi.2026.1759279

Tracz-Gaszewska, Z., & Dobrzyn, P. (2019). Stearoyl-CoA Desaturase 1 as a Therapeutic Target for the Treatment of Cancer. *Cancers*, *11*(7), 948. https://doi.org/10.3390/cancers11070948

Tretiakova, D. S., Volynsky, P. E., Kobanenko, M. K., Alekseeva, A. S., Le-Deygen, I. M., Vodovozova, E. L., & Boldyrev, I. A. (2024). Phosphatidylglycerol in lipid bilayer. Molecular recognition, conformational transitions, hydrogen bonding and microviscosity. *Journal of Molecular Liquids*, *411*, 125688. https://doi.org/10.1016/j.molliq.2024.125688

Triebl, A., & Wenk, M. R. (2018). Analytical Considerations of Stable Isotope Labelling in Lipidomics. *Biomolecules*, *8*(4), 151. https://doi.org/10.3390/biom8040151

Tsugawa, H., Cajka, T., Kind, T., Ma, Y., Higgins, B., Ikeda, K., Kanazawa, M., VanderGheynst, J., Fiehn, O., & Arita, M. (2015). MS-DIAL: Data-independent MS/MS deconvolution for comprehensive metabolome analysis. *Nature Methods*, *12*(6), 523–526. https://doi.org/10.1038/nmeth.3393

Tsugawa, H., Ikeda, K., Takahashi, M., Satoh, A., Mori, Y., Uchino, H., Okahashi, N., Yamada, Y., Tada, I., Bonini, P., Higashi, Y., Okazaki, Y., Zhou, Z., Zhu, Z.-J., Koelmel, J., Cajka, T., Fiehn, O., Saito, K., Arita, M., & Arita, M. (2020). A lipidome atlas in MS-DIAL 4. *Nature Biotechnology*, *38*(10), 1159–1163. https://doi.org/10.1038/s41587-020-0531-2

van der Veen, J. N., Kennelly, J. P., Wan, S., Vance, J. E., Vance, D. E., & Jacobs, R. L. (2017). The critical role of phosphatidylcholine and phosphatidylethanolamine metabolism in health and disease. *Biochimica et Biophysica Acta (BBA) - Biomembranes, Membrane Lipid Therapy: Drugs Targeting Biomembranes*, *1859*(9, Part B), 1558–1572. https://doi.org/10.1016/j.bbamem.2017.04.006

van Meer, G., Voelker, D. R., & Feigenson, G. W. (2008). Membrane lipids: Where they are and how they behave. *Nature Reviews Molecular Cell Biology*, *9*(2), 112–124. https://doi.org/10.1038/nrm2330

Vance, J. E. (2015). Phospholipid Synthesis and Transport in Mammalian Cells. *Traffic*, *16*(1), 1–18. https://doi.org/10.1111/tra.12230

Vásquez, A., Leidy, C., & Manrique-Moreno, M. (2025). Lysyl-Phosphatidylglycerol: A Lipid Involved in the Resistance of Staphylococcus aureus to Antimicrobial Peptide Activity. *Antibiotics*, *14*(4), 349. https://doi.org/10.3390/antibiotics14040349

von Krusenstiern, A. N., Robson, R. N., Qian, N., Qiu, B., Hu, F., Reznik, E., Smith, N., Zandkarimi, F., Estes, V. M., Dupont, M., Hirschhorn, T., Shchepinov, M. S., Min, W., Woerpel, K. A., & Stockwell, B. R. (2023a). Identification of essential sites of lipid peroxidation in ferroptosis. *Nature Chemical Biology*. https://doi.org/10.1038/s41589-022-01249-3

von Krusenstiern, A. N., Robson, R. N., Qian, N., Qiu, B., Hu, F., Reznik, E., Smith, N., Zandkarimi, F., Estes, V. M., Dupont, M., Hirschhorn, T., Shchepinov, M. S., Min, W., Woerpel, K. A., & Stockwell, B. R. (2023b). Identification of essential sites of lipid peroxidation in ferroptosis. *Nature Chemical Biology*. https://doi.org/10.1038/s41589-022-01249-3

Vriens, K., Christen, S., Parik, S., Broekaert, D., Yoshinaga, K., Talebi, A., Dehairs, J., Escalona-Noguero, C., Schmieder, R., Cornfield, T., Charlton, C., Romero-Pérez, L., Rossi, M., Rinaldi, G., Orth, M. F., Boon, R., Kerstens, A., Kwan, S. Y., Faubert, B., … Fendt, S.-M. (2019). Evidence for an alternative fatty acid desaturation pathway increasing cancer plasticity. *Nature*, *566*(7744), 403–406. https://doi.org/10.1038/s41586-019-0904-1

Vvedenskaya, O., Holčapek, M., Vogeser, M., Ekroos, K., Meikle, P. J., & Bendt, A. K. (2022). Clinical lipidomics – A community-driven roadmap to translate research into clinical applications. *Journal of Mass Spectrometry and Advances in the Clinical Lab*, *24*, 1–4. https://doi.org/10.1016/j.jmsacl.2022.02.002

Vvedenskaya, O., Rose, T. D., Knittelfelder, O., Palladini, A., Wodke, J. A. H., Schuhmann, K., Ackerman, J. M., Wang, Y., Has, C., Brosch, M., Thangapandi, V. R., Buch, S., Züllig, T., Hartler,

J., Köfeler, H. C., Röcken, C., Coskun, Ü., Klipp, E., von Schoenfels, W., … Shevchenko, A. (2021). Nonalcoholic fatty liver disease stratification by liver lipidomics. *Journal of Lipid Research*, *62*, 100104. https://doi.org/10.1016/j.jlr.2021.100104

Wang, B., Wu, L., Chen, J., Dong, L., Chen, C., Wen, Z., Hu, J., Fleming, I., & Wang, D. W. (2021a). Metabolism pathways of arachidonic acids: Mechanisms and potential therapeutic targets. *Signal Transduction and Targeted Therapy*, *6*(1), 94. https://doi.org/10.1038/s41392-020-00443-w

Wang, B., Wu, L., Chen, J., Dong, L., Chen, C., Wen, Z., Hu, J., Fleming, I., & Wang, D. W. (2021b). Metabolism pathways of arachidonic acids: Mechanisms and potential therapeutic targets. *Signal Transduction and Targeted Therapy*, *6*(1), 94. https://doi.org/10.1038/s41392-020-00443-w

Weaver, K., & Skouta, R. (2022). The Selenoprotein Glutathione Peroxidase 4: From Molecular Mechanisms to Novel Therapeutic Opportunities. *Biomedicines*, *10*(4), 891. https://doi.org/10.3390/biomedicines10040891

Williams, M. V., Wishnok, J. S., & Tannenbaum, S. R. (2007). Covalent adducts arising from the decomposition products of lipid hydroperoxides in the presence of cytochrome C. *Chemical Research in Toxicology*, *20*(5), 767–775. https://doi.org/10.1021/tx600289r

Wolrab, D., Jirásko, R., Cífková, E., Höring, M., Mei, D., Chocholoušková, M., Peterka, O., Idkowiak, J., Hrnčiarová, T., Kuchař, L., Ahrends, R., Brumarová, R., Friedecký, D., Vivo-Truyols, G., Škrha, P., Škrha, J., Kučera, R., Melichar, B., Liebisch, G., … Holčapek, M. (2022). Lipidomic profiling of human serum enables detection of pancreatic cancer. *Nature Communications*, *13*(1), 124. https://doi.org/10.1038/s41467-021-27765-9

Wu, M., Xu, L.-G., Li, X., Zhai, Z., & Shu, H.-B. (2002). AMID, an Apoptosis-inducing Factor-homologous Mitochondrion-associated Protein, Induces Caspase-independent Apoptosis *. *Journal of Biological Chemistry*, *277*(28), 25617–25623. https://doi.org/10.1074/jbc.M202285200

Wu, W., Ishamuddin, S. H., Quinn, T. W., Yerrum, S., Zhang, Y., Debaize, L. L., Kao, P.-L., Duquette, S. M., Murakami, M. A., Mohseni, M., Chow, K.-H., Miettinen, T. P., Ligon, K. L., & Manalis, S. R.

(2025). High-throughput single-cell density measurements enable dynamic profiling of immune cell and drug response from patient samples. *Nature Biomedical Engineering*, *9*(11), 1972–1981. https://doi.org/10.1038/s41551-025-01408-6

Xu, L., Davis, T. A., & Porter, N. A. (2009). Rate Constants for Peroxidation of Polyunsaturated Fatty Acids and Sterols in Solution and in Liposomes. *Journal of the American Chemical Society*, *131*(36), 13037–13044. https://doi.org/10.1021/ja9029076

Xu, L., Korade, Z., Rosado, J. D. A., Liu, W., Lamberson, C. R., & Porter, N. A. (2011). An oxysterol biomarker for 7-dehydrocholesterol oxidation in cell/mouse models for Smith-Lemli-Opitz syndrome. *Journal of Lipid Research*, *52*(6), 1222–1233. https://doi.org/10.1194/jlr.M014498

Xu, L., & Porter, N. A. (2015). Free radical oxidation of cholesterol and its precursors: Implications in cholesterol biosynthesis disorders. *Free Radical Research*, *49*(7), 835–849. https://doi.org/10.3109/10715762.2014.985219

Xu, Y., Li, X., Cheng, Y., Yang, M., & Wang, R. (2020). Inhibition of ACSL4 attenuates ferroptotic damage after pulmonary ischemia-reperfusion. *The FASEB Journal*, *34*(12), 16262–16275. https://doi.org/10.1096/fj.202001758R

Yamamoto, Y., Komuro, E., & Niki, E. (1990). Antioxidant activity of ubiquinol in solution and phosphatidylcholine liposome. *Journal of Nutritional Science and Vitaminology*, *36*(5), 505–511. https://doi.org/10.3177/jnsv.36.505

Yan, H., Zou, T., Tuo, Q., Xu, S., Li, H., Belaidi, A. A., & Lei, P. (2021). Ferroptosis: Mechanisms and links with diseases. *Signal Transduction and Targeted Therapy*, *6*(1), 49. https://doi.org/10.1038/s41392-020-00428-9

Yang, W. S. (2023). Ferroptosis: whERe is the critical site of lipid peroxidation? *Frontiers in Cell and Developmental Biology*, *11*. https://doi.org/10.3389/fcell.2023.1179245

Yang, W. S., Kim, K. J., Gaschler, M. M., Patel, M., Shchepinov, M. S., & Stockwell, B. R. (2016). Peroxidation of polyunsaturated fatty acids by lipoxygenases drives ferroptosis. *Proceedings of*

the National Academy of Sciences, *113*(34), E4966–E4975. https://doi.org/10.1073/pnas.1603244113

Yang, W. S., & Stockwell, B. R. (2008). Synthetic Lethal Screening Identifies Compounds Activating Iron-Dependent, Nonapoptotic Cell Death in Oncogenic-RAS-Harboring Cancer Cells. *Chemistry & Biology*, *15*(3), 234–245. https://doi.org/10.1016/j.chembiol.2008.02.010

Yasui, Y., Hosokawa, M., Sahara, T., Suzuki, R., Ohgiya, S., Kohno, H., Tanaka, T., & Miyashita, K. (2005). Bitter gourd seed fatty acid rich in 9c,11t,13t-conjugated linolenic acid induces apoptosis and up-regulates the GADD45, p53 and PPARgamma in human colon cancer Caco-2 cells. *Prostaglandins, Leukotrienes, and Essential Fatty Acids*, *73*(2), 113–119. https://doi.org/10.1016/j.plefa.2005.04.013

Yi, J., Zhu, J., Wu, J., Thompson, C. B., & Jiang, X. (2020). Oncogenic activation of PI3K-AKT-mTOR signaling suppresses ferroptosis via SREBP-mediated lipogenesis. *Proceedings of the National Academy of Sciences*, *117*(49), 31189–31197. https://doi.org/10.1073/pnas.2017152117

Yin, H., Xu, L., & Porter, N. A. (2011). Free Radical Lipid Peroxidation: Mechanisms and Analysis. *Chemical Reviews*, *111*(10), 5944–5972. https://doi.org/10.1021/cr200084z

Yoshida, Y., Saito, Y., Hayakawa, M., Habuchi, Y., Imai, Y., Sawai, Y., & Niki, E. (2007). Levels of Lipid Peroxidation in Human Plasma and Erythrocytes: Comparison between Fatty Acids and Cholesterol. *Lipids*, *42*(5), 439–449. https://doi.org/10.1007/s11745-007-3037-5

Yuan, H., Li, X., Zhang, X., Kang, R., & Tang, D. (2016). Identification of ACSL4 as a biomarker and contributor of ferroptosis. *Biochemical and Biophysical Research Communications*, *478*(3), 1338–1343. https://doi.org/10.1016/j.bbrc.2016.08.124

Zhang, X., Barraza, K. M., & Beauchamp, J. L. (2018). Cholesterol provides nonsacrificial protection of membrane lipids from chemical damage at air–water interface. *Proceedings of the National Academy of Sciences*, *115*(13), 3255–3260. https://doi.org/10.1073/pnas.1722323115

Zhao, X., Lian, X., Xie, J., & Liu, G. (2023). Accumulated cholesterol protects tumours from elevated lipid peroxidation in the microenvironment. *Redox Biology*, *62*, 102678. https://doi.org/10.1016/j.redox.2023.102678

Zhao, X., Zhao, Z., Li, B., Huan, S., Li, Z., Xie, J., & Liu, G. (2024). ACSL4-mediated lipid rafts prevent membrane rupture and inhibit immunogenic cell death in melanoma. *Cell Death & Disease*, *15*(9), 695. https://doi.org/10.1038/s41419-024-07098-3

Zhou, Z., Shen, X., Chen, X., Tu, J., Xiong, X., & Zhu, Z.-J. (2019). LipidIMMS Analyzer: Integrating multi-dimensional information to support lipid identification in ion mobility-mass spectrometry based lipidomics. *Bioinformatics (Oxford, England)*, *35*(4), 698–700. https://doi.org/10.1093/bioinformatics/bty661

Zhou, Z., Tu, J., Xiong, X., Shen, X., & Zhu, Z.-J. (2017). LipidCCS: Prediction of Collision Cross-Section Values for Lipids with High Precision To Support Ion Mobility–Mass Spectrometry-Based Lipidomics. *Analytical Chemistry*, *89*(17), 9559–9566. https://doi.org/10.1021/acs.analchem.7b02625

Zielinski, Z. A. M., & Pratt, D. A. (2019). H-Atom Abstraction vs Addition: Accounting for the Diverse Product Distribution in the Autoxidation of Cholesterol and Its Esters. *Journal of the American Chemical Society*, *141*(7), 3037–3051. https://doi.org/10.1021/jacs.8b11524

Zou, Y., Henry, W. S., Ricq, E. L., Graham, E. T., Phadnis, V. V., Maretich, P., Paradkar, S., Boehnke, N., Deik, A. A., Reinhardt, F., Eaton, J. K., Ferguson, B., Wang, W., Fairman, J., Keys, H. R., Dančík, V., Clish, C. B., Clemons, P. A., Hammond, P. T., … Schreiber, S. L. (2020). Plasticity of ether lipids promotes ferroptosis susceptibility and evasion. *Nature*, *585*(7826), 603–608. https://doi.org/10.1038/s41586-020-2732-8